Sensor-based sorting opportunities for hydrothermal ore deposits
Raw material beneficiation in mining

Dalm, Marinus

DOI
10.4233/uuid:70a1e180-ef0c-4226-9af3-7e9dc3938c7f

Publication date
2018

Document Version
Final published version

Important note
To cite this publication, please use the final published version (if applicable).
Please check the document version above.

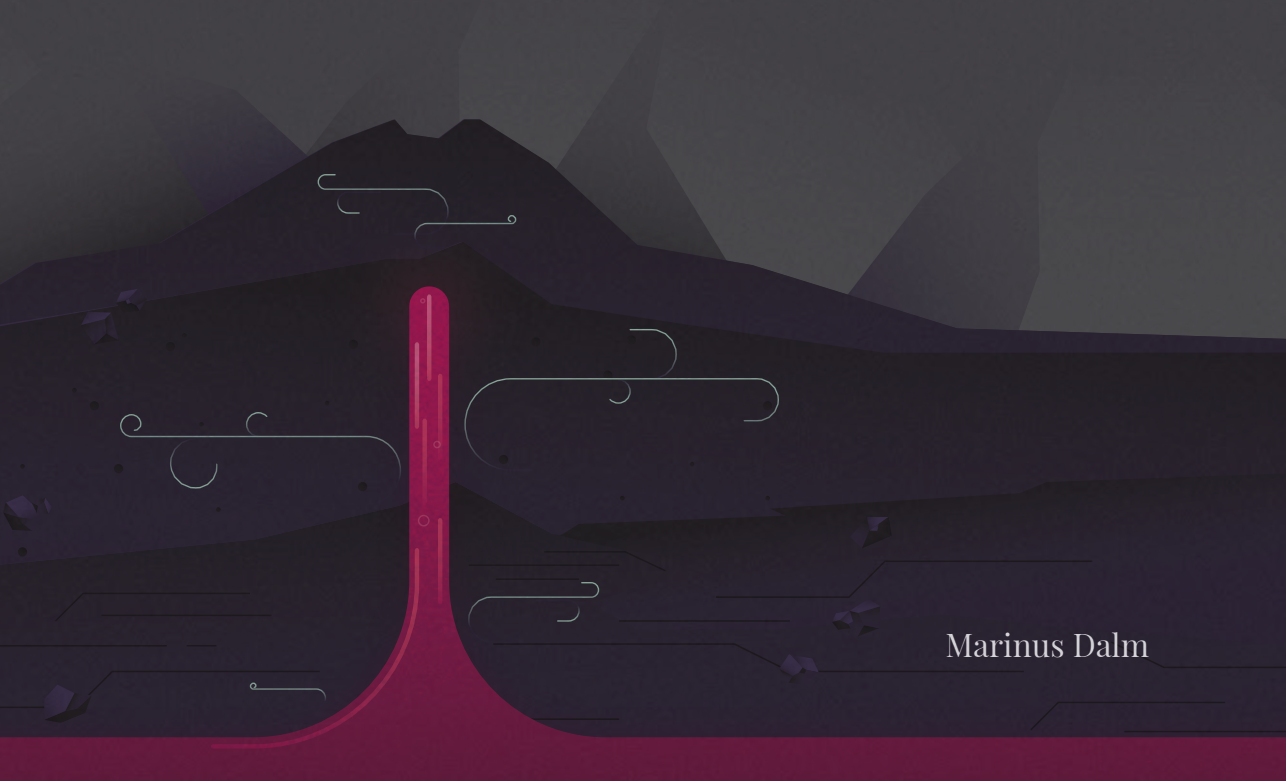Raw material beneficiation in mining

—

sensor-based sorting opportunities for hydrothermal ore deposits

—

Marinus Dalm

Finding Gold

An animated synopsis of the work presented
in this thesis is available here:

vimeo.com/255521448

Raw material beneficiation in mining

sensor-based sorting opportunities for hydrothermal ore deposits

Dit proefschrift is goedgekeurd door de promotoren.

Samenstelling promotiecommissie bestaat uit:

Rector magnificus,	Voorzitter
Prof. dr. ir. J.D. Jansen	Technische Universiteit Delft, promotor
Dr. M.W.N. Buxton	Technische Universiteit Delft, copromotor

Onafhankelijke leden:

Prof. dr. ir. H.J. Glass	University of Exeter, Groot Brittannië
Prof. dr. M. Menenti	Technische Universiteit Delft
Prof. dr. E. Pirard	Liège Université, België
Dr. K.H.A.A. Wolf	Technische Universiteit Delft

Overig lid:

Dr. F.J.A. van Ruitenbeek	Universiteit Twente

Contents

Summary

Sensor-based particle-by-particle sorting is a technique in which singular particles are mechanically separated on certain physical and/or chemical properties after determining these properties with a sensor. Sensor-based sorting machines can be incorporated into mineral processing operations in order to remove waste or sub-economic ore prior to conventional treatment. This has potential to reduce the consumption of energy and water during mineral processing and thereby decrease processing costs. Furthermore, sensor-based sorting can be used to separate different ore types in order to enhance control of the feed to mineral processing facilities and improve processing efficiency.

For most ore types no sensors are known that can be used to detect the grade of ore particles. This is because many ores are polymineralic rocks in which the economically important minerals occur in relatively low concentrations and in small grain sizes. However, the deposition of ore minerals during the formation of hydrothermal ore deposits is often related to specific hydrothermal alteration zones. This means that it might be possible to characterise the grade of such an ore by using sensors that are capable of detecting differences in hydrothermal alteration mineralogy.

Sensors can be applied throughout the entire mining value chain to collect information on the characteristics of the mined ore in real-time. The information that sensors provide can be used to improve deposit models, improve ore quality control and optimise mineral processing. However, the applicability of real-time sensor technologies has not yet been assessed for many types of ore deposits.

The aim of the study was to explore the opportunities and potential benefits of using sensors for real-time raw material characterisation in mining and investigate the opportunities for sensor-based particle-by-particle sorting at hydrothermal ore deposits. Investigating sorting opportunities was aimed at researching the applicability of real-time sensors to segment waste particles from ore particles and to distinguish between ore particles that represent different ore types. This is based on samples taken from the Los Bronces porphyry copper-molybdenum deposit, the Lagunas Norte epithermal gold-silver deposit, and the Cortez Hills carlin-style gold deposit.

For all the deposits included in the study, a fraction of the waste could be segmented by using a Visible to Near-InfraRed (VNIR) and Short-Wavelength InfraRed (SWIR) spectral sensor to detect the hydrothermal alteration mineralogy. For Lagunas Norte and Cortez Hills, this sensor could also be used to distinguish between different ore types. The ability to segment waste was based on indirect relationships between certain alteration mineral assemblages and the copper or gold grade. Since these relationships correspond to the alteration-mineralisation relationships that generally occur at each deposit type, there is potential that sensors can also be used to segment waste at other porphyry, epithermal or carlin-style deposits.

For all three deposits additional research is required to investigate whether it is economically feasible to use the discrimination capabilities of the VNIR-SWIR spectral sensor for sensor-based particle-by-particle sorting. The feasibility may be limited by surface contaminations of the ore particles feeding the sorter, the influence of water on the discrimination capabilities of the VNIR-SWIR sensor, and the sorting efficiency resulting from misclassification.

Samenvatting

Sensor gestuurde deeltje-voor-deeltje sortering is een techniek waarmee individuele deeltjes mechanisch gescheiden worden op bepaalde fysische en/of chemische eigenschappen nadat deze eigenschappen zijn vastgesteld met een sensor. Sensor gestuurde sorteringsmachines kunnen worden geïntegreerd in ertsverwerkingsprocessen om afvalgesteente of erts met een lage economische waarde te verwijderen voordat de reguliere verwerking plaatsvindt. Hierdoor kan de consumptie van energie en water tijdens de verwerking mogelijk worden verminderd waardoor kosten kunnen worden bespaard. Sensor gestuurde sortering kan ook worden gebruikt om verschillende typen erts te scheiden, zodat de invoer van erts naar de verwerkingsfabrieken beter kan worden beheerd en de efficiëntie van de verwerkingsprocessen kan worden verhoogd.

Voor de meeste ertsen zijn geen sensoren bekend die gebruikt kunnen worden om het gehalte waardevolle mineralen te bepalen. Dit is omdat de meeste ertsen meerdere mineralen bevatten en de waardevolle mineralen vaak in lage concentraties en kleine korrelgroottes voorkomen. De afzetting van waardevolle mineralen tijdens de formatie van hydrothermale ertsvoorkomens is echter vaak gerelateerd aan specifieke hydrothermale alteratie zones. Dit betekent dat het wellicht mogelijk is om het gehalte waardevolle mineralen in een erts te karakteriseren door sensoren te gebruiken om verschillen in de hydrothermale alteratie mineralogie te bepalen.

Sensoren kunnen worden toegepast in het gehele mijnbouwproces om real-time informatie te verzamelen over de eigenschappen van het gemijnde erts. De informatie die de sensoren leveren kan worden gebruikt om modellen van ertslichamen te verbeteren, de kwaliteitscontrole van ertsen te verbeteren, en de mineraalverwerking te optimaliseren. Voor veel ertsvoorkomens is de toepasbaarheid van real-time sensor technieken echter nog niet vastgesteld.

Het doel van de studie was het verkennen van de mogelijkheden en potentiele voordelen van grondstofkarakerisering met real-time sensoren en het bestuderen van de mogelijkheden van sensor gestuurde deeltje-voor-deeltje sortering van hydrothermale ertsen. Het bestuderen van de sorteringsmogelijkheden was erop gericht om de toepasbaarheid te onderzoeken van het gebruik van sensor om afvaldeeltjes van ertsdeeltjes te segmenteren en om verschillende ertstypen te onderscheiden. Dit is gebaseerd op monsters die verkregen zijn van de Los Bronces porfiere koper-molybdeen ertsafzetting, de Lagunas Norte epithermale goud-zilver ertsafzetting, en de Cortez Hills carlin-type goud ertsafzetting.

Voor alle ertsafzettingen waarop de studie was gebaseerd was het mogelijk om een deel van het afvalgesteente te segmenteren door een zichtbare tot nabij-infrarood (VNIR) en korte-golflengte infrarood (SWIR) spectrale sensor te gebruiken om de hydrothermale alteratie mineralogie te detecteren. Voor Lagunas Norte en Cortez Hills was het daarnaast ook mogelijk om deze sensor te gebruiken om verschillen ertstypen te onderscheiden. De mogelijkheid om afvalgesteente te segmenteren was gebaseerd op indirecte verbanden tussen de samenstelling van alteratie mineralen en het koper- of goudgehalte. Omdat deze verbanden overeenkomen met de alteratie-mineralisatie verbanden die over het algemeen voorkomen voor elk type ertsafzetting, is er potentie dat sensoren ook gebruikt kunnen worden om afvalgesteente te segmenteren bij andere porfiere, epithermale of carlin-type ertsvoorkomens.

Voor alle drie de ertsvoorkomens is meer onderzoek nodig om te bepalen of het economisch haalbaar is om de scheidingsmogelijkheden van de VNIR-SWIR sensor te gebruiken voor sensor gestuurde deeltje-voor-deeltje sortering. Deze haalbaarheid kan beperkt worden door vervuiling van het oppervlak van de ertsdeeltjes, de invloed van water op het onderscheidingsvermogen van de VNIR-SWIR sensor, en de sorteer efficiëntie die resulteert uit misclassificatie.

List of abbreviations

Regions of the electromagnetic spectrum		spectral range (µm)
UV	UltraViolet	0.01 - 0.3
VIS	Visible	0.3 - 0.77
NIR	Near-InfraRed	0.77 - 1.4
VNIR	Visible to Near-InfraRed	0.3 - 1.4
SWIR	Short-Wavelength InfraRed	1.4 - 2.5
MWIR	Mid-Wavelength InfraRed	2.5 - 7
LWIR	Long-Wavelength InfraRed	7 - 25
FIR	Far-InfraRed	25 - 350

Sensor technologies	
CCD	Charge-Coupled Device
DE-XRT	Dual-Energy X-Ray Transmission
ICP-AES	Inductive Coupled Plasma Atomic Emission Spectroscopy
LIBS	Laser-Induced Breakdown Spectroscopy
LIF	Laser-Induced Fluorescence
MWT	MicroWave Transimission
MWTI	MicroWave heating & Thermal Imaging
PGNAA	Prompt-Gamma Neutron Activation Analysis
RGB imaging	Red-Gree-Blue imaging
Thz-TDS	Terahertz Time Domain Spectroscopy
TI	Thermal Imaging

Sensor technologies

XRD	X-Ray Diffraction
XRF	X-Ray Fluorescence
XRL	X-Ray Luminescence

Other

CIC	Carbon In Column
CIL	Carbon In Leach
hc-mica	High crystalline white mica
lc-mica	Low crystalline white mica
LV	Latent Variable
PC	Principle Component
PCA	Principle Component Analysis
PLS	Partial Least Squares
PLS-DA	Partial Least Squares Discriminant Analysis
SAG	Semi-Autogenous Grinding
SAM	Spectral Angle Mapping
TCM	Total Carbonaceous Material

Introduction

1.1. Problem definition

The demand for mineral resources continuously increases as a result of the growing world population and economy. To provide future generations with adequate resources and opportunities, sustainable development of mining mineral resources is essential. However, the mining industry is challenged with decreasing ore grades, more complex ore deposits, pressure on commodity prices and increasing energy costs. Innovative technologies are therefore required for more efficient, cost-effective and sustainable extraction of mineral resources.

One of the technologies that have undergone rapid developments over the last few decades is that of real-time sensors for material characterisation. Various sensors are currently available that are capable of providing instantaneous information on the characteristics of ores. However, implementation of sensor systems for ore characterisation is still uncommon throughout the mining industry. Collecting information on ores is in most cases only performed by discontinuous sampling and laboratory analyses, which are expensive and time consuming. The information that sensors can provide is usually not fully appreciated and there is often a lack of confidence in the potential benefits of sensor applications.

One specific type of sensor application that has potential to improve the efficiency and costs associated with the processing of ores is sensor-based particle-by-particle sorting. This is a technique in which singular particles are mechanically separated on certain physical and/or chemical properties after determining these properties with a sensor. Sensor-based sorting machines can be incorporated into mineral processing operations in order to remove waste or sub-economic ore prior to conventional treatment. This has potential to reduce the consumption of energy and water during mineral processing and thereby decrease processing costs (Buxton & Benndorf, 2013; Lessard et al., 2014; Salter & Wyatt, 1991; Sivamohan & Forssberg, 1991; Wills & Finch, 2016). Furthermore, sensor-based sorting can be used to separate different ore types in order to enhance control of the feed to mineral processing facilities and improve processing efficiency. Sensors that are currently used on sensor-based sorting machines include optical, Visible to Near-InfraRed (VNIR), Short-Wavelength InfraRed (SWIR), Dual-Energy X-Ray Transmission (DE-XRT), X-Ray Fluorescence (XRF), X-Ray Luminescence (XRL) and natural radioactivity sensors (Wills & Finch, 2016).

Sensor-based sorting machines that are currently available on the market can sort individual particles at throughputs up to 200 tonnes per hour (Wotruba & Harbeck, 2010). In order to achieve such a throughput sensors are required that are able to collect data at relatively high speeds. For most ore types no such sensors are known that can be used to directly detect the grade of the ore particles. This is because most ores are polyminerallic rocks in which the economically important minerals often occur in relatively low concentrations and in small grain sizes. However, the deposition of ore minerals during the formation of hydrothermal ore deposits is often related to specific hydrothermal alteration zones (Pirajno, 1992). This means that it might be possible to characterise the grade of such an ore by using sensors that are capable of detecting differences in hydrothermal alteration mineralogy.

1.2. Aim and objectives

The aim of the study presented in this dissertation is to explore the opportunities and potential benefits of using sensors for real-time raw material characterisation in mining and investigate the opportunities for sensor-based particle-by-particle sorting at hydrothermal ore deposits. Investigating sorting opportunities is aimed at researching the applicability of real-time sensors to segment waste particles from ore particles and to distinguish between ore particles that represent different ore types. Only the applicability of using real-time sensors to characterise ore particles will be investigated. The feasibility of using sensor-based sorting machines to sort ores is out of scope.

The presented study into sensor-based sorting opportunities for hydrothermal ore deposits is based on samples taken from three different deposits. Each sample represents an individual rock particle. The deposits that are included are the Los Bronces porphyry copper-molybdenum deposit, the Lagunas Norte epithermal gold-silver deposit and the Cortez Hills carlin-style gold deposit.

For Los Bronces ore and waste are defined by a cut-off grade of 0.40% Cu. This cut-off grade is the minimum copper grade that is required for economic processing of the ore. Although some of the ore also contains molybdenum, the molybdenum grade is not considered for the definition of ore and waste. The objective of the Los Bronces study is to use real-time sensor data to segment a population of samples that all have copper grades below 0.40%.

For Lagunas Norte ore and waste are defined by an economic cut-off grade of 0.20 ppm Au. Although some of the ore also contains silver, the silver grade is not considered for the definition of ore and waste. Furthermore, different ore types are distinguished at Lagunas Norte. First of all, oxide and sulphide ore are distinguished based on a sulphur content of 0.25%. Secondly, carbonaceous ore is distinguished based on the content of Total Carbonaceous Material (TCM). Ore with a TCM content > 0.5% is considered carbonaceous ore. The objectives of the Lagunas Norte study are to use real-time sensor data to:

- Segment a population of samples that all have gold grades below 0.20 ppm.

- Distinguish samples with a sulphur content above or below 0.25%.

- Distinguish samples with a TCM content above or below 0.5%.

For Cortez ore and waste are defined by an economic cut-off grade of 0.15 ppm Au. Different ore types are also distinguished at Cortez. First of all, low and high grade ore are distinguished based on a cut-off grade of 5.14 ppm Au (0.15 troy ounce per short ton). Secondly, oxide and refractory ore are distinguished based on a gold recovery of 50%. The objectives of the Cortez study are to use real-time sensor data to:

- Segment a population of samples that all have gold grades below 0.15 ppm.

- Segment a population of samples that all have gold grades below 5.14 ppm.

- Distinguish samples with a gold recovery above or below 50%.

When investigating opportunities for sensor-based particle-by-particle sorting of waste it is not necessarily needed to segment all the waste particles. This is because sensor-based sorting can already provide economic benefits if a significant fraction of the waste can be eliminated.

1.3. Dissertation structure

This dissertation is structured as follows:

- Chapter 1 provides a general introduction.

- Chapter 2 presents a discussion of the opportunities and potential benefits of using sensors for real-time raw material characterisation in mining.

- Chapter 3 presents the detailed characteristics and working principles of the sensors that were used in the study.

- Chapter 4 presents a review of the hydrothermal alteration mechanisms that are associated with the three deposit types that are investigated.

- Chapter 5 present a review of multivariate analysis and regression methods that were used to analyse the data obtained from sensor measurements.

- Chapter 6 presents the findings of the Los Bronces case study. This includes a description of the geologic setting, samples and objectives as well as the methods, results and conclusions of testing two different sensors.

- Chapter 7 presents the findings of the Lagunas Norte case study. This includes a description of the geologic setting, samples and objectives as well as the methods, results and conclusions of testing four different sensors by using two different sample sets.

- Chapter 8 presents the findings of the Cortez case study. This includes a description of the geologic setting, samples and objectives as well as the methods, results and conclusions of testing one sensor.

- Chapter 9 presents a discussion of the methods and results of all the tests that were performed.

- Chapter 10 summarises the conclusions of the research.

1.4. References

BUXTON, M. & BENNDORF, J. 2013. The use of sensor derived data in optimization along the Mine-Value-Chain. *Proceedings of the 15th International ISM Congress*, Aachen, Germany, pp. 324-336.

LESSARD, J., DE BAKKER, J. & MCHUGH, L. 2014. Development of ore sorting and its impact on mineral processing economics. *Minerals Engineering*, 65, 88-97.

PIRAJNO, F. 1992. *Hydrothermal mineral deposits: principles and fundamental concepts for the exploration geologist*, Berlin Heidelberg, Springer-Verlag.

SALTER, J. & WYATT, N. 1991. Sorting in the minerals industry: past, present and future. *Minerals Engineering*, 4, 779-796.

SIVAMOHAN, R. & FORSSBERG, E. 1991. Electronic sorting and other preconcentration methods. *Minerals Engineering*, 4, 797-814.

WILLS, B. A. & FINCH, J. A. 2016. Chapter 14 - Sensor-based Ore Sorting. *Wills' Mineral Processing Technology (Eighth Edition)*. Boston: Butterworth-Heinemann.

WOTRUBA, H. & HARBECK, H. 2010. Sensor Based Sorting. *Ullmann's Encyclopedia of Industrial Chemistry*.

Chapter 2.

Sensor applications in mining.

2.1. Introduction

Various sensor systems are available on the market that are designed to gather data on drill core, production drill holes, rock faces, conveyor belts and shovel and truck loads (e.g. Corescan, 2017; IMA Engineering, 2017; Minesense, 2017; Scantech, 2017; Specim, 2017; ThermoFisher, 2017a). Furthermore, sensor-based sorting machines for particle-by-particle sorting are available from a range of manufacturers (e.g. Comex, 2017; Redwave, 2017; SCOTT, 2017; Steinert, 2017; Tomra, 2017). However, implementation of such sensor systems throughout the mining industry is still uncommon. The information that sensors can provide is usually not fully appreciated and there is often a lack of confidence in the potential benefits of sensor applications. Practical concerns regarding the robustness, reliability and throughput of sensor systems often seem to outweigh the mining industry's willingness to test sensor applications in order to investigate their true benefits.

The ability to use sensors to characterise raw materials in real-time provides the opportunity to gather information from relatively large material volumes. This could reduce the need for sampling and provide more representative data by eliminating sampling errors. The fact that the information is instantly available means it can likely be used to; i) optimise mineral processing through improved grade control and/or predicting processing behaviour of the feed to processing plants, ii) sort different material types or remove sub-economic material from subsequent mineral processing operations with sensor-based sorting machines.

The aim of this chapter is to examine the opportunities for sensors applications at different areas within the mining value chain and to evaluate the potential benefits of using sensors for real-time raw material characterisation.

Figure 2.1: Opportunities for sensor applications in the mining process. (next page)

process steps

application of sensors

---

delineation

| exploration | ———● drill core characterisation & downhole logging |

↓

deposit modelling

mine planning

---

development

| mine development | ———● positioning (relative to geology) |

---

extraction

| production drilling | ———● grade control on drill chips & downhole logging |

↓

| blasting | ———● rock face & muck pile classification |

↓

| hauling | ———● classification during transport & bulk sorting |

●———— feed characterisation & particle by particle sorting

processing

comminution

↓

| beneficiation | ———— product quality control & reconciliation |

↓

metallurgy

---

marketing

marketing

2.2. Opportunities for sensor applications

2.2.1. Introduction

Figure 2.1 presents a general overview of the mining value chain on which the possible application areas for sensors are indicated. The value chain is sub-divided into: delineation of a deposit, development of a mine, extraction of resources, processing of the mined material, and finally selling a product on the market. Each of these processes is characterised by several process steps. Considering the extraction of resources, variations exist in the process steps depending on the type of deposit that is mined (e.g. Hartman & Mutmansky, 2002). The steps presented in Figure 2.1 are typical for traditional mining methods in hard rock conditions.

2.2.2. Exploration

Deposit delineation represents all activities from the first discovery of a deposit up to the start of the first development work to mine the deposit. The first step of deposit delineation is exploration. The purpose of exploration is to find new deposits that are economic to mine. After a new deposit has been discovered, exploration involves the acquisition of physical samples from the deposit. This is usually performed by diamond core drilling (Hartman & Mutmansky, 2002). Geochemical assays are performed on the drill core samples in order to obtain information on the chemical, mineralogical and metallurgical properties. Furthermore, geological maps of the deposit are produced by using the drill core. The geochemical information and geological maps are combined to produce a deposit model. Based on the deposit model, different options to mine the deposit are developed and feasibility studies are performed in order to assess whether mining the deposit is economic. If mining the deposit turns out to be economically viable, a mining plan is made by designing a mine, defining the mineable units and developing an extraction sequence.

Since deposit delineation is the first process step in which physical samples are obtained, this is also the first opportunity in the life of a mine to use sensors for raw material characterisation. Instruments are available on the market that are designed to collect mineralogical data on drill core samples by using optical, Visible to Near-InfraRed (VNIR), Short-Wavelength InfraRed (SWIR) and/or Long-Wavelength InfraRed (LWIR) sensors (e.g. Corescan, 2017; Specim, 2017). An example of such an instrument is the SisuRock drill core scanner (SPECIM ltd., Oulu, Finland)

Figure 2.2: SisuRock drill core scanner (SPECIM ltd., Oulu, Finland). Entire core trays of maximum 1.50 x 0.64 m can be fed through the instrument (Specim, 2017).

shown in Figure 2.2. To obtain chemical information, it is possible to use drillcore scanners equipped with X-Ray Fluorescence (XRF) sensors (Sjöqvist et al., 2015; Minalyze, 2017). Chemical information can also be acquired by taking measurments down a drill hole with a Prompt Gamma Neutron Activation Analysis (PGNAA) sensor (e.g. Sodern, 2017). Furthermore, rock quality designations (RQD) can be performed by mapping the topography of the extracted drill core with a 3D laser scanner (Minalyze, 2017). Finally, it is possible to characterise the hardness of a rock mass by recording the operating parameters of the drill rig itself (Khorzoughi & Hall, 2016).

2.2.3. Development

After delineation of the deposit and producing an economically feasible mining plan, the next step in the mining value chain is mine development. This includes building all the required infrastructure, facilities and access to the deposit. When developing the deposit access, sensor-based characterisation of rock faces can be used for positioning relative to the geology. VNIR, SWIR and LWIR sensor systems that are similar to those used for drill core scanning are available to do this (e.g. Specim, 2017). Furthermore, handheld XRF devices can be used to manually collect chemical data anywhere in the field (e.g. Bruker, 2017; ThermoFisher, 2017b).

2.2.4. Extraction

The most common method for mining raw materials is by using traditional drilling and blasting techniques. This includes drilling holes into a rock face, charging the holes with explosives, and detonating the explosives to fragment the rock. The blasted material is loaded using a shovel or wheel loader, and is transported by truck, conveyor belt and/or skip hoist to the mineral processing facilities. When mining in softer rock conditions, mechanical rock breaking techniques such as continuous miners or bucket wheel excavators can be used instead of drilling and blasting (Rostami, 2011). In both cases, sensor-based characterisation of raw materials can be done in the field or during transport of the excavated material. When using drilling and blasting techniques, it is additionally possible to use sensors for characterising the material produced from drilling the blast holes or for measurements down the drill holes. Figure 2.3 presents an overview of the opportunities for sensor-based material characterisation in open pit mining. Similar opportunities exist in an underground mining operation.

Taking sensor measurements in the field includes scanning a rock face or muck pile. The same sensors that allow field measurements to be taken during mine development can be used to do this. For taking sensor measurements during material transport, a wide range of applications are available. First of all, sensor systems integrated on shovels or wheel loaders exist that can be used to gather chemical data with XRF sensors or conductivity data with inductive sensors (e.g. Minesense, 2017). The conductivity of a raw material is related to the amount of conductive minerals that it contains. Conductive minerals include certain metal-sulphides and inductive sensors can therefore be used to characterise the grade of certain metal ores (Sivamohan & Forssberg, 1991). Secondly, it is possible to gather mineralogical information with an application in which a wheel loader or truck passes underneath a Laser-Induced Fluorescence (LIF) sensor (e.g. IMA Engineering, 2017). Finally, applications exist to characterise mined raw materials on a conveyor belt using PGNAA or natural radiation detectors (e.g. Scantech, 2017; ThermoFisher, 2017a).

The information obtained from sensor-based characterisation during material transport can be used directly for sorting purposes. This concept is commonly referred to as sensor-based sorting (Salter & Wyatt, 1991; Sivamohan & Forssberg, 1991; Wills & Finch, 2016). Two different types of sensor-based sorting should be distinguished. First of all, it is possible to use the information derived from sensors that scan a shovel or truck load to directly route the material to different stock piles or processing streams. In a similar fashion, batches of material that are being transported on a conveyor belt can be sorted based on sensor information. This type of sensor-based sorting will be referred to as bulk sorting. Another application of sensor-based sorting is to sort individual rock particles. Sorting equipment is available on the market that is able to mechanically separate singular rock particles after detecting certain physical and/or chemical properties of the particles with a sensor (e.g. Comex, 2017; Redwave, 2017; SCOTT, 2017; Steinert, 2017; Tomra, 2017). This type of sensor-based sorting will be referred to as particle-by-particle sorting.
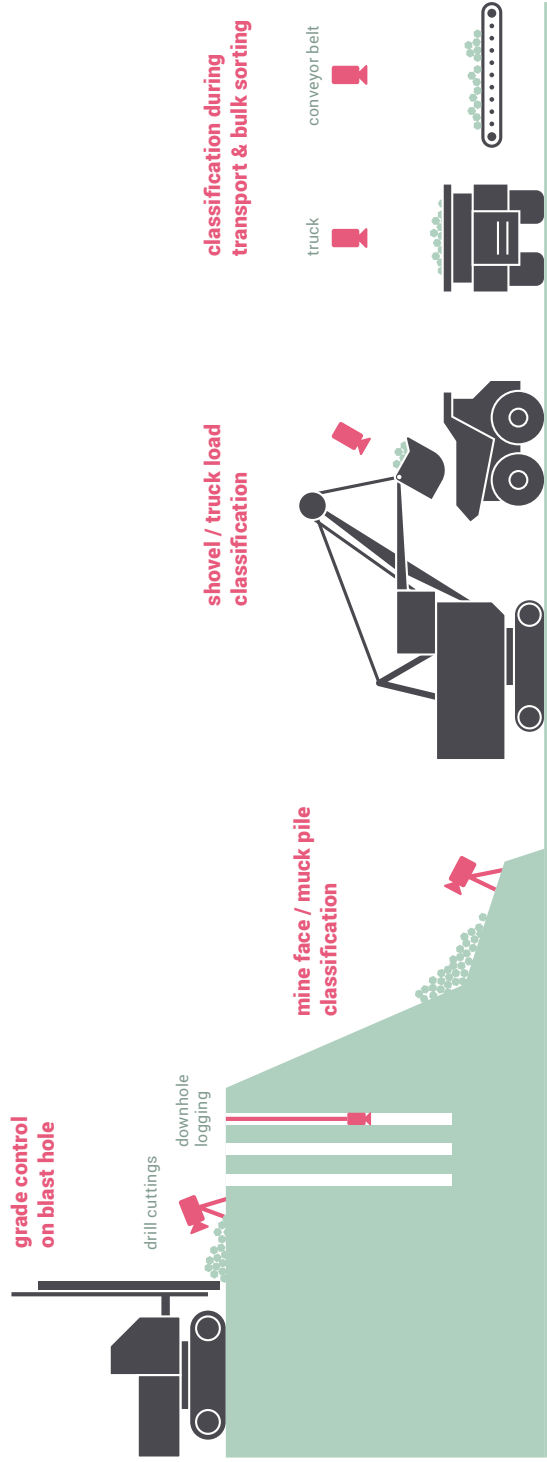
Figure 2.3: Overview of opportunities for sensor-based material characterisation in open pit mining.

grade control
on blast hole

drill cuttings

downhole
logging

mine face / muck pile
classification

shovel / truck load
classification

classification during
transport & bulk sorting

truck

conveyor belt

2.2.5. Processing

The processing of raw materials often involves comminution, beneficiation and metallurgy. Comminution is the crushing and grinding to a certain particle size. When processing metal ores, the required particle size after comminution is usually the size at which it is possible to separate individual minerals. This is because beneficiation of these ores often involves gravity separation, froth flotation or dense medium separation in order to concentrate the ore minerals (Wills & Napier-Munn, 2015). This process step is sometimes also simply referred to as mineral concentration. The final step in processing metal ores is to produce a metal from the ore concentrate via pyrometallurgical, hydrometallurgical and/or electrometallurgical treatment.

Sensor systems that can be applied to characterise materials on a conveyor belt during resource extraction, can also be used before, during and after comminution. Furthermore, sensor-based sorting systems can be integrated in between crushing and grinding or within grinding circuits. Lessard et al. (2016) for example proposes to use particle-by-particle sorting to remove sub-economic ore from the stream of pebbles produced from semi-autogenous grinding.

2.2.6. Marketing

The final stage in the mining value chain is marketing of the product. At this stage, sensors can be applied for product quality control. The same sensor systems that are available to characterise materials during the transport of extracted resources can be applied.

2.3. Real-time raw material characterisation

Real-time raw material characterisation can be defined as using sensors to obtain information about the properties of a raw material without physically removing samples or sample preparation and within a time period that allows the information to be used for decision making. This means that in this context the term "real-time" depends on the application in which sensors are used. However, sensor applications do need to add value and should therefore not obstruct a mine's production rate.

The sensor application that has by far the shortest time period requirement for data acquisition is particle-by-particle sorting. This is because the sensor data needs to be available within microseconds in order to have enough time for data processing, classification, and mechanically separating particles less than a second later. An example of real-time characterisation for which somewhat longer data acquisition times are available is the scanning of batches of material on a conveyor belt. In this case it would be possible to obtain a moving average by gathering sensor data over a time period of several minutes. Even longer data acquisition times are available for scanning a rock face. The obtained sensor information of this application can be used to improve deposit models and data acquisition times up to several days are available in order to keep up with production scheduling.

An important aspect about real-time raw material characterisation is that the information that is provided by a sensor needs to describe relevant material properties. Since mining is a business that aims to generate a profit, a material property is relevant if real-time information about the material property can be used to improve the economics of the mining value chain. When mining industrial minerals, the material property with the largest influence on the economics is usually a specific physical and/or chemical property for which the material is mined. When mining a fossil fuel such as coal it is the quality of the fossil fuel that is the main material property that is affecting the economics. The quality of fossil fuels is often expressed in terms of calorific value and/or ash content. The material property that has the largest influence on the economics of mining metal ores is usually the concentration or grade of a certain metal within the ore. Other material properties affecting the economics of the mining value chain are related

to the processing behaviour of the mined material. Examples are the required comminution energy or the ability to recover valuable minerals.

It is not always possible to use sensors to directly detect a certain material property of interest, such as ore grade. However, in some cases a relationship exists between the material property of interest and some other material property that can be detected with sensors. Such relationships can often be explained by studying the geology of a deposit. As explained in chapter 1.1, it might be possible to use sensors that are capable of detecting differences in hydrothermal alteration mineralogy to characterise the grade of the ore samples included in this study. This is because mineralisation at hydrothermal ore deposits is often related to specific hydrothermal alteration zones (Pirajno, 1992). Using such a calibrated proxy in order to characterise a material property of interest will be referred to as indirect characterisation. Direct characterisation refers to using sensors that are able to detect a material property of interest directly, such as a PGNAA sensor for detecting the sulphur content of coal (Borsaru et al., 2004).

Table 2.1 presents an overview of material properties that can be directly detected with the real-time sensing technologies that are available. The table also shows the physical property that is detected by the sensors and the measured effect on which the characterisation of the material properties is based.

Table 2.1: Material properties that can be detected with real-time sensors. See the list of abbreviations for a description of sensor acronyms.

Physical property	Sensor technology	Measured effect	Material property directly characterised
Reflectance	Reflectance spectrometry (UV-VIS-NIR-SWIR-MWIR-LWIR-FIR)	Mineral absorption features	Mineralogy
	RGB imaging	Visible appearance	Visible appearance
Luminescence (emission)	LIF & XRL	Mineral fluorescence	Mineralogy
	Raman	Raman scattering	Mineralogy
	XRF & LIBS	Atomic fluorescence	Chemistry
	PGNAA & Natural Radioactivity	Atomic radioluminescence	Chemistry
Incandescence (emission)	TI	Blackbody radiation	Heat capacity & transfer
	MWTI	Blackbody radiation after microwave heating	Heat capacity & transfer
Transmitted radiation	DE-XRT & DE-γRT	Transmitted X-rays / γ-rays	Density
	MWT	Transmitted microwaves	Moisture content
	THz-TDS	Transmitted terahertz radiation	Absorption & Refraction index
Electric conductivity	Inductive	Changes in electro-magnetic field	Electric conductivity

2.4. Potential benefits

2.4.1. Introduction

The following sections will discuss the potential benefits of using sensors for real-time raw material characterisation in a qualitative manner. Several published works are also available that have made attempts to quantify the benefits of using sensors for real-time raw material characterisation. Buxton & Benndorf (2013) for example present a semi-quantitative analysis of the potential economic benefits of utilising sensors for raw material characterisation at different stages of the mining value chain. Another example is the work of Lessard et al. (2014) showing the potential savings in comminution energy as a result of particle-by-particle sorting of a molybdenum ore. Furthermore, Lessard et al. (2016) presents potential profits of particle-by-particle sorting at a copper mine based on assumed operational performance of a sorting machine. Apart from these exploratory studies, results of actual cost and energy savings from testing sensors for real-time raw material characterisation are not publicly available. Unfortunately, the mining industry is rather conservative and new technologies are therefore only rarely adopted unless the added value of these has been demonstrated. The paradox in this is that the only way to properly assess the true benefits of real-time raw material characterisation is to test it at an operating mine.

2.4.2. Improve deposit models

Perhaps the most obvious benefit of using sensors for real-time raw material characterisation is that the sensor information can be used to improve the understanding of how mineralisation and other relevant material properties are spatially and quantitatively distributed throughout a deposit. This can be used to better define different zones within the deposit and construct more accurate deposit models. More accurate deposit models can in turn be used to improve mine design, mine planning and grade control. Furthermore, mineral exploration can be improved by using sensor information to better define chemical and mineralogical traces that can act as vectors of mineralisation.

Utilising sensors to characterise the drill core samples produced from exploration drilling offers potential to maximise the amount of information that is obtained from exploration studies. This is likely to be cost effective, since drill core samples are relatively expensive to obtain and analyse. With traditional practices only a geologist's interpretation from visual inspection and geochemical assays taken over one or two meter intervals are produced. Sensors can additionally provide detailed mineralogical information and chemical data that is representative of

smaller intervals. When sensor technologies further mature and become more reliable, the need to perform lab work in order to obtain geochemical data might even be eliminated. Furthermore, it is likely possible to automate material classifications performed by geologists and obtain a more objective representation of the geology of a deposit.

2.4.3. Ore quality control and downstream process optimisation

It is likely possible to enhance the performance of mineral processing facilities by using real-time sensor data to provide a more constant feed quality through improved stockpiling and/or sensor-based sorting. Control of the feed can also be improved by using sensor data that is gathered during the life of a mine to update the deposit models and improve mine planning (Benndorf & Jansen, 2017; Benndorf et al., 2015). Furthermore, sensor data can likely be used to predict the processing behaviour of a material, such as the required comminution energy or the recovery from metal ores. This can be achieved by recording the process parameters and performance of a mineral processing plant and linking these recordings to previously obtained sensor data in order to produce predictive models. Research is still required to investigate the practical feasibility of producing such predictive models and the levels of precision that can be achieved. However, the construction of such models is in theory possible considering the fact that the processing behaviour of a material is related to its chemical and mineralogical composition and sensors exist that can provide this information through either direct or indirect characterisation. It would mean that the control of the feed to processing facilities can be further improved by incorporating mineral processing behaviour into deposit models or using this information for stockpiling and/or sensor-based sorting. Finally, it might be possible to enhance processing performance by using real-time sensors to detect the characteristics of the feed and dynamically adjust the settings of the processing plant to optimize processing for those characteristics.

2.4.4. Sensor–based sorting

As mentioned in chapter 2.2.4, we distinguish two types of sensor-based sorting; bulk sorting and particle-by-particle sorting. However, it should be noted that many other authors do not make this distinction and refer only to particle-by-particle sorting by using the term "sensor-based sorting", "ore sorting", "electronic sorting" or "automated sorting" (e.g. Lessard et al., 2016; Salter & Wyatt, 1991; Sivamohan & Forssberg, 1991; Wills & Finch, 2016; Wotruba & Harbeck, 2010). The concept of bulk sorting and particle by particle sorting is illustrated in Figure 2.4 and Figure 2.5 respectively.

The main difference between particle-by-particle sorting and bulk sorting is that with particle-by-particle sorting each individual particle is evaluated and sorted while bulk sorting deals with batches of material consisting of many different particles. In both methods the material

is sorted by setting sorting criteria on a certain material characteristic that is detected by the sensor. In bulk sorting, that material characteristic represents the average of all the particles in the batch that is sorted. This means that the individual particles of the sorted product can still have characteristics that fall outside the sorting criteria for that product. In particle-by-particle sorting this may also occur due to misclassifications by the sorting mechanism. However, the amount of misclassifications at the particle level will be larger for bulk sorting than particle-by-particle sorting.

The disadvantage of particle-by-particle sorting over bulk sorting is that the throughput that can be achieved with particle-by-particle sorting is limited, unless many different sorting machines are operated in parallel. Particle-by-particle sorting machines that are currently available on the market have a maximum throughput of around 200 tonnes per hour (Wotruba & Harbeck, 2010). Furthermore, it is recommended to keep the ratio between the maximum and minimum particle size below three to be able to mechanically separate the particles with sufficient accuracy (Wills & Finch, 2016; Wotruba & Harbeck, 2010). Finally, particle-by-particle sorting is usually limited to particles within a size range of 0.5 to 350 mm, although it is often not economically feasible to sort raw materials with a particle size below 10 mm (Wills & Finch, 2016). The reason for this is that the efficiency and throughput of sorting machines decreases with decreasing particle size of the material that is sorted.

The main advantage of particle-by-particle sorting is that it offers potential economic benefits by using it as a pre-concentration or pre-processing step in processing facilities in order to eliminate waste or sub-economic material from subsequent processing steps (Lessard et al., 2016; Salter & Wyatt, 1991; Sivamohan & Forssberg, 1991; Wills & Finch, 2016; Wotruba & Harbeck, 2010). This is largely due to the fact that it can provide significant energy savings by reducing the amount of material in comminution processes (Lessard et al., 2014). Furthermore, removing waste with particle-by-particle sorting can in many cases also reduce the water consumption per tonne of material processed. Particle-by-particle sorting can therefore provide both economic and environmental benefits.

Another application of particle-by-particle sorting is to improve the efficiency of mineral processing by eliminating material that has deleterious effects on processing performance and finished products. Furthermore, particle-by-particle sorting can be used to separate different ore types in order to enhance control of the feed to processing facilities. In this application it is likely possible to improve processing by tailoring different processing methods to specific material types. In the processing of certain metal ores for example, particle-by-particle sorting could be used to separate oxide and sulphide ores.

Bulk sorting can also be applied for sorting different material types and improving feed control by using it in combination with stockpiling and blending. Although bulk sorting of waste also provides potential economic benefits (e.g. Valery et al., 2016), it is likely less effective due to the relatively high amount of misclassifications at the particle level. If a batch of material is characterised as waste, this means that on average it is uneconomic to process all particles within this batch. However, a portion of the particles might actually be valuable enough for economic processing. This means that valuable material will be discarded when bulk sorting of waste

diverter gate
Switches the stream
of material, based on
sensor information.
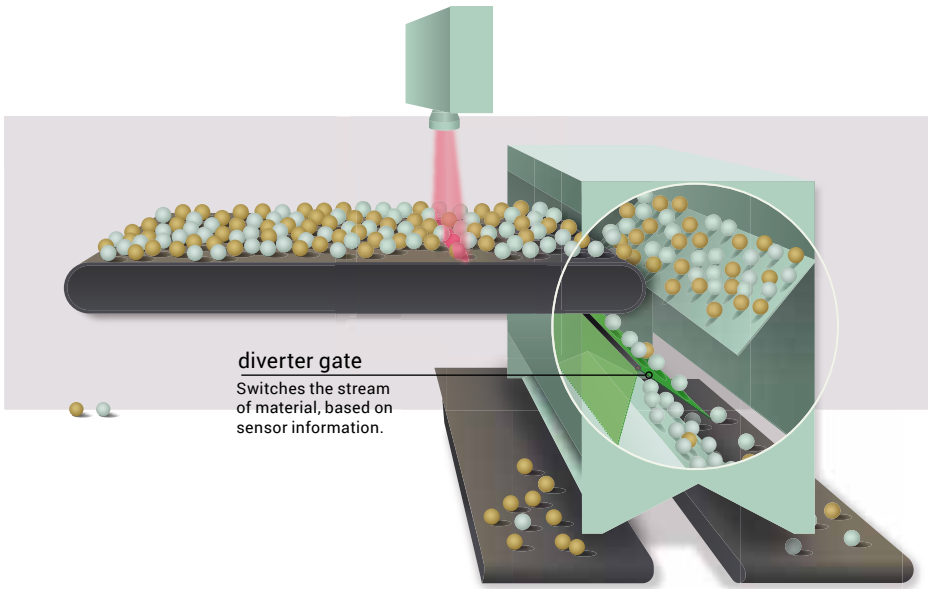
Figure 2.4: Bulk sorting concept.
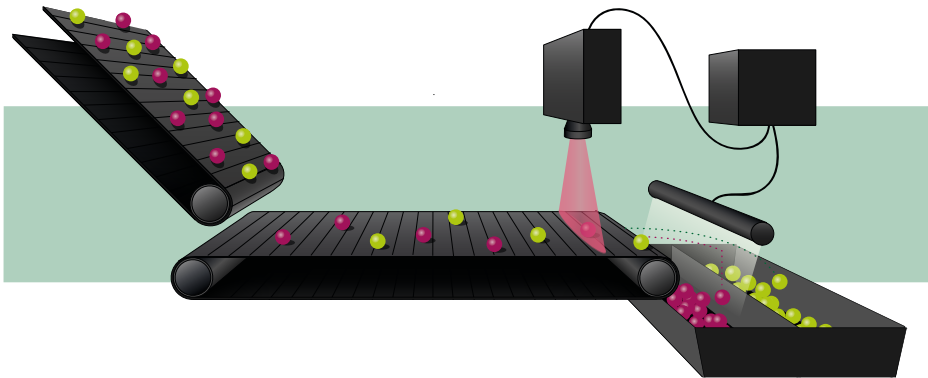
Figure 2.5: Particle-by-particle sorting concept.

is applied. The amount of valuable material that is discarded depends on the volume of the batches that are sorted. Discarding too much valuable material, however, should not be encouraged since this is not a responsible use of mined resources. It is important to consider this in any sensor-based sorting application, including particle-by-particle sorting. Finally, it should be noted that utilising sensors during the exploration phase of a mining project has the additional advantage that the sensor data can be used to assess sensor-based sorting opportunities at an early stage of the mining process.

2.5. Discussion

The number of research papers that investigate the applicability of sensors for real-time raw material characterisation is continuously increasing. Most papers in the field focus on investigating sensor-based sorting applications. Examples of sensor-based sorting in mining include the sorting of uranium ore based on the detection of natural radioactivity (Sivamohan & Forssberg, 1991), sorting diamonds using X-Ray Luminescence (XRL) (Rylatt & Popplewell, 1999) and sorting coal with Dual-Energy X-Ray Transmission (DE-XRT) sensors (von Ketelhodt & Bergmann, 2010). Apart from sensor-based sorting, sensors systems exist that can be installed on conveyor belts to allow continuous quality control of the raw material that is being transported. Examples in which this has been successful are the use of PGNAA sensors to detect the quality parameters of iron ore (Kurth, 2015) and using natural radioactivity sensors to measure the ash content of coal (Taylor et al., 2013). Furthermore, sensor systems for scanning the drill core obtained from exploration drilling have shown to be successful in providing relevant information, such as predicting the lump-fine ratio of iron ore with VNIR spectrometry (Haest et al., 2015).

Investigations into the applicability of sensors for real-time raw material characterisation are usually performed on material from one specific deposit. However, the results obtained from these investigations can often not be extrapolated to other deposit styles. This is mainly because the style of deposit defines the material properties that are relevant for sensor-based characterisation. The limit up to which a certain property can be detected and the detection accuracy that can be achieved varies between different material properties. This means that an assessment of the applicability of sensors is required for each individual deposit style in order to determine the feasibility of using sensors to characterise the materials that are mined from a deposit.

It might be possible that a certain material property of interest can be characterised indirectly by using some other material property as a calibrated proxy. However, it is uncertain if such an indirect relationship also occurs at other deposits of the same style since it could be restricted to a specific geological setting. In order to assess whether it is possible to use indirect relationships for real-time raw material characterisation, investigations into these relationships are required for each individual deposit.

2.6. Conclusions

Sensors for real-time raw material characterisation can be applied throughout the entire mining value chain and can potentially provide both economic and environmental benefits. The information provided by sensors may be used to improve deposit models, improve ore quality control and optimise mineral processing. Sensor-based sorting can be used to eliminate waste from subsequent processing steps or to sort different ore types. However, for many types of ore deposits it is unkown to what extent real-time sensor technologies can be used to characterise the ore quality parameters.

2.7. References

BENNDORF, J. & JANSEN, J. D. 2017. Recent Developments in Closed-Loop Approaches for Real-Time Mining and Petroleum Extraction. *Mathematical Geosciences*, 49, 277-306.

BENNDORF, J., YUEKSEL, C., SHISHVAN, M. S., ROSENBERG, H., THIELEMANN, T., MITTMANN, R., LOHSTRÄTER, O., LINDIG, M., MINNECKER, C. & DONNER, R. 2015. RTRO−Coal: Real-Time Resource-Reconciliation and Optimization for Exploitation of Coal Deposits. *Minerals*, 5, 546-569.

BORSARU, M., BERRY, M., BIGGS, M. & ROJC, A. 2004. In situ determination of sulphur in coal seams and overburden rock by PGNAA. *Nuclear Instruments and Methods in Physics Research Section B: Beam Interactions with Materials and Atoms*, 213, 530-534.

BRUKER. 2017. *Handheld XRF spectrometry* [Online]. Available: https://www.bruker.com/products/x-ray-diffraction-and-elemental-analysis/handheld-xrf.html [Accessed February 2017].

BUXTON, M. & BENNDORF, J. 2013. The use of sensor derived data in optimization along the Mine-Value-Chain. *Proceedings of the 15th International ISM Congress*, Aachen, Germany, pp. 324-336.

COMEX. 2017. *Comex sorting technology* [Online]. Available: http://www.comex-group.com/en/products-and-solutions/sorting-technology [Accessed February 2017].

CORESCAN. 2017. *The corescan system* [Online]. Available: http://www.corescan.com.au/services/the-corescan-system [Accessed February 2017].

HAEST, M., MITTRUP, D. & DOMINGUEZ, O. 2015. Reaping the first fruits - Infrared Spectroscopy: the new standard tool in BHP Billiton iron ore exploration. *Iron Ore Conference*. Perth, Australia.

HARTMAN, H. L. & MUTMANSKY, J. M. 2002. *Introductory mining engineering*, John Wiley & Sons.

IMA ENGINEERING. 2017. *Products & Sevices* [Online]. Available: http://www.ima.fi/products-amp-services/products [Accessed February 2017].

KHORZOUGHI, M. B. & HALL, R. 2016. Processing of measurement while drilling data for rock mass characterization. *International Journal of Mining Science and Technology*, 26, 989-994.

KURTH, H. 2015. Geoscan elemental analyzer for optimising plant feed quality and process performance. *SAG 2015 - conference proceedings*. Vancouver, Britisch Columbia, Canada.

LESSARD, J., DE BAKKER, J. & MCHUGH, L. 2014. Development of ore sorting and its impact on mineral processing economics. *Minerals Engineering*, 65, 88-97.

LESSARD, J., SWEETSER, W., BARTRAM, K., FIGUEROA, J. & MCHUGH, L. 2016. Bridging the gap: Understanding the economic impact of ore sorting on a mineral processing circuit. *Minerals Engineering*, 91, 92-99.

MINALYZE. 2017. *Minalyzer CS Geolytical Core Scanner* [Online]. Available: http://minalyze.com/ [Accessed Oktober 2017].

MINESENSE. 2017. *Products* [Online]. Available: http://www.minesense.com/products/ [Accessed February 2017].

PIRAJNO, F. 1992. *Hydrothermal mineral deposits: principles and fundamental concepts for the exploration geologist*, Berlin Heidelberg, Springer-Verlag.

REDWAVE. 2017. *Mineral sorting* [Online]. Available: http://www.redwave.at/en/mining-solutions/ [Accessed February 2017].

ROSTAMI, J. 2011. Chapter 7.1. Mechanical rock breaking. *SME mining engineering handbook.* SME.

RYLATT, M. G. & POPPLEWELL, G. M. 1999. Diamond processing at Ekatie in Canada. *Mining Engineering*, 51, 19-25.

SALTER, J. & WYATT, N. 1991. Sorting in the minerals industry: past, present and future. *Minerals Engineering*, 4, 779-796.

SCANTECH. 2017. *Scantech products* [Online]. Available: http://www.scantech.com.au/ [Accessed February 2017].

SCOTT. 2017. *Applied Sorting Technology: Sorting and Inspection* [Online]. Available: http://www.scott.co.nz/sorting-and-inspection/ [Accessed February 2017].

SIVAMOHAN, R. & FORSSBERG, E. 1991. Electronic sorting and other preconcentration methods. *Minerals Engineering*, 4, 797-814.

SJÖQVIST, A., ARTHURSSON, M., LUNDSTRÖM, A., ESTRADA, E. C., INERFELDT, A. & LORENZ, H. 2015. An innovative optical and chemical drill core scanner. *Scientific Drilling*, 19, 13.

SODERN. 2017. *Material analysers* [Online]. Available: http://www.sodern.com/website/en/ref/Neutronic_235.html [Accessed Oktober 2017].

SPECIM. 2017. *Hyperspectral imaging in geology* [Online]. Available: http://www.specim.fi/hyperspectral-imaging-in-geology [Accessed February 2017].

STEINERT. 2017. *Innovative sensor systems for new solutions* [Online]. Available: http://www.steinertglobal.com/de/en/products/sensor-sorting/ [Accessed February 2017].

TAYLOR, P. M., COOKE, A. & KNIGHT, C. B. 2013. Natural Gamma for the On-line Measurement of the Ash Content of Conveyed Coal - 25 Years of Success. *Coal preparation congress 2013 - conference proceedings*. Istanbul, Turkey.

THERMOFISHER. 2017a. *ECA Elemental Crossbelt Analyzer* [Online]. Available: https://www.thermofisher.com/order/catalog/product/19187 [Accessed February 2017].

THERMOFISHER. 2017b. *Portable XRF analyzer selection guide* [Online]. Available: https://www.thermofisher.com/nl/en/home/industrial/spectroscopy-elemental-isotope-analysis/portable-analysis-material-id/portable-xrf-analyzer-selection-guide.html [Accessed February 2017].

TOMRA. 2017. *Mining sorting solutions* [Online]. Available: https://www.tomra.com/en/solutions-and-products/sorting-solutions/mining/sorting-equipment/ [Accessed February 2017].

VALERY, W., DUFFY, K.-A. & ROSARIO, P. 2016. Techno-economic evaluation of bulk ore sorting for copper ore at the PanAust Phu Kham operation. *International Mineral Processing Congress - conference proceedings*. Quebec, Canada.

VON KETELHODT, L. & BERGMANN, C. 2010. Dual energy X-ray transmission sorting of coal. *Journal of the Southern African Institute of Mining and Metallurgy*, 110, 371-378.

WILLS, B. A. & FINCH, J. A. 2016. Chapter 14 - Sensor-based Ore Sorting. *Wills' Mineral Processing Technology (Eighth Edition)*. Boston: Butterworth-Heinemann.

WILLS, B. A. & NAPIER-MUNN, T. 2015. *Wills' mineral processing technology: an introduction to the practical aspects of ore treatment and mineral recovery*, Butterworth-Heinemann.

WOTRUBA, H. & HARBECK, H. 2010. Sensor Based Sorting. *Ullmann's Encyclopedia of Industrial Chemistry*.

Chapter 3.

Sensor characteristics

3.1. Introduction

The data that is obtained by almost all the real-time sensors that can be used for material characterisation represents some kind of interaction of the material with electromagnetic radiation. These interactions involve the absorption or emission of photons with a specific energy by the constituent elements and/or minerals. It is generally known that the energy of photons is related to the wavelength by Planck's constant (Hollas, 2004). The wavelength positions at which photons are absorbed or emitted therefore provide information on the mineralogical and/or elemental composition of a material. Measurement of the intensity of electromagnetic radiation versus the wavelength is commonly performed with spectrometers.

Figure 3.1 presents an overview of the electromagnetic spectrum and the different spectral regions that are generally distinguished. This figure also shows the wavelength ranges on which the different types of real-time sensor technologies are based.

This chapter presents some of the characteristics and working principles of the sensor technologies that were used in this study. The sensor technology that was most often used is reflectance spectrometry on the VNIR-SWIR spectral range. The reason for this is that it was known that the occurrence of different alteration minerals can be detected from the reflectance on this spectral range (e.g. Sabins, 1999; Thompson et al., 1999; van Ruitenbeek et al., 2005). As explained in chapter 1.1, it might be possible to use differences in hydrothermal alteration mineralogy to characterise the grade of hydrothermal ores because mineralisation at these types of deposits is often related to specific hydrothermal alteration zones (Pirajno, 1992).

Apart from reflectance spectrometry, a DE-XRT sensor was used in the Lagunas Norte study. This type of sensor was selected because it can be used to detect density differences. At the Lagunas Norte deposit, gold mineralisation was associated with the formation of pyrite. Pyrite is an iron-sulphide mineral that has a higher density than most of the host rock, which mainly represents quartzite (Si-oxides). Because of this, it was investigated if the detection of pyrite with DE-XRT can be used as an indicator of gold grade. Furthermore, a Laser-Induced Breakdown Spectroscopy (LIBS) sensor was used in the Lagunas Norte study. LIBS was used to investigate whether this type of sensor can be used to detect the occurrence of gold directly.

In the Cortez study a Red-Green-Blue (RGB) imaging sensor was additionally tested. This sensor technique is well known from digital photography and can be used to characterise materials on their visible appearance. Because there are clear visible differences between the different rock types of the Cortez Hills deposit, it was investigated whether the RGB imaging sensor can be used to characterise these differences in order to distinguish waste or specific ore types.

spectral region	Y-Ray	X-Ray	Ultraviolet	Visible		Infrared					Terahertz	Microwave	Radiowave
sub-region					NIR	SWIR	MWIR	LWIR	FIR				
wavelength (µm)	10^{-6}	$5 \cdot 10^{-5}$	10^{-2}	0.3	0.77	1.4	2.5	7	25	350	10^3		$3 \cdot 10^5$

sensors

- Natural radioactivity
- PGNAA
- DE-YRT
- DE-XRT
- XRF
- XRL
- LIF
- LIBS
- Raman
- RGB imaging
- Hyperspectral imaging
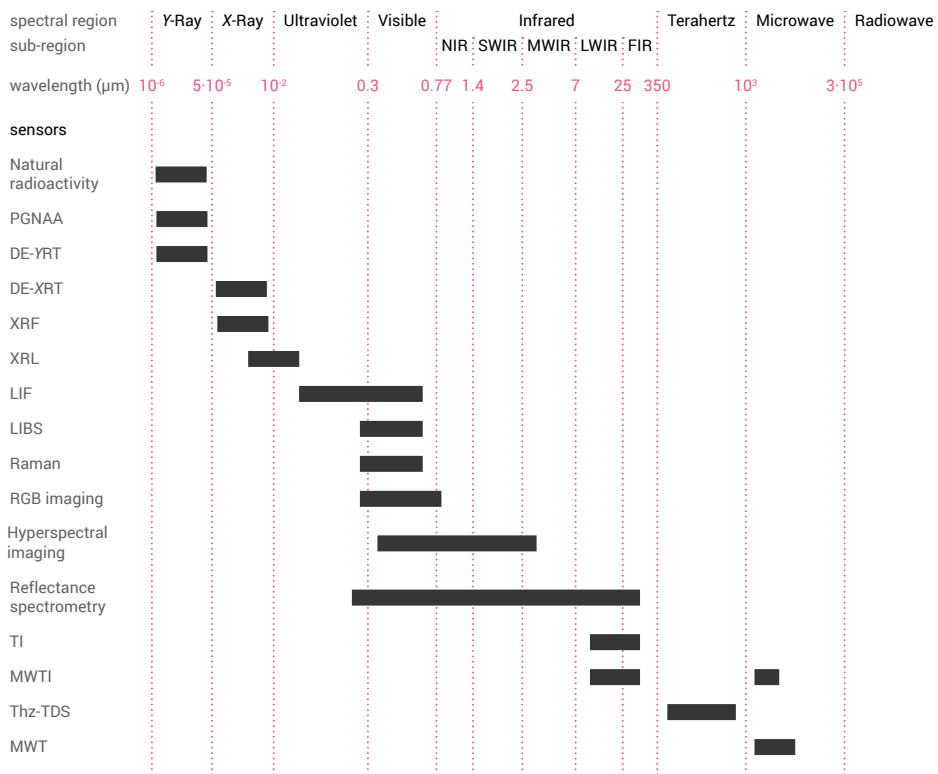- Reflectance spectrometry
- TI
- MWTI
- Thz-TDS
- MWT

Figure 3.1: The electromagnetic spectrum and wavelength ranges on which the different types of real-time sensor technologies are based. See the list of abbreviations for a description of all acronyms.

3.2. Spectrometer characteristics

3.2.1. Introduction

Spectrometers are instruments used to measure the intensity of electromagnetic radiation that is emitted by a material, reflected off the surface of a material or transmitted through a material versus the wavelength of the radiation. The acquired data is generally referred to as a spectrum. The capabilities of spectrometers are usually described in terms of spectral resolution, signal-to-noise ratio and spectral range. The spectral resolution is the smallest wavelength difference that can be distinguished with a spectrometer. Spectral resolution can be described in terms of bandwidth and spectral sampling (Clark, 1999). Bandwidth represents the wavelength range that is covered by each individual intensity measurement. The individual intensity measurements are also referred to as spectral channels or spectral bands and usually follow a Gaussian profile (Clark, 1999). The bandwidth is the wavelength range at half the intensity of the Gaussian profile. Spectral sampling is the wavelength distance between the centres of the Gaussian profiles of the individual channels. The spectral sampling determines the number of data points that are recorded by the spectrometer.

The signal-to-noise ratio is the ratio between the measured signal intensity and the instrumental noise produced by the detection mechanism, which represents the precision of the spectrometer. The spectral range is the wavelength range over which reflections are measured. The spectral ranges that are commonly distinguished are presented in Figure 3.1.

We distinguish two types of spectrometry: point spectrometry and hyperspectral imagery. With point spectrometry each measurement produces a single spectrum. The spectrum represents the measured surface area of the material, which is commonly referred to as the spot size. Hyperspectral imagery is the acquisition of digital images at many different wavelengths. The result is that each pixel in the acquired image constitutes a spectrum. By using hyperspectral imagery many different spectra are therefore acquired simultaneously and the spatial distribution of the spectral data is automatically captured.

3.2.2. Point spectrometry

Point spectra can be acquired by using a dispersive spectrometer or a Fourier-transform spectrometer. Dispersive spectrometers collect spectra by dispersing a light beam using a prism or diffraction grating. By rotating the prism or grating, the intensity of the different wavelengths can be measured one by one on a single detector. Alternatively, an array of detectors can be used in combination with a stationary prism or grating to measure all the different wavelengths simultaneously, which reduces the integration time of the spectrometer. Furthermore, a higher spectral resolution can be achieved by using a Charge-Coupled Device (CCD) (i.e. 2D image detector) in combination with two prisms or gratings that disperse the light beam in perpendicular directions.

Fourier-transforms spectrometers collect spectra by first splitting a collimated light beam that contains the full range of wavelengths and then directing both beams through a certain configuration of mirrors. By moving one of the mirrors, the path length of one of the splitted beams is altered. After recombining both beams, certain wavelengths are extinguished by wave interference. The data that is collected represents the intensity of the radiation versus the position of the mirror, which is commonly referred to as an interferogram (Griffiths & De Haseth, 1986). A signal processing technique known as the Fourier-transform is used to transform the interferogram into a spectrum of intensity versus wavelength.

3.2.3. Hyperspectral imaging

Hyperspectral images are usually acquired by using a line scan sensor. The detection system is similar to that of a dispersive spectrometer. The reflected light over a line is dispersed by using a prism or diffraction grating, and a CCD (i.e. 2D image detector) is used to measure the intensity of the radiation (Grahn & Geladi, 2007). The image that is detected by the CCD contains the reflected intensity of the different pixels in one direction and that of the different wavelengths in the other direction. An alternative method for acquiring hyperspectral images is by using a CCD detector in combination with bandpass filters to capture the images on the different wavelengths one by one (Grahn & Geladi, 2007).

Table 3.1: Minerals that can be identified on the VNIR and SWIR spectral ranges (based on Terracore, 2017). Good and moderate refers to how well diagnostic minerals can be identified from VNIR or SWIR spectra, which mainly depends on the intensity and distinctiveness of the absorption features that the minerals generally produce.

Mineral structure	Mineral group	Example	VNIR	SWIR
Inosilicates	Amphibole	Actinolite	non-diagnostic	**good**
	Pyroxene	Diopside	**good**	moderate
Cyclosilicates	Tourmaline	Elbaite	non-diagnostic	**good**
Nesosilicates	Garnet	Grossular	moderate	non-diagnostic
	Olivine	Forsterite	**good**	non-diagnostic
Sorosilicates	Epidote	Epidote	non-diagnostic	**good**
Phyllosilicates	Mica	Muscovite	non-diagnostic	**good**
	Chlorite	Clinochlore	non-diagnostic	**good**
	Clay mineral	Kaolinite	non-diagnostic	**good**
		illite	non-diagnostic	**good**
Tectosilicates	Feldspar	Orthoclase	non-diagnostic	non-diagnostic
		Albite	non-diagnostic	non-diagnostic
	Silica	Quartz	non-diagnostic	non-diagnostic
Carbonates	Calcite	Calcite	non-diagnostic	moderate
	Dolomite	Dolomite	non-diagnostic	moderate
Hydroxides		Gibbsite	non-diagnostic	**good**
Sulphates	Alunite	Alunite	moderate	**good**
	Gypsum	Gypsum	non-diagnostic	**good**
Borates	Borax	Borax	non-diagnostic	moderate
Halides	Halite	Halite	non-diagnostic	unknown
Phosphates	Apatite	Apatite	moderate	non-diagnostic
Hydrocarbons		Bitumen	unknown	moderate
Oxides	Hematite	Hematite	**good**	non-diagnostic
	Spinel	chromite	non-diagnostic	non-diagnostic
Sulphides	Pyrite	Pyrite	non-diagnostic	non-diagnostic

3.3. VNIR-SWIR reflectance spectrometry

3.3.1. Introduction

Spectral reflectance data is acquired by illuminating a material using a light source and directing the light that is reflected off the surface of the material onto a spectrometer. The collected data can provide information on the mineralogy since certain minerals produce characteristic abosrption features at specific wavelength positions. The following sections will discuss the characteristics of spectral reflectance sensors on the VNIR and SWIR spectral ranges separately. This is because the spectral reflectance of materials on these ranges is dominated by different physical processes.

Table 3.1 presents an overview of how well different types of minerals can be identified based on the spectral reflectance on the VNIR and SWIR spectral ranges. Table 3.2 presents an overview of different environments of ore deposit formation and the characteristic mineral assemblages that can be detected with VNIR-SWIR spectrometers. VNIR-SWIR spectrometry is mainly used for qualitative analysis. For certain applications quantitative analysis may be possible, but careful calibration of the sensor system is required.

3.3.2. VNIR

Introduction

Spectral reflectance data on the Visible to Near-InfraRed (VNIR) spectral range can be acquired by using a point spectrometer or hyperspectral imager. VNIR spectral reflectance data is often acquired simultaneously with reflectance data on the SWIR range. This is because the detection mechanism that is used to capture the data on both these spectral ranges is similar. Most of the sensor systems that measure the entire VNIR-SWIR spectral range still contain separate detectors for the VNIR range and the SWIR range.

Table 3.2: Characteristic mineral assemblages at different environments of ore deposit formation (based on Thompson et al., 1999).

Environment of formation	Common terminology of alteration assemblage	Associated minerals detectable with spectral reflectance sensors
Intrusion-related	potassic, K-silicate, biotitic	biotite, phlogopite, actinolite, sericite, chlorite, epidote, muscovite & anhydrite
	sodic, sodic-calcic	actinolite, clinopyroxene (diopside), chlorite, epidote & scapolite
	phyllic, sericitic	sericite (muscovite-illite), chlorite, anhydrite
	(intermediate) argillic, sericit-chlo-rite-clay (SCC)	sericite (illite-smectite), chlorite, kaolinite, dickite, montmorillonite, calcite & epidote
	advanced argillic	pyrophyllite, sericite, diaspore, alunite, topaz, tourmaline, dumortierite & zunyite
	greisen	topaz, muscovite & tourmaline
	skarn	clinopyroxene, wollastonite, actinolite-tremolite, vesuvianite, epidote, serpentine-talc, calcite, chlorite, illite-smectite & nontronite
	porpylitic	chlorite, epidote, calcite, actinolite, sericite & clay
High-sulphida-tion epithermal	advanced argillic, acid-sulphate	kaolinite, dickite, alunite, diaspore, pyrophyllite & zunyite
	(intermediate) argillic	kaolinite, dickite, montmorillonite & illite-smectite
	propylitic	calcite, chlorite, epidote, sericite & clay
Low-sulphidation epithermal	adularia-sericite, sericitic, argillic	sericite (illite-smectite), kaolinite, chalcedony, opal, montmorillonite, calcite & dolomite
	advanced argillic, acid-sulphate (steam heated)	kaolinite, alunite, cristobalite & jarosite
	propylitic, zeolitic	calcite, epidote, wairakite, chlorite, illite-smectite & montmorillonite

Table 3.2 (continued)

Environment of formation	Common terminology of alteration assemblage	Associated minerals detectable with spectral reflectance sensors
Mesothermal	carbonate	calcite, ankerite, dolomite, muscovite & chlorite
	chloritic	chlorite, muscovite & actinolite
	biotitic	biotite & chlorite
Sediment-hosted gold	argillic	kaolinite, dickite & illite
Volcanogenic massive sulphide	sericitic	sericite, chlorite & chloritoid
	chloritic	chlorite, sericite & biotite
	carbonate	dolomite, siderite, ankerite, calcite, sericite & chlorite
Sediment-hosted massive sulphide	tourmalinite	tourmaline & muscovite
	carbonate	ankerite, siderite, calcite & muscovite
	sericitic	sericite & chlorite
	albitic	chlorite, muscovite & biotite

Point spectrometers and hyperspectral imagers operating in the VNIR spectral range are available from a wide range of manufacturers. For point spectrometry, both laboratory and handheld instruments exist (e.g. ASD, 2017; Spectral Evolution, 2017). Figure 3.2 presents an example of a handheld point spectrometer that collects VNIR and SWIR data simultaneously. The drill core scanner presented in Figure 2.2. is an example of a sensor system that can be equipped with both VNIR and SWIR hyperspectral sensors. VNIR spectral sensors can also be used for particle-by-particle sensor-based sorting (Redwave, 2017; Steinert, 2017; Tomra, 2017).

Point measurements with a handheld VNIR spectrometer at a reasonable signal-to-noise ratio can be taken within a microsecond (e.g. ASD, 2017). Using a line scan sensor to collect imagery data is currently possible up to 700 frames per second (fps) (e.g. HySpex, 2017). However, the framerate also depends on the desired spectral resolution, the spatial resolution and the signal-to-noise ratio. For some applications a lower framerate might therefore be required. Higher frame rates can be achieved if reflectance measurements on several wavelength bands already provide all the relevant information and it is not needed to measure the entire spectral range. Scanning a single band is possible up to 9900 fps (e.g. Specim, 2017).

Figure 3.2: Handheld SWIR spectrometer (ASD, 2017).

VNIR spectral reflectance sensors can be used to characterise Fe-bearing minerals and Fe ores (Haest et al., 2015; Szalai et al., 2013; Cudahy & Ramanaidou, 1997). It is also possible to use these sensors to identify certain sulphide minerals in ultramafic platinum-palladium ores (Bolin & Moon, 2003). Furthermore, VNIR spectral sensors are found to be useful for the characterisation of zinc and copper slurries in a flotation circuit (Haavisto & Kaartinen, 2009).

Working principle

In the VNIR spectral range, minerals absorb electromagnetic radiation through crystal field effects, colour centres, conduction band transitions and charge transfer (Clark, 1999; Hunt, 1977). Certain minerals and mineral characteristics can be identified by analysing the wavelength position and intensity of absorption features.

The absorption mechanism that is most often observed in the VNIR spectra of minerals is the crystal field effect (Clark, 1999). Crystal field effects are absorptions of electromagnetic radiation by electrons that change between the orbital energy levels of transition metal complexes. The wavelength of absorption is related to the energy difference between the orbitals. This energy difference depends on the type of transition metal and ligand that form the complex, the valence state and coordination number of the transition metal, the metal-ligand interatomic distance and the symmetry and distortion of the site that is occupied by the transition metal (Clark, 1999; Hunt, 1977). In other words, the wavelength of absorption is related to the mineral in which the transition metal resides. Transition metals for which absorptions due to crystal field effects are often observed include Fe, Ni, Cu, Mn, Cr and Ti (Hunt, 1977).

Another type of absorption that is produced by certain minerals are colour centres. As with crystal field effects, colour centres are also absorptions produced by electrons that change between energy levels. However, the ability to change between energy levels results in this case from a crystallographic defect. Two types of colour centres can be distinguished. The first

type is due to a vacancy defect in which an electron can reside in discrete energy levels (Hunt, 1977; Nassau, 1978). This is referred to as an electron colour centre. An example of a mineral for which an electron colour centre is often observed is fluorite (Hunt, 1977; Nassau, 1978). The other type of colour centre is referred to as a hole colour centre and is produced when an electron is missing from a location where there is normally an electron pair (Nassau, 1978). This can be caused by the presence of an impurity ion. A hole colour centre is for example responsible for the colour of smoky quartz (Nassau, 1978).

Conduction band transitions can often be observed in the VNIR spectra of semiconductor minerals, such as many types of sulphides (e.g. Boldish & White, 1998). In these minerals electrons can be attached to individual atoms, known as the valence band, or they can move freely through the lattice, known as the conduction band (Clark, 1999; Hunt, 1977). The energy difference between these two bands is known as the band gap. Electrons can transfer from the valence band to the conduction band by absorbing electromagnetic radiation with energies larger than the band gap (Hunt, 1977). This produces a step function in the VNIR spectra of these minerals. The wavelength location of the step function is related to the band gap of the semiconductor mineral. VNIR mineral spectra that show such a step function due to conduction band transitions include for example realgar, stibnite, and native sulphur (Hunt, 1977).
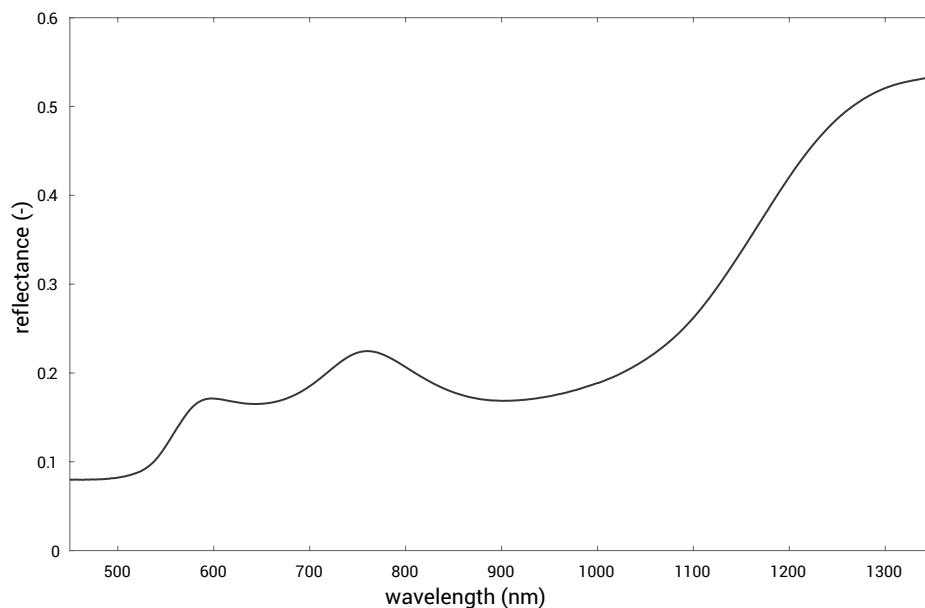

Figure 3.3: Example of a VNIR spectrum of goethite.

Charge transfer is the migration of electrons between neighbouring ions or between ions and ligands (Clark, 1999; Hunt, 1977). This can also occur between neighbouring ions of transition metals in different valence states, such as Fe^{2+} and Fe^{3+}. Unlike conduction band transitions, the electrons that migrate do not enter the conduction band but remain localised in their new

position (Hunt, 1977). The wavelength of absorption depends on the energy that is required for the charge transfer. Charge transfer absorptions are commonly seen in the reflectance spectra of iron oxides (Hunt, 1977). As an example, Figure 3.3 presents the VNIR spectrum of the iron-oxide mineral goethite. The reflectance drop-off towards 500 nm in this spectrum is produced by charge transfer absorption. The absorption features that occur around 650 and 900 nm are caused by electronic transitions.

3.3.3. SWIR

Introduction

Spectral reflectance data on the Short-Wavelength InfraRed (SWIR) spectral range can be acquired by using a point spectrometer or hyperspectral imager. Point spectrometers and hyperspectral imagers operating in the SWIR spectral range are available from a wide range of manufacturers. For point spectrometry, both laboratory and handheld instruments exist (e.g. ASD, 2017; Spectral Evolution, 2017; Spectral International, 2017). An example of a handheld SWIR point spectrometer is shown in Figure 3.2. SWIR hyperspectral imaging sensors are most often used for mapping the mineralogy of drill core samples and rock faces. Sensor systems are available on the market that are specifically designed for these purposes (e.g. Corescan, 2017; Specim, 2017). Figure 2.2. shows an example of a drill core scanner that is equipped with a SWIR hyperspectral camera. SWIR hyperspectral cameras can also be used for particle-by-particle sensor-based sorting (Redwave, 2017; Steinert, 2017; Tomra, 2017).

Point measurements with a handheld SWIR spectrometer at a reasonable signal-to-noise ratio can be taken within a microsecond (e.g. ASD, 2017). Using a line scan sensor to collect imagery data is currently possible up to 450 fps (e.g. Specim, 2017). However, the framerate also depends on the desired spectral resolution, the spatial resolution and the signal-to-noise ratio. For some applications a lower framerate might therefore be required.

Spectral reflectance measurements on the SWIR spectral range can be used to detect minerals produced by hydrothermal alteration. SWIR spectral sensors are therefore useful tools for the exploration of hydrothermal ore deposits (Hunt, 1979; Thompson et al., 1999). Furthermore, it has been shown that SWIR spectral reflectance sensors can be used to characterise the mineralogy of raw materials on a moving conveyor belt (Goetz et al., 2009).

Working principle

In the infrared minerals absorb electromagnetic radiation through molecule bond vibrations. The energy of a photon is transferred into an increased vibrational energy level of the molecule bond when the vibration produces a change in the dipole moment of the molecule (Farmer, 1974; Hollas, 2004). The wavelength at which electromagnetic radiation is absorbed depends on the energy that is associated with the change in dipole moment. Minerals for which vibrating molecule bonds do not change the dipole moment will not absorb electromagnetic radiation.

Molecule bonds vibrate by stretching of the bond or by bending of the angle of the bond. In polyatomic molecules, multiple bonds vibrate at the same time and produce different types of group vibrations (Hollas, 2004). Furthermore, multiples of the normal vibrational modes are produced when a bond vibration is excited with two or more energy quanta (Clark, 1999; Hollas, 2004). These multiples are commonly referred to as overtones, whereas the normal vibrational modes are referred to as fundamental vibrations. Additionally, two or more fundamentals and/ or overtones of different modes can add or subtract to form so-called combinations (Clark, 1999; Hollas, 2004). Minerals and mineral characteristics can be identified from the wavelength position and intensity of a specific combination of absorption features resulting from the fundamental, overtone and combinations of molecule bond vibrations.

No fundamental vibrational absorptions occur at wavelengths shorter than 2.5 μm. Absorption bands in the SWIR wavelength range are all overtones and combinations (Hunt, 1970). Relatively high fundamental absorption frequencies are required, however, in order to produce diagnostic overtones and combinations in the SWIR wavelength range (Hunt, 1970). Because of this, mainly minerals containing OH, CO3, SO4 and NH3 groups can be identified with SWIR spectrometry (AusSpec, 2008; Hunt, 1970). Especially overtone combinations involving Al-OH, Fe-OH and Mg-OH bonds are often characteristic for specific minerals and variations in their composition (AusSpec, 2008; Clark et al., 1990). The occurrence of water also produces diagnostic absorption features in the SWIR. This water can be physically adsorbed on the surface of mineral grains, it can occupy specific lattice sites or it can be part of the crystal structure (Clark et al., 1990). Figure 3.4 presents an example of the SWIR spectra of several minerals on which the wavelength ranges at which the most diagnostic molecule bond vibrations that commonly occur are indicated. Since not all molecule bonds are diagnostic in the SWIR spectral region, the use of SWIR spectrometry is limited to the following groups of minerals; phyllosilicates, hydroxylated silicates, sulphates, carbonates and ammonium-bearing minerals (AusSpec, 2008).
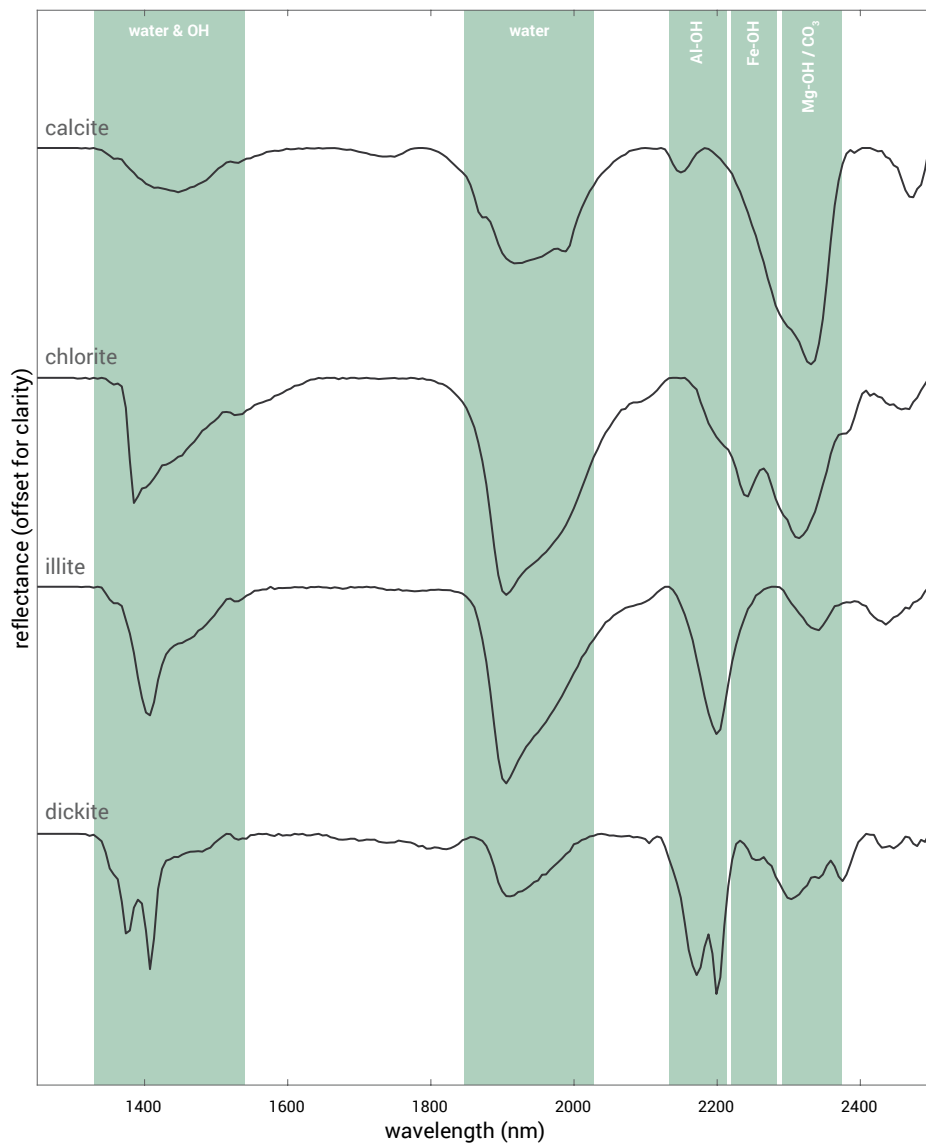
Figure 3.4: Examples of SWIR mineral spectra and the wavelength ranges at which the most diagnostic molecule bond vibrations commonly occur (based on AusSpec, 2008).

3.4. DE-XRT

3.4.1. Introduction

Dual-Energy X-Ray Transmission (DE-XRT) utilizes the transmission of X-rays through a material to characterise the density. DE-XRT sensors can be used for conveyor belt scanning (RTI, 2017; Scantech, 2017) and particle-by-particle sensor-based sorting (Comex, 2017; SCOTT, 2017; Steinert, 2017; Tomra, 2017). Line scan cameras for collecting De-XRT images can reach frame rates in the order of several thousand fps (Hamamatsu, 2017). The frame rate depends on the desired spatial resolution.

The DE-XRT sensor data can be used to indirectly characterise certain rock properties from the measured density distributions. An example of such indirect characterisation is detection of the content of pyritic sulphide in lignite based on the relatively dense sulphide inclusions that are fairly distinct from the lower density lignite in the DE-XRT images of lignite particles (e.g. von Ketelhodt & Bergmann, 2010). The same method can be applied to characterise the content of tungsten minerals in a tungsten ore (Robben et al., 2013). Furthermore, the ash content of coal affects the density of coal particles which can therefore be characterised by DE-XRT sensors (de Jong et al., 2004; Kuilman, 2006; Yazdi & Esmaeilnia, 2003). Particle-by-particle sorting with DE-XRT sensors is used for the sorting of coal (von Ketelhodt & Bergmann, 2010; Kuilman, 2006) and massive sulphide type ores (Kleine et al., 2010).

It is in theory also possible to characterise the texture of ore materials from the density distributions in a DE-XRT image. Cross-cutting veins of relatively heavy minerals through a matrix of lighter minerals for example can be characterised for drill core samples of certain ore deposits.

3.4.2. Working principle

The transmission of X-rays through a material is described by the Lambert's law:

$$I_{det} = I_0 e^{-\mu(\lambda)\rho d}$$

Where I_{det} is the detected intensity, I_0 is the intensity used to irradiate the material, $\mu(\lambda)$ is the attenuation coefficient at wavelength λ, ρ is the density and d the thickness of the material. The attenuation coefficient is related to the composition of a material and is described by:

$$\mu = \sum_{i=1}^{n} f_i \mu_i$$

Where f_i is the mass fraction of element i and μ_i is the attenuation coefficient of this element. In order to be able to characterise materials independent of the materials' thickness, transmitted radiation is measured on two different wavelengths, or energy levels: $I_1 = I_{det1} / I_{01}$ and $I_2 = I_{det2} / I_{02}$. For the transmission on the two energy levels, Lambert's law can be rewritten to:

$$\frac{I_1}{I_2} = e^{-\Delta\mu\rho d} = \left(e^{-\Delta\mu\rho}\right)^d = C^d$$

In which C is a constant that depends only on the density of the material and on the difference in the absorption coefficient at the two energy levels at which the transmission is measured. This means that if C of two materials is different, these materials can be distinguished from the X-ray transmission measurements. In applications of DE-XRT the constant C of a known material is usually characterised by measuring the radiative transmission on both energy levels for different material thicknesses. The result is a transmission curve such as the one presented in Figure 3.5. This transmission curve can be used to evaluate the density of an unknown material relative to the material that was used to construct the curve. In practice, multiple transmission curves are usually used to evaluate density differences. To distinguish between materials on a specific density cut-off it is best to use the transmission curve of a material that has a density that is equal or very close to this cut-off.
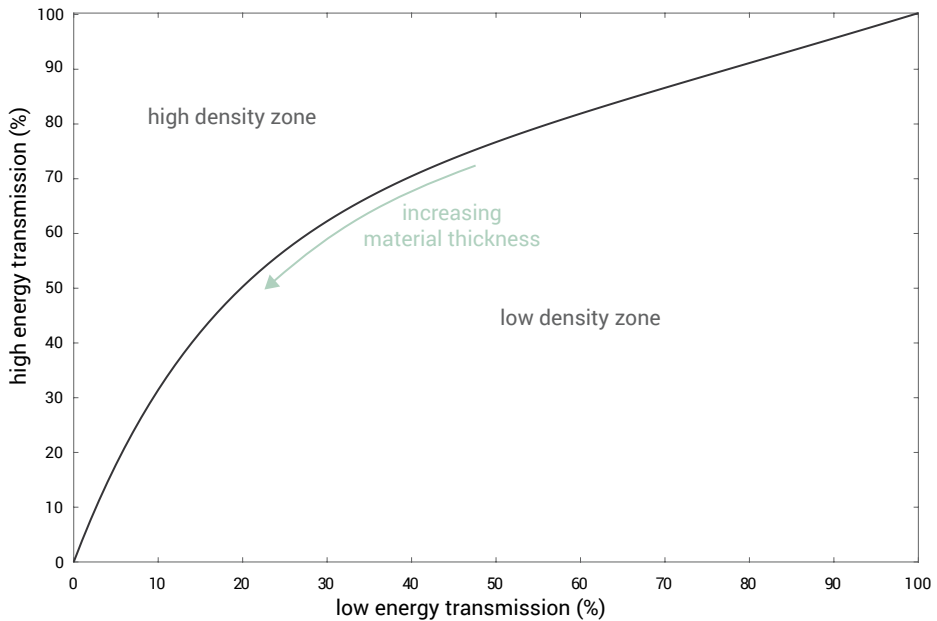

Figure 3.5: Example of a DE-XRT transmission curve of aluminium. The high and low density zones indicate the relative density difference to aluminium based on the resulting X-ray transmission measurements.

3.5. LIBS

3.5.1. Introduction

Laser-Induced Breakdown Spectroscopy (LIBS), sometimes also referred to as Laser-Induced Plasma Spectroscopy (LIPS), utilizes a pulsed laser beam to ablate a small amount of material on the surface of a sample and break it down into a plasma consisting of atoms, ions and free electrons. The chemical composition of a material can be characterised by measuring the radiative emission of the plasma with a spectrometer. The LIBS technique can be used for both qualitative and quantitative characterisation. LIBS sensor systems that are currently available include laboratory instruments, handheld instruments (SciAps, 2017) and conveyor belt scanners (Secopta, 2017; SonicSampDrill, 2017; Laser Distance Spectrometry, 2017).

Only point spectrometers are available to measure LIBS spectra. Hyperspectral imagery data can only be collected by measuring LIBS spectra point-by-point. The main reasons for this is that a high intensity pulsed laser beam is required to generate a plasma, which makes it difficult to integrate this technique into a line scanning setup. Furthermore, a relatively high spectral resolution is required to be able to distinguish LIBS emission features, which cannot be achieved with the line scan sensors that are currently available. The data acquisition speed of a LIBS spectrum is typically less than one second of which most of the time is consumed by the plasma generation with the laser. Handheld LIBS instruments are equipped with 50 Hz pulsed lasers (SciAps, 2017). The number of pulses that are required for plasma generation depend on the application, but multiple pulses are commonly used resulting in several hundreds of milliseconds to generate the plasma. VNIR spectrometers can be used to measure the LIBS spectra within a microsecond.

LIBS applications that are currently in use include the on-line characterisation of the quality of phosphate ore and coal (Gaft et al., 2007). Furthermore, LIBS has showed promising results for characterizing the quality of a variety of ore types including; iron ore, copper ore, uranium ore, phosphate ore, nickel laterite and coal (Death et al., 2009; Gaft et al., 2007; Kim et al., 2012; Pořízka et al., 2014; Rosenwasser et al., 2001). However, in most of these results a sample preparation was performed to create a homogenous sample in the form of a powder or pellet. This means that the heterogeneity that naturally occurs in most rock types is not accounted for. Since the acquisition of LIBS data is highly influence by matrix effects, this heterogeneity may have serious complications for characterizing the composition of rock samples from LIBS surface measurements. For many ore types it is therefore uncertain if a LIBS sensor system can detect the elements that define ore quality with the required precision. LIBS can also be used

to characterise mineralogy. Kaski et al. (2003) for example shows that LIBS data can be used to characterise sulphide mineralogy in drill core samples.

3.5.2. Working principle

The electromagnetic radiation that is emitted by the laser generated plasma is produced by free electrons that transfer their kinetic energy in the form of photons when they are captured into ionic or atomic energy levels (Cremers & Knight, 2006). Elements can be identified by inspecting the wavelength positions at which the emissions are produced. Furthermore, the quantity of each element can be characterised by inspecting the intensity of the emission.

The electrons that produce emissions are mainly those that are captured into the outer-shell orbits of atoms. Since the energy levels of these orbits are relatively low, the emission spectrum is measured on the VNIR spectral range. The disadvantage of this is that for certain transition metals many different energy levels exist in on which electrons can be captured. As an example, Figure 3.6 presents the theoretical LIBS emission features of Fe and Al taken from the NIST atomic spectra database (Kramida et al., 2015). Figure 3.6 clearly shows that a transition element such as Fe produces much more emission features than Al. This means that if a sample contains significant amounts of Fe, the emission bands produced by Fe can completely dominate the measured spectrum and overlap with the emission bands that are produced by many other elements, which limits the ability to characterise these other elements.

Another disadvantage of the LIBS technique is that it is highly influenced by matrix effects. This is mainly because the electron density of the laser generated plasma depends on the ionization energies of all chemical species that form it. If the occurrence of a certain element in a sample would be replaced by a more easily ionisable element, the electron density of the plasma will increase, which decreases the concentration of elements with higher ionization energies (Cremers & Knight, 2006). Furthermore, variations in plasma generation occur as a result of an uneven energy distribution between laser pulses and differences in sample composition, crystallinity, density, grain size, hardness and surface roughness (Harmon et al., 2013; Yaroshchyk et al., 2010). Careful calibration of a LIBS system is therefore required before quantitative compositional information can be extracted from the measured data.
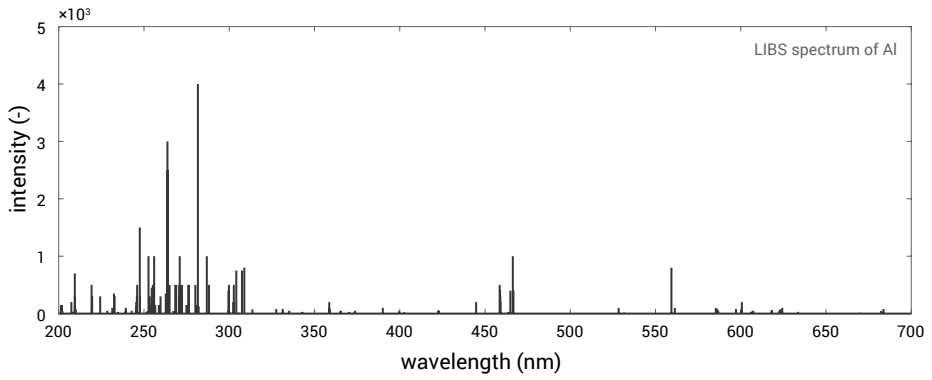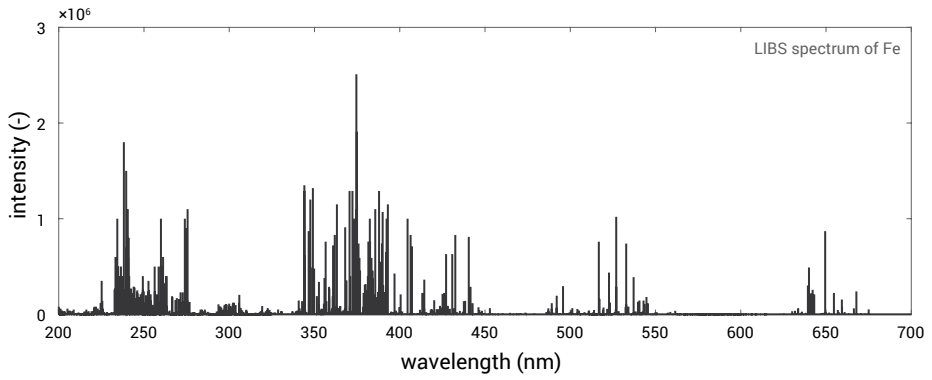
Figure 3.6: Examples of LIBS spectra (Kramida et al., 2015).

3.6. RGB imaging

3.6.1. Introduction

Red-Green-Blue (RGB) imaging is a sensor technique that is well known from digital photography. RGB imaging sensors measure spectral reflectance on the red, green and blue regions of the visible part of the electromagnetic spectrum. It is a very mature and relatively cheap technology due to the production of digital cameras as consumer products. The images can be used to characterise materials on their visible appearance, such as colour and texture. RGB imaging sensors are often used to document drill core samples and this type of sensor is therefore usually integrated into drill core scanners such as the one shown in Figure 2.2 in chapter 2. RGB imaging sensors are also used in particle-by-particle sensor based sorting in order to sort raw materials having visible differences (Comex, 2017; Redwave, 2017; Steinert, 2017; Tomra, 2017).

3.6.2. Working principle

RGB images are generally captured by using a line scan sensor or a Charge-Coupled Device (CCD) (i.e. 2D image detector). The three colour bands are usually separated with a Bayer filter. The working principle of a Bayer filter is presented in Figure 3.7.

A whole range of digital image processing techniques are available to extract meaningful information from RGB images (e.g. Umbaugh, 2016). One of the most promising techniques is automated image recognition through machine learning techniques. This type of digital image analysis is already used in various industries for quality control and sorting. Richter et al. (2016) shows that it is also possible to use such techniques to distinguish between different types of rock pebbles. However, no applications in the mining industry utilising automated image recognition for classification and sorting of ores and industrial minerals have been published so far. There is great potential though that automated classification of RGB images of rocks and minerals can be successfully used in a wide range of applications.
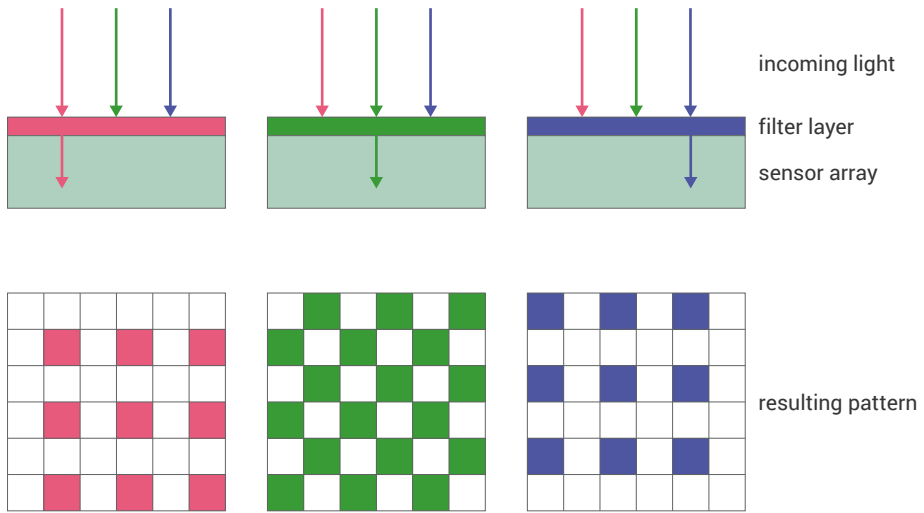
incoming light

filter layer

sensor array

resulting pattern

Figure 3.7: Working principle of a Bayer filter (based on Burnett, 2017).

3.7. References

ASD. 2017. *Products and services* [Online]. Available: https://www.asdi.com/products-and-services [Accessed March 2017].

AUSSPEC 2008. *G-MEX Spectral Interpretation Field manual*, AusSpec International ltd.

BOLDISH, S. I. & WHITE, W. B. 1998. Optical band gaps of selected ternary sulfide minerals. *American Mineralogist*.

BOLIN, B. J. & MOON, T. S. 2003. Sulfide detection in drill core from the Stillwater Complex using visible/near-infrared imaging spectroscopy. *Geophysics*, 68, 1561-1568.

BURNETT, C. 2017. *Bayer filter* [Online]. Available: https://en.wikipedia.org/wiki/Bayer_filter [Accessed May 2017].

CLARK, R. N. 1999. Spectroscopy of rocks and minerals, and principles of spectroscopy. *Manual of remote sensing*, 3, 3-58.

CLARK, R. N., KING, T. V., KLEJWA, M., SWAYZE, G. A. & VERGO, N. 1990. High spectral resolution reflectance spectroscopy of minerals. *Journal of Geophysical Research: Solid Earth*, 95, 12653-12680.

COMEX. 2017. *Comex sorting technology* [Online]. Available: http://www.comex-group.com/en/products-and-solutions/sorting-technology [Accessed February 2017].

CORESCAN. 2017. *The corescan system* [Online]. Available: http://www.corescan.com.au/services/the-corescan-system [Accessed February 2017].

CREMERS, D. A. & KNIGHT, A. K. 2006. *Laser Induced Breakdown Spectroscopy*, Wiley Online Library.

CUDAHY, T. & RAMANAIDOU, E. 1997. Measurement of the hematite: goethite ratio using field visible and near infrared reflectance spectrometry in channel iron deposits, Western Australia. *Australian Journal of earth sciences*, 44, 411-420.

DE JONG, T. P. R., VAN HOUWELINGEN, J. A. & KUILMAN, W. 2004. Automatic sorting and control in solid fuel processing: opportunities in European perspective. *Geologica belgica*, 7, 325-333.

DEATH, D., CUNNINGHAM, A. & POLLARD, L. 2009. Multi-element and mineralogical analysis of mineral ores using laser induced breakdown spectroscopy and chemometric analysis. *Spectrochimica Acta Part B: Atomic Spectroscopy*, 64, 1048-1058.

FARMER, V. C. 1974. *Infrared spectra of minerals*, Mineralogical society.

GAFT, M., SAPIR-SOFER, I., MODIANO, H. & STANA, R. 2007. Laser induced breakdown spectroscopy for bulk minerals online analyses. *Spectrochimica Acta Part B: Atomic Spectroscopy*, 62, 1496-1503.

GOETZ, A. F., CURTISS, B. & SHILEY, D. A. 2009. Rapid gangue mineral concentration measurement over conveyors by NIR reflectance spectroscopy. *Minerals Engineering*, 22, 490-499.

GRAHN, H. & GELADI, P. 2007. *Techniques and applications of hyperspectral image analysis*, John Wiley & Sons.

GRIFFITHS, P. R. & DE HASETH, J. A. 1986. *Fourier transform infrared spectrometry*, New York, Wiley.

HAAVISTO, O. & KAARTINEN, J. 2009. Multichannel reflectance spectral assaying of zinc and copper flotation slurries. *International Journal of Mineral Processing*, 93, 187-193.

HAEST, M., MITTRUP, D. & DOMINGUEZ, O. 2015. Reaping the first fruits - Infrared Spectroscopy: the new standard tool in BHP Billiton iron ore exploration. *Iron Ore Conference*. Perth, Australia.

HAMAMATSU. 2017. *X-ray line scan camera* [Online]. Available: https://www.hamamatsu.com/jp/en/product/category/5000/5005/index.html [Accessed May 2017].

HARMON, R. S., RUSSO, R. E. & HARK, R. R. 2013. Applications of laser-induced breakdown spectroscopy for geochemical and environmental analysis: A comprehensive review. *Spectrochimica Acta Part B: Atomic Spectroscopy*, 87, 11-26.

HOLLAS, J. M. 2004. *Modern spectroscopy*, John Wiley & Sons.

HUNT, G. R. 1970. Visible and near-infrared spectra of minerals and rocks: I silicate minerals. *Modern geology*, 1, 283-300.

HUNT, G. R. 1977. Spectral signatures of particulate minerals in the visible and near infrared. *Geophysics*, 42, 501-513.

HUNT, G. R. 1979. Near-infrared (1.3–2.4) μm spectra of alteration minerals—Potential for use in remote sensing. *Geophysics*, 44, 1974-1986.

HYSPEX. 2017. *HySpex cameras* [Online]. Available: http://www.hyspex.no/products/ [Accessed May 2017].

KASKI, S., HÄKKÄNEN, H. & KORPPI-TOMMOLA, J. 2003. Sulfide mineral identification using laser-induced plasma spectroscopy. *Minerals Engineering*, 16, 1239-1243.

KIM, Y.-S., HAN, B.-Y., SHIN, H., KIM, H., JUNG, E., JUNG, J. & NA, S. 2012. Determination of uranium concentration in an ore sample using laser-induced breakdown spectroscopy. *Spectrochimica Acta Part B: Atomic Spectroscopy*, 74, 190-193.

KLEINE, C., RIEDEL, F., VON KETELHODT, L. & MURRAY, R. 2010. XRT Sorting of Massive Quartz Sulphide Type Gold Ore. *Sensor-based sorting - conference proceedings*. Aachen, Germany.

KRAMIDA, A., RALCHENKO, Y., READER, J. & NIST ASD TEAM. 2015. *NIST Atomic Spectra Database (ver. 5.3)* [Online]. Available: http://physics.nist.gov/asd [Accessed May 2017].

KUILMAN, W. 2006. DE-XRT sorting of coal. *Sensor-based sorting - conference proceedings*. Aachen, Germany.

LASER DISTANCE SPECTROMETRY. 2017. *Laser online elemental analyzers MAYA* [Online]. Available: http://www.laser-distance-spectrometry.com/products/conveyoranalyzer.html [Accessed April 2017].

NASSAU, K. 1978. The origins of colour in minerals. *American Mineralogist*, 63, 219.

PIRAJNO, F. 1992. *Hydrothermal mineral deposits: principles and fundamental concepts for the exploration geologist*, Berlin Heidelberg, Springer-Verlag.

POŘÍZKA, P., DEMIDOV, A., KAISER, J., KEIVANIAN, J., GORNUSHKIN, I., PANNE, U. & RIEDEL, J. 2014. Laser-induced breakdown spectroscopy for in situ qualitative and quantitative analysis of mineral ores. *Spectrochimica Acta Part B: Atomic Spectroscopy*, 101, 155-163.

REDWAVE. 2017. *Mineral sorting* [Online]. Available: http://www.redwave.at/en/mining-solutions/ [Accessed February 2017].

RICHTER, M., VIETH, K., LANGLE, T. & BEYERER, J. 2016. Bag of visual words - A computer vision method applied to bulk material sorting. *Sensor-based sorting and control - conference proceedings*. Aachen, Germany.

ROBBEN, M. R., KNAPPL, H., DEHLER, M. & WOTRUBA, H. 2013. X-ray transmission sorting of tungsten ore. *OCM 2013 - conference proceedings*. Karlsruhe, Germany: KIT Scientific Publishing.

ROSENWASSER, S., ASIMELLIS, G., BROMLEY, B., HAZLETT, R., MARTIN, J., PEARCE, T. & ZIGLER, A. 2001. Development of a method for automated quantitative analysis of ores using LIBS. *Spectrochimica Acta Part B: Atomic Spectroscopy*, 56, 707-714.

RTI. 2017. *Realtime Instruments* [Online]. Available: http://www.realtimegrp.com/ [Accessed May 2017].

SABINS, F. F. 1999. Remote sensing for mineral exploration. *Ore Geology Reviews*, 14, 157-183.

SCANTECH. 2017. *Scantech products* [Online]. Available: http://www.scantech.com.au/ [Accessed February 2017].

SCIAPS. 2017. *LIBS, XRF and RAMAN products* [Online]. Available: https://www.sciaps.com [Accessed April 2017].

SCOTT. 2017. *Applied Sorting Technology: Sorting and Inspection* [Online]. Available: http://www.scott.co.nz/sorting-and-inspection/ [Accessed February 2017].

SECOPTA. 2017. *Laser based sensor systems* [Online]. Available: http://www.secopta.com/applications/raw-materials [Accessed April 2017].

SONICSAMPDRILL. 2017. *Sorting ore with the speed of light* [Online]. Available: http://www.sonicsampdrill.com/news/sorting-ore-with-the-speed-of-light-1000-tons-per-hour-.htm [Accessed April 2017].

SPECIM. 2017. *Hyperspectral imaging in geology* [Online]. Available: http://www.specim.fi/hyperspectral-imaging-in-geology [Accessed February 2017].

SPECTRAL EVOLUTION. 2017. *Full Range / High Resolution Field Portable UV-VIS-NIR-SWIR Spectroradiometers* [Online]. Available: http://www.spectralevolution.com/portable_spectroradiometer.html [Accessed March 2017].

SPECTRAL INTERNATIONAL. 2017. *The PIMA field spectrometer* [Online]. Available: http://www.spectral-international.com/pima2.html [Accessed March 2017].

STEINERT. 2017. *Innovative sensor systems for new solutions* [Online]. Available: http://www.steinertglobal.com/de/en/products/sensor-sorting/ [Accessed February 2017].

STEMMER IMAGING. 2017. *Line scan cameras* [Online]. Available: https://www.stemmer-imaging.nl/en/products/category/line-scan-cameras/ [Accessed May 2017].

SZALAI, Z., KISS, K., JAKAB, G., SIPOS, P., BELUCZ, B. & NÉMETH, T. 2013. The use of UV-VIS-NIR reflectance spectroscopy to identify iron minerals. *Astronomische Nachrichten*, 334, 940-943.

TERRACORE. 2017. *How GeoSpectral Imaging works* [Online]. Available: http://terracoregeo.com/ [Accessed May 2017].

THOMPSON, A. J., HAUFF, P. L. & ROBITAILLE, A. J. 1999. Alteration mapping in exploration: application of short-wave infrared (SWIR) spectroscopy. *SEG newsletter*, 39, 16-27.

TOMRA. 2017. *Mining sorting solutions* [Online]. Available: https://www.tomra.com/en/solutions-and-products/sorting-solutions/mining/sorting-equipment/ [Accessed February 2017].

UMBAUGH, S. E. 2016. *Digital image processing and analysis: human and computer vision applications with CVIPtools*, CRC press.

VAN RUITENBEEK, F. J., CUDAHY, T., HALE, M. & VAN DER MEER, F. D. 2005. Tracing fluid pathways in fossil hydrothermal systems with near-infrared spectroscopy. *Geology*, 33, 597-600.

VON KETELHODT, L. & BERGMANN, C. 2010. Dual energy X-ray transmission sorting of coal. *Journal of the Southern African Institute of Mining and Metallurgy*, 110, 371-378.

YAROSHCHYK, P., DEATH, D. L. & SPENCER, S. J. 2010. Quantitative measurements of loss on ignition in iron ore using laser-induced breakdown spectroscopy and partial least squares regression analysis. *Applied spectroscopy*, 64, 1335-1341.

YAZDI, M. & ESMAEILNIA, S. 2003. Dual-energy gamma-ray technique for quantitative measurement of coal ash in the Shahroud mine, Iran. *International Journal of Coal Geology*, 55, 151-156.

Chapter 4.

Alteration at hydrothermal ore deposits

4.1. Introduction

Hydrothermal ore deposits are formed by hydrothermal activity that is usually driven by a magmatic intrusion occurring below the Earth's surface. Hydrothermal activity is the movement of hot aqueous (hydrothermal) fluids through the Earth's crust and interaction between these fluids and the rocks through which they pass. The hydrothermal fluids that are responsible for the formation of many types of hydrothermal deposits originate from a magmatic intrusion and are released due to cooling of the magma (Pirajno, 1992). Base and precious metals can be dissolved within these fluids as ions or complex ions. After release from the magma, the hydrothermal fluids flow towards the surface due to the relatively high pressure and temperature. The ascending magmatic fluids may subsequently mix with meteoric fluids which changes the fluid chemistry and temperature. During deposit formation, the hydrothermal fluids introduce, remove and/or redistribute pre-existing components of the host rock. This is referred to as hydrothermal alteration (Pirajno, 1992). Hydrothermal alteration results in the formation of alteration minerals. The type of alteration minerals that are formed depends on the pressure and temperature of the hydrothermal fluids and on the composition of the hydrothermal fluids and the host rock (Pirajno, 1992). Because mineralisation of base and precious metals also depends on hydrothermal fluid properties, it is often related to the formation of specific alteration minerals.

4.2. Porphyry copper deposits

Porphyry copper deposits form at depths of approximately 1 to 6 km below the surface. Figure 4.1 and Figure 4.2 present schematic models of the different hydrothermal alteration zones and ore mineralisation zones of a generalised porphyry copper system. It can be observed from these figures that the main ore zone is related to the boundary between potassic and phyllic hydrothermal alteration. In practice, the relations between hydrothermal alteration and copper mineralisation are often more complicated than displayed in this figure. This is mainly due to the fact that the vertical distribution of the different hydrothermal alteration zones depends on the degree of telescoping within the porphyry system (Sillitoe, 2010). Telescoping refers to overprinting of the older hydrothermal alteration types by the younger ones. If the degree of telescoping at a porphyry system is limited, all hydrothermal alteration zones are spatially distributed as displayed in Figure 4.1. But in highly telescoped systems, the propylitic alteration can impinge downward upon the potassic alteration zone and (partially) overprint the previously formed hydrothermal alteration types.

The distribution of hydrothermal alteration zones at porphyry deposits can also be affected by superimposed breccia and/or diatreme intrusions (Lowell & Guilbert, 1970; Pirajno, 1992; Sillitoe, 2010). These types of intrusions are commonly associated with porphyry deposits and can locally overprint the previously formed hydrothermal alteration types (Sillitoe, 2010). Overprinting of the alterations by telescoping, breccia intrusions and/or diatreme intrusions distorts the general relations between hydrothermal alteration and copper mineralisation. The extent and characteristics of these relations therefore depend on the local geology of the porphyry deposit.

Alteration type	Alteration mineralogy
Propylitic	Chlorite, Epidote, Carbonate
Argillic	Quartz, Kaolinite, Chlorite
Phyllic	Quartz, Sericite, Pyrite
Potassic	Quartz, K-feldspar, Biotite, ± Anhydrite, ± Sericite
Inner deep zone	Quartz, Sericite, Chlorite, K-feldspar
Outer deep zone	Chlorite, Sericite, Epidote, Magnetite

Figure 4.1: Hydrothermal alteration zones of a generalised porphyry copper deposit (based on Lowell & Guilbert, 1970). Typical dimensions are 1.2 x 2 km horizontally and 3 km vertically.

Mineralisation zone	Ore mineralogy
Peripheral	Chalcopyrite, Galena, Other sulphides, Au & Ag
Low pyrite shell	Pyrite (±2%)
Pyrite shell	Pyrite (±10%), Chalcopyrite (0.1-3%), Molybdenite (trace)
Ore shell	Pyrite (±1%), Chalcopyrite (1-3%), Molybdenite (±0.003%)
Low grade core	Pyrite, Chalcopyrite, Molybdenite (low total sulphide grade)
Inner deep zone	Magnetite > Pyrite, Chalcopyrite
Outer deep zone	Magnetite > Pyrite

Figure 4.2: Ore mineralisation zones of a generalised porphyry copper deposit (based on Lowell & Guilbert, 1970). Typical dimensions are 1.2 x 2 km horizontally and 3 km vertically. > indicates relative mineral proportions.

4.3. Epithermal gold–silver deposits

Epithermal gold-silver deposits form at depths up to 1500 m below the surface where sharp pressure and temperature gradients result in boiling of the hydrothermal fluids, which changes fluid composition and forces gold and silver to precipitate (Pirajno, 1992; Simmons et al., 2005). Two different types of epithermal deposits are generally distinguished. The first is a high-sulphidation type which is formed by acidic, sulphur-rich, and oxidised hydrothermal fluids. The second is a low-sulphidation type which is formed by near-neutral, sulphur-poor, and reduced hydrothermal fluids (Sillitoe, 1993; Simmons et al., 2005). Figure 4.3 presents schematic models of the alteration zoning that generally occurs near epithermal veins and breccias. It can be observed from this figure that the main ore zone is associated with the vuggy quartz alteration at high-sulphidation deposits and with crustified quartz alteration at low-sulphidation deposits. Similar to porphyry ore deposits, the alteration-mineralisation relationship can be affected by later alteration events that overprint the previously formed alteration mineralogy.
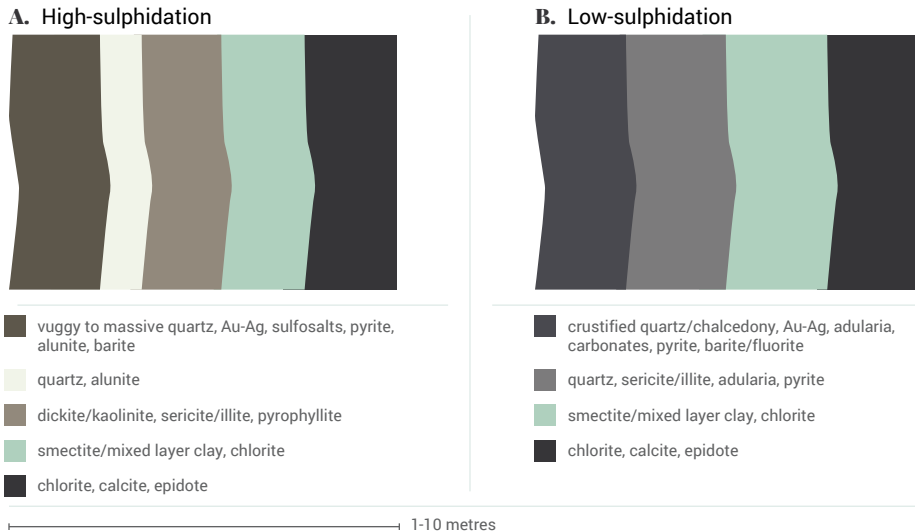
A. High-sulphidation

B. Low-sulphidation

- vuggy to massive quartz, Au-Ag, sulfosalts, pyrite, alunite, barite
- quartz, alunite
- dickite/kaolinite, sericite/illite, pyrophyllite
- smectite/mixed layer clay, chlorite
- chlorite, calcite, epidote

- crustified quartz/chalcedony, Au-Ag, adularia, carbonates, pyrite, barite/fluorite
- quartz, sericite/illite, adularia, pyrite
- smectite/mixed layer clay, chlorite
- chlorite, calcite, epidote

1-10 metres

Figure 4.3: Schematic alteration zoning outward (left to right) from epithermal alteration veins or other geometrical forms (based on Sillitoe, 1993. and Simmons et al., 2005). The patterns result from fluid-rock interactions and declining fluid temperatures.

4.4. Carlin-type gold deposits

Carlin-type gold deposits, also known as sediment-hosted disseminated gold deposits form in extensional settings at approximately 2 to 4 km below the surface. Contrary to epithermal deposits, precipitation of gold probably did not result from boiling, but rather from mixing, cooling and oxidation of the hydrothermal fluids (Arehart, 1996). Alteration at Carlin-type deposits typically consists of decarbonatisation, silicification and argillisation (Arehart, 1996; Cline et al., 2005). Mineralisation-alteration zoning is usually irregular since the reactions that formed Au-bearing pyrite are generally not the same as the ones that formed the alteration minerals (Cline et al., 2005).

Decarbonatisation is often the most areally extensive alteration effect and comprises removal of the carbonate portion of the host rock. Complete carbonate dissolution near fluid conduits is commonly zoned outward to dolomite- and then calcite-stable zones, and further out to zones with abundant calcite veins (Cline et al., 2005). Silicification is the second most extensive alteration type and is mainly characterised by jasperoid formation. Silicification often ranges from weak cementation effects to complete replacement of the pre-existing rock (Arehart, 1996). Some jasperoids may be related to gold mineralisation, but they often range from being barren to containing high grade ore (Arehart, 1996; Cline et al., 2005). Argillisation mainly affects basalts, lamprophyres and other igneous rocks and is often minimal in relatively pure carbonate rocks (Cline et al., 2005). Argillisation is characterised by kaolinite-dickite formation near fluid conduits and zones outward to muscovite-illite formation and further out to K-feldspar stable zones (Arehart, 1996; Cline et al., 2005).

4.5. References

AREHART, G. B. 1996. Characteristics and origin of sediment-hosted disseminated gold deposits: A review. *Ore Geology Reviews*, 11, 383-403.

CLINE, J. S., HOFSTRA, A. H., MUNTEAN, J. L., TOSDAL, R. M. & HICKEY, K. A. 2005. Carlin-type gold deposits in Nevada: Critical geologic characteristics and viable models. *Economic Geology 100th anniversary volume*, 100, 451-484.

LOWELL, J. D. & GUILBERT, J. M. 1970. Lateral and vertical alteration-mineralization zoning in porphyry ore deposits. *Economic Geology*, 65, 373-408.

PIRAJNO, F. 1992. *Hydrothermal mineral deposits: principles and fundamental concepts for the exploration geologist*, Berlin Heidelberg, Springer-Verlag.

SILLITOE, R. 1993. Epithermal models: genetic types, geometrical controls and shallow features. *Mineral Deposit Modeling: Geological Association of Canada Special Paper*, 40, 403-417.

SILLITOE, R. H. 2010. Porphyry copper systems. *Economic geology*, 105, 3-41.

SIMMONS, S. F., WHITE, N. C. & JOHN, D. A. 2005. Geological characteristics of epithermal precious and base metal deposits. *Economic Geology 100th anniversary volume*, 29, 485-522.

Multivariate analysis and regression of sensor data

5.1. Introduction

Multivariate analysis and/or regression was used to facilitate the analysis of large sets of sensor data. In some cases the multivariate methods were also applied to processed sensor data, such as mineralogy maps that were produced from VNIR-SWIR hyperspectral images. The purpose of using multivariate analysis and/or regression is that this is a relatively quick and easy method to investigate the relationships between many different variables. This was used to determine whether the data that is captured by a sensor provides information that can be used to segment waste from ore or distinguish between different ore types. The multivariate methods were also used to identify exactly which information that is provided by the sensor is important for producing these classifications.

5.2. Multivariate logistic regression

Multivariate logistic regression is a technique that is similar to linear regression, but handles outcome variables that are binary or dichotomous (Hosmer & Lemeshow, 2000). This means that instead of estimating a real value, the outcome of a logistic regression model is a probability for the presence or absence of a certain characteristic. Various studies have shown a wide variety of applications for logistic regression, including its usefulness for the analysis of spectral data (e.g. Aspinall, 2002; Hosmer & Lemeshow, 2000; Koutsias & Karteris, 1998; van Ruitenbeek et al., 2006).

The multivariate logistic regression model is described by equation (Hosmer & Lemeshow, 2000).

$$P(x) = \frac{e^{g(x)}}{1 + e^{g(x)}}$$

with,

$$g(x) = \beta_0 + \beta_1 x_1 + \cdots + \beta_p x_p$$

where,

$P(x)$ The conditional probability that the predictors in $x_{n,p}$ correspond to a certain group or characteristic.

x Vector containing p predictor variables.

β Vector containing $p+1$ regression coefficients.

5.3. Principle com- ponent analysis

Principle Component Analysis (PCA) is a procedure in which a matrix with data for different samples and variables is projected onto a k-dimensional space by a linear orthogonal transformation (Jolliffe, 2002; Wold et al., 1987; Eriksson et al., 2006). These k-dimensions are commonly referred to as the k number of principle components. The first Principle Component (PC) represents the direction that describes the largest amount of variance in the variable space of the original data. Each subsequent PC represents the direction of the largest remaining variance that is orthogonal to those of the previous PCs. The projection of data on the first few PCs can therefore be used to easily distinguish between samples that are relatively similar and those that are more different. Furthermore, the contributions of the original variables to each PC can be used to identify the variables for which the samples differ most (Eriksson et al., 2006). The projected data onto the PC space is referred to as the sample scores and the contributions of the original variables are known as the loadings.

Prior to a PCA, the data matrix is often centered by setting the mean of each variable to 0. This places the average of the data at the origin of the variable space which ensures that the PCs describe maximum variance (Jolliffe, 2002). In some cases the data matrix is also scaled by setting the standard deviation of each variable to 1. This prevents the PCA model being dominated by a variable that has a much higher variance than all the others. This is often needed when different types of variables with different ranges of values are used in the PCA.

5.4. Partial least squares regression and discriminant analysis

This section is based on: Dalm, M., Buxton, M.W.N., van Ruitenbeek, F.J.A., 2015. Application of near-infrared (NIR) spectroscopy to sensor based sorting of an epithermal Au-Ag ore. OCM 2015 – conference proceedings. Karlsruhe, Germany.

Partial Least Squares (PLS) regression is a method that is used to calibrate a multivariate linear regression model (Næs & Martens, 1984; Wold et al., 2001). It can be used to investigate the possibilities of predicting a set of response variables from a large set of predictor variables. PLS regression is based on a projection of the original data that is similar to PCA. However, instead of finding PCs that describe maximum variance, PLS regression finds orthogonal components that describe the maximum covariance between the predictor data and the responses (Abdi, 2010; Wold et al., 2001). The orthogonal components in PLS regression are referred to as Latent Variables (LVs). Similar to PCA, scores and loadings are obtained from a PLS regression can be used to identify the variables that are most relevant for predicting the responses. The advantage of PLS regression over most other methods for calibrating multivariate linear regression models is that, by using the LVs, the model is able to handle strongly collinear and noisy predictor variables (Wold et al., 2001).

Partial Least Squares Discriminant Analysis (PLS-DA) is based on PLS regression (Sjöström et al., 1986). The difference is that instead of predicting one or more response variables, PLS-DA is used to predict a certain class analogy. This is performed by simply calibrating a PLS regression model in which the set of response variables is replaced by a dummy matrix with assigned class memberships (Sjöström et al., 1986). As with PCA, it is common to centre the predictor data before applying the PLS regression or discriminant analysis. Scaling is in some cases also applied.

When using PLS regression and discriminant analysis, it is important to select the optimal number of LVs that are used by the model. A higher number of LVs increase the accuracy of the model on data used for calibration, but the predictive power on other data may be decreased due to overfitting (Wold et al., 2001; Abdi, 2010). A common method for selecting the optimal number of LVs is by removing a fraction of the samples from the dataset during model calibration. The

fraction that is removed is usually around 20–35% and referred to as the validation set or test set. The performance of the model on the calibration set and validation set are compared when the model is calibrated with different numbers of LVs. In PLS regression this is usually performed by analysing the mean squared error (MSE) of prediction and in PLS-DA by analysing the error rate of classification. Overfitting generally occurs when the MSE or error rate of the calibration and validation subsets start to diverge from each other.

5.5. References

ABDI, H. 2010. Partial least squares regression and projection on latent structure regression (PLS Regression). *Wiley Interdisciplinary Reviews: Computational Statistics*, 2, 97-106.

ASPINALL, R. J. 2002. Use of logistic regression for validation of maps of the spatial distribution of vegetation species derived from high spatial resolution hyperspectral remotely sensed data. *Ecological Modelling*, 157, 301-312.

ERIKSSON, L., JOHANSSON, E., KETTANEH-WOLD, N., TRYGG, J., WIKSTROM, C. & WOLD, S. 2006. Chapter 3: PCA. *Multi- and Megavariate data analysis*. Umea: Umetrics AB.

HOSMER, D. W. & LEMESHOW, S. 2000. *Applied logistic regression*, New York, John Wiley & Sons.

JOLLIFFE, I. 2002. *Principal component analysis*, Wiley Online Library.

KOUTSIAS, N. & KARTERIS, M. 1998. Logistic regression modelling of multitemporal Thematic Mapper data for burned area mapping. *International Journal of Remote Sensing*, 19, 3499-3514.

NÆS, T. & MARTENS, H. 1984. Multivariate calibration. II. Chemometric methods. *Trends in Analytical Chemistry*, 3, 266-271.

SJÖSTRÖM, M., WOLD, S. & SÖDERSTRÖM, B. 1986. PLS discriminant plots. *Pattern recognition in practice II*, pp. 461-470.

VAN RUITENBEEK, F. J., DEBBA, P., VAN DER MEER, F. D., CUDAHY, T., VAN DER MEIJDE, M. & HALE, M. 2006. Mapping white micas and their absorption wavelengths using hyperspectral band ratios. *Remote Sensing of Environment*, 102, 211-222.

WOLD, S., ESBENSEN, K. & GELADI, P. 1987. Principal component analysis. *Chemometrics and intelligent laboratory systems*, 2, 37-52.

WOLD, S., SJÖSTRÖM, M. & ERIKSSON, L. 2001. PLS-regression: a basic tool of chemometrics. *Chemometrics and intelligent laboratory systems*, 58, 109-130.

Los Bronces Porphyry copper–molybdenum deposit

6.1. Introduction

The Los Bronces mine is an open pit copper and molybdenum mine located about 65 kilometres northeast of Santiago, Chile. It is situated in the Andes Mountains at 3500 metres above sea level. The Los Bronces mine is operated by Anglo American, which currently has a 50.1% ownership. The remainder is for 29.5% owned by the Codelco-Mitsui joint venture and for 20.4% by Mitsubishi. During 2016, Los Bronces produced 307.2 thousand tonnes of copper, of which 36 thousand tonnes was produced as copper cathodes and 271.2 thousand tonnes in copper concentrate (Anglo American, 2016a). Proven and probable reserves are currently 1141 Mt of ore at an average grade of 0.59% Cu and 0.014% Mo (Anglo American, 2016b).

Operations at Los Bronces include traditional open pit truck and shovel mining. Ore treatment is performed by using two different processing streams. The low grade ore is crushed and placed on a heap leach where it is irrigated with sulphuric acid, which leaches out the copper and forms a copper sulphate solution. The copper is extracted from this solution through solvent extraction and electro winning. The higher grade ore is crushed, grinded and mixed with water to create an ore slurry. The ore slurry is pumped through a 56 km long pipeline to the Las Tortolas flotation plant. At the Las Tortolas plant a copper concentrate is produced through flotation, thickening and filtering. A part of the copper concentrate is directly sold. The rest transported to the Chagres smelter, where copper anodes are produced.

6.2. Study description

6.2.1. Geologic setting

This section provides a brief overview of the main characteristics of the Los Bronces deposit. A more extensive description of the geology of Los Bronces is presented by Warnaars et al. (1985).

The Los Bronces deposit is a large hydrothermal copper-tourmaline breccia complex that was superimposed on the western part of an earlier porphyry system. The breccia complex consists of at least seven different breccias that form one body of around 2 km long and 0.7 km wide (Warnaars et al., 1985). Formation of the deposit was driven by volcanic activity that was associated with tectonic changes that accompanied the subduction of the Juan Fernandez ridge at the Chilean trench (Serrano et al., 1996).

The Los Bronces deposit was created by several different alteration and mineralisation events. The first event is the formation of a porphyry system, which is characterised by disseminated and stockwork copper-iron-molybdenum sulphide mineralisation and propylitic, sericitic, silicic and potassic alteration (Warnaars et al., 1985). The second event is the formation of the breccia complex. The breccias were formed over a relatively short time period as a result of pressure build-up during retrogression of the porphyry system (Warnaars et al., 1985). The mineralisation and alteration characteristics of each breccia are different. The third alteration and mineralisation event is related to the emplacement of the La Copa diatreme. The La Copa volcanic eruption took place northeast of Los Bronces and removed a large section of the northern part of the porphyry system. Hydrothermal activity was cut off after the La Copa eruption (Warnaars et al., 1985). Finally, supergene copper enrichment occurred at some areas of the Los Bronces deposit. Supergene enrichment was related to the groundwater regime and therefore more a function of permeability than initial mineral distribution. The extent of the supergene enrichment is unknown, but in some places more than 500 m thick (Warnaars et al., 1985).

Figure 6.1 presents an overview of the sequence of hydrothermal events that led to the formation of the Los Bronces porphyry deposit. This figure shows the hydrothermal activity at Los Bronces versus the approximate occurrence of the initial porphyry mineralisation, the formation of the different breccia systems, and the emplacement of the La Copa volcanic neck.
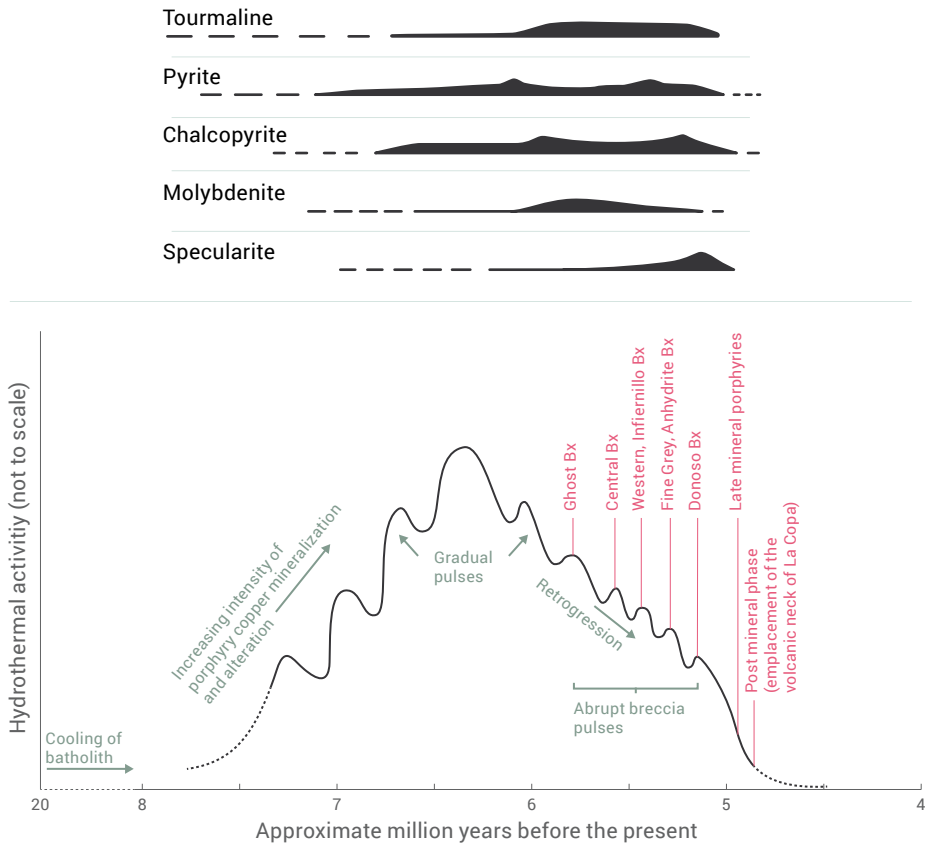
Figure 6.1: Schematic overview of the hydrothermal activity that produced the Los Bronces deposit (based on Warnaars et al., 1985).

6.2.2. Samples

The research described in this chapter is based on 150 samples that were supplied by the Los Bronces mine. The samples are individual rock particles of about 5-7 cm large. The samples originate from the oversize output of the Semi-Autogenous Grinding (SAG) mill of the mineral processing facility. The origin of the samples with respect to the geology of the deposit is therefore unknown. Figure 6.2 shows an example of four of the samples that were used in the study.

Figure 6.2: Example of four samples obtained from the Los Bronces mine.

6.2.3. Objectives

The aim of the Los Bronces study was to investigate the opportunities for sensor-based particle-by-particle sorting at this mine. This was focussed at researching the applicability of real-time sensors to segment waste from ore particles. Only the applicability of using real-time sensors to characterise ore particles was investigated. The feasibility of using sensor-based sorting machines to sort the ore is out of scope.

At Los Bronces, ore and waste are defined by a cut-off grade of 0.40% Cu. This cut-off grade is the minimum copper grade that is required for economic processing of the ore. Although some of the ore also contains molybdenum, the molybdenum grade is not considered for the definition of ore and waste. Most of the samples with low copper grades also have a relatively low molybdenum grade.

The objective of the Los Bronces study is to use real-time sensor data to segment a population of samples that all have copper grades below 0.40%. It is not necessarily needed to segment all samples that contain less than 0.40% Cu since sensor-based particle-by-particle sorting can already provide economic benefits if a significant fraction of the waste can be eliminated.

6.2.4. Geochemistry

All the 150 samples were cut in halves to provide a smooth surface for the sensor measurements. For 94 samples one half was used for X-Ray Fluorescence (XRF), X-Ray Diffraction (XRD) and/or petrographic analysis. This provided data on the mineralogy and chemical composition of the samples. Table 6.1 presents an overview of the different combinations of XRF, XRD and petrographic analyses that were performed on five subsets of the sample set. Sample selection for these subsets was based on visual inspection. Samples were selected in such a way that the variability of the subsets represented the variability of the entire sample set as much as possible. It should be noted that set 5 that is shown in Table 6.1 was not yet available for the study described in chapter 6.3.

The thin sections used in petrography were taken from the cut surface of the samples, so that each thin section represents the surface that is measured with the sensors as much as possible. The XRD and XRF analyses were both based on the bulk of half a sample. Unfortunately, these do not necessarily represent the sample surface. This was not considered a problem, however, since in a sensor-based sorting application it will also be required to predict a bulk grade from surface measurements, unless a sensor is used that is able to measure a material volume. Relating the bulk grade of the ore samples to surface information is one of the challenges that are associated with sensor-based sorting.

Table 6.1: Overview of the different types of analysis that were performed on five subsets of the sample set.

Type of analysis	Set 1 18 samples	Set 2 30 samples	Set 3 17 samples	Set 4 13 samples	Set 5 16 samples
XRF	●	●	●	○	●
XRD	○	●	○	○	○
Petrography	○	○	●	●	○

6.3. VNIR–SWIR point spectrometry

This section is based on: Dalm, M., Buxton, M.W.N., van Ruitenbeek, F.J.A., Voncken, J.H.L., 2014. Application of near-infrared spectroscopy to sensor based sorting of a porphyry copper ore. Minerals Engineering, 58, 7–16.

6.3.1. Introduction

It was explained in chapter 4.2. that the deposition of copper at porphyry ore deposits is related to the formation of specific alteration minerals. As described in chapter 3, spectral reflectance measurements on the SWIR spectral range can often be used to detect alteration mineralogy. It was therefore investigated if it is possible to use VNIR-SWIR spectral reflectance data to segment a population of samples that are all waste. As discussed in chapter 6.2.3, ore and waste are defined by an economic cut-off grade of 0.40% Cu.

6.3.2. Methods

General approach

Several VNIR-SWIR reflectance measurements were collected on each sample with an ASD Fieldspec3 point spectrometer (ASD Inc., Longmont, Colorado, USA). This instrument records spectral reflectance on a 350-2500 nm range using three detectors. The spectral resolution is around 3 nm on the 350-1000 nm range and around 10 nm on the 1000-2500 nm range. The spot size that is measured by the spectrometer is a circular area with a radius of 1 cm. The VNIR-SWIR reflectance measurements were performed on the cut surface of the samples since this surface is smooth and uncontaminated by dust.

The acquired VNIR-SWIR spectra needed pre-processing to convert the recorded data to relative reflections. This was performed by using a white reference and a dark current calibration. A white reference is a measurement of a material with almost 100% reflection over the entire spectral range that is measured. A dark current is a measurement that is performed when no light enters the sensor in order to capture instrumental noise. Spectra of relative reflectance

were calculated by dividing the measured spectrum by the white reference after subtracting the dark current from both these measurements.

A splice correction was also performed on the VNIR-SWIR reflectance spectra. A splice correction is the correction of the step in reflectance values that sometimes occurs at the wavelength position where the data from the different detectors are joined. The step in reflectance values was removed by shifting the reflectance values on the 1000-2500 nm range to match those on the 350-1000 nm range.

The VNIR-SWIR reflectance spectra were analysed for characteristic mineral absorptions by comparing them to reference spectra from the USGS spectral library by Clark et al. (2007) and the spectral interpretation field manual (G-MEX) by Pontual et al. (1997). One to three minerals were determined from each VNIR-SWIR reflectance spectrum. For certain minerals, also mineral characteristics such as crystallinity and compositional variations were determined from the VNIR-SWIR spectra.

SWIR spectroscopy of white mica

SWIR spectroscopy permits characterisation of differences in composition and crystallinity for certain species of white mica (e.g. Clark et al., 1990; Pontual et al., 1997). White mica is sometimes also referred to as sericite (figure 1), which is an umbrella term for all fine grained mica minerals. White mica species that were of main interest are muscovite and illite. Both these minerals are dioctahedral phyllosilicates that have similarities in chemical composition (Ralph & Chau, 1993; Rieder et al., 1998). By definition, muscovite differs from illite by the relative amount of inter-layer cation positions that are occupied by potassium (Rieder et al., 1998). In other words, illite is a K-deficient form of muscovite. But apart from this definition, muscovite and illite are also often distinguished from each other in terms of crystallinity (Nieto & Sánchez-Navas, 1994; Pontual et al., 1997). Crystallinity can be defined as the degree of order, or periodic arrangement of all atoms, ions or molecules within a solid. Due to the K-deficiency, illite generally has a lower crystallinity than muscovite. But apart from this interlayer cation deficiency, the crystallinity of phyllosilicates is also affected by other interlayer material arrangements, stacking sequences and isomorphous substitutions where various ions or vacancies occur on certain coordination sites (Guggenheim et al., 2002). Although such other types of disorder are also commonly characterised at a higher degree for illite than for muscovite (Pontual et al., 1997), they are not officially defined by these (Nieto & Sánchez-Navas, 1994; Rieder et al., 1998). This is because in practice the term crystallinity is qualitative and depends on the type of order that is described, the dimensional nature of the periodicity that is present and the technique that is involved to characterise it (Guggenheim et al., 2002). The term crystallinity is therefore considered inappropriate for classification of minerals and mineral characteristics.

The main SWIR spectral difference between muscovite and illite is the depth of an absorption around 1900 nm (Pontual et al., 1997). The 1900 nm absorption is a vibrational overtone combination of the O-H stretch and the H-O-H bend caused by molecular water (Clark et al., 1990; Hunt, 1977). It will be referred to as the H2O absorption. The water that produces this absorption

can either be physically adsorbed on the surface of mineral grains, it can occupy specific lattice sites or it can be part of the crystal structure (Clark et al., 1990). Because the lower crystalline illite generally has more interlayer sites that are occupied by water molecules, this mineral produces deeper H_2O absorptions than the higher crystalline muscovite (e.g. Pontual et al., 1997). Based on this characteristic, the depth of the H_2O absorption can be used to quantify a degree of white mica crystallinity. In practice, a degree of white mica crystallinity was quantified by calculating the ratio between the depth of the H_2O absorption and the depth of the deepest white mica absorption that occurs around 2200 nm. Using a ratio of absorption depths instead of absolute depths reduces the influence of spectral variability due to the overall reflection and texture of the samples. The 2200 nm absorption in the ratio is a vibrational overtone combination of the Al-OH bend and the O-H stretch caused by the white mica molecule bonds (Clark et al., 1990; Hunt, 1977). It will be referred to as the Al-OH absorption. Because the term crystallinity is considered inappropriate for classification of minerals, the crystallinity that is calculated from SWIR spectra will be referred to as the SWIR crystallinity. Calculation of the SWIR crystallinity for white mica is illustrated in Figure 6.3 and Figure 6.4. Figure 6.3 also shows the definition of absorption depth and several other spectral features in a VNIR-SWIR spectrum.

Spectral features from VNIR–SWIR reflectance spectra

Several spectral features of characteristic mineral absorptions were calculated from the measured VNIR-SWIR reflection spectra. The aim was to use these spectral features as predictors in the multivariate logistic regression. Prior to the spectral feature calculations, each spectrum was normalised to average reflection 1. This corrects for albedo differences and allows comparison of absolute absorption depths between different samples.

By using the 1st and 2nd order derivatives of the normalised VNIR-SWIR spectra, the minimum location and depth of the most dominant mineral absorptions were calculated. Also the minimum and maximum of the first derivative on respectively an inclining and declining slope of a dominant mineral absorption were calculated. This represents the sharpness of the absorption and/or the impact of superimposed secondary mineral absorptions that result in shoulder shapes or shallow absorption minima. Additionally, the impact of ferrous ion absorption was quantified by calculating the reflection difference between 1450 and 1850 nm. The above mentioned spectral characteristics are illustrated in Figure 6.3. Derivative VNIR-SWIR spectra used in the calculations were determined by using a numerical central difference approximation.

$$\text{Mica SWIR crystallinity} = \frac{\text{depth Al-OH absorption}}{\text{depth } H_2O \text{ absorption}}$$
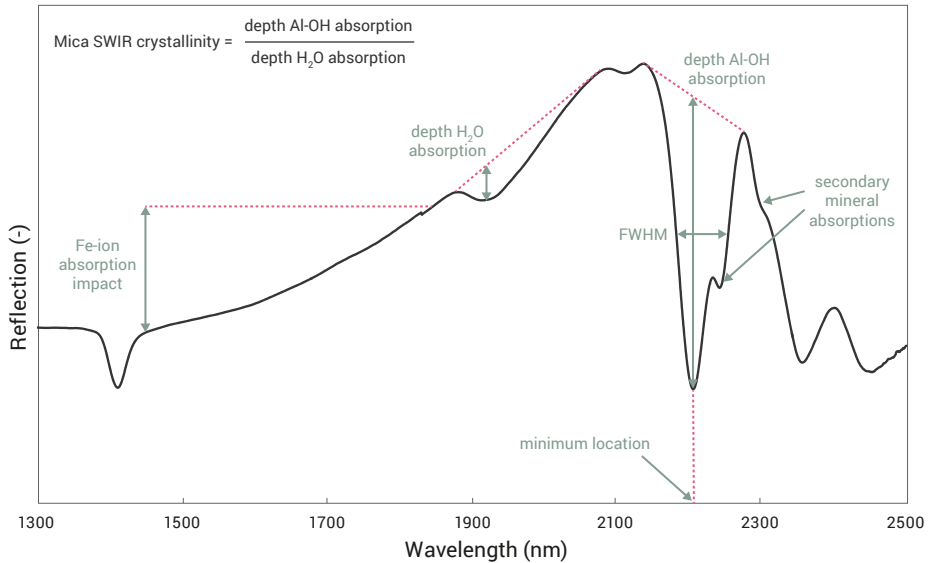
Figure 6.3: Overview of spectral features on a VNIR-SWIR spectrum of mica + minor tourmaline. Shown spectral features include mica crystallinity, absorption depth, minimum location, full width half-maximum (FWHM), Fe-ion absorption impact, and secondary absorptions of tourmaline.

Multivariate logistic regression

Multivariate logistic regression modelling was applied to estimate a probability that the copper grade of a sample is below or above a certain economic cut-off grade. Only 67% of the 65 samples on which XRF was performed was used for calibration of the logistic regression model to allow validation of the results. Selection of calibration and validation subsets was random, but based on an optical classification. This was to ensure that the variability of the subsets represented the variability of the entire sample set.

A set of calculated spectral features from the measured VNIR-SWIR reflectance spectra were used as predictor variables in the logistic regression. Selection of these spectral features was based on the characteristic absorptions of the determined VNIR-SWIR active mineralogy. The significance of the predictor variables for logistic regression modelling was tested by calculating two types of p-values. First of all, the software used for logistic regression calculates p-values (p1) for each predictor by using a t-test statistic. This software also calculates the deviance of the resulting model. By applying a sequential elimination of the predictors by their highest p-value (p1), the difference in model deviance that each predictor produces was calculated. This allowed calculation of a second p-value (p2) by relating the difference in deviance to a χ-square distribution. All calculated spectral features that resulted with p1 and p2 values below a significance level of α=0.05 were considered significant for calibration of the multivariate logistic regression model.

Matlab R2011b statistics toolbox was used to perform the logistic regression. The logistic regression function within this toolbox uses the maximum likelihood method for determination of the regression coefficients.

6.3.3. Results

Mineralogy from VNIR–SWIR reflectance spectra

Dominant mineral absorptions – white mica

White mica is the dominant SWIR active mineral in almost all measured VNIR-SWIR reflectance spectra. The presence of white mica was validated for all samples analysed by XRD or petrography. White mica species determined by VNIR-SWIR spectrometry range from muscovite to illite. As explained previously, VNIR-SWIR spectrometry can discriminate between these minerals based on the SWIR crystallinity.

The spectral analysis showed that the different SWIR crystallinities of white mica do not constitute discrete groups, but range from typical muscovite SWIR crystallinity to typical illite SWIR crystallinity. Muscovite and illite are not officially defined by their crystallinity and a general boundary value on the SWIR crystallinity between these minerals is not available. As a result, it was not possible to reliably distinguish between higher SWIR crystalline illite and lower SWIR crystalline muscovite. It was therefore considered more appropriate to refer to the different white mica species as either high SWIR crystalline white mica (hc-mica) or low SWIR crystalline white mica (lc-mica).

Figure 6.4 shows several measured VNIR-SWIR spectra of the resulting white mica classification. From top to bottom, the VNIR-SWIR spectra are ordered with a decreasing SWIR crystallinity value. Exact minimum locations of the Al-OH absorption are between 2200 – 2210 nm. This indicates potassic white mica compositions, resulting in muscovite and illite classifications (Pontual et al., 1997). It can be observed from Figure 6.4 that with a decreasing SWIR crystallinity value, also the 2450 nm absorption of white mica disappears. This corresponds to Clark et al. (1990)'s observation that the 2450 nm absorption is usually poorly defined for illite.

Petrography showed that the white mica resulted from hydrothermal alteration of pre-existing feldspars. It also showed that a difference is present in the extent of feldspar alteration between samples on which a high and a low SWIR crystallinity for white mica was determined. If hc-mica was determined from the VNIR-SWIR spectra on a sample, all feldspars are (almost) completely converted to white mica / sericite. When lc-mica was determined, significant remnants of the feldspars are still present. It was interpreted that this is caused by the fact that the formation of lower crystalline white mica is generally associated with a lower temperature, argillic type of hydrothermal alteration, while the formation of higher crystalline white mica is generally associated with a higher temperature, phyllic type of alteration. This is confirmed by Corbett & Leach (1998) and Pontual et al. (1997). Hydrothermal alteration at relatively low temperatures alters less feldspars than a higher temperature and more intense hydrothermal alteration. This

interpretation validated determinations of different SWIR crystallinities for white mica. Theoretically, it is also possible to characterise a crystallinity index for white mica by XRD (Guggenheim et al., 2002; Nieto & Sánchez-Navas, 1994). However, mixing of the measured diffraction patterns with other minerals prevented a reliable determination of such an index.
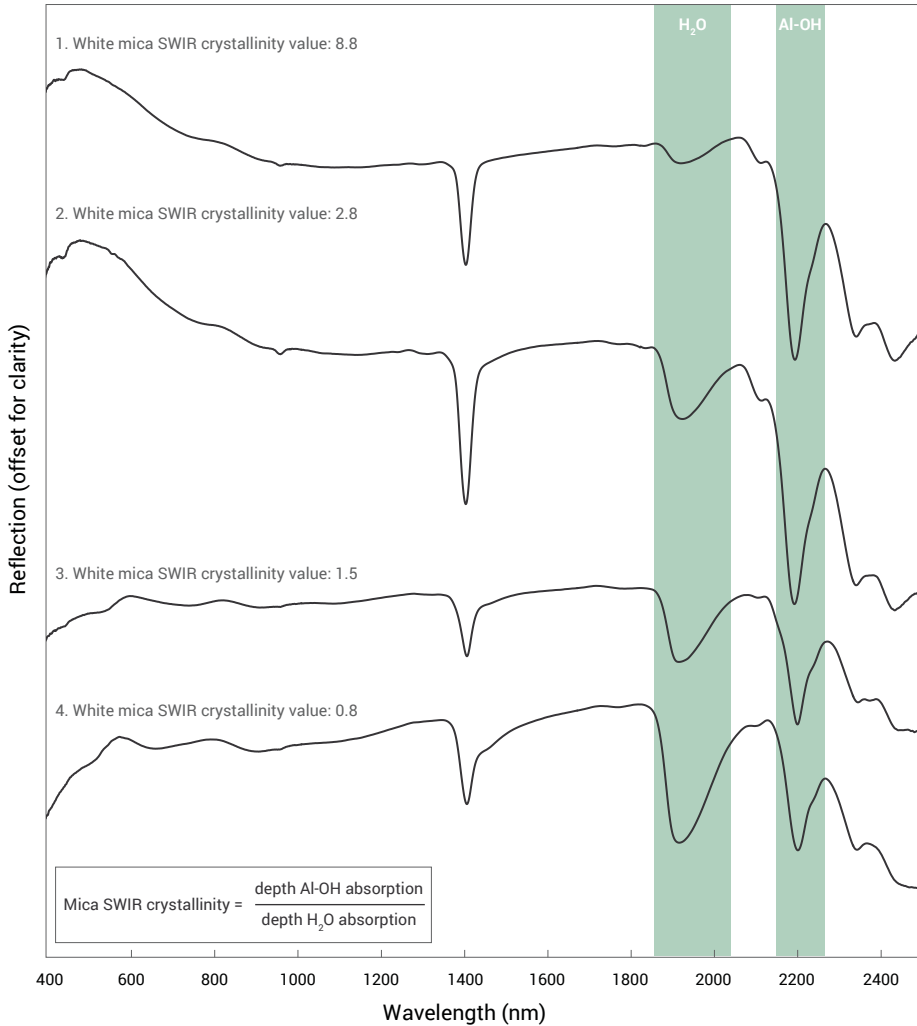

Figure 6.4: Examples of measured VNIR-SWIR reflectance spectra of white mica with varying crystallinity.

Secondary mineral absorptions – chlorite, tourmaline & kaolinite

Absorptions by chlorite, tourmaline and/or kaolinite were also determined from the measured VNIR-SWIR reflection spectra. These minerals mainly occur as a secondary SWIR active mineral, inflicting absorption features that are superimposed on the white mica spectrum. At

several VNIR-SWIR spectra the chlorite or tourmaline absorptions can also be considered dominant. White mica absorptions are still present in this case.

Measured VNIR-SWIR reflectance spectra indicating chlorite, tourmaline and kaolinite are presented in Figure 6.5. It can be observed from this figure that both chlorite and tourmaline (spectrum 1 & 2) give rise to an additional absorption on the white mica spectrum around 2250 nm. Unlike chlorite, tourmaline also causes a weak absorption around 2300 nm that was used to distinguish between these two minerals. However, because the 2250 nm absorption of chlorite and tourmaline coincides, it was not possible to determine if both these minerals produce absorptions in a single VNIR-SWIR spectrum.

The absorption by chlorite that is indicated in Figure 6.5 is caused by the Fe-OH molecule bonds of chlorite (Pontual et al., 1997). The indicated tourmaline absorptions can be assigned to the Fe-OH and Mg-OH molecule bonds of tourmaline (Pontual et al., 1997), although some authors assign these to the B-OH bonds (Clark et al., 1990).

Spectrum 3 in Figure 6.5 shows a very weak shoulder on the left slope of the 2200 nm white mica absorption. This was determined to be caused by the left part of the doublet absorption by kaolinite (2160 nm) and was therefore indicative for this mineral. Spectrum 3 also weakly shows the 2380 nm absorption by kaolinite that is known to persist in mixed SWIR spectra (Pontual et al., 1997). The absorptions that were indicative for kaolinite are caused by the Al-OH molecule bonds of this mineral (Pontual et al., 1997).

The presence of chlorite or tourmaline was validated for all samples analysed by XRD or petrography. The presence of kaolinite however could not be validated for any sample. This was already expected since kaolinite showed only very weak absorptions in the VNIR-SWIR spectra, indicating relatively low proportions in respect to the white mica.

Regarding the chlorite, petrography showed that this mineral is a product of biotite alteration and at several samples remnants of biotite are still present. Biotite is also a SWIR active mineral that produces absorptions which are very similar to those of chlorite (Clark et al., 2007; Pontual et al., 1997). However, since all VNIR-SWIR spectra also show intense white mica absorptions, it was not possible to reliably distinguish between chlorite and biotite absorptions. Influence of biotite on the intensity of the chlorite absorptions can therefore not be excluded. Because the petrography showed that at samples where biotite is present, larger abundances of chlorite occur, it was assumed that the absorptions observed in the VNIR-SWIR spectra were mainly caused by the presence of chlorite.
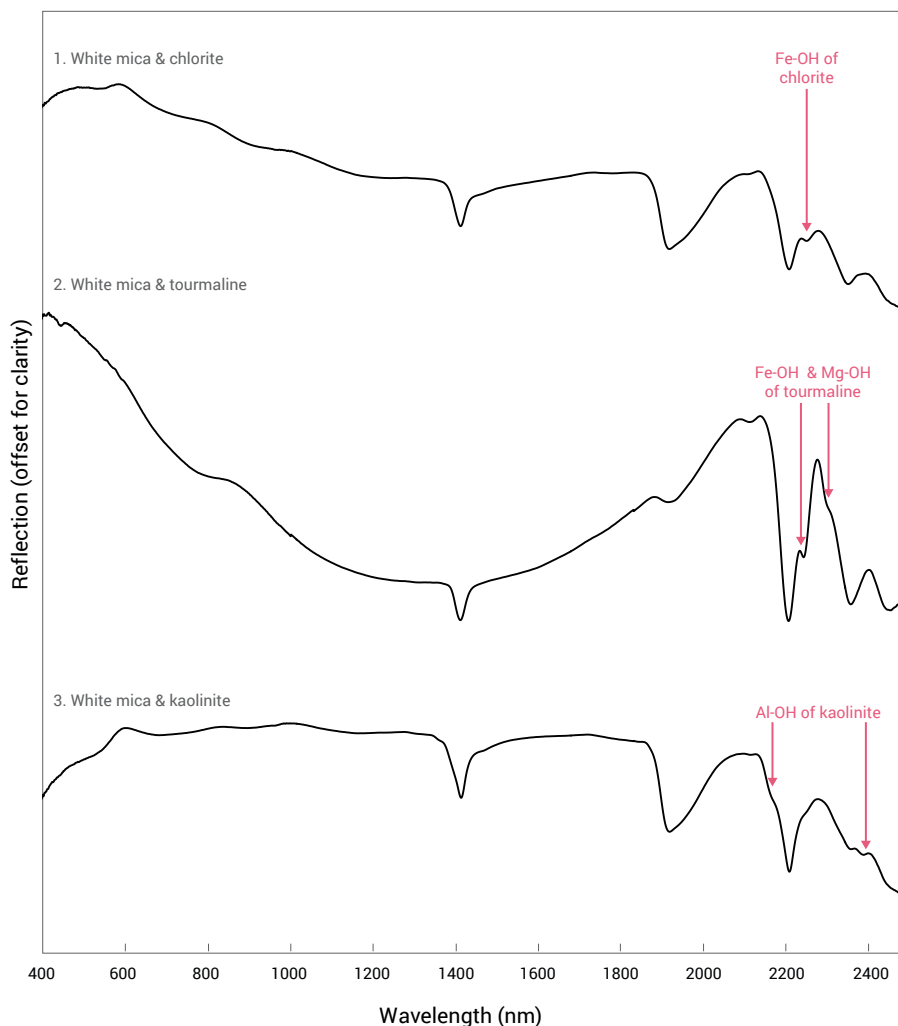
Figure 6.5: Examples of measured VNIR-SWIR mineral spectra.

Copper–bearing minerals

The following copper-bearing minerals were determined from the sample set by petrography: chalcopyrite, chalcocite, covellite, digenite and bornite. All these minerals are copper sulphides that do not produce any diagnostic absorption feature in the VNIR-SWIR (e.g. Clark et al., 2007; Hunt et al., 1971; Grove et al., 1992). Although iron-bearing copper sulphides such as chalcopyrite and bornite do produce ferrous ion absorptions (e.g. Clark et al., 2007; Grove et al., 1992; Hunt et al., 1971), the presence of other iron-bearing minerals such as pyrite, hematite and magnetite prevent these absorptions from being diagnostic for copper.

A limitation of petrography is that the thin section on which it is performed does not necessarily represent an entire sample. It is therefore not possible to exclude the presence of any other copper-bearing minerals. However, the used thin sections were taken from the cut surface of the samples and represent the surface measured by VNIR-SWIR spectrometry. The samples selected for petrography furthermore covered all variability between the determined VNIR-SWIR active mineral assemblages. The absence of any indication of minerals in petrography therefore strongly suggests that any possible occurrence must be in insignificant proportions to have an impact on the measured VNIR-SWIR spectra. It can therefore be assumed that not a single absorption feature is present in the VNIR-SWIR spectra of the samples that relates directly to the copper grade. This was verified by a Partial Least Squares (PLS) regression on the VNIR-SWIR responses and copper grades.

Classification on VNIR–SWIR active mineralogy

The ore samples were classified based on the VNIR-SWIR active mineralogy. This demonstrated that a relation is present between the VNIR-SWIR active mineralogy and copper grades of the ore samples. Since the VNIR-SWIR active mineralogy did not include any copper-bearing minerals, this is an indirect relationship. It is based on differences in the copper grade distribution of sample groups with different VNIR-SWIR active mineral assemblages.

A group of 44 samples is distinguished if the sample set is constrained to samples with VNIR-SWIR spectra that represent lc-mica (2200/1900 nm absorption depth ratio < 2) combined with chlorite absorptions that at least produce a minimum around 2250 nm in one of the measured spectra on the sample. This group represents 29.3% of the entire sample set at an average copper grade of 0.26%. Compared to an average copper grade of the entire sample set of 0.64%, it results that based on the VNIR-SWIR active mineralogy a significant distinction between copper grades can be made. At a cut-off grade of 0.40% Cu, 82% of the group of 44 samples has copper grades below cut-off grade. Compared to 44.6% of the samples from the entire sample set with copper grades below cut-off grade, it results that it is possible to use VNIR-SWIR spectrometry to identify a population of waste samples.

Multivariate logistic regression

A logistic regression was applied to estimate a probability that the copper grade of a sample is below the economic cut-off grade of 0.40% Cu. The aim was to investigate additional possibilities to discriminate waste samples in order to improve the results from classification on the VNIR-SWIR active mineralogy. A set of calculated VNIR-SWIR spectral features was used as predictor variables for the logistic regression. These spectral features are related to the characteristic absorptions of the determined VNIR-SWIR active mineralogy.

In the first logistic regression attempt, all samples were classified as waste or ore based on an economic cut-off grade of 0.40% Cu. The predictors used in this logistic regression with their corresponding p1 and p2 values are presented in Table 6.2. The results of this logistic regression are presented in Figure 6.6.

| Parameter	Parameter description	p1-value	p2-value
2450 / 2200 nm absorption depth ratio	Characterises the white mica mineralogy by the 2450 nm absorption	0.0103	0.0104
1900 / 2200 nm absorption depth ratio	Characterises the SWIR crystallinity of white mica	0.0029	0.0080
2250 nm 1st derivative absorption impact	Characterises the influence of a secondary absorption by chlorite / tourmaline	0.0001	0.0000
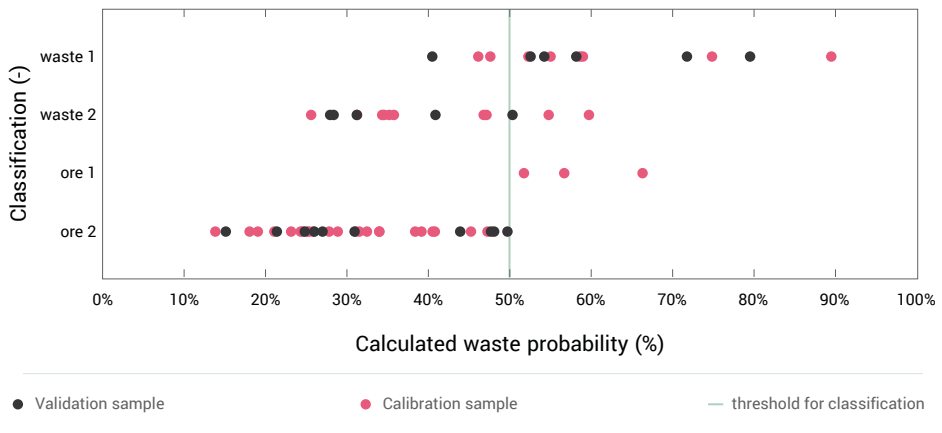
Figure 6.6: Calculated waste probabilities from the 1st logistic regression. Waste 1 and Ore 1 groups represent all samples with VNIR-SWIR spectra showing lc-mica combined with chlorite absorptions that at least produce a minimum around 2250 nm in one of the spectra. Waste 2 and Ore 2 groups represent all other samples. The difference between the waste and ore groups is the copper grade with respect to the cut-off grade of 0.40% Cu.

The dots in Figure 6.6 represent the average waste probability (below cut-off) of all VNIR-SWIR reflectance measurements on each sample. The pink dots represent samples that were used for calibration of the logistic regression model, and the black dots samples used for validation. Both the waste and ore samples are displayed as two separate groups in Figure 6.6. This is because a difference resulted in the ability of the model to discriminate on specific types of waste. The Waste 1 and Ore 1 groups in Figure 6.6 represent all samples on which VNIR-SWIR spectra were measured that represent lc-mica combined with chlorite absorptions that at least produce a minimum around 2250 nm in one of the spectra on a sample. The Waste 2 and Ore 2 groups represent all other samples. A SWIR crystallinity value of 2 was used as a boundary value between lc-mica and hc-mica.

Figure 6.6 shows that the highest calculated waste probabilities result for the Waste 1 samples. All Waste 2 samples have waste probabilities that overlap the probabilities of the Ore 1 and Ore 2 groups. This indicates that the only sorting possibility on the sample set is to sort out the Waste 1 samples. This also resulted from classification on the VNIR-SWIR active mineralogy.

In order to improve the results of the 1st logistic regression, a second logistic regression was performed where only the Waste 1 samples were defined as waste for calibration of the model. The Waste 2 samples were combined with the Ore 2 group and defined as ore for model calibration. This is because the 1st logistic regression showed that the Waste 2 samples cannot be distinguished from any of the ore samples. This does mean that for calibration of the 2nd logistic regression model, the samples defined as ore include samples with copper grades below cut-off grade. The predictors used in the 2nd logistic regression with corresponding p1 and p2 values are presented in Table 6.3. The results of the 2nd logistic regression are presented in Figure 6.7.

By comparing Figure 6.6 and Figure 6.7, it can be observed that the 2nd logistic regression produces better results considering the separation of waste probabilities between the Waste 1 samples and all ore samples. Table 6.4 presents a summary of the results from the 2nd logistic regression model for each of the waste and ore groups. From this table it can be observed that the model allows samples from the Waste 1 and the Ore 2 + Waste 2 groups to be segmented, which results in significant differences in the average copper grade of both groups. Segmenting samples from the Waste 1 and Ore 1 groups on the other hand is not performed well by the 2nd logistic regression model. This can also be observed from Figure 6.7, where it is shown that the waste probabilities of the Ore 1 group completely overlap with the Waste 1 group. This can be explained by the fact that the VNIR-SWIR active mineralogy of the samples in the Waste 1 and Ore 1 groups is similar.

It can be observed from Figure 6.7 that the 2nd logistic regression model allows a group of samples to be segmented that all have copper grades below the economic cut-off grade for further processing of the ore. Although the discriminating power between the Waste 1 and Ore 1 samples is low, Table 6.4 shows that the Ore 1 samples constitute only a low fraction of the sample set at an average copper grade that is significantly lower than that of the Ore 2 + Waste 2 group. This means that the influence of the Ore 1 samples on the average copper grade will be relatively low if some of these samples are misclassified into the waste fraction by an actual sorting application. It results that based on the 150 ore samples, a sorting application with a VNIR-SWIR spectral sensor and well defined sorting algorithms is capable to discriminate on a fraction of the waste material.

| Parameter	Parameter description	p1-value	p2-value
2450 / 2200 nm absorption depth ratio	Characterises the white mica mineralogy by the 2450 nm absorption	0.0039	0.0000
1900 / 2200 nm absorption depth ratio	Characterises the SWIR crystallinity of white mica	0.0154	0.0000
2250 nm 1st derivative absorption impact	Characterises the influence of a secondary absorption by chlorite / tourmaline	0.0001	0.0080
2300 nm 1st derivative absorption impact	Characterises the influence of a secondary absorption by tourmaline	0.0000	0.0295
1450 - 1850 nm 1st derivative summation	Characterises the slope that is produced by ferrous ion absorption	0.0000	0.0019
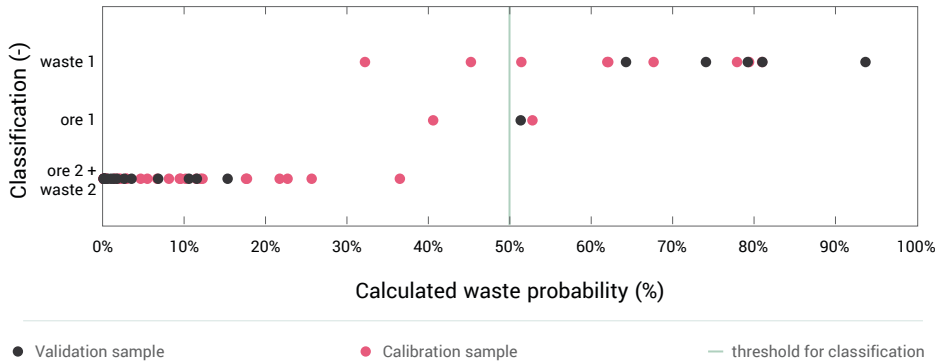
Figure 6.7: Calculated waste probabilities from the 2nd logistic regression. Waste 1 and Ore 1 groups represent all samples with VNIR-SWIR spectra showing lc-mica combined with chlorite absorptions that at least produce a minimum around 2250 nm in one of the spectra. Waste 2 and Ore 2 groups represents all other samples. The difference between the waste and ore groups is the copper grade with respect to the cut-off grade of 0.40% Cu.

Table 6.4: Summary of results from the 2nd logistic regression model.

	Fraction of samples (%)	Classification success (%) i.r.t. 50% waste probability		Average waste probability (%)	Average Cu grade (%)
		Calibration	Validation		
Waste 1	21.5	78	100	67.9	0.20
Ore 1	4.6	50	0	48.2	0.47
Ore 2 + Waste 2	73.9	100	100	6.2	0.78

6.3.4. Evaluation of sensor–based sorting solutions

The VNIR-SWIR spectral sensor was tested without a sensor-based sorting machine. Evaluation of sensor-based sorting solutions is therefore only based on the discrimination capabilities of the VNIR-SWIR spectral sensor. The results of the 2nd logistic regression model (Figure 6.7) will be used for this. This model provided the best classification result because it allows a group of samples that all have copper grades below the economic cut-off grade of 0.40% to be distinguished. In Figure 6.8 and Figure 6.9, the average copper grade and amount of samples are presented if the estimated waste probability from this logistic regression is used as a threshold for classification. The average copper grade of the ore and waste groups in Figure 6.8 is calculated for the 65 samples on which XRF analysis was performed. Sample amounts in Figure 6.9 are calculated for all 150 samples.

The costs for processing ore material with sensor-based sorting machines are generally lower than with the conventional methods (Salter & Wyatt, 1991; Sivamohan & Forssberg, 1991; Wotruba & Riedel, 2005). However, when sensor-based sorting is applied, ore material with little value will be discarded while valuable metals are still recovered from this material with conventional processing. This is an important factor when evaluating sensor-based particle-by-particle sorting solutions. Sensor-based particle-by-particle sorting only provides economic benefits if the costs of sorting combined with the value of lost metals are lower than the conventional processing methods.
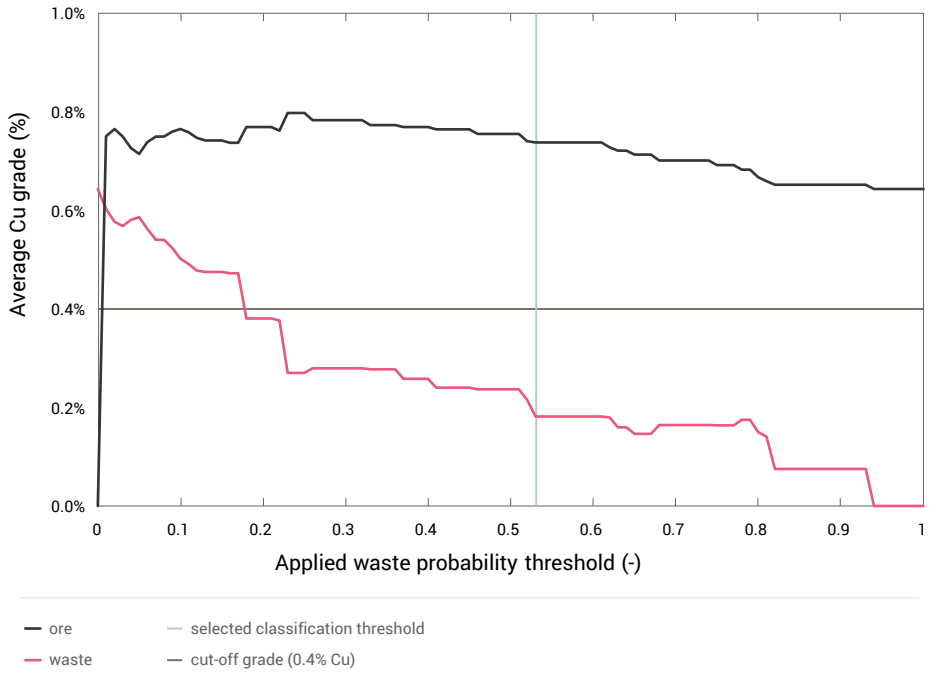
Figure 6.8: Average copper grade from XRF vs. waste probability threshold for the 2nd logistic regression.
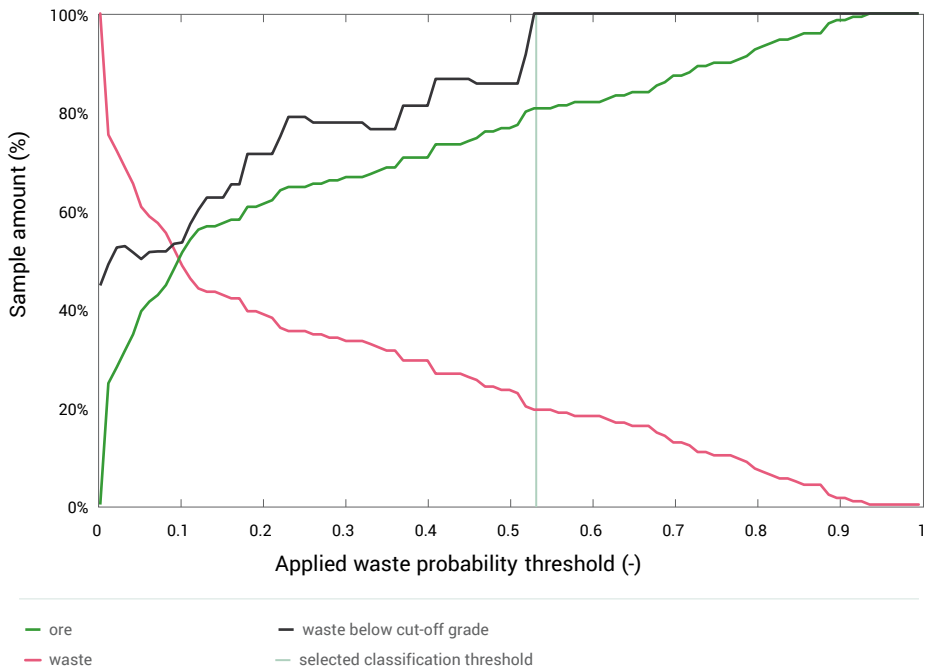

Figure 6.9: Sample amounts vs. waste probability threshold for the 2nd logistic regression.

The best sensor-based particle-by-particle sorting solution results when a significant amount of material can be discarded at the highest possible material loss / valuable metal loss ratio. However, it was not possible to reliably calculate this ratio for the obtained results. This is because the highest material loss / copper loss ratio results for the lowest average copper grade (0.81 – 0.94 waste probability). Compared to Figure 6.7, the lowest average copper grade is based on only one sample since only one sample has a waste probability > 0.81. Because of this, the ideal sorting solution from Figure 6.8 and Figure 6.9 was interpreted to be the waste probability threshold for which only samples below economic cut-off grade are distinguished. In this case, every individual particle that is discarded provides no economic benefit when it is processed by conventional processing methods. Figure 6.9 shows that 100% of the waste fraction is below cut-off grade for a waste probability threshold larger than 0.53. It also shows that at this threshold, 19.3% of all samples are classified as waste. Figure 6.8 shows that the average grade of this waste fraction is 0.18% Cu. It results that the VNIR-SWIR spectral sensor allows discriminating a significant amount of material at a copper grade that is less than half the economic cut-off grade. This indicates that there is potential that sensor-based particle-by-particle sorting can provide economic benefits for processing this ore. However, a more detailed analysis of a sensor-based sorting application on porphyry copper ore still has to prove the feasibility of this technique.

6.3.5. Discussion

Petrography showed that the white mica species that were determined from the VNIR-SWIR spectra of all samples are a product of hydrothermal alteration of feldspars. As described by Pontual et al. (1997), the SWIR crystallinity of white mica is related to the intensity of hydrothermal alteration. The different white mica species can therefore be assigned to different zones of hydrothermal alteration within the porphyry system. Apart from white mica, also secondary VNIR-SWIR active minerals were determined from the VNIR-SWIR spectra including chlorite, tourmaline and kaolinite. The occurrence of these minerals can also be assigned to different zones of hydrothermal alteration (Lowell & Guilbert, 1970; Pontual et al., 1997; Sillitoe, 2010; Thompson et al., 1999). It results that VNIR-SWIR spectrometry is an excellent tool to distinguish between different assemblages of hydrothermal alteration minerals. This means that VNIR-SWIR spectrometry can be used to characterise hydrothermal alteration zones within a porphyry ore deposit. This result was already expected based on publications by Pontual et al. (1997), Thompson et al. (1999) and Franchini et al. (2007).

None of the copper-bearing minerals that were determined by petrography produce diagnostic absorptions in the VNIR-SWIR spectral range (e.g. Clark et al., 2007; Grove et al., 1992; Hunt et al., 1971). This means that predicting copper grades from the VNIR-SWIR response of the ore samples can only be based on indirect indicators.

A relationship between the VNIR-SWIR response and copper grades of the 150 ore samples was found. This is based on the VNIR-SWIR active mineralogy that was determined from the measured VNIR-SWIR reflectance spectra. Since the VNIR-SWIR active mineralogy did not

include any copper-bearing minerals, the found relationship is indirect. It can be explained by the fact that the different VNIR-SWIR active mineral assemblages represent different zones of hydrothermal alteration that likely constitute different ranges of copper grades throughout the porphyry system.

All ore samples that show absorptions of low SWIR crystalline white mica and chlorite in the VNIR-SWIR spectra, have relatively low copper grades. The difference between these samples and ore samples with higher copper grades is that all higher grade samples either lack intense chlorite absorptions or show high SWIR crystalline white mica in the VNIR-SWIR spectra. Additionally, absorptions by tourmaline and kaolinite were occasionally determined from the VNIR-SWIR spectra of the higher grade ore samples.

A Partial Least Squares (PLS) regression was performed on the copper grades and the VNIR-SWIR responses of the ore samples. PLS regression is a standard tool in chemometrics and has proven usefulness in sensor evaluation (Næs & Martens, 1984; Wold et al., 2001). The aim of using PLS regression was to determine if there is any relation between the copper grade and VNIR-SWIR response that can be modelled by a linear regression model. This allows any VNIR-SWIR spectral feature that relates to the copper grade of the ore samples to be identified. The reflection values at all measured wavelengths from each VNIR-SWIR spectrum were used as predictor variables in the PLS regression. The mean squared error of the copper grade estimations on a validation subset did not decrease with an increasing number of Latent Variables (LVs). This means that none of the LVs contribute to the estimation of copper grades. This reconfirms that none of the spectral features in the VNIR-SWIR spectra of the ore samples relate directly to the copper grade.

Multivariate logistic regression showed that the only possibility for segmenting waste samples with a VNIR-SWIR spectral sensor is to discriminate samples that contain low SWIR crystalline white mica and chlorite as the dominant VNIR-SWIR active mineralogy. A logistic regression that was aimed at discriminating these samples showed satisfying results (2nd logistic regression, Figure 6.7). Based on the predictors used in this logistic regression (Table 6.3), it are the white mica SWIR crystallinity and relative contents of chlorite, tourmaline and ferrous ions that allow identification of samples with copper grades below the cut-off grade. This means that the VNIR-SWIR active mineralogy contains additional features that relate to the copper grade than those identified by classification of the spectra by visual inspection. It results that logistic regression is a good method in order to classify samples on a specific VNIR-SWIR active mineralogy that represents a certain range of copper grades.

6.3.6. Conclusions

The following conclusions were drawn from testing VNIR-SWIR point spectrometry on 150 porphyry copper ore samples:

- VNIR-SWIR spectrometry could be used to distinguish between different assemblages of hydrothermal alteration minerals of the ore samples collected from the Los Bronces porphyry copper-molybdenum deposit.

- No copper-bearing minerals could be determined with VNIR-SWIR spectrometry.

- An indirect relationship is present between the copper grade of samples and the mineralogy that can be determined with VNIR-SWIR spectrometry. This indirect relationship is based on sample groups with different VNIR-SWIR active mineral assemblages that represent different zones of hydrothermal alteration and constitute different ranges of copper grades.

- VNIR-SWIR spectrometry could be used to segment a population of waste samples. This is based on detecting specific alteration mineral assemblages.

- The best copper grade discrimination was provided by a logistic regression model that uses calculated spectral features of the VNIR-SWIR active mineralogy as predictors.

6.4. SWIR hyper-spectral imagery

This section is based on: *Dalm, M., Buxton, M.W.N., van Ruitenbeek, F.J.A., 2017. Discriminating ore and waste in a porphyry copper deposit using short-wavelength infrared (SWIR) hyperspectral imagery. Minerals Engineering, 105, 10–18.*

6.4.1. Introduction

This chapter investigates the applicability of SWIR hyperspectral imagery for characterizing the copper grade of 43 of the porphyry copper ore samples. The most different samples that were observed within the sample set of 150 samples were selected for this investigation. The copper grades of all 43 samples included in this study were determined by XRF analysis.

Chapter 6.3. showed that an indirect relationship exists between the copper grade of the samples and the alteration mineralogy that can be determined with SWIR point spectrometry. However, each spectrum that is acquired with a commonly used point spectrometer represents a sample surface of several cm2 (e.g. ASD, 2015). Since most hyperspectral imagers acquire spectra on a pixel size below 1 mm2 (e.g. Corescan, 2015; Specim, 2015), these instruments can provide more detailed information about the abundance and spatial distribution of the SWIR-active mineralogy. It is therefore expected that SWIR hyperspectral imagery will reveal additional differences between samples, which might be used to improve upon the indirect characterisation of copper grades.

This chapter gives an example of how SWIR hyperspectral images can be processed to produce maps that show the distribution of SWIR-active minerals. It will also be shown how certain mineral characteristics such as the white mica crystallinity can be mapped from these images. Furthermore, a method is presented that uses these maps as input variables in a Principle Component Analysis (PCA) in order to find samples that have similar mineralogical composition and to identify the mineralogical differences between sample groups. Finally, we will show how this can be used to segment populations of ore and waste.

6.4.2. Methods

Data acquisition

The copper grades of all the samples which SWIR hyperspectral imagery was performed were known from the XRF analyses described in chapter 6.2.4. SWIR hyperspectral images of the samples were acquired with a SisuCHEMA instrument (SPECIM ltd., Oulu, Finland). The hyperspectral images were recorded on a 940 – 2540 nm spectral range and at a spectral resolution of 10 nm. The images were made from the cut surface of the samples because this surface is flat, smooth and uncontaminated by dust. The pixel size of the images is around 0.2 mm.

Image pre-processing

The SWIR hyperspectral images needed pre-processing to convert the recorded data to relative reflections. This was performed by using a white reference and a dark current calibration. Spectra of relative reflectance were calculated by dividing the measured spectrum by the white reference after subtracting the dark current from both these measurements. This was performed with Specim's in-house software.

Image processing

The SWIR hyperspectral images were processed using ENVI 4.5 image processing software (ITT visual information studios, 2008). The first step was to mask the images by removing the data of pixels that do not represent a sample. This was performed by manually selecting regions of interest on the images. Subsequently, a mineral map was produced from the masked image of each sample by using the Spectral Angle Mapping (SAM) algorithm (Kruse et al., 1993) in combination with a set of reference spectra. SAM classifies each image pixel by assigning the mineral or mineral assemblage to it that is represented by the reference spectrum to which the pixel spectrum has the smallest multi-dimensional angle. A maximum angle of 0.2 radians was applied as a threshold to ensure a positive correlation between the image pixels and reference spectra. The SAM method was chosen for constructing mineral maps because numerous studies show that it is an effective method to classify the pixels of hyperspectral images (e.g. Girouard et al., 2004; Kruse, 2012; Rowan et al., 2005).

The reference spectra used with SAM were selected from the measured SWIR hyperspectral images so that the spectral range and resolution of the used references and the image pixels are equal. The mineral or mineral assemblage that is represented by each reference spectrum was determined by comparing the spectrum with the SWIR spectra of the USGS spectral library (Clark et al., 2007) and the spectral interpretation field manual, G-MEX (AusSpec, 2008). This comparison was performed by inspecting the wavelength positions and relative intensities of the absorption features in the spectra.

An initial set of reference spectra was collected by manually selecting spectra that represented the observed variability in the measured SWIR hyperspectral images. SAM was applied to produce mineral maps and the classification of randomly chosen pixels was checked by inspecting the spectra. Pixels that were incorrectly classified or that were not classified due to the maximum angle threshold were added to the set of reference spectra after the minerals that produced the spectrum were identified. This process was repeated until no unclassified pixels remained and no incorrect classifications were observed.

Apart from the mineralogy, the following mineral characteristics were also mapped from the SWIR hyperspectral images of the samples: white mica composition, white mica crystallinity, and chlorite composition. This was based on the wavelength positions and depth ratios of specific mineral absorption features. These spectral properties were calculated with the Hyperspectral Python (HypPy) toolbox (Bakker, 2012). The algorithms in this toolbox fit a parabola to the wavelength channels around an absorption feature to interpolate the wavelength position of the absorption minimum. The absorption depth is calculated by dividing the reflectance value of the absorption minimum by that of the continuum around the absorption feature. Mineral characteristics were only mapped for pixels that represent pure mineral spectra (i.e. spectra that only show absorption features of a single mineral). This was done by masking the image with the resulting mineral map.

PCA

Principle Component Analysis (PCA) was performed on a data matrix containing the relative abundance of all the identified SWIR-active minerals for each sample and the sample averages of the features representing white mica crystallinity and white mica composition. Spectral features that describe the composition of chlorite were not included in the PCA since not all samples contained chlorite. The relative abundance of the SWIR-active minerals was calculated by dividing the number of pixels that represent a certain mineral by the number of pixels that represent the sample. A multiplicative zero replacement followed by a centered log-ratio transformation was subsequently applied to this data (Aitchison, 1986; Martín-Fernández et al., 2003). This was required to correct for the fact that the mineralogical compositions sum up to a constant (i.e. 100%). This constant sum constraint can influence the outcomes of the PCA since it places restrictions on the correlation structure of the data (Aitchison, 1986). Furthermore, the data matrix was centered and scaled before applying the PCA.

The PCA sample scores were compared with the XRF results to investigate if there is a relationship between the copper grade of the ore particles and the mineralogical information that can be derived from SWIR hyperspectral imagery. The PCA loadings were used to identify the minerals and/or mineral characteristics that describe this relationship.

6.4.3. Results

Minerals identified from SWIR hyperspectral images

White mica

White mica is the most abundant SWIR-active group of minerals in almost all SWIR hyperspectral images of the samples. White mica is an umbrella term that usually refers to muscovite, paragonite, celadonite, aluminoceladonite, illite, illite-smectite or any coexisting occurrence of these minerals. These different white mica species can be distinguished from each other with SWIR spectrometry (AusSpec, 2008; Clark et al., 2007; Duke, 1994).

Figure 6.10 presents several SWIR spectra of white mica that were used as reference spectra for producing mineral maps with SAM. As mentioned in section 6.4.2, these reference spectra originate from the measured SWIR hyperspectral images. Spectrum 1 in Figure 6.10 is characteristic for muscovite and spectrum 5 is characteristic for illite. The other spectra represent intermediate muscovite-illite species. The absorption features that can be observed in the spectra are produced by vibrating molecule bonds. The diagnostic white mica absorption occurs around 2200 nm and is produced by an overtone combination of the O-H stretch and the Al-OH bend vibration (Clark et al., 1990; Hunt, 1977). This absorption will be referred to as the white mica Al-OH absorption feature.

The exact wavelength position of the minimum of the Al-OH absorption feature correlates with the Al content of white mica (Duke, 1994; Post & Noble, 1993). Muscovite is a common endmember of white mica for which the Al-OH absorption minimum is located around 2200 nm (AusSpec, 2008; Duke, 1994; Post & Noble, 1993). Substitution of the Al by Fe and Mg in the muscovite crystal structure through octahedral exchange (Al ⇌ (Fe,Mg)) or octahedral-tetrahedral Tschermak exchange (AlAl ⇌ (Fe,Mg)Si) shifts the minimum position of this feature to longer wavelengths (Duke, 1994). The white mica endmembers resulting from this substitution are aluminoceladonite and celadonite. These endmembers often form solid solutions with muscovite, which are referred to as phengite (Rieder et al., 1998). The Al-OH absorption minimum for phengite is located around 2225 nm (AusSpec, 2008). Minimum positions of the white mica Al-OH absorption feature in the measured SWIR hyperspectral images range from 2198 to 2220 nm. This indicates that the white mica in the samples has a muscovitic to phengitic composition.

Figure 6.10 shows that the intensity of the white mica absorption around 1900 nm is variable. This absorption is produced by an overtone combination of the O-H stretch and H-O-H bend vibration of molecular water (Clark et al., 1990; Hunt, 1977). It will be referred to as the H_2O absorption feature. It was discussed in chapter 6.3.2. that it is possible to characterize the white mica crystallinity from the intensity of this feature. A white mica crystallinity index was calculated by dividing the absorption depth of the Al-OH absorption by that of the H_2O absorption. Muscovite and phengite are white mica species with a high crystallinity index. White mica species with similar composition, but a low crystallinity index, are referred to as illite and phengitic illite.

The absorption that is located around 1410 nm is an overtone of the O-H stretch vibration (Clark et al., 1990; Hunt, 1977). All minerals that contain OH bonds will produce such an absorption feature. The exact minimum position of this absorption feature depends on the cation that the OH bond is attached to (Clark et al., 1990; Hunt, 1977).
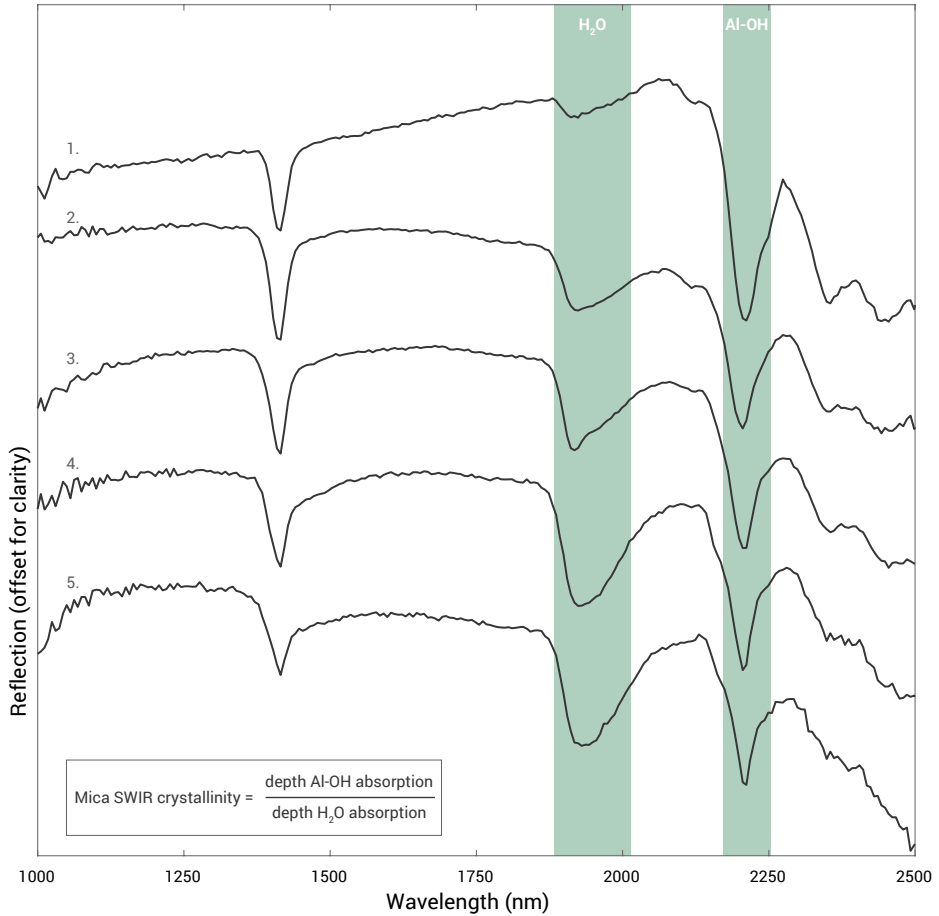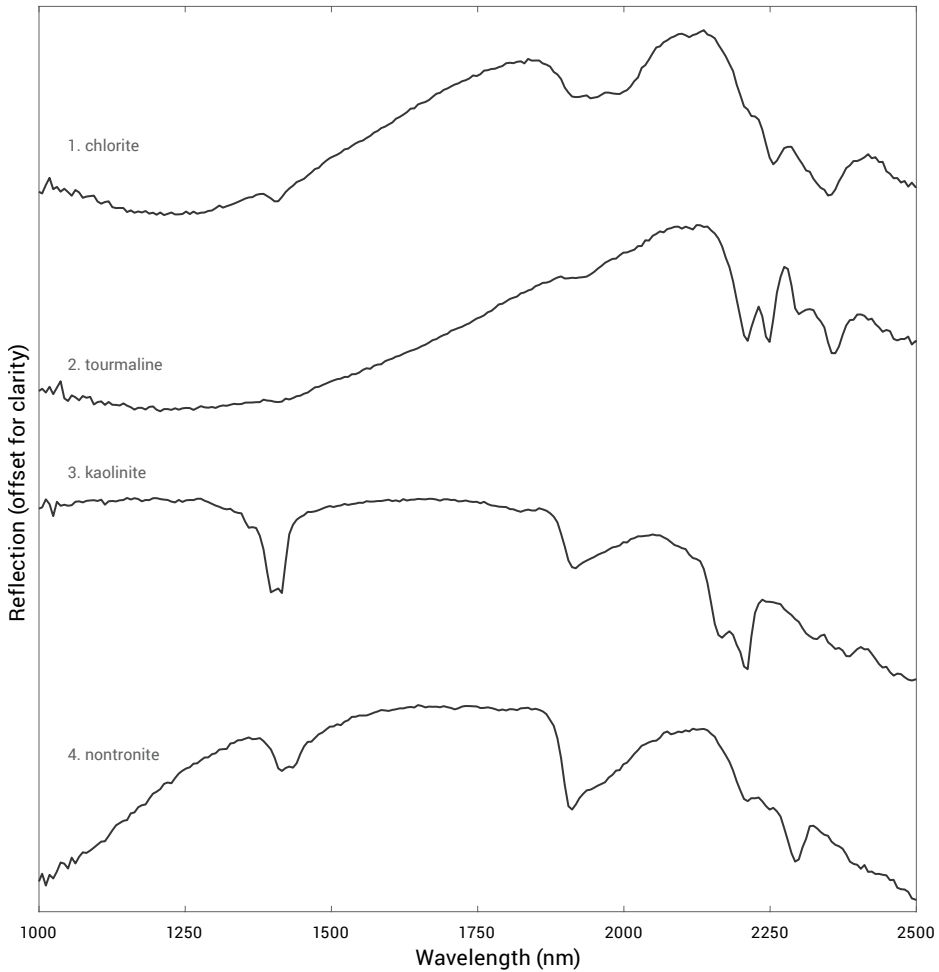

Figure 6.10: Examples of measured SWIR spectra of white mica with decreasing crystallinity from spectrum 1 to 5. Spectrum 1 is characteristic for muscovite and spectrum 5 is characteristic for illite. Spectra 2-4 represent intermediate muscovite-illite species.

Figure 6.11: Examples of measured SWIR mineral spectra.

Chlorite

Minerals from the chlorite group were identified from the SWIR hyperspectral images of some of the samples. Chlorite is an umbrella term that usually refers to clinochlore, chamosite, or a solid solution between these two endmembers. One of the reference spectra that were used for the SAM classification of chlorite is spectrum 1 in Figure 6.11. Chlorite produces diagnostic absorptions around 2250 and 2350 nm (AusSpec, 2008; Clark et al., 2007). Mineral absorptions in the 2230 – 2295 nm range commonly result from O-H stretch and Fe-OH bend vibration (AusSpec, 2008; Clark et al., 1990). Furthermore, absorptions produced by O-H stretch and Mg-OH bend vibration commonly occur in the 2300 – 2370 nm range (AusSpec, 2008; Clark et al., 1990). The chlorite absorptions that occur around 2250 and 2350 nm will therefore be referred to as the chlorite Fe-OH and Mg-OH absorption feature respectively.

The exact wavelength position of the minimum of the Fe-OH and Mg-OH absorption features are related to the relative amount of Mg versus Fe ions that occur within the chlorite crystal structure (AusSpec, 2008; McLeod et al., 1987). If the chlorite is rich in Mg the minimum position of the Fe-OH and Mg-OH absorptions are around 2245 and 2320 nm (AusSpec, 2008; McLeod et al., 1987). When the Mg is partly substituted by Fe, the minimum of both absorption features shift to longer wavelengths. For Fe-rich chlorite the minimum of the Fe-OH and Mg-OH absorptions are located around 2265 and 2365 nm (AusSpec, 2008; McLeod et al., 1987). Minimum positions of the chlorite Fe-OH and Mg-OH absorptions in the measured SWIR hyperspectral images range from 2248 to 2261 nm and from 2324 to 2360 nm respectively. This indicates that the chlorite in the samples varies from Mg-rich to Fe-rich, corresponding to clinochlore-chamosite chlorite species.

Tourmaline, kaolinite and nontronite
Spectra 2 to 4 in Figure 6.11 are examples of reference spectra that were used for the SAM classification of tourmaline, kaolinite and nontronite. Tourmaline produces diagnostic absorptions at 2210, 2250, 2300 and 2360 nm (AusSpec, 2008; Clark et al., 2007). These absorption features are mainly produced by the Fe-OH and Mg-OH bonds of tourmaline (AusSpec, 2008). However, some authors suggest that the tourmaline absorption features can also be caused by overtone combination of the O-H stretch and B-OH bend vibration (Clark et al., 1990).

Spectrum 3 in Figure 6.11 shows double absorption features around 1400 and 2200 nm that are diagnostic for kaolinite. The absorptions around 1400 nm are produced by the O-H bonds and the ones around 2200 nm by the Al-OH bonds of kaolinite (Clark et al., 1990; Hunt, 1977). The reason that a double absorption feature, or doublet, is produced at both wavelength positions is related to the fact that kaolinite has OH groups at different locations in the crystal structure. O-H stretch vibration of OH groups located on the exterior surface of the octahedral sheets absorb radiation at a slightly shorter wavelength than that of the OH groups located in between the tetrahedral and octahedral sheets (Crowley & Vergo, 1988). The double feature around 2200 nm is produced because both types of OH groups form Al-OH bonds.

Spectrum 4 in Figure 6.11 has a double absorption feature around 1420 nm and a single feature around 2290 nm that are diagnostic for nontronite. Most nontronite spectra in spectral libraries only show a single absorption feature around 1420 nm (e.g. AusSpec, 2008; Clark et al., 2007). However, a double absorption feature at this wavelength position has been reported for nontronite by Clark et al. (1990). It is produced by different O-H stretching vibrations similar to that of kaolinite. The absorption around 2290 nm is produced by the Fe-OH bonds of nontronite (AusSpec, 2008; Clark et al., 1990).

Other minerals
Apart from the SWIR spectra presented in Figure 6.10 and Figure 6.11, spectra with a relatively low reflection and no mineral absorption features were found in the measured SWIR hyperspectral images. Minerals that were not identified from the SWIR hyperspectral images, but that were determined by XRD and petrography include quartz, feldspars (orthoclase, albite and anorthite), hematite, magnetite, pyrite and the ore minerals chalcopyrite, digenite, bornite, chalcocite and

covellite. None of these minerals contain molecule bonds that produce absorption features in the SWIR (Clark et al., 2007). However, quartz and feldspars are somewhat transparent and the spectra of the hyperspectral images will therefore show absorption features of underlying SWIR-active minerals where quartz and feldspars are located. All the other minerals that were determined by XRD and petrography are opaque minerals that are known to have a low reflection in the SWIR (Clark et al., 2007; Baldridge et al., 2009). Since it is not possible to distinguish between the different types of opaque minerals from the SWIR spectra, all spectra with a low reflection and without mineral absorption features were classified as opaque minerals when producing the mineral maps with SAM.

Mapping SWIR-active mineralogy

Figure 6.12 presents four examples of the results of mapping the SWIR-active mineralogy from the measured SWIR hyperspectral images. The figure shows a photo of each sample, the mineral map resulting from the SAM classifications and maps of the Al-OH feature position and the crystallinity index of white mica.

For all samples white mica minerals were mapped. A relatively high abundance of either chlorite or tourmaline was common. Several samples contain both chlorite and tourmaline. In that case, the abundance of chlorite was always higher than that of tourmaline. Nontronite, kaolinite and opaque minerals only occurred in relatively low abundances. Furthermore, nontronite was not observed in the mineral maps of samples with relatively high tourmaline contents.
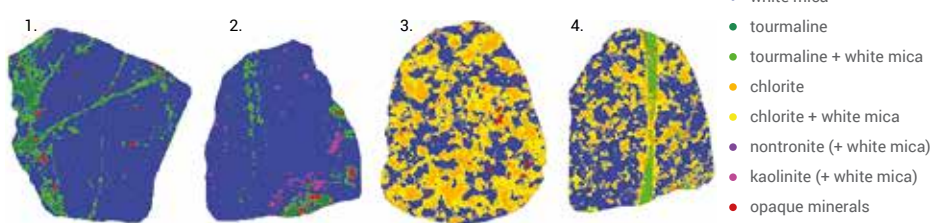
The mineral maps in Figure 6.12b show classifications of pure mineral spectra as well as mixtures with white mica. These mixtures are SWIR spectra in which the absorption features of white mica as well as some other mineral can be observed. For nontronite and kaolinite, the same color was assigned to the pure spectra and the spectral mixtures. This was done to improve the visibility of these minerals, since the number of pixel spectra that contain absorption features of nontronite or kaolinite is relatively low. Mixed spectra with opaque minerals were not classified. A pixel was only classified as an opaque mineral when no mineral absorptions could be observed in the spectrum due to a low reflection.

Calculating the white mica crystallinity index and the Al-OH absorption minimum was only performed on pixels with pure white mica spectra. This is because absorptions by other minerals might affect the shape and intensity of these features. Figure 6.12c and 6.12d show that mapping the characteristics of white mica reveals additional differences between samples. Furthermore, these maps provide information on the texture of samples since vein structures containing white mica with a different composition and/or crystallinity become visible.
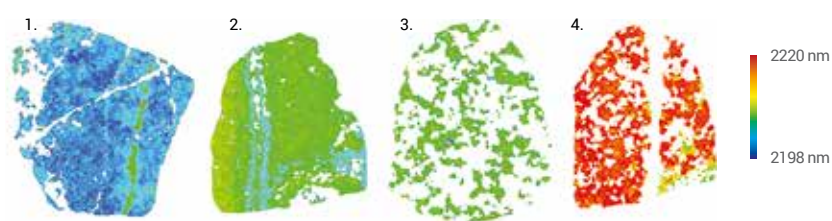
A. photo

5 cm

B. mineral map

- white mica
- tourmaline
- tourmaline + white mica
- chlorite
- chlorite + white mica
- nontronite (+ white mica)
- kaolinite (+ white mica)
- opaque minerals

C. wavelength position white mica Al-OH absorption feature[1]
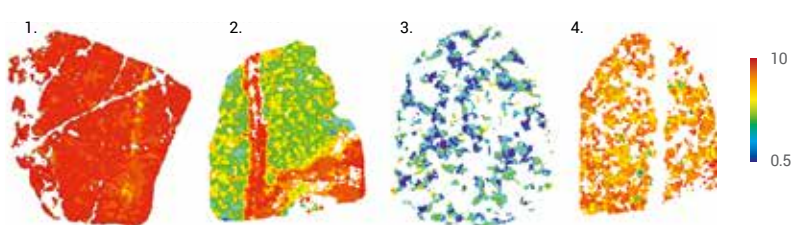

2220 nm

2198 nm

D. white mica crystallinity index[1]

10

0.5

Figure 6.12: Selected examples of mineral maps produced from the SWIR hyperspectral images. [1]Mapping the wavelength position of the white mica Al-OH absorption feature and the white mica crystallinity index was only performed on pure white mica spectra (i.e. no absorption features by any other mineral).

Figure 6.13: Selected examples of maps showing the wavelength position of the chlorite Mg-OH absorption feature. Mapping was only performed on pure chlorite spectra (i.e. no absorption features by any other mineral).

Figure 6.13 presents two maps of the wavelength position of the chlorite Mg-OH absorption minimum. These maps correspond to sample 3 and 4 presented in Figure 6.12. Calculating the minimum position of the chlorite Mg-OH absorption was only performed on pixels with pure chlorite spectra. Figure 6.13 shows that mapping this characteristic of chlorite reveals additional differences between samples.

PCA

Figure 6.14 presents the PCA sample scores of the first and second Principle Component (PC). The black dots in this figure represent samples that are ore and the pink dots samples that are waste. As discussed in chapter 6.2.3, the definition of ore and waste is based on an economic cut-off grade of 0.40% Cu.

PCA was performed on a data matrix containing the relative SWIR-active mineral abundances for each sample and the sample averages of the white mica crystallinity index and the wavelength position of the white mica Al-OH absorption feature. The black lines in Figure 6.14 represent the loadings of these variables. These were all equally scaled to fit the figure and therefore do not represent the actual loading values. The capital letters indicate the type of mineral that is represented by the loadings. Cryst and Al-OH refers to the white mica crystallinity index and the minimum position of the white mica Al-OH absorption. The chlorite Mg-OH absorption was not included in the PCA since not all samples contain chlorite.

The green rectangle in Figure 6.14 indicates a region in the score plot where mainly waste samples occur. It results that these can be distinguished by using the first PC. It can be inferred from the loadings of this PC that the samples in the green rectangle have relatively high contents of chlorite and low contents of white mica, tourmaline and opaque minerals. Furthermore, these samples contain white mica with relatively low crystallinity values and with Al-OH features that occur at longer wavelengths. The white mica species of the samples in the green rectangle are therefore close to a phengitic illite while that of the other samples are closer to muscovite.
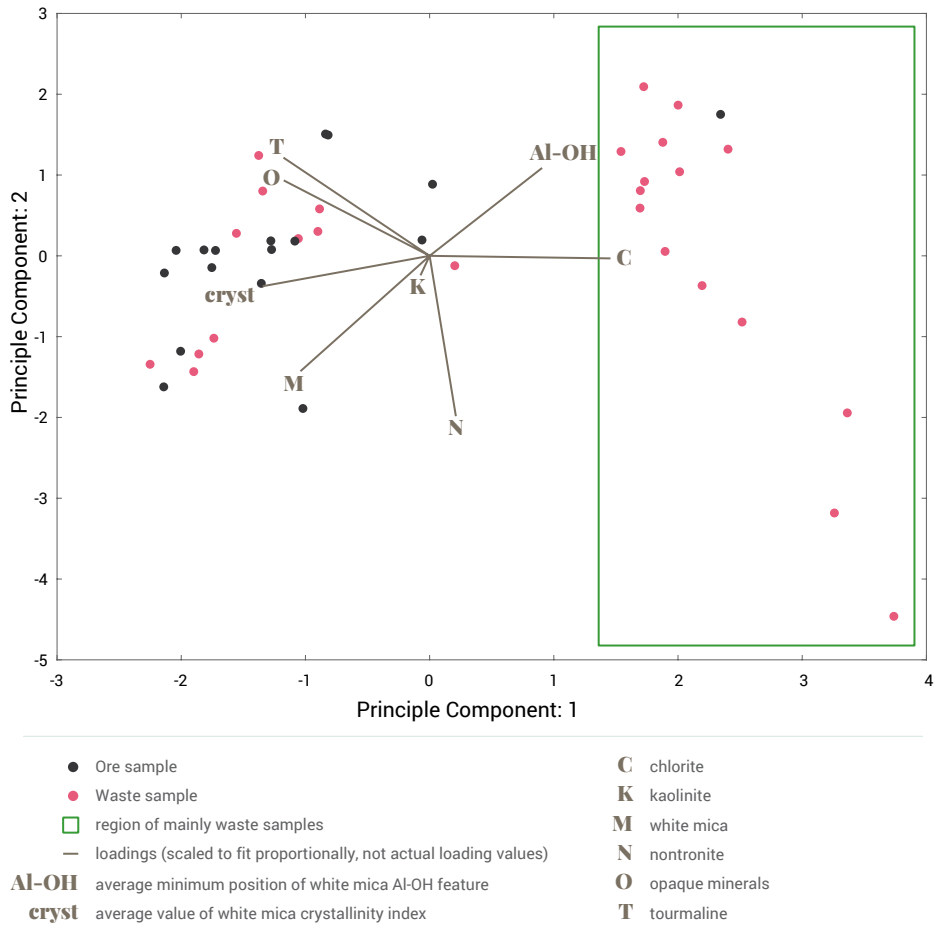
Figure 6.14: Sample scores and loadings of the PCA on data derived from mineralogy maps.

It can be observed from Figure 6.14 that the green rectangle contains one ore sample. This sample has a relatively high score on the second PC. It can be inferred from the loadings of this PC that this relates to relatively high contents of tourmaline and opaque minerals and low contents of nontronite and white mica. Furthermore, high scores on the second PC are associated with white mica Al-OH features that occur at longer wavelengths.

Figure 6.15 presents the resulting copper grade distributions when the samples are classified on the PCA scores of the first PC. A score of 1 was used as a threshold for the classification. Samples with PCA scores above this threshold are all samples inside the green rectangle in Figure 6.14. Although Figure 6.14 shows that the second PC can be used to also distinguish the ore sample in the green rectangle from most of the waste samples, this was not performed for the classification result presented in Figure 6.15. The reason is that this ore sample has a copper grade of 0.47%, which is only just above the economic cut-off grade of 0.40% Cu. Furthermore,
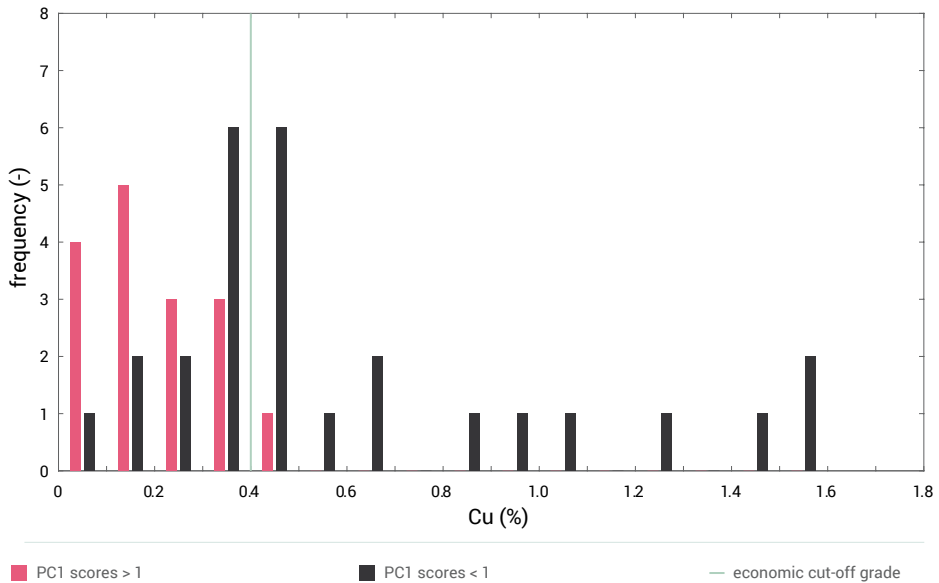
Figure 6.15: Distribution of copper grades after classifying the samples on the PCA scores of the first PC. A score of 1 was used as a threshold for the classification. Copper grades were determined by XRF analysis.

the PCA scores of this ore sample are relatively close to the scores of a significant portion of the waste samples. This means that the ore sample cannot be separated from these waste samples unless thresholds are used that are based on relatively small differences between the SWIR-active mineralogy of the samples. Using such thresholds will likely decrease the robustness of the resulting classification.

Figure 6.15 shows that classifying the samples on a PCA score threshold of 1 on the first PC distinguishes a group of 16 samples of which 15 samples are waste. This group contains 58% of all the waste samples in the sample set and has an average grade of 0.20% Cu. Since this average copper grade is well below the economic cut-off grade, it results that SWIR hyperspectral imagery in combination with mineralogy mapping and PCA can be used to discriminate a significant portion of the sub-economic ore. Removing these sub-economic ore samples from the sample set will increase the average copper grade from 0.45% to 0.60%.

6.4.4. Discussion

PCA proved to be an effective method to display the systematic variation of the data that was extracted from mineralogy maps. It makes it relatively easy to find samples that have similar mineralogical composition and to identify the mineralogical differences between sample groups. The method can save a lot of time when hyperspectral images of sample sets in the order of hundreds of samples or more need to be analyzed.

Petrography and XRD validated that white mica, chlorite and tourmaline were correctly identified from the SWIR hyperspectral images. Validation of the specific white mica species was not carried out. Furthermore, kaolinite and nontronite were not determined with petrography or XRD. However, when these minerals occur in any of the mineral maps they cover only a relatively small surface area. It is therefore possible that they were missed in the thin sections on which petrography was performed or that their concentration was below the detection limit of XRD. No other minerals were identified with petrography or XRD that could be responsible for the measured SWIR spectra that were classified as kaolinite and nontronite. Furthermore, the wavelength position of the absorption features in these SWIR spectra clearly indicate the occurrence of two minerals that were not determined by XRD or petrography. This means that even if the identification of kaolinite and/or nontronite was incorrect, the PCA results presented in section 6.4.3. that are based on SWIR-active mineralogical differences between samples are still valid.

The different mineral assemblages that resulted from mapping the mineralogy from the SWIR hyperspectral images are characteristic for different zones of hydrothermal alteration within the porphyry system (AusSpec, 2008; Thompson et al., 1999). The ability to segment a population of waste samples with SWIR hyperspectral imagery is therefore based on a relationship between copper mineralisation and the formation of alteration minerals. This was expected since this relationship was also established in chapter 6.3. As discussed in chapter 6.3.5, the detection of alteration minerals with SWIR spectral sensors can be used as indirect indicators for sensor-based sorting if the relationship between alteration mineralogy and copper mineralisation persists throughout the entire ore deposit. Validation of the results on a sample set that is representative of the full mineralogical variability of the deposit is required to be able to conclude on the applicability of sensor-based particle-by-particle sorting. The results of this study do show potential for using SWIR spectral sensors for sensor-based sorting of porphyry copper ores.

Comparing the results in section 6.4.3. with those in chapter 6.3.3. shows that using SWIR hyperspectral imaging did not improve upon the indirect characterisation of copper grades that was achieved using SWIR point spectrometry. However, SWIR hyperspectral imaging has several advantages over SWIR point spectrometry regarding the mineralogical information that can be extracted from the data. These advantages are related to the capability of SWIR hyperspectral imaging sensors to acquire SWIR data at a relatively high spatial resolution (i.e. small pixel size).

First of all, the surface area that is represented by a single SWIR spectrum is much smaller with most hyperspectral imagers than with commonly used point spectrometers. The spot size of SWIR point spectrometers is often in the order of several cm2 (e.g. ASD, 2015), while SWIR hyperspectral imagers usually acquire spectra on a pixel size below 1 mm2 (e.g. Corescan, 2015; Specim, 2015). This relatively small pixel size allows minerals to be detected that occur in relatively low quantities. Examples of such minerals in the sample set are nontronite, opaque minerals, and sometimes kaolinite and/or tourmaline. The absorption features of these minerals often became completely obscured by those of the surrounding minerals when SWIR point spectra were measured.

The relatively small pixel size in hyperspectral imaging also provides spectra of pure minerals while point spectrometry frequently yields mixed spectra with absorption features by two or three minerals. The pure mineral spectra can be used to extract parameters that describe differences in the composition or crystallinity of certain minerals. Although these parameters can also be extracted from mixed mineral spectra, these will be less accurate since they can be affected by the absorption features of the other minerals.

Another advantage of SWIR hyperspectral imaging is that a large number of spectra (± 50 000 per sample) are acquired simultaneously. This allows the SWIR-active mineralogy at the surface of samples to be quantified by classifying each spectrum on the mineral and/or mineral characteristic that it represents and counting the number of times that a certain classification occurs. This can be used to distinguish between smaller compositional differences such as the occurrence of specific white mica species and the relative amount of chlorite or tourmaline that the samples contain.

Finally, SWIR hyperspectral imaging has the advantage that the spectral information can be displayed in an image. This provides data about the distribution of the SWIR-active mineralogy which can be used to characterize differences in texture including grain sizes and cross-cutting vein structures. Examples of such textural characteristics can be seen in the different maps of Figure 6.12.

The variability in texture between the samples is relatively high considering the size of the sample set. Because of this, many characteristics that can be observed from the mineralogy maps are often not shared by a sufficient amount of samples to produce statistically meaningful classifications. An example is the vein structure in the white mica crystallinity map of sample 2 in Figure 6.12d. Although such a characteristic provides information about the hydrothermal alteration environment from which the samples originate, it occurs on only two samples in the sample set. Both these samples have significant copper grades (0.62% & 0.96% Cu), but it is uncertain if this relationship between vein structures and copper grades is not coincidental.

The limited size of the sample set is likely the main reason that SWIR hyperspectral imagery did not improve upon the indirect characterisation of copper grades that was possible with SWIR point spectrometry. However, considering the advantages of SWIR hyperspectral imaging, it is expected that the characterisation of copper grade distribution will be improved when this

technique is tested on a sample set that is larger and more representative of the full mineralogical variability of the deposit. An ideal sample set for further testing would be drill core samples.

6.4.5. Conclusions

The following conclusions were drawn from testing SWIR hyperspectral imaging on 43 porphyry copper ore samples:

- The information contained by mineralogy maps that are produced from SWIR hyperspectral images could be used as input variables in a PCA. This provided an effective method to cluster samples that have similar mineralogical composition and to identify the mineralogical differences between sample groups.

- SWIR hyperspectral imagery in combination with mineralogy mapping and PCA could be used to discriminate 58% of the samples with sub-economic copper grades. The average grade of this group of samples is 0.20% Cu, which is well below the economic cut-off grade of 0.40% Cu.

- SWIR hyperspectral imaging did not improve upon the indirect characterisation of copper grades that was achieved using SWIR point spectrometry. The high textural variability between samples and limited size of the sample set are considered to be key contributing factors.

- SWIR hyperspectral imaging has the capability to acquire SWIR data at a relatively high spatial resolution. Because of this, it has the following advantages over SWIR point spectrometry:

  - Provides more complete data of the mineral composition of a sample including minerals that are present in relatively low quantities.

  - Enables the identification and extraction of pure mineral spectra that can be used to characterize mineral composition and/or crystallinity.

  - Enables quantification of the SWIR-active mineralogical composition at the surface of a sample by counting the number pixels representing certain minerals and/or mineral characteristics.

  - Enables the characterisation and evaluation of the texture of samples apparent from mineral maps.

Considering the advantages of SWIR hyperspectral imaging, it is expected that the characterisation of copper grade distribution and ore-waste designations will be improved when this technique is tested on a sample set that is larger and more representative of the full mineralogical variability of the deposit.

6.5. Discussion

VNIR-SWIR spectral sensors could be used to segment a fraction of the waste. This was based on an indirect relationship between the detected hydrothermal alteration mineral assemblages and the copper grade. It resulted that low crystalline white mica and chlorite could be used as indicators of waste. Ore samples mainly contain high crystalline white mica and tourmaline. It was explained in chapter 6.3.3. that the low crystalline white mica is more associated with an argillic type of alteration while high crystalline white mica is more associated with a phyllic type of alteration. Furthermore, the occurrence of chlorite is also more associated with argillic alteration while occurrence of tourmaline is more associated with phyllic alteration (AusSpec, 2008; Corbett & Leach, 1998; Pirajno, 1992). It was shown in chapter 4.2. that the main ore zone at porphyry copper deposits is related to the boundary between potassic and phyllic hydrothermal alteration, and not to the argillic alteration zone. This confirms that the minerals associated with argillic alteration can be used as indicators of waste.

Additional research is required to investigate whether it is economically feasible to use sensor-based sorting machines to remove the waste that can be distinguished with VNIR-SWIR spectral sensors. This depends on the costs of sorting, the costs of conventional processing, the sorting efficiency, the amount of waste that is rejected and the value of the copper that is contained by the waste. Sensor-based sorting provides economic benefits if the value of the amount of copper that is lost by discarding material does not exceed the difference in costs between sensor-based sorting and conventional ore processing. Figure 6.8 and Figure 6.9 in chapter 6.3.4. show that 19.3% of the samples can be rejected at an average copper grade of 0.18%. This is a significant amount of material at a copper grade that is less than half of the economic cut-off grade of 0.40% Cu. Since sensor-based particle-by-particle sorting is generally cheaper than conventional processing methods (Buxton & Benndorf, 2013; Lessard et al., 2014; Salter & Wyatt, 1991; Sivamohan & Forssberg, 1991; Wills & Finch, 2016), this means there is potential that removing this waste with sensor-based sorting can provide economic benefits.

Regarding the application of VNIR-SWIR spectral sensors on actual sensor-based sorting machines, there are some limitations. First of all, VNIR-SWIR spectrometry is a surface technique. This means that the surfaces of the particles that are sorted need to be free of contaminations such as dust. For measuring the VNIR-SWIR spectra, the samples were cut in halves to provide a clean surface. However, a comparison of the VNIR-SWIR spectral sensor responses between the cut surface and the outer surfaces of the samples was left out of scope. In practice, surface contaminations on the ore particles can be removed by washing or dedusting prior to sensor-based sorting.

Another limitation of VNIR-SWIR spectrometry is that the presence of free water results in intense water absorptions in the VNIR-SWIR reflectance spectra. These water absorptions can influence the determination of the VNIR-SWIR active mineralogy. For example, it resulted that the SWIR crystallinity of white mica is an important parameter for classification of the samples. Determination of the white mica SWIR crystallinity is based on the water absorption around 1900 nm, as was explained in chapter 6.3.2. The influence of free water on the discrimination possibilities with the VNIR-SWIR spectral sensor was left out of scope during this research. It was made sure that the samples were dry while taking the VNIR-SWIR reflectance measurements. In an actual sensor-based sorting application free water likely needs to be removed by drying before the ore particles can be sorted.

Finally, sensor-based sorters operate with a certain sorting efficiency due to possible misclassification of particles. The sorting efficiency depends on the characteristics of the sorter and is influenced by the distinctiveness between the VNIR-SWIR spectral sensor responses of ore and waste and the variability of the particles that are sorted.

An additional limitation of using SWIR hyperspectral imaging sensors for sensor-based sorting may be the time needed to acquire the data at a relatively high spatial resolution. In order to reach sufficient throughput on sensor-based sorting machines, the SWIR data needs to be acquired in a relatively short time period which places restrictions on the maximum spatial resolution that can be achieved. It is uncertain to what extent this limits the advantages of SWIR hyperspectral imaging over point spectrometry that were discussed in chapter 6.4.4. For applications of SWIR hyperspectral imaging that are not restricted by data acquisition time, such as drill core scanning, this is not an issue. Spatial resolution in SWIR hyperspectral imaging is, however, an important parameter for any application since it governs the level of detail of the mineralogical information that can be extracted from the data.

The results presented in this chapter are based on 150 ore samples that are randomly collected from a mine's processing operations. It is unknown to what extent these results are representative for the entire deposit. It can be expected though that the results are not fully representative because the samples originate from the oversize output of a SAG mill that generally represents the harder portion of the ore feeding the processing plant. Furthermore, all samples were collected at one moment in time and it is therefore likely that they mainly represent the portion of the deposit that was being mined at the time. Validation of the results on a sample set that is representative of the full mineralogical variability of the deposit is therefore required to be able to conclude on the applicability of using sensors to segment waste. The results of this study

do show potential for using VNIR-SWIR spectral sensors for sensor-based particle-by-particle sorting of porphyry copper ores.

For future research into the feasibility of sensor-based sorting it is recommended to use spatially constrained samples that cover the geological and mineralogical variability of the deposit. Additionally, a geological model of the deposit that includes information on the overprinting relationships by multiple hydrothermal alteration events would be useful in understanding the relations between hydrothermal alteration and copper mineralisation for the entire porphyry system. As explained in chapter 4.2, these relationships can be complicated due to telescoping of the porphyry system and/or superimposition of breccia and diatreme intrusions.

6.6. Conclusions

The following conclusions were drawn from testing VNIR-SWIR spectral sensors on the samples from Los Bronces:

- VNIR-SWIR spectral sensors could be used to distinguish between different assemblages of hydrothermal alteration minerals of the ore samples collected from the Los Bronces porphyry copper-molybdenum deposit.

- VNIR-SWIR spectral sensors could not be used to detect copper-bearing minerals.

- An indirect relationship is present between the copper grade of samples and the alteration mineralogy that could be detected with VNIR-SWIR spectral sensors. This indirect relationship is based on sample groups with different VNIR-SWIR active mineral assemblages that represent different zones of hydrothermal alteration and constitute different ranges of copper grades.

- VNIR-SWIR spectral sensors could be used to segment a population of waste samples. This was based on detecting specific alteration mineral assemblages.

- Additional research is required to investigate whether it is economically feasible to use sensor-based sorting machines to remove the waste that can be distinguished with VNIR-SWIR spectral sensors.

- The following limitations apply to the use of VNIR-SWIR spectral sensors on sensor-based sorting machines:
  - Degree of surface contamination of the ore particles feeding the sorter.
  - Influence of water on the discrimination capabilities of the VNIR-SWIR spectral sensor.
  - Sorting efficiency of sensor-based sorting.

- The sample set used in the Los Bronces study is probably not fully representative of the geological and mineralogical variability of entire deposit. Validation of the results on a sample set that is representative of the full mineralogical variability of the deposit is required to be able to conclude on the applicability of using sensors to segment waste.

6.7. References

AITCHISON, J. 1986. *The statistical analysis of compositional data*.

ANGLO AMERICAN. 2016a. *Annual report* [Online]. Available: http://www.angloamerican.com/investors/annual-reporting [Accessed May 2017].

ANGLO AMERICAN. 2016b. *Ore reserves and mineral resources report* [Online]. Available: http://www.angloamerican.com/investors/annual-reporting [Accessed May 2017].

ASD. 2015. *ASD products & services* [Online]. Available: https://www.asdi.com/products-and-services [Accessed February 2015].

AUSSPEC 2008. *G-MEX Spectral Interpretation Field manual*, AusSpec International ltd.

BAKKER, W. 2012. *Hyperspectral Python (HypPy)* [Online]. Available: https://www.itc.nl/personal/bakker/hyppy.html [Accessed 2015].

BALDRIDGE, A., HOOK, S., GROVE, C. & RIVERA, G. 2009. The ASTER spectral library version 2.0. *Remote Sensing of Environment*, 113, 711-715.

BUXTON, M. & BENNDORF, J. 2013. The use of sensor derived data in optimization along the Mine-Value-Chain. *Proceedings of the 15th International ISM Congress*, Aachen, Germany, pp. 324-336.

CLARK, R. N., KING, T. V., KLEJWA, M., SWAYZE, G. A. & VERGO, N. 1990. High spectral resolution reflectance spectroscopy of minerals. *Journal of Geophysical Research: Solid Earth*, 95, 12653-12680.

CLARK, R. N., SWAYZE, G. A., WISE, R., LIVO, E., HOEFEN, T., KOKALY, R. & SUTLEY, S. J. 2007. *USGS digital spectral library splib06a: U.S. Geological Survey, Digital Data Series 231* [Online]. Available: https://speclab.cr.usgs.gov/spectral-lib.html [Accessed January 2012].

CORBETT, G. J. & LEACH, T. M. 1998. *Southwest Pacific Rim gold-copper systems: structure, alteration, and mineralization*, Society of Economic Geologists.

CORESCAN. 2015. *The corescan system* [Online]. Available: http://www.corescan.com.au/services/the-corescan-system [Accessed February 2015].

CROWLEY, J. K. & VERGO, N. 1988. Near-infrared reflectance spectra of mixtures of kaolin-group minerals: use in clay mineral studies. *Clays and clay minerals*, 36 (4), 310.

DUKE, E. F. 1994. Near infrared spectra of muscovite, Tschermak substitution, and metamorphic reaction progress: Implications for remote sensing. *Geology*, 22, 621-624.

FRANCHINI, M., IMPICCINI, A., MEINERT, L., GRATHOFF, G. & SCHALAMUK, I. B. 2007. Clay mineralogy and zonation in the Campana Mahuida porphyry Cu deposit, Neuquén, Argentina: implications for porphyry Cu exploration. *Economic Geology*, 102, 27-54.

GIROUARD, G., BANNARI, A., EL HARTI, A. & DESROCHERS, A. Validated spectral angle mapper algorithm for geological mapping: comparative study between QuickBird and Landsat-TM. *XXth ISPRS Congress, Geo-Imagery Bridging Continents*, Istanbul, Turkey, 2004. 12-23.

GROVE, C. I., HOOK, S. J. & PAYLOR, E. D. 1992. *Laboratory reflectance spectra for 160 minerals 0.4 - 2.5 micrometers*. Pasadena, CA.

GUGGENHEIM, S., BAIN, D. C., BERGAYA, F., BRIGATTI, M. F., DRITS, V. A., EBERL, D. D., FORMOSO, M. L., GALÁN, E., MERRIMAN, R. J. & PEACOR, D. R. 2002. Report of the Association Internationale pour l'Etude des Argiles (AIPEA) Nomenclature Committee for 2001: Order, disorder and crystallinity in phyllosilicates and the use of the 'Crystallinity Index'. *Clay Minerals*, 37, 389-393.

HUNT, G. R. 1977. Spectral signatures of particulate minerals in the visible and near infrared. *Geophysics*, 42, 501-513.

HUNT, G. R., SALISBURY, J. W. & LENHOFF, C. J. 1971. Visible and near infrared spectra of minerals and rocks. IV. Sulphides and sulphates. *Modern geology*, 3, 1-14.

ITT VISUAL INFORMATION STUDIOS 2008. ENVI 4.5 (commercial computer software).

KRUSE, F., LEFKOFF, A., BOARDMAN, J., HEIDEBRECHT, K., SHAPIRO, A., BARLOON, P. & GOETZ, A. 1993. The spectral image processing system (SIPS)—interactive visualization and analysis of imaging spectrometer data. *Remote sensing of environment*, 44, 145-163.

KRUSE, F. A. 2012. Mapping surface mineralogy using imaging spectrometry. *Geomorphology*, 137, 41-56.

LESSARD, J., DE BAKKER, J. & MCHUGH, L. 2014. Development of ore sorting and its impact on mineral processing economics. *Minerals Engineering*, 65, 88-97.

LOWELL, J. D. & GUILBERT, J. M. 1970. Lateral and vertical alteration-mineralization zoning in porphyry ore deposits. *Economic Geology*, 65, 373-408.

MARTÍN-FERNÁNDEZ, J. A., BARCELÓ-VIDAL, C. & PAWLOWSKY-GLAHN, V. 2003. Dealing with zeros and missing values in compositional data sets using nonparametric imputation. *Mathematical Geology*, 35, 253-278.

MCLEOD, R., GABELL, A., GREEN, A. & GARDAVSKY, V. Chlorite infrared spectral data as proximity indicators of volcanogenic massive sulphide mineralization. *Pacific Rim Congress, 1987*. 26-29.

NÆS, T. & MARTENS, H. 1984. Multivariate calibration. II. Chemometric methods. *Trends in Analytical Chemistry*, 3, 266-271.

NIETO, F. & SÁNCHEZ-NAVAS, A. 1994. A comparative XRD and TEM study of the physical meaning of the white mica «crystallinity» index. *European Journal of Mineralogy*, 6, 611-621.

PIRAJNO, F. 1992. *Hydrothermal mineral deposits: principles and fundamental concepts for the exploration geologist*, Berlin Heidelberg, Springer-Verlag.

PONTUAL, S., MERRY, N. & GAMSON, P. 1997. *Spectral Interpretation Field Manual (GMEX)*, AusSpec International.

POST, J. L. & NOBLE, P. N. 1993. The near-infrared combination band frequencies of dioctahedral smectites, micas, and illites. *Clays and clay minerals*, 41, 639-639.

RALPH, J. & CHAU, I. 1993. *Mineralogical database* [Online]. United Kingdom: Mysterious Ways. Available: https://www.mindat.org/ [Accessed January 2012].

RIEDER, M., CAVAZZINI, G., D'YAKONOV, Y. S., FRANK-KAMENETSKII, V. A., GOTTARDI, G., GUGGENHEIM, S., KOVAL, P. V., MUELLER, G., NEIVA, A. M. & RADOSLOVICH, E. W. 1998. Nomenclature of the micas. *Clays and clay minerals*, 46, 586-595.

ROWAN, L. C., MARS, J. C. & SIMPSON, C. J. 2005. Lithologic mapping of the Mordor, NT, Australia ultramafic complex by using the Advanced Spaceborne Thermal Emission and Reflection Radiometer (ASTER). *Remote sensing of Environment*, 99, 105-126.

SALTER, J. & WYATT, N. 1991. Sorting in the minerals industry: past, present and future. *Minerals Engineering*, 4, 779-796.

SERRANO, L., VARGAS, R., STAMBUK, V., AGUILAR, C., GALEB, M., HOLMGREN, C., CONTRERAS, A., GODOY, S., VELA, I. & SKEWES, M. 1996. The late miocene to early pliocene Río Blanco-Los Bronces copper deposit, central Chilean Andes. Andean copper deposits: new discoveries, mineralization, styles and metallogeny. *Society of Economic Geologists Special Publication*, 5, 119-130.

SILLITOE, R. H. 2010. Porphyry copper systems. *Economic geology*, 105, 3-41.

SIVAMOHAN, R. & FORSSBERG, E. 1991. Electronic sorting and other preconcentration methods. *Minerals Engineering*, 4, 797-814.

SPECIM. 2015. *Hyperspectral imaging in geology* [Online]. Available: http://www.specim.fi/hyperspectral-imaging-in-geology [Accessed February 2015].

THOMPSON, A. J., HAUFF, P. L. & ROBITAILLE, A. J. 1999. Alteration mapping in exploration: application of short-wave infrared (SWIR) spectroscopy. *SEG newsletter*, 39, 16-27.

WARNAARS, F. W., HOLMGREN, C. & BARASSI, S. 1985. Porphyry copper and tourmaline breccias at Los Bronces-Rio Blanco, Chile. *Economic Geology*, 80, 1544-1565.

WILLS, B. A. & FINCH, J. A. 2016. Chapter 14 - Sensor-based Ore Sorting. *Wills' Mineral Processing Technology (Eighth Edition)*. Boston: Butterworth-Heinemann.

WOLD, S., SJÖSTRÖM, M. & ERIKSSON, L. 2001. PLS-regression: a basic tool of chemometrics. *Chemometrics and intelligent laboratory systems*, 58, 109-130.

WOTRUBA, H. & RIEDEL, F. 2005. Ore preconcentration with sensor based sorting. *Aufbereitungs technik*, 46, 4-13.

Chapter 7.

Lagunas Norte Epithermal gold–silver deposit

7.1. Introduction

The Lagunas Norte mine is an open pit gold and silver mine located about 140 kilometres east of the city of Trujillo in the Quiruvilca District, Santiago de Chuco Province, Peru. It is situated in the Peruvian Andes at 4200 meters above sea level. The Lagunas Norte mine is fully owned and operated by Barrick gold. During 2016, Lagunas Norte produced 435 thousand ounces of gold (Barrick, 2016a). Proven and probable reserves are currently 70.7 Mt of ore at an average grade of 1.86 g/t Au and 4.97 g/t Ag (Barrick, 2016c).

Operations at Lagunas Norte include traditional open pit truck and shovel mining. Ore treatment consists of primary and secondary crushing and heap leaching. On the heap leach the crushed ore is irrigated with a cyanide acid solution, which leaches out the gold by forming gold-cyanide complexes. The pregnant solution from the heap leach facility is temporarily stored in the pregnant leach solution pond and then pumped to a Merrill-Crowe plant. In this plant the suspended solids are first removed by a clarifier after which the solution passes through a cone where powdered zinc is added and the gold and silver precipitate out of the solution. The precipitate is recovered by filter presses and placed in mercury retorts. After retorting, the precipitate is mixed with flux and smelted in a furnace. Here the impurities are removed and a mixture of gold and silver is recovered as doré. The doré is transported to a refinery for further processing.

7.2. Study description

7.2.1. Geologic setting

This section provides a brief overview of the main characteristics of the Lagunas Norte deposit. A more extensive description of the geology of Lagunas Norte is presented by Cerpa et al. (2013) and Montgomery (2012).

The Lagunas Norte deposit is a high-sulphidation epithermal gold and silver deposit hosted in Miocene volcanic rocks and upper Jurassic to lower Cretaceous sedimentary rocks (Cerpa et al., 2013; Montgomery, 2012). The deposit lies within the Tertiary volcanic arc of Northern Peru. Lagunas Norte differs from most high-sulphidation epithermal deposits because approximately 85% of the gold mineralisation is hosted in unreactive quartzites (Cerpa et al., 2013; RPA, 2012).

The host rock at Lagunas Norte consists of thrusted and folded sedimentary rocks of the Chicama and Chimu formations that are unconformably overlain by the volcanic and volcano-clastic rocks of the Calipuy group (Cerpa et al., 2013). The Chicama formation is present below the mineralised zone and consists of a succession of dark carbonaceous shale and siltstone with occasional thin beds of sandstone. The Chimu formation consists of compositionally mature quartz sandstone with occasional coal beds, siltstone and shale intercalations. The sandstone of the Chimu formation is weakly metamorphosed to quartzite. The transition from Chicama to Chimu is gradual and characterised by an increasing abundance of quartzite inter-calations (Cerpa et al., 2013). Gold is hosted by the Chimu formation and the overlying volcanic strata.

Four different hydrothermal alteration stages and one supergene oxidation stage have been defined at Lagunas Norte (Cerpa et al., 2013). Figure 7.1 presents the paragenetic sequence associated with the hydrothermal alteration. The first alteration stage introduced minor gold and is characterised by fine-grained yellowish to tan-coloured aggregates of quartz, pyrite and minor rutile, which is also referred to as silice parda (Cerpa et al., 2013). Gold introduced during this stage is associated with pyrite and present as solid solution or as nanoparticles.

The second hydrothermal alteration stage is characterised by the emplacement of two diatremes, which are referred to as Dafne and Josefa. This stage did not deposited significant amounts of gold, but was important for subsequent gold mineralisation by fracturing the adja-cent rock (Cerpa et al., 2013).
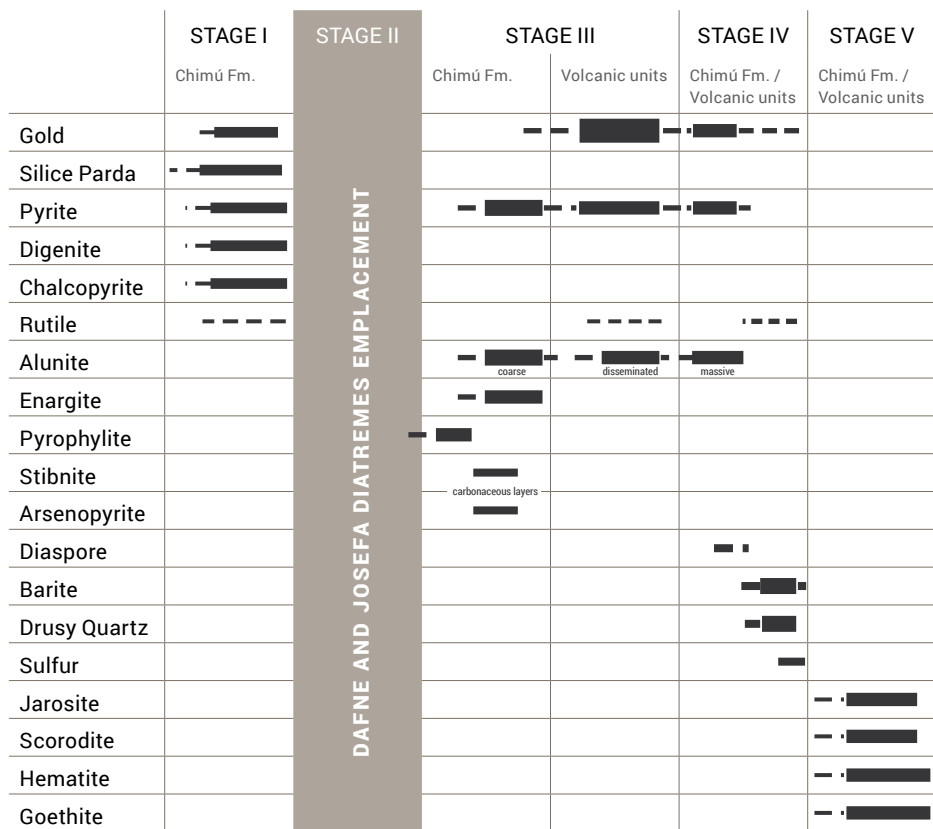
Figure 7.1: Paragenetic sequence at Lagunas Norte. Thickness of the lines represents the relative mineral abundance (based on Cerpa et al., 2013).

The third hydrothermal alteration stage introduced most of the gold, which is contained within pyrite. Within the Chimu formation this alteration stage is characterised by fracture infill of coarse alunite associated with pyrite and enargite. Furthermore, the hydrothermal alteration affected each of the lithologies of the Chimu formation in a different way (Cerpa et al., 2013). Disseminated kaolinite alteration occurs in the quartz sandstones. In the silty beds, pyrophyllite alteration affected the core of the deposit and kaolinite alteration the periphery parts. Within the coal beds the alteration is characterised by sulphide assemblages of pyrite, stibnite and arsenopyrite.

At the Dafne diatreme, the third hydrothermal alteration stage exhibits different characteristics in each of the lithofacies (Cerpa et al., 2013). The diatreme margin is intensively silicified with minor alunite. At the main body, dickite-kaolinite alteration affected juvenile fragments, and fracture controlled silification is locally present. The crater lithofacies contain weak dickite-kaolinite alteration. In the apron lithofacies, hydrothermal alteration depends on matrix composition. If the matrix is dominantly carbonaceous alunite-dickite-kaolinite alteration occurs, while

beds with a volcanic matrix are affected by quartz-alunite alteration. The Josefa diatreme has been pervasively altered to quartz-alunite and juvenile fragments have commonly been replaced by pyrite and alunite (Cerpa et al., 2013). In the volcanic sediments the third hydrothermal alteration stage created alteration zoning patterns that are typical for high-sulphidation epithermal deposits (Cerpa et al., 2013).

The fourth hydrothermal alteration stage introduced minor gold and is characterised by massive alunite that fills thin fractures in the Chimu formation and forms the cement of local fault controlled breccias (Cerpa et al., 2013). The alunite has cut pyrophyllite-altered siltstone beds and overgrown coarse-grained alunite. Also traces of pyrite, kaolinite and diaspore alteration occur. In open spaces of volcanic rocks barite, rutile, drusy quartz and native sulphur were deposited during this alteration stage (Cerpa et al., 2013).

The hydrothermal alteration was followed by extensive supergene oxidation. The extent of this oxidation ranges from a few meters up to 300 m below the surface (RPA, 2012). The supergene oxidation produced hematite, goethite and locally jarosite and scorodite (Cerpa et al., 2013). These occur as cement in tectonic and hydrothermal breccias and as fracture infill.

7.2.2. Samples

The research described in this chapter is based on two different sample sets. First of all, two buckets containing a random selection of samples were supplied by Lagunas Norte. One of the buckets was collected at one of the ore zones in the mine and the other bucket was collected at one of the waste zones. Figure 7.2 shows a map of the topography and final pit limit of the Lagunas Norte mine on which the sampling locations of these two buckets are indicated. 80 rock particles of about 5-15 cm large were selected from the bucket collected at the ore zone and 14 particles of about the same size were selected from the bucket collected at the waste zone. Each individual rock particle represents a sample and the total sample set therefore consists of 94 samples. This sample set will be referred to as the initial sample set. Figure 7.3 shows an example of four of the samples in the initial sample set.
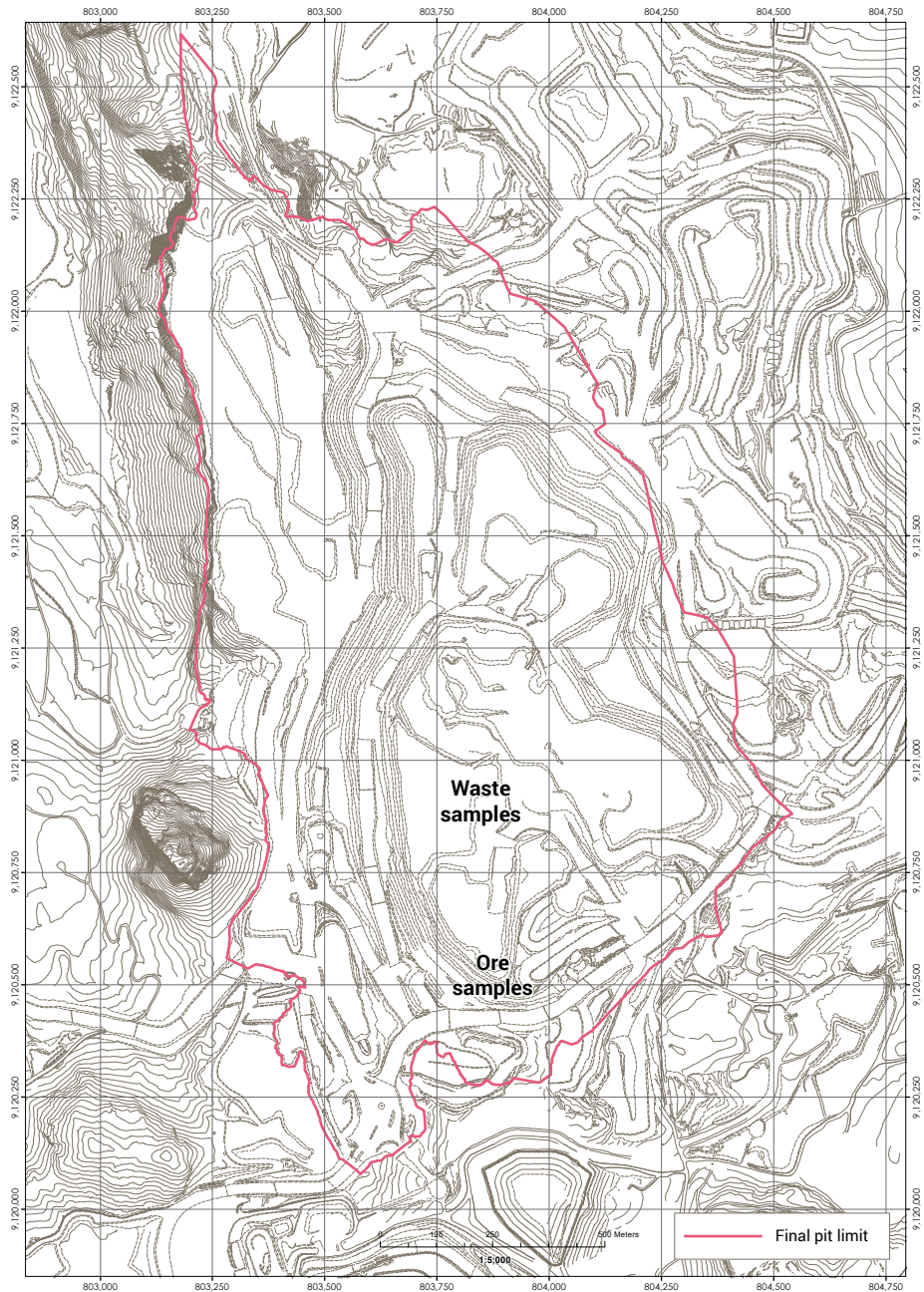
Figure 7.2: Sampling locations of the initial sample set.

Figure 7.3: Example of four samples of the initial sample set.

The second sample set consists of 952 drill core particles of about 5 – 20 cm long that were selected from half of the splitted drill core of 28 different drill holes. The other half of the drill core was used for geochemical analyses by the exploration department of the mine and no longer available. The diameter of the drill core is 6.5 cm. The drill core particles were taken at 0.5 – 2 m intervals and the selection was based on capturing the observed variability between lithologies as much as possible. Each individual drill core particle represents a sample.

Selection of the drill holes used for sampling was based on geological cross sections and geochemical data that was made available by the mine. The drill holes were selected in such a way that the sample set would represent the variability of the deposit as much as possible. Furthermore, most of the samples were selected from the drill hole interval that represented the part of the deposit that was not yet mined at the time of sampling. Figure 7.4 shows a map of the topography and final pit limit of the Lagunas Norte mine on which the drill holes from which samples were selected are indicated. The green line on this figure indicates the location of the cross section that is shown in Figure 7.5. This cross section shows that the selected drill holes intersect all the different lithologies that are within the final pit limit. Figure 7.6 presents an example of some of the samples in the drill core sample set.
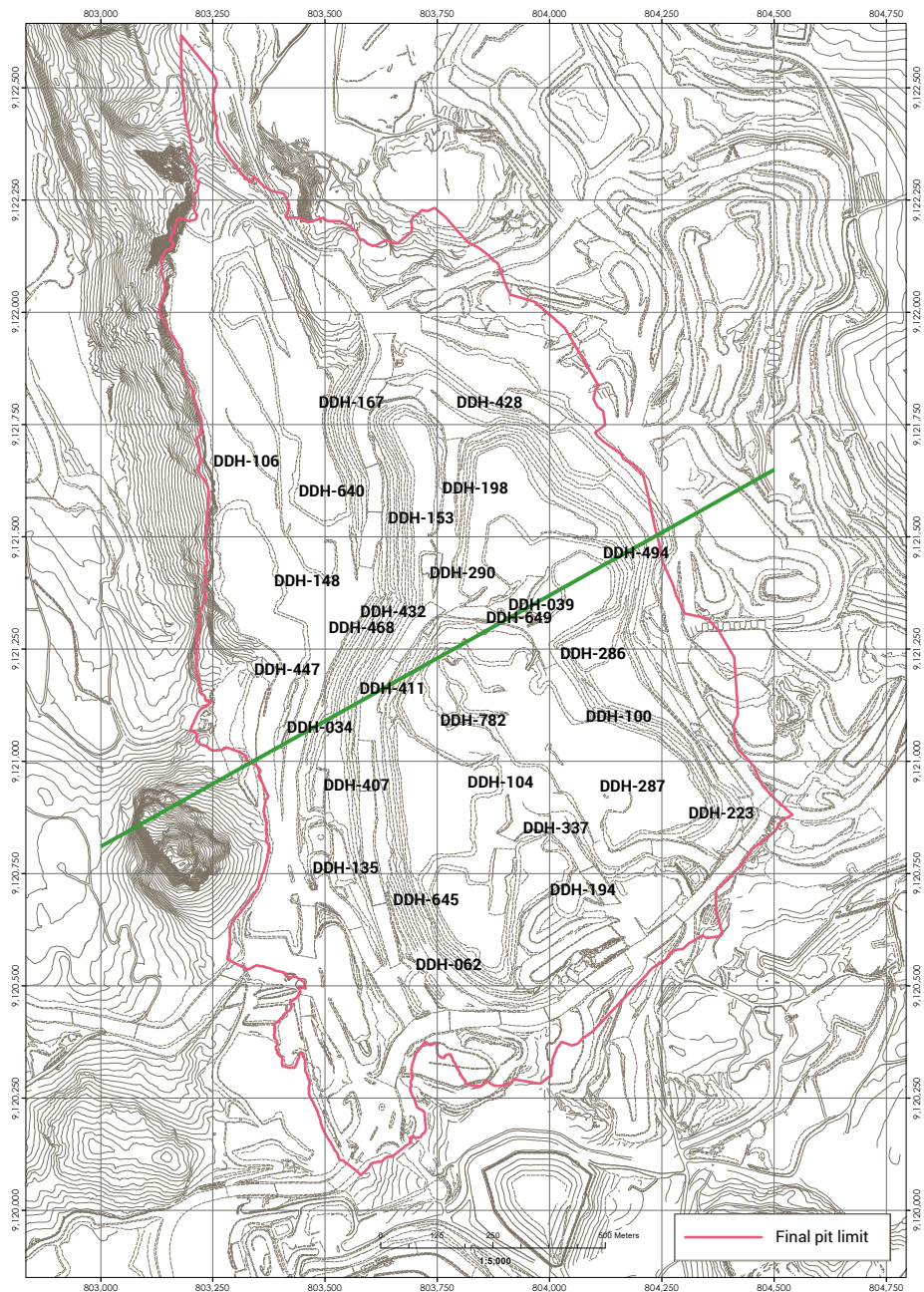
Figure 7.4: Locations of drill holes used for collecting the drill core sample set. The green line indicates the location of the cross section shown in Figure 7.5.
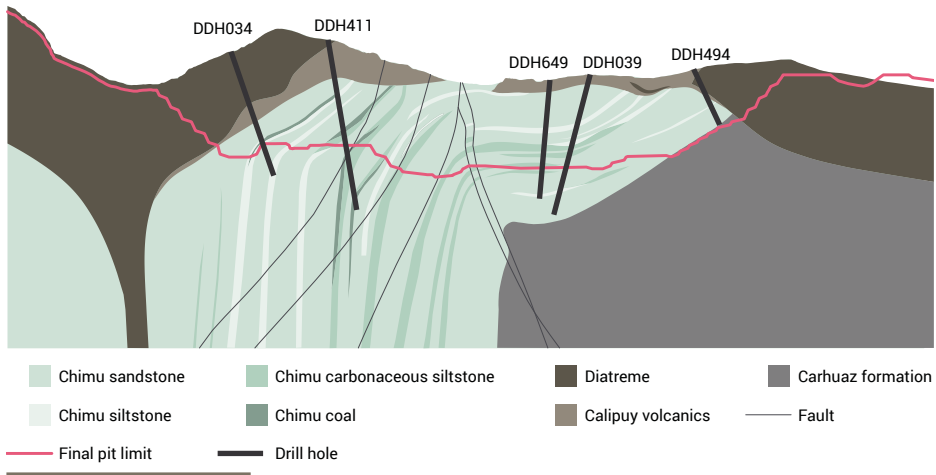
Figure 7.5: Cross section through the Lagunas Norte deposit showing the different lithologies, selected drill holes and final pit limit. The location of the cross section is indicated on Figure 7.4.

7.2.3. Objectives

The aim of the Lagunas Norte study was to investigate the opportunities for sensor-based particle-by-particle sorting at this mine. This was focussed at researching the applicability of real-time sensors to segment waste from ore and to distinguish between different ore types. Only the applicability of using real-time sensors to characterise ore particles was investigated. The feasibility of using sensor-based sorting machines to sort the ore is out of scope.

At Lagunas Norte, ore and waste are defined by a cut-off grade of 0.20 ppm Au. This cut-off grade is the minimum gold grade that is required for economic processing of the ore. Although some of the ore also contains silver, the silver grade is not considered for the definition of ore and waste. Most of the samples with low gold grades also have a relatively low silver grade.

Table 7.1 presents an overview of all the different ore types that are distinguished at Lagunas Norte. It can be observed from this table that the main distinction is between oxide ore and sulphide ore. The oxide ore is a product of the supergene oxidation stage that took place after the gold was deposited. The sulphide ore is the part of the deposit that is not affected by the supergene oxidation. It was discussed in section 7.2.1. that most of the gold was originally deposited within pyrite. Since the pyrite is impermeable it occludes the gold when the ore is processed by cyanide leaching methods. The result of the supergene oxidation is that the pyrite is oxidised, which liberated the gold and made it more amenable to cyanide leaching. The recovery of gold by heap leaching is therefore higher for the oxide ore than for the sulphide ore. Table 7.1 shows that oxide and sulphide ores are defined by the sulphur content.

Figure 7.6: Example of drill core samples.

Table 7.1: Ore types at Lagunas Norte (based on RPA, 2012). TCM stands for Total Carbonaceous Material content.

Material	Type	Description	Au (g/t)	TCM (%)	S (%)	Cu (ppm)
Waste	D1	Non acid-generating	< 0.2		< 0.10	-
	D2	Acid-generating	< 0.2		≥ 0.10	
	D3	Carbonaceous (visual interpretation)	< 0.2			
Oxide ore	M1	Clean oxide	> 0.2	< 0.1	< 0.25	-
	M1A	Clean with little sulphides	> 0.2	< 0.1	< 0.40	< 350
	M2AL	Slightly carbonaceous	> 0.2	< 0.2	< 0.25	-
	M2AH	Carbonaceous	> 0.2	< 0.5	< 0.25	-
	M2B	Highly carbonaceous	> 0.2	≥ 0.5	< 0.25	-
Sulphide ore	M3	High sulphide content	> 0.2	< 0.1	≥ 0.40	< 350
	M3A	With sulphides and copper	> 0.2	< 0.1	≥ 0.25	≥ 350
	M3B_Low	With sulphides and slightly carbonaceous	> 0.2	< 0.5	≥ 0.25	-
	M3B_Med	With sulphides and carbonaceous	> 0.2	< 1.5	≥ 0.25	-
	M3B_High	With sulphides and highly carbonaceous	> 0.2	≥ 1.5	≥ 0.25	-

It can be observed from Table 7.1 that also carbonaceous ore types are distinguished. Carbonaceous ores decrease the gold recovery of the heap leaching process because the carbon within the ore adsorbs the gold-cyanide complex from the pregnant cyanide solution. This phenomenon is also referred to as preg-robbing. Table 7.1 shows that carbonaceous ore types are defined by the content of Total Carbonaceous Material (TCM).

In 2020 Lagunas Norte will start the construction of a refractory ore processing facility (Barrick, 2016b). The term refractory refers in this case to the carbonaceous and sulphidic ore types. The facility for processing refractory ores will include an autoclave that can be used to oxidise the sulphide ore and burn carbonaceous materials prior to the cyanide leaching. This will increase the gold recovery of these ore types, but also increases the ore processing costs. Because of the higher processing costs, it was investigated if real-time sensors can be used to distinguish between oxide and sulphide ore and between carbonaceous and non-carbonaceous ore.

Based on the classification of ore types presented in Table 7.1, the objectives of the Lagunas Norte study are to use real-time sensor data to:

- Segment a population of samples that all have gold grades below 0.20 ppm.

- Distinguish samples with a sulphur content above or below 0.25%.

- Distinguish samples with a TCM content above or below 0.5%.

It is not necessarily needed to segment all samples that contain less than 0.20 ppm Au since sensor-based particle-by-particle sorting can already provide economic benefits if a significant fraction of the waste can be eliminated.

7.2.4. Geochemistry

On the initial sample set geochemical analyses were performed on 36 of the 94 samples. Selection of this subset was based on a classification of samples on the mineralogy that was determined by VNIR-SWIR spectrometry. Determination of the mineralogy with VNIR-SWIR spectrometry is further discussed in chapter 7.5.

The geochemical analyses that were performed on the initial samples included X-Ray Diffraction (XRD) for determination of mineralogy, fire assay followed by Atomic Absorption Spectroscopy (AAS) to determine gold and silver grades, and Inductive Coupled Plasma Atomic Emission Spectrometry (ICP-AES) with aqua regia digestion for determining whole rock composition. Furthermore, the total sulphur and Total Carbonaceous Material (TCM) contents were determined by using a LECO analyser (LECO, 2015). All the geochemical analyses were performed on pulverised samples after the data with real-time sensors was acquired. All the analyses were performed by the Barrick technology centre.

On the drill core sample set two types of geochemical datasets were available. First of all, geochemical analyses were performed on drill core sections of 1 – 2 m long by the exploration

department of the mine. These analyses included determination of gold grade by fire assay and determination of total sulphur and TCM content by using a LECO analyser (LECO, 2015). This data was linked to the samples based on the drill hole interval from which a sample was collected. This geochemical dataset will be referred to as the drill hole data. It should be noted that the drill hole data is not fully representative of the samples since the samples are much smaller than the interval on which the drill hole data was collected. Furthermore, assays for total sulphur and TCM contents were not performed on every drill core interval. Selection of the assayed intervals was based on the gold grade and the interpretation of the mine geologists. The drill hole data contained the total sulphur content of 286 samples and the TCM content of 274 samples.

Because the drill hole dataset was not fully representative of the samples, additional geochemical analyses were performed on 104 drill core samples after the real-time sensor data was collected. This was done in three batches with slightly different combinations of the types of analyses that were performed. On all 104 samples fire assay followed by AAS was performed to determine gold and silver grades and whole rock geochemistry was performed by aqua regia digestion followed by ICP-AES. On 94 of the 104 samples also the total sulphur content was determined by using a LECO analyser (LECO, 2015). Furthermore, the mineralogy of 19 samples was determined by XRD. All the analyses were performed by the Barrick technology centre. The drill hole data of the 104 samples on which the additional assays were performed was replaced by the results of these assays.

7.3. DE-XRT on the initial samples

7.3.1. Introduction

It was explained in chapter 3.4 that Dual-Energy X-Ray Transmission (DE-XRT) allows materials to be characterised on the density. It was explained in chapter 7.2.1. that gold mineralisation at Lagunas Norte is associated with the occurrence of pyrite and iron-oxides. These iron-bearing minerals have a higher density than quartzite and siltstone, which are the main host rocks at Lagunas Norte. It was therefore investigated if it is possible to use DE-XRT to map the occurrences of iron-bearing minerals in order to predict the gold content of the ore samples. This was performed on all samples of the initial sample set.

7.3.2. Methods

Each sample of the initial sample set was scanned with a Vivid APS airport luggage scanner (Vivid Technologies Inc., Woburn, Massachusetts, USA). This device captures the transmission of low and high energy X-rays through the samples on a 1 mm pixel size. The difference between the transmitted X-rays and the transmission curve of aluminium was calculated for each pixel to produce a density map. The density maps represent the relative difference in density to aluminium that is independent of sample thickness. The density differences are given in counts of X-ray intensity. For each sample also an average density difference as well as the pixel fractions above certain density thresholds were calculated from the density maps.

7.3.3. Results

Figure 7.7 presents the DE-XRT density maps of four sandstone samples. The pixels of the original images were averaged over a 3x3 pixel window to produce these images. This reduces the local variability in the images that is related to instrumental noise. Pixel size of the images in Figure 7.7 is 3x3 mm.

Most of the samples are fairly homogeneous with respect to their density. However, several samples can be clearly separated into a higher and lower density zone, as is the case for sample

3 and 4 in Figure 7.7. The relatively high density zones are produced by higher concentrations of iron-bearing minerals. For sample 3 in Figure 7.7 the photo shows that the higher density results from an iron-oxide vein at the surface of this sample. It can be observed that the high density zone in the DE-XRT map of sample 3 is somewhat thinner than the iron-oxide vein that can be observed from the photo. This is because the orientation of the sample in the photo is slightly different than in the DE-XRT density map. For sample 4 in Figure 7.7 visual inspection of the sample showed that the higher density zone is a result of relatively fine grained pyrite mineralisation. Unfortunately, this is not very well visible in the photo of this sample.
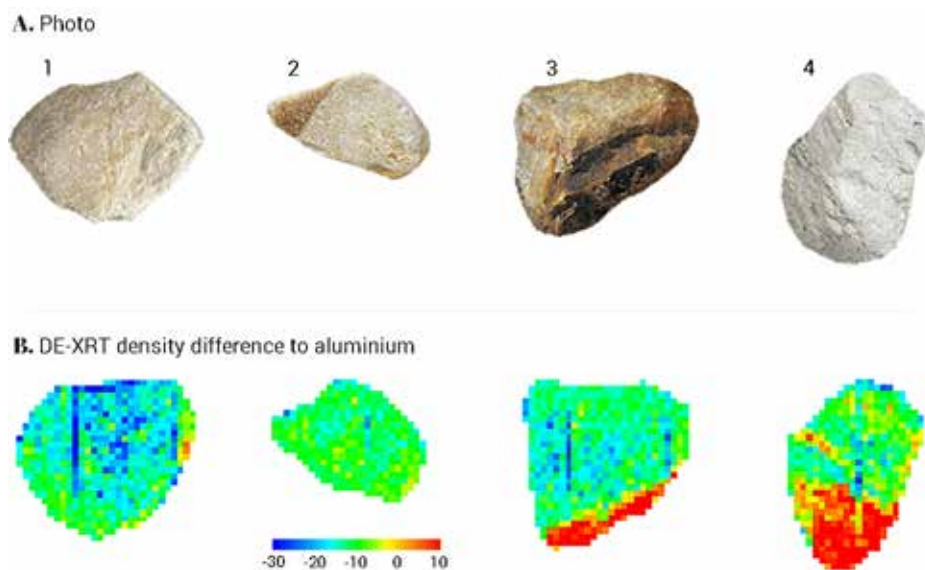
Figure 7.7: Maps of the DE-XRT density difference to aluminium of four sandstone samples.

Figure 7.8 and Figure 7.9 present the average density difference to the X-ray transmission curve of aluminium versus the iron content and the gold grade of each sample. These figures are based on all 36 samples from the initial sample set on which geochemical assays were performed. Figure 7.8 shows that for average DE-XRT density differences > 8 there is a correlation between the iron content of the samples and the DE-XRT density difference. However, Figure 7.9 shows that the average DE-XRT density difference of samples is not related to the gold grade. When the pixel fractions above certain DE-XRT density thresholds were compared to the gold grades also no relationships were observed. It results that even though mineralisation of gold was related to the formation of iron-bearing minerals such as pyrite and hematite-goethite, the occurrence of these iron-bearing minerals cannot be used as an indicator of higher gold grade.
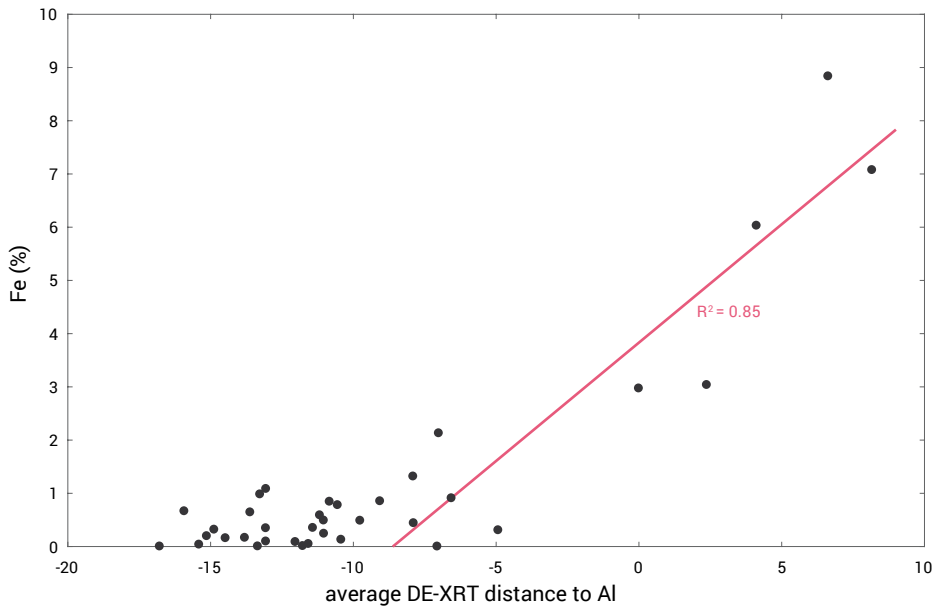
Figure 7.8: Average DE-XRT difference to aluminium versus the iron content of samples obtained with ICP-AES. The pink line represents the linear correlation for average DE-XRT differences > -8.
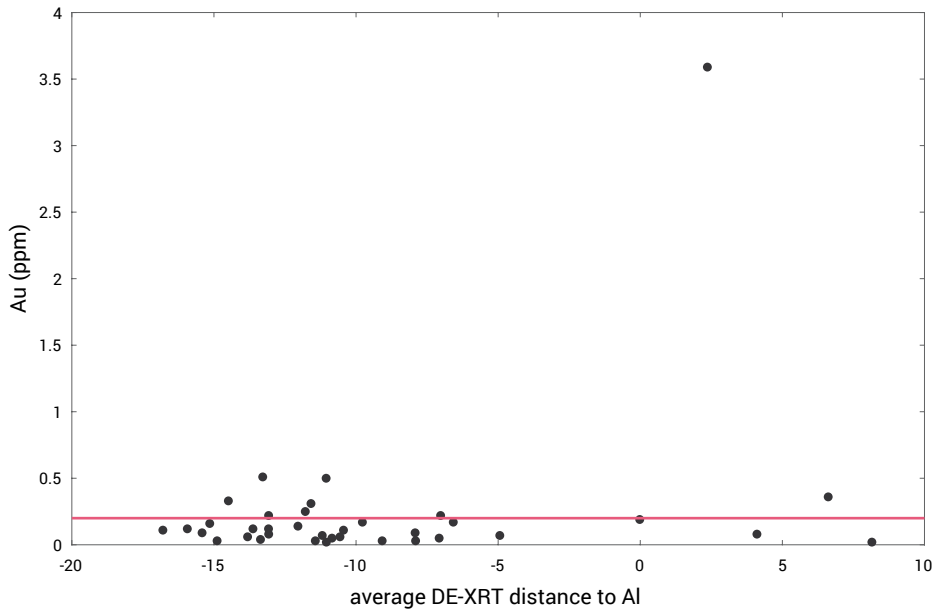

Figure 7.9: Average DE-XRT difference to aluminium versus the gold grade of samples obtained with fire assay. The pink line represents the economic cut-off grade of 0.20 ppm Au.

7.3.4. Conclusions

The following conclusions can be drawn from testing DE-XRT on the initial sample set:

- DE-XRT can be used to characterise the iron content of samples.

- DE-XRT can be used to identify veins of iron-bearing minerals.

- DE-XRT cannot be used to characterise the gold grade of samples.

- DE-XRT cannot be used to segment a significant population of waste samples.

7.4. LIBS on the drill core samples

This section is based on: Dalm, M., Buxton, M.W.N., 2015. Characterizing the economic value of an epithermal Au-Ag ore with laser induced breakdown spectroscopy (LIBS): possibilities and limitations. Sensor-Based Sorting and Control (SBSC) 2016 – conference proceedings. Aachen, Germany.

7.4.1. Introduction

It was explained in chapter 3.5 that Laser-Induced Breakdown Spectroscopy (LIBS) can be used to detect the chemical composition of materials. In the presented study, LIBS was applied to 19 samples from the drill core sample set. The samples were selected in order to cover the full range of gold grades of the entire sample set. This was based on the drill hole data. LIBS spectra were measured on the surface of each sample to investigate if these spectra can be used to segment waste samples by either detecting the gold grade directly or by using other elements as indirect indicators.

7.4.2. Methods

Data acquisition

The setup that was used for acquiring LIBS spectra consisted of a pulsed Nd:YAG laser (Litron Nano LG), operated at 1064 nm and at 2 mJ per pulse. 10 pulses were used in each LIBS measurement. The light emitted by the generated plasma was recorded with a CCD spectrometer of Spectral Industries using a 210 – 840 nm spectral range. The spectral resolution of the LIBS spectra varied from 0.04 nm (@ 210 nm) to 0.12 nm (@ 840 nm). The gate delay was set at 1.2 µs. 41 LIBS spectra were acquired along a 4 cm long line (1 mm spacing) on the surface of each sample. Subsequently, all the samples were pulverized and used for geochemical analyses.

Spectral pre-processing

The acquired LIBS spectra were corrected for instrumental noise by subtracting the dark current from the measured spectra. The dark current is a measurement of the spectrometer response when there is no radiation entering it. Subsequently, a continuum background correction was performed on the LIBS spectra. The continuum background is radiation that occurs due to bremsstrahlung and recombination radiation (Yaroshchyk & Eberhardt, 2014). Correcting the continuum background was required because significant differences in the baseline intensity of the LIBS spectra were observed. The correction was performed by following the approach presented by Yaroshchyk & Eberhardt (2014). This approach estimates the continuum by using a moving minimum together with a smoothing function. The correction is made by subtracting the estimated continuum background from the original spectrum.

Data analysis

The LIBS spectra were corrected for signal intensity fluctuations by cantering and scaling the spectra (setting the mean and standard deviation to 0 and 1 respectively). The result is that the total signal intensity of all spectra becomes equal. The 10 purest LIBS spectra were calculated from the corrected dataset by using the SIMPLISMA method of Windig & Guilment (1991). The elements responsible for the 30 most intense peaks in each of the purest spectra were identified by comparing the wavelength position of these peaks with the NIST atomic spectra database (NIST, 2015). This analysis was aided by calculating correlation coefficients from the LIBS data to find peaks that strongly correlate to each other. This was used to identify peaks that are produced by the same element.

Thirteen different elements were found from the purest LIBS spectra. Unfortunately, these did not include gold. It was therefore investigated if any of the measured LIBS spectra contained a peak at the wavelength position at which the NIST database reports the most intense gold peaks.

Two peaks were identified that could represent gold. However, the maximum intensity that was observed for these peaks is only just above the noise level. Because of this, it is unsure if the peaks are really produced by gold, or that they are noise peaks. Correlation coefficients between the two gold peaks showed no correlation. This indicates that at least one of the two peaks that were identified for gold is not representative.

The intensities of all the gold peaks were calculated from every corrected LIBS spectrum. Furthermore, the intensity of the most diagnostic peak of each of the other thirteen elements was calculated. In these calculations peaks had to follow the condition of being a local maximum that matches the wavelength position of the element peak within a 0.3 nm range. Using a wavelength range for matching peaks was required because small shifts in the element peak locations were sometimes observed. These shifts can be attributed to differences in the stark effect that are caused by variable electron densities resulting from the chemical matrix effect (Martin & Wiese, 2006). In case an element peak was not found for a certain LIBS spectrum a peak intensity of 0 was assigned. An average peak intensity was calculated for each

sample from all the LIBS spectra that were measured on it. These average peak intensities were compared with the results of the geochemical analyses.

Apart from centering and scaling, also an internal standard was used to correct the LIBS spectra for signal intensity fluctuations. This involved calculating peak intensity ratios between the peak of an element of interest and the peak of a common matrix element. The disadvantage of using peak intensity ratios, however, is that these only provide information on the relative abundance between elements. This therefore requires a relationship between the occurrence of an element of interest and the relative abundance between this element and some other element. The peak intensities for calculating peak ratios were extracted by using the same approach as with the centred and scaled data.

The final step in the LIBS data analysis was to apply a Principle Component Analysis (PCA) to the centred and scaled LIBS spectra. Prior to the PCA, each variable (wavelength channel) was also centred.

7.4.3. Data analysis results

None of the calculated LIBS element peak intensities correlated with the element concentrations determined by geochemistry. Most of the peak intensity ratios also did not correlate with the geochemical data. It resulted that it was not possible to characterize the gold grade of the samples by detecting gold with a LIBS sensor. Although peaks were found in the LIBS spectra that could possibly represent gold, no difference in peak intensity was observed between samples with low and high gold grades. This concerns the individual LIBS spectra as well as the sample averages.

The only correlation that was found is between the Fe / Si peak intensity ratio from LIBS and the iron content determined by ICP-AES. This linear correlation has an R^2 value of 0.81 and is presented in Figure 7.10. It can be observed from this figure that based on the available data this correlation is not very strong since no samples with iron contents in between 5% and 20% were available.

The reason that the Fe / Si peak ratio from LIBS was compared with the iron concentration and not the Fe / Si concentration ratio was because the ICP-AES results for silicium were not accurate due to the aqua regia digestion. However, XRD showed that the iron in the samples does not occur as iron-bearing silicates, but only as iron-oxides or iron-sulphides. This implies that an inverse relationship exists between the iron and silicium content of the samples. For this reason it was assumed that the Fe / Si peak ratio from LIBS represents the absolute iron concentration determined by geochemistry.

There are several possible causes for the fact that no correlation resulted between LIBS and geochemistry for almost all elements. Most of these are related to the heterogeneous composition of the samples. Almost all samples are quartzites or mudstones containing variable

amounts of veins and fractures that are infilled with mainly iron-bearing minerals. Furthermore, the samples originated from different locations within the deposit and were therefore subjected to different intensities of hydrothermal alteration during deposit formation. This produced different assemblages of alteration minerals in the samples.
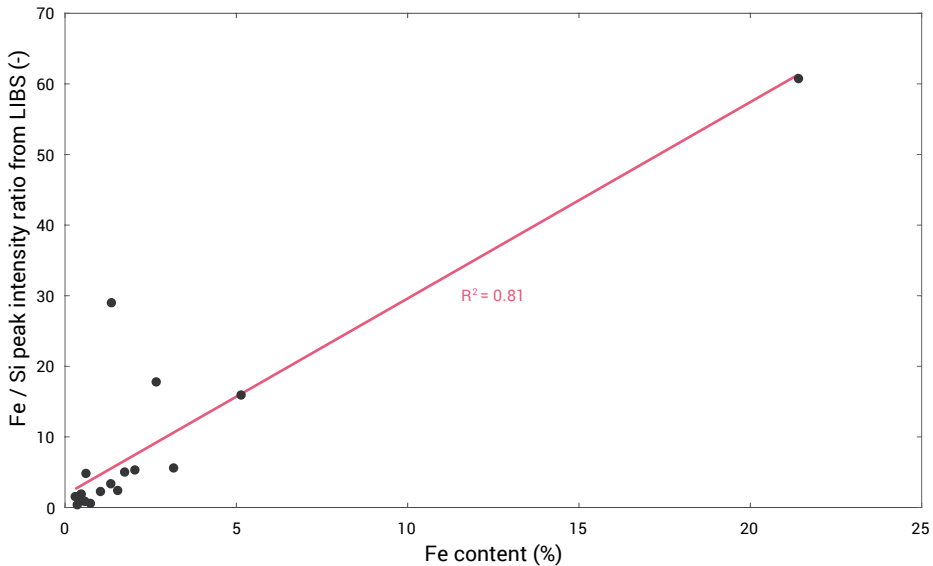

Figure 7.10: Fe / Si peak intensity ratio from LIBS vs. Fe content of samples obtained with ICP-AES.

The spot size of a single LIBS measurement was around 100 μm in diameter. This means that the total surface area that was measured by the 41 LIBS spectra on each sample is only about 0.32 mm2. Given the heterogeneous nature of the samples, the chemical information on such a small surface area does not necessarily correspond to the geochemistry of a sample volume that is in the order of tens of cm3. Even if the entire sample surface would have been measured with LIBS, it would still be unsure if the surface information represents the volumetric composition of the sample.

Because of the relatively small spot size of the LIBS measurements and the heterogeneity of the samples, completely different mineral assemblages were measured. Due to the matrix effect, the relationships between LIBS peak intensities and element concentrations will be different for each of these mineral assemblages. The standard approach to deal with matrix effects is to construct calibration curves (Harmon et al., 2013; Radziemski & Cremers, 2006). However, since the differences between sample matrices are relatively large, different calibration curves are likely required for each type of mineral assemblage (e.g. Pořízka et al., 2014). This could be an explanation for the fact that no correlation was observed between the LIBS spectra and the geochemical data. A way to deal with this is to investigate the relationships between LIBS and geochemistry for each mineral assemblage separately. However, this requires separate

geochemical analyses of all the veins, infilled fractures and host rock minerals. Since some of these veins and fractures are very small (< 1 mm) this may become very challenging to achieve.

The most dominant matrix minerals in the samples are either silicates or iron-oxides. The matrix effects are therefore largely related to the occurrence of iron and silicium. Rationing the peak intensities of these two elements corrects for the matrix effect that is produced by them. This could be the reason that some correlation resulted between the Fe / Si peak intensity ratio from LIBS and the iron content from geochemistry, while no correlation resulted for any of the other elements. Furthermore, since iron- and silicium-bearing minerals are fairly abundant in the samples it is also possible that the representation of these elements on a small surface reflects the volumetric composition of the sample much better than that of elements that are less abundant.

Finally, it should be noted that the aqua regia digestion that was performed in the geochemical analysis is a fairly weak digestion method that is not very well suited for dissolving silicates. It is therefore possible that the geochemical results of some of the elements that occur in silicates (e.g. Al, K, Na, etc.) are not accurate. The aqua regia digestion was selected however to get more accurate results on the arsenic concentration. Characterizing arsenic contents with LIBS was initially also of interest, but was left out of scope because of problems with detecting arsenic with LIBS.

7.4.4. PCA results

Figure 7.11 presents the scores of the LIBS spectra on the 1st and 2nd Principle Component (PC) of the PCA model. The black and pink dots in this figure refer to LIBS spectra that were measured on ore and waste samples respectively. Ore and waste samples were defined on the basis of an economic cut-off grade of 0.20 ppm Au.

The green rectangle in Figure 7.11 indicates a region on the score plot where predominantly LIBS spectra of waste samples occur. It can be observed that by using only the 1st PC waste samples can already be distinguished. The loadings of the 1st PC are presented in Figure 7.12. It should be noted that the peaks of H, O and N in this figure are partly produced by the air that surrounds the sample during the LIBS measurements. These elements are therefore not fully representative of the composition of the samples.

Since waste samples have relatively high score values on the 1st PC, it can be inferred from the loadings in Figure 7.12 that the LIBS spectra of waste samples are associated with relatively intense Al and Ti peaks compared to the intensity of the Na, Ca, Si and Fe peaks. According to the XRD results, elevated Al and Ti concentrations are produced by a higher abundance of clay minerals and rutile in the samples. These minerals are products of hydrothermal alteration. It therefore results that waste samples can be indirectly identified by using LIBS to determine the content of Al- and Ti-bearing alteration minerals.
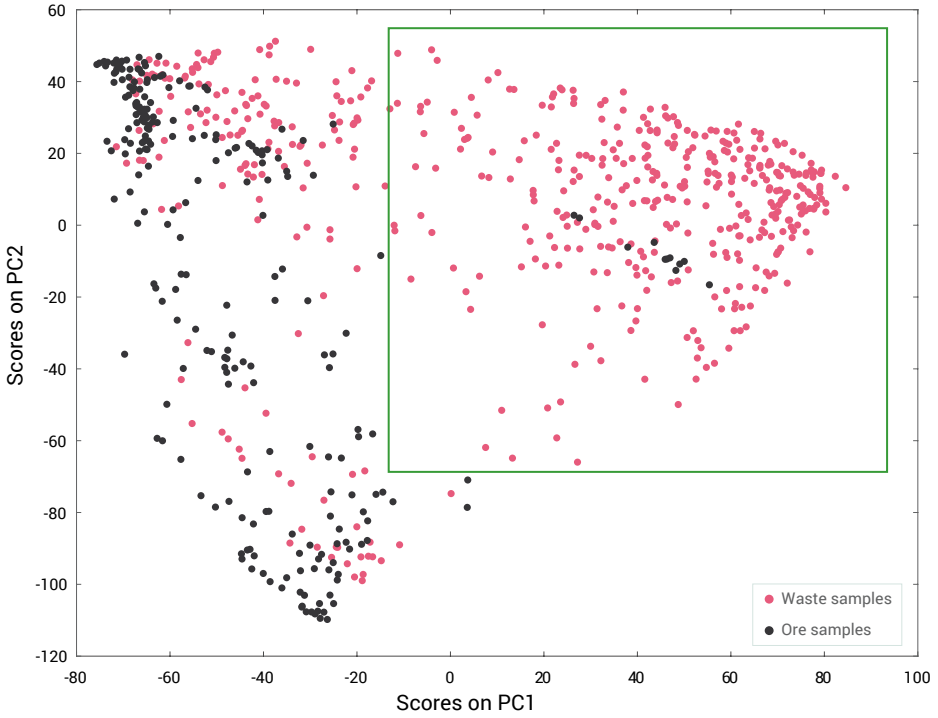
Figure 7.11: PCA scores on PC1 vs. PC2. The green rectangle indicates a region where predominantly LIBS spectra of waste samples result.
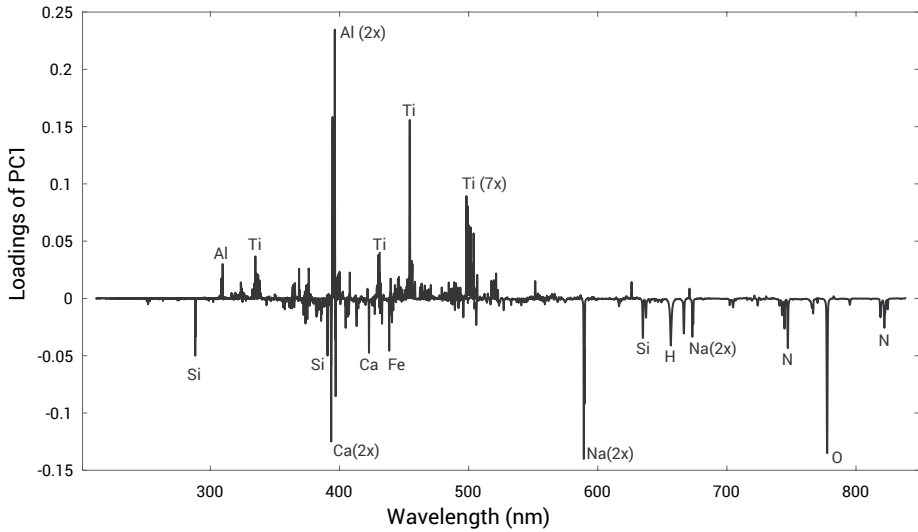

Figure 7.12: PCA loadings of PC1.

7.4.5. Discussion

The results showed that the LIBS technique is not able to directly detect the gold grade of the ore samples used in this study. It was also uncertain if the peaks that were identified for gold were correct since these peaks were only observed with a peak intensity that is just above the noise level. However, even if distinct peaks were found it would still be unsure if the detection of these elements can be used to characterize the economic value of the ore. This is because the LIBS peak intensities of many other elements also did not correlate with the geochemical data. This lack of correlation is likely produced by the heterogeneity of the ore material.

By applying a PCA to the LIBS dataset it was discovered that LIBS can be used to distinguish waste samples by using the spectra as chemical fingerprints of alteration mineralogy. This means that the occurrence of certain LIBS spectra can be used to predict whether a sample is more likely to be ore or waste. Classification techniques such as Partial Least Squares Discriminant Analysis (PLS-DA) for example are available to achieve this (Sjöström et al., 1986). Considering sample heterogeneity, an approach that utilizes classification models would be more robust than one based on extracted compositional information. This is because a classification model will be less sensitive to the chemical matrix effects resulting from sample heterogeneity.

The results presented in this section are based on a sample set of only 19 samples that were selected to cover the full range of gold grades of the entire drill core sample set. Additional research will therefore be required on a sample set that covers the mineralogical variability of the ore deposit to validate the relationships between the detected alteration mineralogy and gold grade.

7.4.6. Conclusions

The following conclusions were drawn from testing LIBS on 19 drill core samples:

- Sample heterogeneity imposes difficulties for extracting quantitative compositional information from LIBS spectra. This is because the heterogeneity produces significant signal intensity variations and chemical matrix effects.

- Peaks for gold were identified from the measured LIBS spectra, but these could not be used to characterise the gold grade of the samples.

- A relationship is present between the content of Al- and Ti-bearing alteration minerals and the gold grade of the samples.

- LIBS could be used to segment a population of waste samples by using the LIBS spectra as chemical fingerprints of the alteration mineralogy.

- Classification models that use the LIBS spectra as chemical fingerprints of alteration mineralogy are considered to be the best approach for identifying waste material. This is because these models will be less sensitive to the chemical matrix effects resulting from sample heterogeneity.

7.5. VNIR–SWIR point spectrometry on the initial samples

This section is based on: Dalm, M., Buxton, M.W.N., van Ruitenbeek, F.J.A., 2015. Application of near-infrared (NIR) spectroscopy to sensor based sorting of an epithermal Au-Ag ore. OCM 2015 – conference proceedings. Karlsruhe, Germany.

7.5.1. Introduction

As described in chapter 3.3, spectral reflectance measurements on the SWIR spectral range can be used to detect minerals produced by hydrothermal alteration. Furthermore, it was explained in chapter 4.3. that the deposition of gold and silver at epithermal deposits is related to the formation of specific alteration minerals. Chapter 6 showed that the detection of alteration mineralogy from VNIR-SWIR spectral reflectance data can be used to segment waste samples from a porphyry copper deposit. Because of this, VNIR-SWIR point spectra were measured on all samples in the initial sample set in order to investigate if this type of data also allows ore and waste samples from an epithermal gold-silver deposit to be segmented. Furthermore, it was investigated if the VNIR-SWIR spectral reflectance data can be used to distinguish between oxide and sulphide ore samples and carbonaceous and non-carbonaceous samples. The cut-off grades that define ore and waste, oxide and sulphide ore and carbonaceous ore were presented in chapter 7.2.3.

7.5.2. Methods

General approach

Seven VNIR-SWIR reflectance spectra were collected on each sample with an ASD Fieldspec3 point spectrometer (ASD Inc., Longmont, Colorado, USA). This device records reflected radiation on a 350-2500 nm range using three detectors. The spectral resolution is around 3 nm on

the 350-1000 nm range and around 10 nm on the 1000-2500 nm range. The spot size that is measured by the spectrometer is a circular area with a radius of 1 cm.

The acquired VNIR-SWIR spectra needed pre-processing to convert the recorded data to relative reflections. This was performed by using a white reference and a dark current calibration. Spectra of relative reflectance were calculated by dividing the measured spectrum by the white reference after subtracting the dark current from both these measurements. Furthermore, a splice correction was performed by shifting the reflectance values on the 1000-2500 nm range to match those on the 350-1000 nm range.

The spectral range of the measured VNIR-SWIR spectra was subdivided into a VNIR region (350 to 1300 nm) and a SWIR region (1300 to 2500 nm). As explained in chapter 3.3, two different types of mineral absorptions take place on these spectral ranges. In the VNIR spectral region the pixel spectra are dominated by absorptions of the Fe-ion (Fe^{2+} and Fe^{3+}) that can be used to determine iron-bearing mineralogy. In the SWIR spectral region the pixel spectra are dominated by absorptions that are produced by molecule bond vibrations. These absorptions can be used to determine hydrothermal alteration mineralogy.
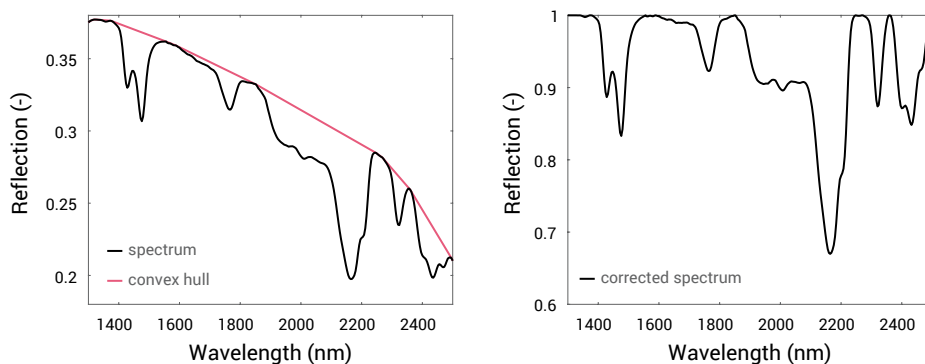

Figure 7.13: Example of the hull quotient correction.

Finally, the SWIR spectra were corrected for variations in the overall reflection of samples by using a hull quotient correction. This was performed to reduce the influence of absorption effects that are not related to the mineralogy such as light scattering, particle-size effects, surface roughness and detector artefacts. A hull quotient correction is performed by first calculating the convex hull of the spectrum, which represents the shape of the spectrum without the absorption features. Each wavelength band of the spectrum is then divided by the convex hull to produce the corrected spectrum. The hull quotient correction is illustrated in Figure 7.13. The spectra on the VNIR region were not corrected. This was not needed because the overall reflection of the spectrum is dominated by the mineral absorptions.

The VNIR-SWIR active mineralogy was determined from the measured VNIR and SWIR spectra by comparing the spectra with reference spectra from the G-MEX spectral interpretation field

manual (AusSpec, 2008) and the USGS spectral library (Clark et al., 2007). Based on the determined mineralogy, a subset of samples was selected for geochemical analysis. Selecting the subset was performed in such a way that the subset covered the variability of the VNIR-SWIR active mineralogy of the initial sample set.

Classification with PLS-DA

Partial Least Squares Discriminant Analysis (PLS-DA) was applied to investigate the potential of using the VNIR-SWIR spectral data to distinguish between pre-defined groups of samples. PLS-DA was performed on the VNIR and SWIR spectra separately. 7 measured spectra on each sample were used in the PLS-DA. To calibrate the PLS-DA models, the spectra were assigned to the class that the sample belongs to. Only two different classes were used in each PLS-DA model. Definition of the classes was based on the sorting objectives stated in chapter 7.2.3. The PLS-DA model predicts a response for each measured spectrum. Responses for samples were calculated by averaging the responses that resulted for the individual measurements. Classification of samples was performed by applying a threshold to these averaged responses.

To select the optimal number of LVs, only 75% of the samples were used for model calibration. The remaining samples were used to validate the resulting classifications. The error rate of classification versus the number of LVs was calculated for 100 randomly chosen calibration and validation subsets. The number of LVs at which the lowest average error rate resulted for the validation subset was selected for creating the PLS-DA classification model. The response threshold used to perform the classification during cross-validation was based on Bayes theorem. The PLS-DA was performed with algorithms from the classification toolbox for Matlab from the Milano Chemometrics and QSAR Research Group (Ballabio, 2013). Before applying the PLS-DA, the data was mean-centred.

7.5.3. Results

Minerals identified from VNIR–SWIR spectra

Figure 7.14 presents an overview of measured VNIR and SWIR spectra of all the different minerals that were determined on the samples with VNIR-SWIR spectrometry. Almost all spectra in Figure 7.14 match those of single minerals (e.g. AusSpec, 2008; Clark et al., 2007). Only the SWIR spectra of diaspore and dickite are mixed with other minerals. The spectrum of diaspore in Figure 7.14 shows additional features by pyrophyllite around 1400 and 2170 nm. The presented spectrum of dickite is actually dominated by broad water absorptions that occur around 1400 and 1940 nm. Dickite was determined from the small absorption features that occur at 1380, 1415, 2175 and 2205 nm. The spectrum of water that is presented in Figure 7.14 is likely produced by fluid inclusions in quartz. The occurrence of quartz with fluid inclusions is common at epithermal deposits (Simmons et al., 2005). For samples on which all measured spectra represented that of water, also quartz contents > 90% were determined by XRD. It was made sure that all samples were dry while taking the measurements.

The SWIR spectra often contain absorptions by 2 or 3 different minerals. The VNIR spectra on the other hand only show a dominant mineralogy because all the characteristic mineral absorptions overlap. A fraction of the measured VNIR spectra also had no characteristic shape at all, indicating an absence of significant amounts of iron-bearing minerals. In total, 22 different combinations of VNIR-SWIR active mineral assemblages were determined from the samples. Minerals that were most often identified include pyrophyllite, quartz (water spectrum), hematite and goethite. Diaspore and zunyite were often determined from mixed spectra with pyrophyllite. Dickite always occurred together with quartz.

Apart from the spectra presented in Figure 7.14, also spectra with an average reflection < 10% over the entire VNIR-SWIR spectral range and no diagnostic mineral absorptions were measured. It resulted that these spectra represent the carbonaceous ore materials. The low reflection of carbonaceous samples is also visible from their dark black colour.
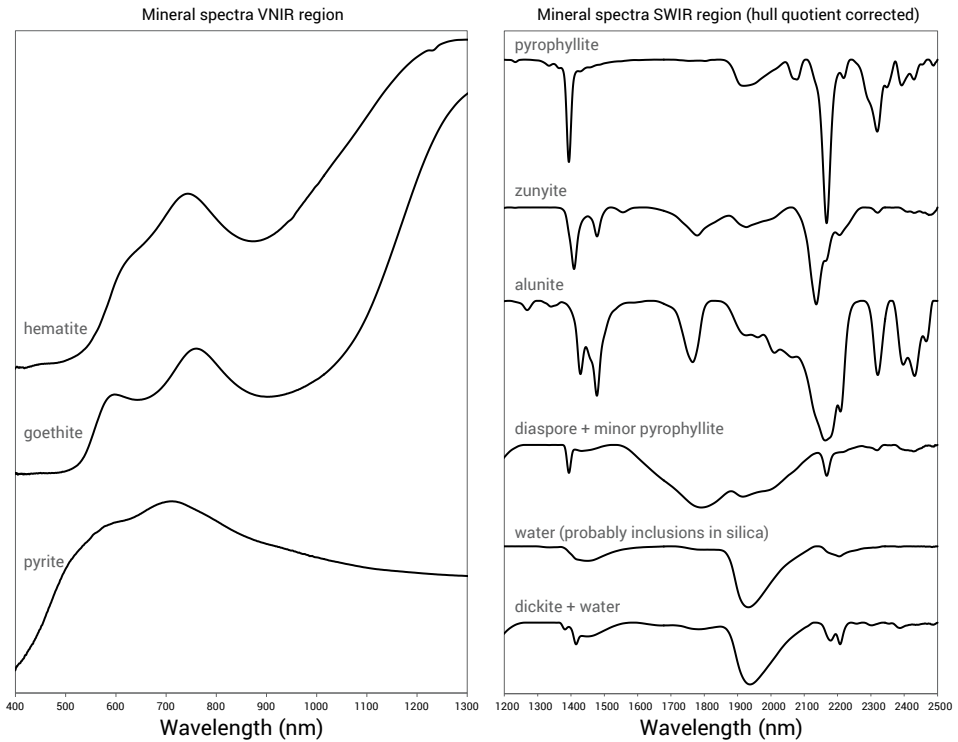

Figure 7.14: Examples of measured VNIR and SWIR mineral spectra.

XRD validated the occurrence of almost all minerals that were identified with VNIR-SWIR spectrometry. The only mineral that was not validated by XRD is dickite. However, it is possible that the weight fraction of dickite in the samples is below the limit of detection of XRD. The SWIR spectra from which dickite was identified also showed only weak absorption features of this

mineral, which indicates relatively low concentrations. The occurrence of dickite at Lagunas Norte was observed by Cerpa et al. (2013) and Montgomery (2012). These authors also validate the occurrence of all other minerals identified with VNIR-SWIR spectrometry.

Classification model for segmenting ore and waste

Different PLS-DA classification models have been produced to classify the samples on the sorting objectives stated in chapter 7.2.3. This section presents an overview of the results from a PLS-DA model that was aimed at distinguishing samples with gold grades < 0.20 ppm. Processing of ore samples below this grade is not profitable. The classification was performed on the SWIR spectra.

Carbonaceous samples were excluded from the classification on gold grade. This was done because the SWIR spectra of these samples are very different from those of rest of the sample set (i.e. low reflection and lacking mineral absorption features). Including the spectra of carbonaceous samples in the PLS-DA will therefore produce more complex models which will make the interpretation of scores and loadings more difficult. Carbonaceous samples can be distinguished from the rest of the sample set by using the average reflection of the VNIR-SWIR spectra. Because 5 carbonaceous samples ocurred in the subset of samples on which geochemical assays were performed, the presented PLS-DA results are based on 31 samples.

The first step in the PLS-DA classification was to select the optimal number of LVs that are used by the model. This was performed by calculating the error rate of classification versus the number of LVs for 100 randomly chosen calibration and validation subsets. Figure 7.15 presents the average of these classifications. This figure shows that there is no significant decrease in the error rate of the validation subset when more than 7 LVs are used. 7 LVs were therefore selected for performing the PLS-DA classification.
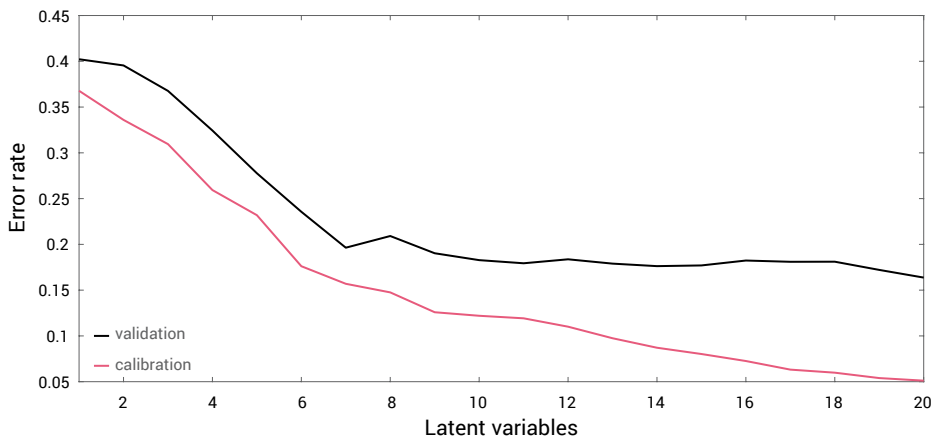

Figure 7.15: Average error rate versus the number of LVs of 100 PLS-DA classifications on ore and waste samples with random calibration and validation subsets. 75% of the samples were used for calibration.
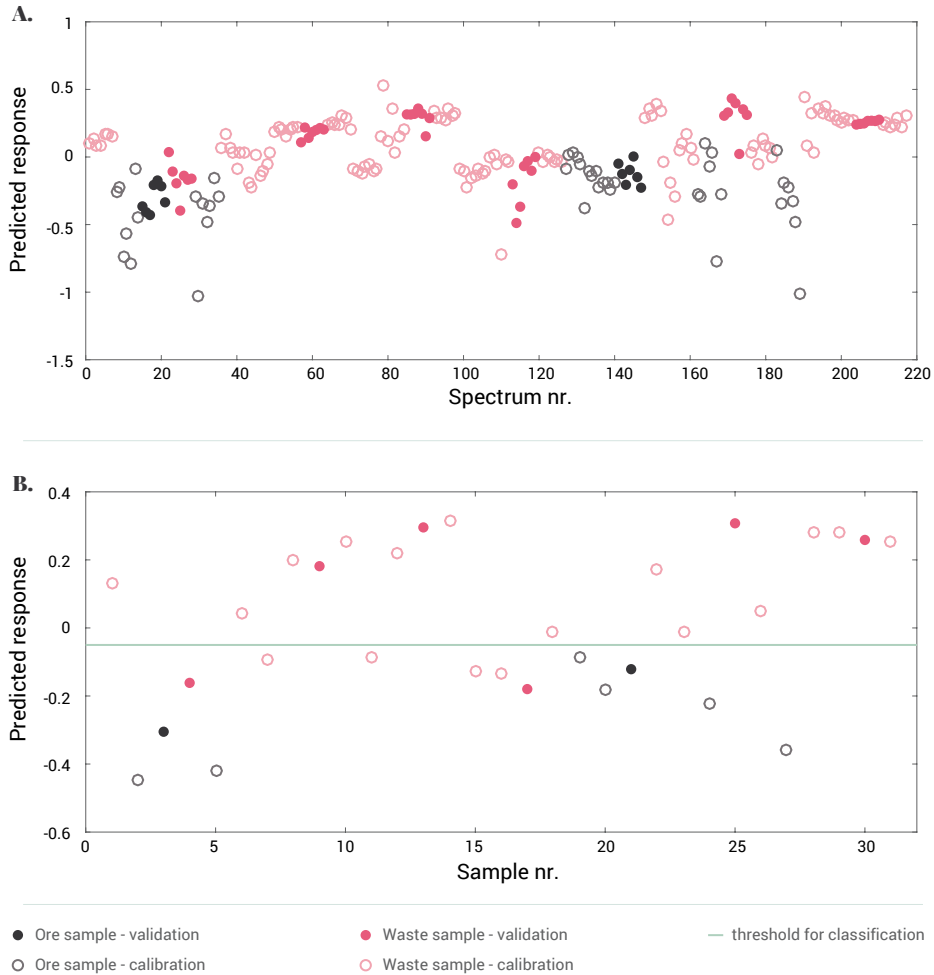
Figure 7.16: Responses of the PLS-DA classification on ore and waste using 7 LVs. a: Responses on SWIR spectra. b: Averaged responses on samples.

Figure 7.16a presents the responses that the PLS-DA model calculated for each measured SWIR spectrum. The different colours in this figure refer to the different classes on which the model was calibrated. Model calibration with PLS-DA is performed in such a way that the difference between the predicted responses of the two classes is maximised. Figure 7.16b shows the sample responses, which were calculated by averaging the responses of the SWIR spectra that were measured on each sample. The circles and dots in Figure 7.16 refer to samples that were used for calibration and validation of the model. It can be observed that for each class the responses of the validation subset fall within the range of responses of the calibration subset. The classification results are therefore consistent for samples that were not included during model calibration. Using different calibration and validation subsets produced similar results.

Figure 7.16b shows that there is overlap between the predicted responses of the two classes. However, it also shows that calculated responses > -0.05 only result on samples with low gold grades. By applying a threshold to the responses it is therefore possible to segment a population of samples that all have gold grades < 0.20 ppm. To investigate which SWIR spectral features allow identification of these samples, the scores and loadings of the model were analysed.

Figure 7.17 and Figure 7.18 present the scores and loadings for the first two LVs that are used by the PLS-DA model. The green rectangle indicates a region on the score plot where only measurements on waste samples result. The first loadings plot shows that these measurements can be distinguished on the basis of absorption features relating either to water (pink circles) or pyrophyllite (brown circles). The second loadings plot shows that the distinction between spectra is also based on the occurrence of either pyrophyllite (brown circles) or zunyite (green circles). The scores of the low grade samples in the green rectangle are positive on both the 1st and 2nd Latent Variable (LV). This relates to SWIR spectra that are represented by absorption features in the negative direction of the loadings of both LVs. It results that low grade samples can be identified from the occurrence of spectral features relating to pyrophyllite and absence of features relating to water (quartz) and zunyite. Analysis of the scores and loadings of other LVs of the model also showed that features relating to diaspore are characteristic for waste grade samples. These results were confirmed with XRD and visual inspection of the spectra.
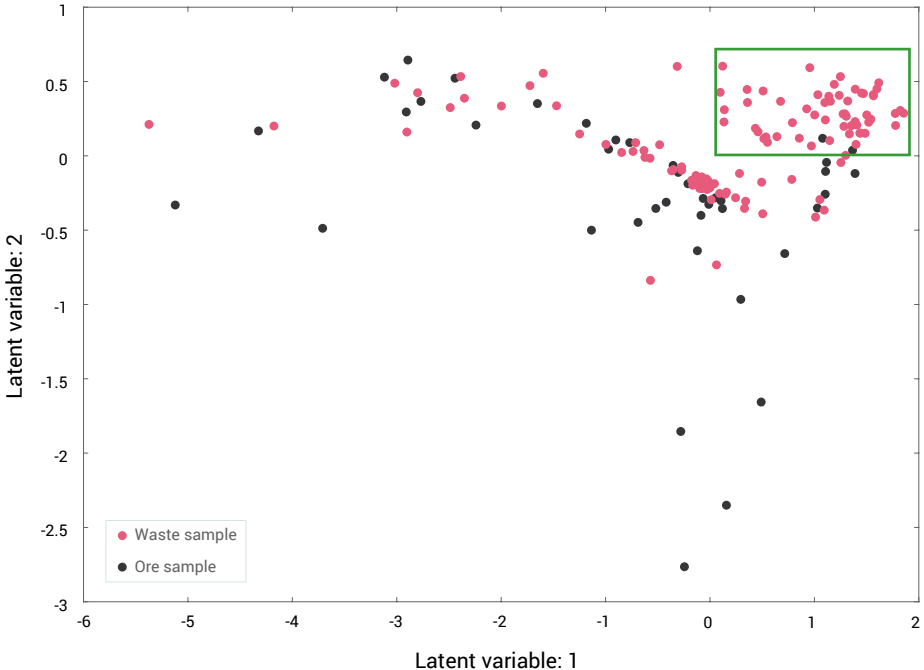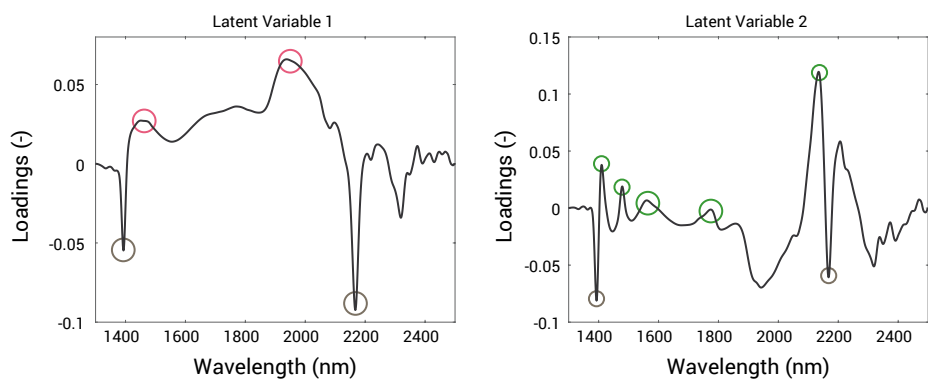

Figure 7.17: Scores of the PLS-DA classification on ore and waste using 7 LVs. The green rectangle indicates an area where predominantly measurements on waste samples result.

Figure 7.18: Loadings of the first and second LV of the PLS-DA classification on ore and waste.

Table 7.2: PLS-DA classification results based on VNIR-SWIR spectral data.

a. PLS-DA classification on C (cut-off grade: 0.50 %)

	All samples	Class 1 (14 %)	Class 2 (86 %)
C (%)	0.72	5.19	0.00

b. PLS-DA classification on Au (cut-off grade: 0.20 ppm)

	All samples	Class 1 (55 %)	Class 2 (45 %)
Au (ppm)	0.26	0.08	0.48
Ag (ppm	1.59	0.48	2.94

c. PLS-DA classification on S (cut-off grade: 0.25 %)

	All samples	Class 1 (29 %)	Class 2 (71 %)
S (%)	0.76	2.15	0.19

Classification results

The previous section presented an example of how PLS-DA was used to identify minerals from the SWIR spectra that are characteristic for samples with gold grades < 0.20 ppm. The same method was applied to the carbon and sulphur content of samples. Furthermore, the VNIR spectra were investigated by using the same approach. Based on the information that this provided, certain assemblages of VNIR-SWIR active minerals could be defined that only occur on samples with gold, carbon or sulphur contents within a certain range. Table 7.2 presents the results of three classifications that were based on distinguishing samples that contain these mineral assemblages. PLS-DA modelling showed that it was possible to make this distinction from the VNIR-SWIR spectral data.

The classification result shown in Table 7.2a is based on distinguishing samples with a low overall reflection. The samples that contain carbon generally absorb most of the VNIR-SWIR radiation which is also visible from their dark black colour. Classifying the VNIR or SWIR spectra on the average reflection therefore allows carbonaceous ore samples to be distinguished. It should be noted that in this case no hull quotient correction was applied to the SWIR spectra because this corrects for differences between the overall reflection of samples.

The classification result in Table 7.2b is based on distinguishing samples that contain pyrophyllite and diaspore while zunyite is absent. This classification was based on the responses shown in Figure 7.16b by using a response threshold of -0.05. Carbonaceous samples were excluded from this classification because their spectra do not contain mineral absorption features. The result presented in Table 7.2b is therefore based on 31 of the 36 samples on which geochemical assays were performed. Table 7.2a already showed that carbonaceous samples can be distinguished from the rest of the sample set. Table 7.2b shows significant differences between the average gold and silver grades of both sample groups. The maximum gold grade of group 1 is furthermore 0.19 ppm. It therefore results that the SWIR spectrometry can be used to segment a population of waste samples.

The classification result presented in Table 7.2c is based on distinguishing samples of which the VNIR spectra are characteristic for pyrite. The VNIR spectra of other samples either showed iron-oxide minerals or no diagnostic mineral absorptions. By distinguishing samples containing pyrite, significant differences between the average sulphur content of both sample groups result. Carbonaceous samples were excluded from this classification.

7.5.4. Discussion

PLS-DA proved to be an effective method to investigate the possibilities of using the VNIR-SWIR spectral data to classify the samples on gold grade, carbon content and sulphur content. The main advantage of this method is that by inspecting the scores and loadings of the PLS-DA model it is relatively easy to identify the spectral differences on which the classifications are based. It is important though that cross-validation is carried out properly to ensure that the model is not overfitting.

The different minerals that were identified from the SWIR spectra are characteristic for different zones of hydrothermal alteration within epithermal deposits (Sillitoe, 1993; Simmons et al., 2005; White & Hedenquist, 1995). The ability to segment a population of waste samples is therefore based on a relationship between gold mineralization and the formation of alteration minerals. This means that the detection of alteration minerals with SWIR spectral sensors can be used as indirect indicators for sensor-based sorting if the relationship between alteration mineralogy and gold grade persists throughout the entire ore deposit. Since the results are based on only 36 samples that were collected from two locations within the mine, it can be expected that the results are not fully representative. This is also indicated by the fact that the average gold grade of the samples used in this study is 0.26 ppm, while the average gold grade of the open pit proven and probable reserves at the time of sampling was around 1 ppm (RPA, 2012). Validation of the results on a sample set that is representative of the full mineralogical variability of the deposit is therefore required to be able to conclude on the applicability of sensor-based particle-by-particle sorting. The results presented in this chapter do show potential for using SWIR spectral sensors for sensor-based particle-by-particle sorting of epithermal gold ores.

7.5.5. Conclusions

The following conclusions were drawn from testing VNIR-SWIR point spectrometry on the initial sample set:

- VNIR-SWIR spectrometry could be used to distinguish between different assemblages of hydrothermal alteration minerals of the ore samples collected from the Lagunas Norte epithermal gold-silver deposit.

- An indirect relationship is present between the gold grade of samples and the mineralogy that can be determined from VNIR-SWIR spectrometry. This indirect relationship is based on sample groups with different VNIR-SWIR active mineral assemblages that represent different zones of hydrothermal alteration and constitute different ranges of gold grades.

- VNIR-SWIR spectrometry could be used to segment a population of waste samples. This is based on detecting specific alteration mineral assemblages.

- The average VNIR-SWIR reflection of samples could be used to identify carbonaceous ore samples. This distinction can also be made visually because the low reflection of carbonaceous samples is related to their dark black colour.

- VNIR-SWIR spectrometry could be used to distinguish between samples with high and low sulphur contents. This is based on detecting pyrite from the VNIR region of the spectra (350 – 1300 nm).

- PLS-DA is an effective technique for investigating classification possibilities based on VNIR-SWIR point spectra.

- The results are likely not fully representative of the entire ore deposit due to the relatively small size of the sample set and the fact that samples were selected from only two locations within the mine.

7.6. VNIR–SWIR hyper-spectral imagery on the initial samples

7.6.1. Introduction

This chapter investigates the applicability of VNIR-SWIR hyperspectral imagery to distinguish between ore and waste, oxide and sulphide ore and carbonaceous and non-carbonaceous ore. This was based on the 36 samples from the initial sample set on which geochemical analyses were performed. Chapter 7.5. already showed that an indirect relationship exists between the gold grade of the samples and the alteration mineralogy that can be determined with VNIR-SWIR point spectrometry. Furthermore, it was discussed that carbonaceous samples can be distinguished by using the overall reflection of the samples. Chapter 7.5. also showed that sulphide ore samples can be identified from the detection of pyrite. Since it was shown in Chapter 6.4. that SWIR hyperspectral imagery has several advantages over SWIR point spectrometry, it was investigated whether these advantages can be used to improve upon the indirect characterisation of gold grade, sulphur content and TCM content of the samples.

7.6.2. Methods

Data acquisition

VNIR-SWIR hyperspectral images of the samples were acquired with a HCI-3 (Corescan, Perth, Australia). This instrument records hyperspectral images on wavelengths ranging from 450 to 2500 nm by using three hyperspectral cameras. The spectral resolution of the images is around 4 nm over the entire spectral range. The pixel size of the images is around 0.5 mm.

Image pre-processing

A series of pre-processing steps were required in order to prepare the recorded VNIR-SWIR hyperspectral data for analysis. The first pre-processing step that was applied was to convert the data to relative reflections. This was performed with Corescan's in-house software by using a calibration of a white reference and a dark current. The Corescan software also performed a splice correction.

The second pre-processing step that was applied was to mask the image by removing the data of pixels that do not represent a sample. This was performed by manually selecting regions of interest on the image. Some of the pixel spectra are defect since they have reflections above 100% or below 0% on multiple wavelength bands. The reflections above 100% are mainly caused by specular reflection on the glossy surfaces of some of the samples. The reflections below 0% are likely caused by errors in the detection mechanism of the hyperspectral camera or problems during the acquisition of the dark current and white reference calibrations. The data of the defect pixels was also removed. Figure 7.20 presents the 1400 nm wavelength band of the hyperspectral image after masking and removal of defect pixels. The order in which samples are presented in this figure is equal to that of Figure 7.19. It can be observed from both figures that it are mainly de black carbonaceous samples that have defect pixels.

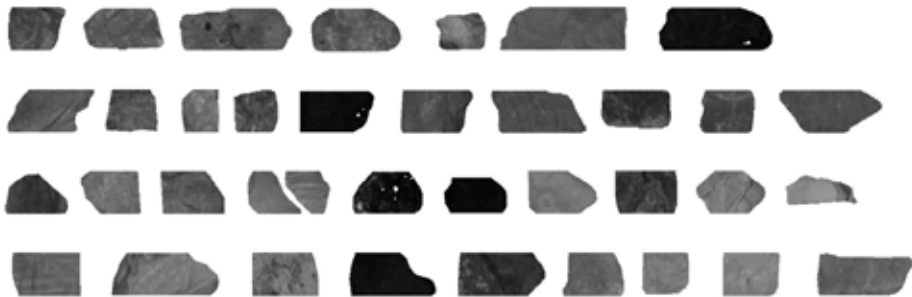Figure 7.19: Photograph of the sample set.

Figure 7.20: Masked 1400 nm wavelength band of the measured VNIR-SWIR hyperspectral image.

The third pre-processing step was to subdivide the spectral range of the VNIR-SWIR hyperspectral images into a VNIR region (450 to 1330 nm) and a SWIR region (1330 to 2500 nm). As with the spectral data processing described in chapter 7.5, the VNIR spectral region was used to determine iron-bearing mineralogy and the SWIR region to determine alteration mineralogy.

The final pre-processing step that was applied was a noise reduction by smoothing the spectral data and a correction for the variation in the overall reflection of samples. This was performed to improve the mineral mapping with correlation coefficients that will be discussed in the next section. On the VNIR hyperspectral images smoothing was performed on a window of 15 wavelength bands using a Savitzky-Golay filter with a second order polynomial. Variations in the overall reflection were not corrected since the reflection of the spectrum is dominated by the absorptions that occur in this spectral range. On the SWIR hyperspectral images smoothing was also performed by using a Savitzky-Golay filter with a second order polynomial, but here a window of only 5 wavelength bands was used. The reason for this is that the absorption features on the SWIR spectral range are narrower and therefore smoothed out if a larger window is selected. Correcting the variation in the overall reflection of samples was performed with a hull quotient correction. The hull quotient correction was illustrated in Figure 7.13.

Image processing

By using the SIMPLISMA method (Windig & Guilment, 1991), the purest pixel spectra were extracted from the VNIR and SWIR hyperspectral images. The VNIR-SWIR active mineralogy was determined from these pure spectra by comparing the spectra with those from the G-MEX spectral interpretation field manual (AusSpec, 2008) and the USGS spectral library (Clark et al., 2007). Subsequently, a list of mineral reference spectra was selected from the pure spectra. The pixels of the VNIR and SWIR hyperspectral images were classified on mineralogy by using correlation coefficients between the pixel spectra and the list of reference spectra. This classification was used to create mineral distribution maps. The mineral distribution maps were checked manually and the spectra of misclassified pixels were added to the list of reference spectra. The classification of pixel spectra was then performed again to produce new mineral distribution maps. This was carried out in an iterative manner until no more misclassified pixels were observed.

7.6.3. Results

Minerals identified from VNIR–SWIR hyperspectral images

Figure 7.21 presents an overview of measured VNIR and SWIR spectra of all the different minerals that were determined on the samples with VNIR-SWIR hyperspectral imagery. Almost all spectra in this figure match those of single minerals (AusSpec, 2008; Clark et al., 2007). Only the SWIR spectrum of dickite is mixed with other minerals. The absorption features that led to identification of dickite from this spectrum are those that occur at 1380, 1415, 2175 and 2205 nm. The broad feature that occurs at 1920 nm is produced by water and the small feature at 1476 nm by alunite.

The spectrum of hematite / goethite that is presented in Figure 7.21 is actually more representative of goethite than hematite. However, it was not always possible to distinguish between hematite and goethite from the VNIR pixel spectra. This is because these minerals often occur together and their absorption features overlap. For this reason, hematite and goethite were classified as one group to produce mineral distribution maps from the VNIR hyperspectral images.

As explained in chapter 7.5.3, the spectrum of water that is shown in Figure 7.21 is likely produced by fluid inclusions in quartz. The occurrence of quartz with fluid inclusions is common at epithermal deposits (Simmons et al., 2005). Furthermore, pixel spectra with a relatively low reflection over the entire VNIR-SWIR spectral range were again measured on the carbonaceous ore samples.

The SWIR pixel spectra often contain absorption features of 2 or 3 different minerals. In total, 13 different combinations of SWIR active mineral assemblages were classified to produce mineral distribution maps from the SWIR region of the hyperspectral images. From the VNIR region of the pixel spectra only a dominant mineralogy was classified. A fraction of the pixel spectra also contained no characteristic absorptions on the VNIR region at all, indicating an absence of iron-bearing minerals.
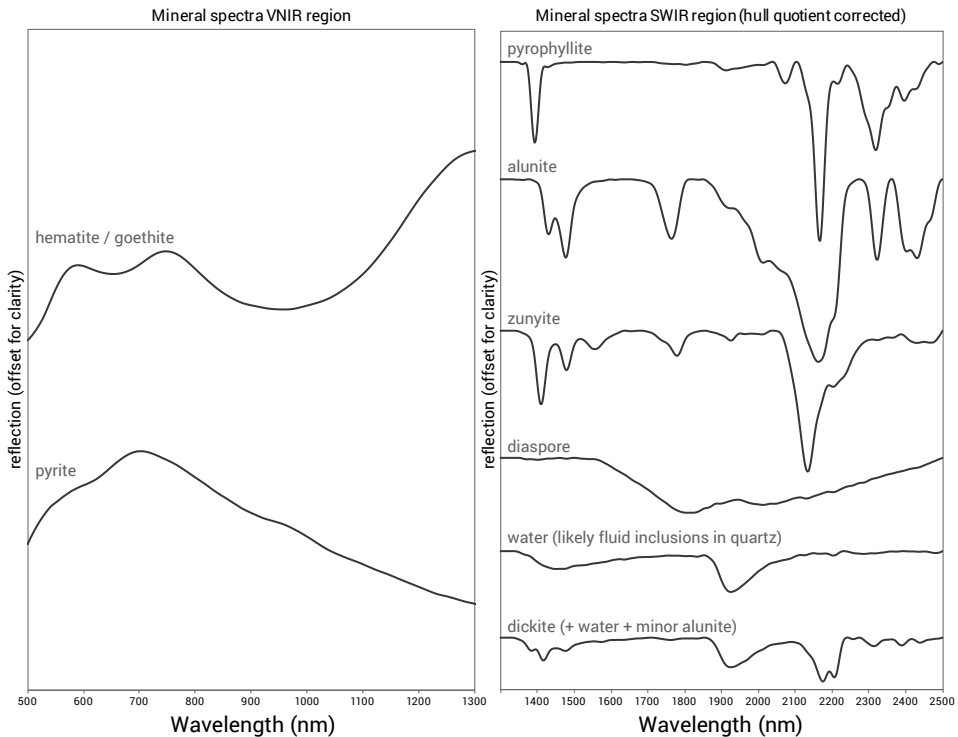

Figure 7.21: Examples of measured VNIR and SWIR mineral spectra.

The same minerals that were identified with VNIR-SWIR hyperspectral imagery were also identified with point spectrometry (see Chapter 7.5.3). The occurrence of all minerals except dickite was therefore validated by XRD. However, diaspore, alunite and hematite / goethite were not validated on each individual sample on which these minerals were identified with VNIR-SWIR hyperspectral imagery. Diaspore was validated on 7 out of 12 samples, hematite / goethite was validated on only 1 out of 18 samples, and alunite was not validated on any of the 4 samples on which it was determined with hyperspectral imagery, but was determined by XRD on one other sample. On this sample no SWIR spectra representing alunite were found among the pixels of the hyperspectral image.

The fact that XRD did not always validate the mineralogy identified with VNIR-SWIR hyperspectral imagery is likely caused by the way in which the samples are used in both techniques. XRD was performed on pulverized samples and the mineralogy determined by this technique therefore represents the whole volume of the sample. With hyperspectral imagery, however, only the mineralogy on the outer surface of the sample was determined. The samples are not homogeneous and formed by breakage of rock formations that consist of many small veins and fractures. When the rocks break along these veins and fractures, the outer surfaces of the samples may have a different mineral composition than the entire sample volume. When small veins and fractures cross-cut the sample on the other hand, the sample volume may contain minerals that are not visible from the surface. Furthermore, both XRD and VNIR-SWIR hyperspectral imagery have a certain detection limit. It is therefore possible that minerals occurring in low concentrations were not detected. Since the same minerals were determined from the sample set using both techniques, the identification of mineralogy from the VNIR-SWIR hyperspectral images was considered to be correct. Furthermore, all minerals that were identified with VNIR-SWIR hyperspectral imagery were also observed by Cerpa et al. (2013) and Montgomery (2012).

Image classification

Classification of carbonaceous ore
The first step in the hyperspectral image classification was to classify spectra that represent carbonaceous ore material. The pixel spectra of carbonaceous materials have a relatively low reflection over the entire VNIR-SWIR spectral range, resulting in a low signal to noise ratio. Furthermore, these pixel spectra usually do not contain mineral absorption features. This has detrimental effects on the techniques applied for extracting the pure pixel spectra and the classification with correlation coefficients. It was therefore necessary to remove the pixels of carbonaceous ore material from the dataset. Figure 7.22 presents the 1400 nm wavelength band of the hyperspectral image on which pixels with an average reflection < 10 % over the entire 450 to 2500 nm spectral range are assigned a red colour. The black rectangles in this figure indicate samples that have carbon contents > 0.50 %. All other samples have carbon contents < 0.50 %. It is clear from Figure 7.22 that samples with relatively high carbon contents can be distinguished with VNIR-SWIR hyperspectral imagery. These samples were removed from the dataset for producing mineral distribution maps.
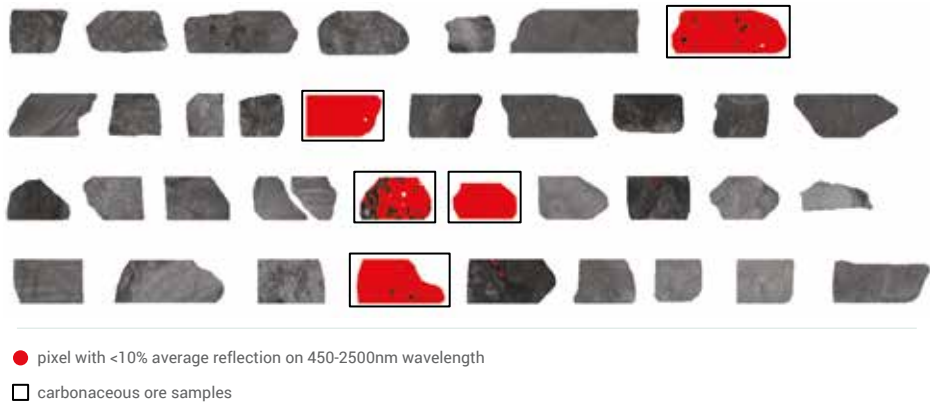
● pixel with <10% average reflection on 450-2500nm wavelength

☐ carbonaceous ore samples

Figure 7.22: Map of pixels with a low reflection in the VNIR-SWIR hyperspectral image.

● none   ● hematite / goethite   ● pyrite
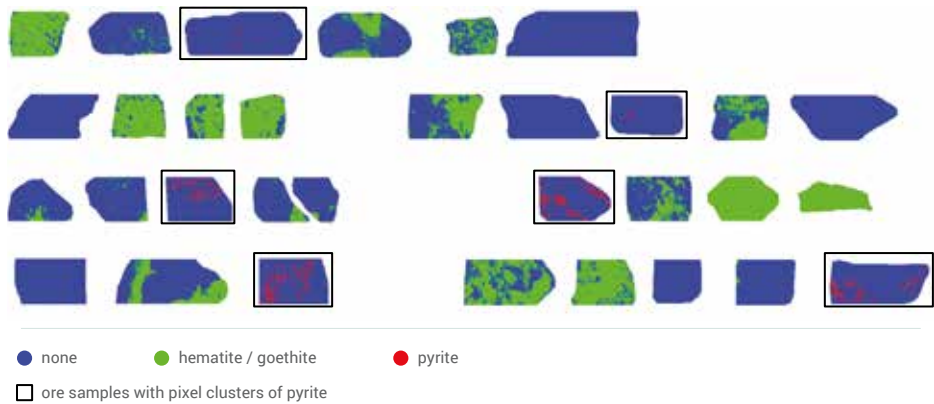
☐ ore samples with pixel clusters of pyrite

Figure 7.23: Mineral map produced from the VNIR hyperspectral image.

Classification of oxide and sulphide ore

Figure 7.23 presents the mineral distribution map that was produced from VNIR hyperspectral images. The black rectangles in this figure indicate samples on which clusters of pixels occur that are classified as pyrite. According to the XRD results, pyrite (FeS_2) is the only sulphide mineral that occurs in the samples. Table 7.3 presents the differences in sulphur content if the samples with clusters of pyrite pixels in the mineral distribution map of Figure 7.23 are distinguished from all other samples. This table shows that significant differences result between the average sulphur content of both groups. Furthermore, the table shows that samples containing cluster of pyrite pixels have a minimum sulphur content of 0.57 %. It therefore results that VNIR-SWIR hyperspectral imagery can be used to distinguish ore particles with relatively high sulphur contents. However, samples could not be distinguished on a certain sulphur content cut-off.

Table 7.3 shows that there is still overlap between the distributions of the sulphur content of both groups.

Table 7.3: Classification results based on pyrite pixel clusters in the VNIR mineral map.

	Total	Samples with pyrite clusters in Figure 7.22	Other samples
Fraction of samples (%)	100	19.4	80.6
S (%) minimum	0.00	0.57	0.00
S (%) maximum	9.48	9.48	2.22
S (%) average	0.76	2.80	0.27

Classification of ore and waste

Figure 7.24 presents the mineral distribution map that was produced from the SWIR hyperspectral images. This map shows that the SWIR active mineralogy of almost all samples is dominated by either pyrophyllite or water (fluid inclusions in quartz). One sample occurs on which diaspore is the most abundant SWIR active mineral. Alunite and dickite only occur on samples where water spectra dominate. Diaspore and zunyite only occur when pyrophyllite is present. Mixed pixel spectra of water and pyrophyllite are also observed on the samples, but their occurrence is usually minor. On 2 samples this mixture is present in a relatively large amount (Figure 7.24: 3rd row, first 2 samples from the right).
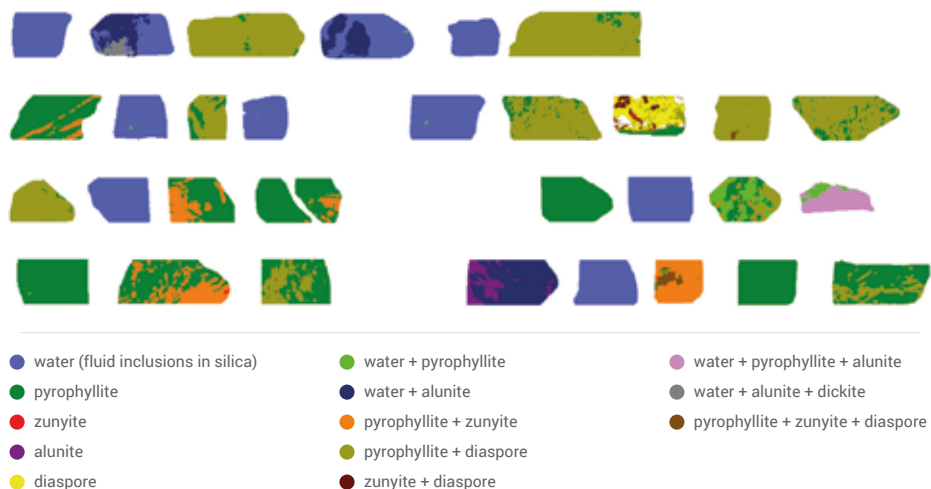

- ● water (fluid inclusions in silica)
- ● pyrophyllite
- ● zunyite
- ● alunite
- ● diaspore
- ● water + pyrophyllite
- ● water + alunite
- ● pyrophyllite + zunyite
- ● pyrophyllite + diaspore
- ● zunyite + diaspore
- ● water + pyrophyllite + alunite
- ● water + alunite + dickite
- ● pyrophyllite + zunyite + diaspore

Figure 7.24: Mineral map produced from the SWIR hyperspectral image.

By comparing the mineral distribution map of Figure 7.24 with the gold grade of samples, it resulted that samples dominated by pyrophyllite have lower gold grade than those dominated by water. It also resulted that samples containing pyrophyllite and zunyite have higher gold grades than samples that contain only pyrophyllite or samples that contain pyrophyllite and diaspore. Based on these results, the mineral distribution map of Figure 7.24 was modified to produce the waste discrimination map that is presented in Figure 7.25. The red pixels on the map in Figure 7.25 represent spectra of pyrophyllite and pyrophyllite + diaspore that are indicators of low gold grades. The green pixels represent all spectra that contain zunyite absorptions, which indicates that a sample can have a higher gold grade. All other pixels in Figure 7.25 show the 1400 nm wavelength band of the hyperspectral image and have no influence the identification of waste samples. Table 7.4 presents the results when samples containing red pixels and no green pixels in the waste discrimination map of Figure 7.25 are distinguished from the rest of the sample set. These samples are also indicated by the black rectangles in Figure 7.25.

Table 7.4 shows significant differences between the average gold and silver grades when samples are distinguished by using the waste discrimination map of Figure 7.25. Furthermore, the table shows that the samples that can be distinguished contain no silver and have a maximum gold grade of only 0.17 ppm. It therefore results that VNIR-SWIR hyperspectral imagery can be used to segment a population of waste samples. However, not all samples below the cut-off grade of 0.20 ppm Au could be identified with VNIR-SWIR hyperspectral imagery.

● pyrophyllite or pyrophyllite + diaspore
indicates waste

● all spectra with zunyite absorptions
sample is not waste, regardless of any red pixels

☐ samples with red pixels and without green pixels

Figure 7.25: Waste discrimination map.

Table 7.4: Classification results based on the waste discrimination map of figure 7.25.

	Total	Samples with red pixels and no green pixels in Figure 7.24	Other samples
Fraction of samples (%)	100	35.5	64.5
Au (ppm) minimum	0.02	0.02	0.02
Au (ppm) maximum	3.59	0.17	3.59
Au (ppm) average	0.26	0.08	0.36
Ag (ppm) minimum	0.00	0.00	0.00
Ag (ppm) maximum	14.90	0.00	14.90
Ag (ppm) average	1.59	0.00	2.47

7.6.4. Discussion

The different mineral assemblages that can be observed in Figure 7.24 are characteristic for different zones of hydrothermal alteration within epithermal deposits (Sillitoe, 1993; Simmons et al., 2005; White & Hedenquist, 1995). The ability to segment a population of waste samples is therefore based on a relationship between gold mineralization and the formation of alteration minerals. This was expected since this relationship was also established in chapter 7.5.

The mineral maps shown in Figure 7.23 and Figure 7.24 show mineral occurrences that were not observed with VNIR-SWIR point spectrometry. Furthermore, the mineral maps can be used to quantify the VNIR-SWIR active mineralogy at the surface of a sample by counting the number of pixels that represent the different minerals. This confirms two of the advantages of VNIR-SWIR hyperspectral imagery over point spectrometry that were discussed in chapter 6.4.

The possibility to characterise the texture of samples with hyperspectral imagery is less apparent from the mineral maps in Figure 7.23 and Figure 7.24 than from those in Figure 6.12. in chapter 6.4. This is partly because the samples originate from different types of deposits, but is also caused by the fact that the VNIR-SWIR hyperspectral images that were used in chapter 6.4. were taken from a smooth surface that resulted from cutting the samples. The effects of shadows and differences in surface orientation, surface roughness and scattering therefore have less influence on the resulting mineral maps and the ability to recognize textural features.

The advantage of VNIR-SWIR hyperspectral imagery regarding the ability to characterise differences in the composition and/or crystallinity of minerals was not applicable. This is because the measured VNIR-SWIR spectra of the minerals that were identified did not reflect such differences.

By comparing the results of Table 7.3 and Table 7.4 with Table 7.2 in chapter 7.5, it results that VNIR-SWIR hyperspectral imagery cannot be used to improve upon the indirect characterisation of gold grade and sulphur content that was possible with VNIR-SWIR point spectrometry. It is expected though that the advantages of hyperspectral imagery for ore characterisation become more apparent when this technique is tested on a larger sample set.

7.6.5. Conclusions

The following conclusions were drawn from testing VNIR-SWIR hyperspectral imagery on 36 samples of the initial sample set:

- The average reflection over the entire 450 – 2500 nm spectral range could be used to separate samples with relatively high carbon contents.

- VNIR-SWIR hyperspectral imagery could be used to segment a population of samples with high sulphur contents. This is based on detecting pyrite from the VNIR region of the pixel spectra (350 – 1300 nm).

- VNIR-SWIR hyperspectral imagery could be used to segment a population of waste samples. This is based on detecting specific alteration mineral assemblages.

- VNIR-SWIR hyperspectral imagery did not improve upon the indirect characterisation of gold grade and sulphur content that was possible with VNIR-SWIR point spectrometry.

- The following advantages of VNIR-SWIR hyperspectral imagery over point spectrometry that were presented in chapter 6.4. were confirmed:

  - Provides more complete data of the mineral composition of a sample including minerals that are present in relatively low quantities.

  - Enables quantification of the SWIR-active mineralogical composition at the surface of a sample by counting the number pixels representing certain minerals.

7.7. VNIR-SWIR hyper-spectral imagery on the drill core samples

This section is based on: Dalm, M., Buxton, M.W.N., van Ruitenbeek, F.J.A., 2018. Ore—waste discrimination in epithermal deposits using near—infrared to short—wavelength infrared (NIR-SWIR) hyperspectral imagery. Mathematical geosciences, 1-27.

7.7.1. Introduction

VNIR-SWIR hyperspectral imagery data was acquired on all 952 samples in the drill core sample set. The aim was to assess whether the results presented in chapter 7.6. are still valid if the same type of sensor is tested on a sample set that is larger and more representative of the geologic and mineralogical variability of the deposit. The objective was to investigate if the VNIR-SWIR hyperspectral data can be used to segment populations of samples that meet the objectives presented in chapter 7.2.3.

7.7.2. Methods

Data acquisition

VNIR-SWIR hyperspectral images of all the drill core samples within core trays were collected with a SisuRock instrument (SPECIM ltd., Oulu, Finland). Figure 7.26 shows an example of the 1400 nm band of one of the hyperspectral images that was collected. The reflectance values on this wavelength band were multiplied by a factor of 2 in order to increase the brightness of the image and enhance the visibility of the samples. The hyperspectral images were recorded on a 380-2500 nm spectral range by using two hyperspectral cameras. The spectral resolution of the images is around 6 nm on the 380-975 nm range and around 10 nm on the 975-2500 nm range. The pixel size of the images is around 2 mm.

After the VNIR-SWIR hyperspectral imagery data was acquired it was discovered that some of the pixel spectra of the samples are contaminated with absorption features that are produced by shadows of the plastic sample labels within the core trays. The position of one of the sample labels is indicated by the pink circle in Figure 7.26. The sample labels are also clearly visible in the photograph in Figure 7.6. The absorption effects produced by the shadows could not be corrected.
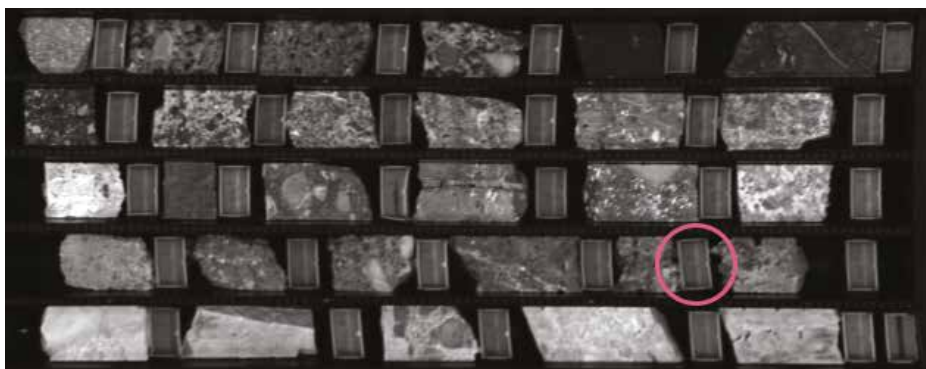

Figure 7.26: 1400 nm band of one of the VNIR-SWIR hyperspectral images. The pink circle indicates a sample label.

Image pre-processing

A series of pre-processing steps were required in order to prepare the recorded VNIR-SWIR hyperspectral data for analysis. The first pre-processing step that was applied was to convert the data to relative reflections. This was performed by using a white reference and a dark current calibration. The second step was to perform a splice correction by shifting the reflectance values on the 380-975 nm range to match those on the 975-2500 nm range. The third pre-processing step was to remove the data on the 380-500 nm range. This was needed because the reflectance data on this wavelength range was relatively noisy due to a low detector sensitivity. This spectral region generally does not contain any relevant mineralogical information.

The fourth pre-processing step was a spike correction. Spikes are extremely low or high reflectance values that occur as a result of detector artefacts. Spikes were identified by finding local maxima and minima and by applying a threshold to the difference in reflectance that the local maximum or minimum has compared to the surrounding wavelength bands. The threshold that was used was 10 times the average reflection difference between consecutive wavelength bands in the pixel spectrum. By using this threshold no reflectance minima produced by mineral absorptions were incorrectly identified as spikes. However, relatively small spikes still remain in the hyperspectral imagery data. The correction of spikes was performed by using a linear interpolation. The linear interpolation was also applied to replace data points with NAN values. These NAN values occasionally occurred within a pixel spectrum as a result of errors in the detection mechanism.

The fifth pre-processing step was masking the hyperspectral images by removing the data of pixels that do not represent a sample. This was performed by manually selecting regions of interest on the image. While selecting the regions of interest it was attempted to exclude the pixels that are contaminated with absorption effects from the shadows of the sample labels as much as possible. However, this was not always successful and on some samples these absorption effects therefore still occur. A new hyperspectral image for each individual sample was produced from the regions of interest that could be used to easily extract the mineralogical properties of every sample after the image processing was completed.

The sixth pre-processing step was to subdivide the spectral range of the VNIR-SWIR hyperspectral images into a VNIR region (500 to 1250 nm) and a SWIR region (1250 to 2500 nm). As with the spectral data processing described in chapter 7.5 and 7.6, the VNIR spectral region was used to determine iron-bearing mineralogy and the SWIR region to determine alteration mineralogy.

The final pre-processing step on the VNIR range of the hyperspectral images was to smooth the spectra in order to reduce the influence of spectral noise. Smoothing was performed on a window of 11 wavelength bands using a Savitzky-Golay filter with a second order polynomial. On the SWIR range of the hyperspectral images no smoothing was performed since some of the absorption features on this range are relatively sharp and smoothing on the smallest possible window removed features with a relatively low absorption intensity.

The final pre-processing step on the SWIR range of the hyperspectral images was to apply a hull quotient correction in order to reduce the influence of absorption effects that are not related to the mineralogy such as light scattering, particle-size effects, surface roughness and detector artefacts. This type of correction was not needed on the VNIR hyperspectral images because on this spectral range the overall reflectance of the spectrum is dominated by the absorption features that occur. The hull quotient correction was illustrated in Figure 7.13.

Image processing

Identification of carbonaceous samples
It was discussed in chapter 7.5 and 7.6. that carbonaceous samples can be identified from a relatively low reflection on the entire VNIR-SWIR spectral range. However, the drill core sample set also contains several non-carbonaceous samples with a relatively low reflection. It should be noted that no TCM assays were performed on any of the drill core samples and this observation is based on the TCM assays and lithological descriptions of the drill hole data.

From visual inspection of the samples, most of the non-carbonaceous samples with a low reflection were classified as strongly altered sandstones with finely disseminated pyrite mineralisation. The low reflection probably also resulted from the occurrence of fine-grained pyrite. Other samples with a low reflection were classified as sulphide breccias consisting of a pyrite matrix with intensely altered sandstone clasts. Furthermore, relatively dark limonite samples occur within the drill core sample set. Limonite is an umbrella term for rock types consisting of a mixture of iron oxides-hydroxides (usually hematite-goethite) in varying composition. These

samples are more easily distinguished from the carbonaceous samples because they have a higher reflection on the 600 to 1200 nm range and therefore a dark red appearance. However, on the SWIR spectral range (1250 – 2500 nm) the reflection of these samples is similar to that of the carbonaceous samples.

In order to distinguish the carbonaceous material from the dark sandstone and dark limonite, correlation coefficients with a pyrite spectrum, a dark sandstone spectrum, and a dark limonite spectrum were calculated for each pixel in the hyperspectral images. An example of these spectra as well as a spectrum that is typically measured on the carbonaceous samples is presented in Figure 7.27. The reflection of the spectra presented in this figure is similar, but was offset to enhance the visibility.

Correlation coefficients with a pyrite spectrum were calculated because the dark sandstone samples often contain a relatively high amount of pyrite mineralisation while the carbonaceous samples do not. The pyrite spectrum differs from the spectra of carbonaceous samples because of the maximum around 700 nm that is produced by absorptions around 300 and 1000 nm resulting from charge transfer and electronic transitions of the Fe-ion (Hunt et al., 1971b; Hunt et al., 1971a). The pyrite spectrum that was used to calculate correlation coefficients was an average of 17 spectra that were collected manually from the measured VNIR hyperspectral images of samples on which high abundances of pyrite were observed. An average was used to reduce the noise on the pyrite spectrum. Correlation coefficients were calculated using the VNIR hyperspectral images.

The dark sandstone spectra that were not characteristic of pyrite often showed a subtle absorption feature around 1900 nm that is produced by water. This water feature usually does not occur in the pixel spectra of carbonaceous samples. The occurrence of the water feature is indicated on Figure 7.27. The water feature is likely produced by fluid inclusions within quartz, which is common at epithermal deposits (Simmons et al., 2005). An average of 25 dark sandstone spectra that all contained the water feature was used to calculate correlation coefficients. These spectra were collected manually from the measured SWIR hyperspectral images of the dark sandstone samples. Correlation coefficients were calculated on an 1800 – 2100 nm spectral range of the SWIR hyperspectral images. This range was selected in order to focus on the occurrence of the water feature.

Figure 7.27 shows that the shape of the dark limonite spectrum clearly differs from the spectrum that is typically measured on the carbonaceous samples. The shape of this spectrum on the VNIR spectral range is typical for hematite and produced by absorptions resulting from electronic transitions of the Fe-ion around 660 and 890 nm (AusSpec, 2008; Hunt et al., 1971a). The drop in reflectance around 500 nm is produced by charge transfer absorption (Hunt, 1977). The low reflection on the 1250 – 2500 nm range is not typical for hematite (e.g. AusSpec, 2008; Clark et al., 2007). Even though the drill hole data shows relatively low TCM contents for most of the dark limonite samples, the low reflection on the 1250 – 2500 nm range is most probably caused by minor occurrences of carbonaceous matter within the dark limonite samples. As mentioned in chapter 7.2.4, the drill hole data is not fully representative of the samples used in this study. However, the occurrence of carbonaceous matter within the dark limonite samples

was not confirmed with additional geochemical assays. An average of 25 dark limonite spectra was used to calculate correlation coefficients. The spectra were collected manually from the measured VNIR hyperspectral images of dark limonite samples. Correlation coefficients were calculated using the VNIR hyperspectral images.

In order to identify carbonaceous samples from the VNIR-SWIR hyperspectral images each pixel was classified as pyrite or dark limonite if the correlation coefficient between the pixel spectrum and the average spectrum of these classes was ≥ 0.95. A pixel was classified as carbonaceous if the correlation to the pyrite, dark limonite or dark quartz spectrum was < 0.95 and the average reflection over the entire VNIR-SWIR spectra range was < 0.15.
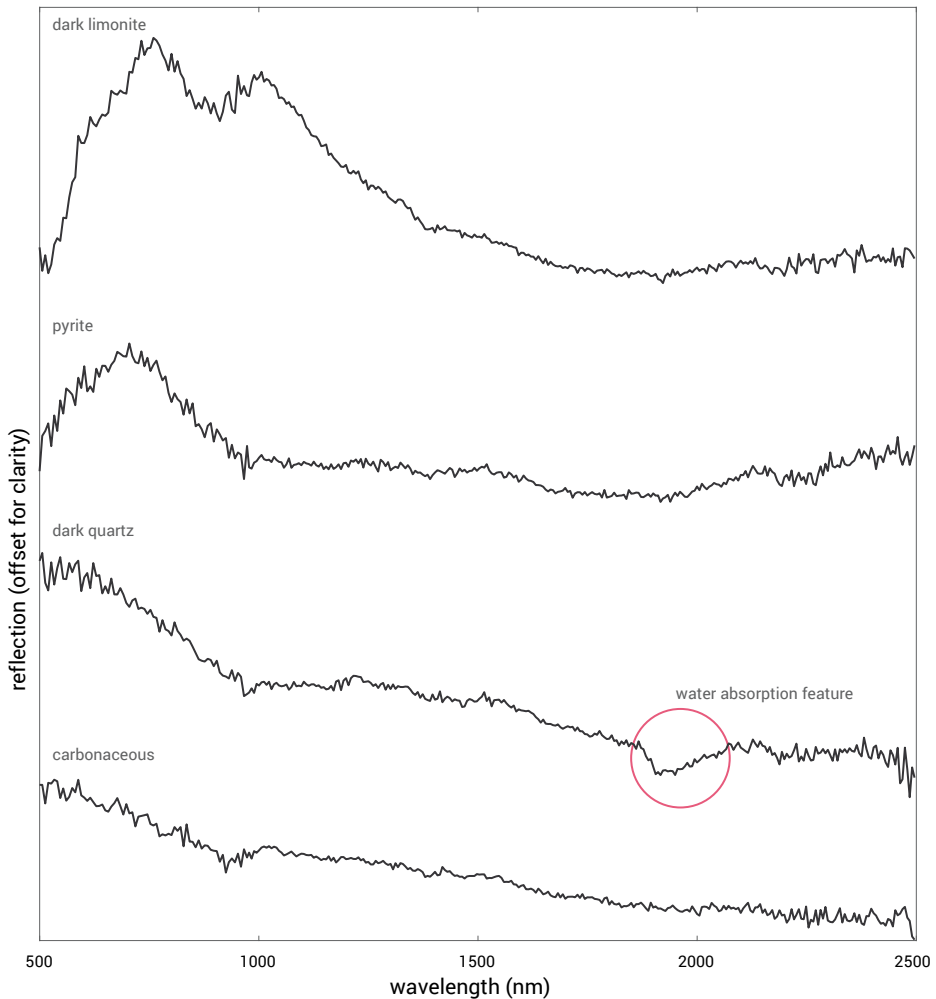
Figure 7.27: Examples of dark spectra.

Mineralogy mapping from VNIR hyperspectral images

Mapping the mineralogy from the VNIR hyperspectral images was mainly focussed on extracting features that represent characteristics of the iron oxide mineralogy. The first image processing step on these images was to use correlation coefficients to classify the pixels as either pyrite, iron-oxide or no diagnostic mineral occurrence. The classification of pyrite was based on the correlation to the same average spectrum that was used for identifying carbonaceous samples. The classification of iron-oxide was based on correlations to 389 iron-oxide spectra that were selected manually from the measured VNIR hyperspectral images. A large number of iron-oxide spectra were needed because the variability between these spectra is relatively high. The SIMPLISMA method of Windig & Guilment (1991) was used to extract spectra from the VNIR hyperspectral image of each sample to ensure that the variability of the iron-oxide spectra throughout the sample set was captured.

Additional to the correlation to pyrite and iron-oxide spectra, correlation coefficients were calculated to a spectrum that is similar to iron-oxide, but that does not represent iron-oxide mineralogy. This was needed to avoid misclassification of iron-oxide since the similarity between spectra results in relatively high correlation coefficients. It is unknown which mineral produces the spectra that are similar to iron-oxide. This was also not further investigated since these spectra were observed in the VNIR hyperspectral image of only one sample. The spectrum that was used to avoid misclassification of iron-oxide was an average of 8 spectra that were collected manually from the sample on which these spectra were observed.

The pixel spectra of the VNIR hyperspectral images of all samples were classified as pyrite or iron-oxide if the correlation coefficient to these spectra was ≥ 0.90. In case the correlation to both pyrite and iron-oxide was ≥ 0.90, the pixel was classified on the mineral to which the highest correlation coefficient resulted. Pixels were classified as having no diagnostic mineralogy in case the correlation coefficient to pyrite or iron-oxide was < 0.90 or when the correlation to the spectrum used to avoid misclassification of iron-oxide was highest.

The absorption intensity and minimum position of the iron-oxide absorption feature that occurs around 900 nm was calculated for all pixels on which this mineral was classified. The minimum position of this feature usually occurs on a 860-890 nm range for hematite and on a 910-940 nm range for goethite (AusSpec, 2008). It can therefore be used to characterise the hematite-goethite mineralogy. Hematite and goethite spectra were presented in Figure 7.14.

Calculating the absorption intensity and minimum position of the 900 nm absorption feature of iron-oxide was performed by first finding the reflectance maximum on both sides of the absorption feature and then subsetting the spectrum to the spectral range in between both maxima. In case the maximum on the right side of the absorption feature occurs outside the VNIR spectral range, the spectrum was subsetted to the spectral range in between the left maximum and 1250 nm. After subsetting, a hull quotient correction was applied and a two-term Gaussian function was fitted to the absorption feature from which the minimum position and the absorption intensity were calculated. Fitting a Gaussian function was performed to reduce the influence of spectral noise on the calculated feature properties. The procedure for subsetting, hull quotient correction and fitting the Gaussian function is illustrated in Figure 7.28 for two example spectra.

The minimum position of the iron-oxide absorption feature was only calculated if the absorption intensity of the feature > 0.05.

A. the original spectrum
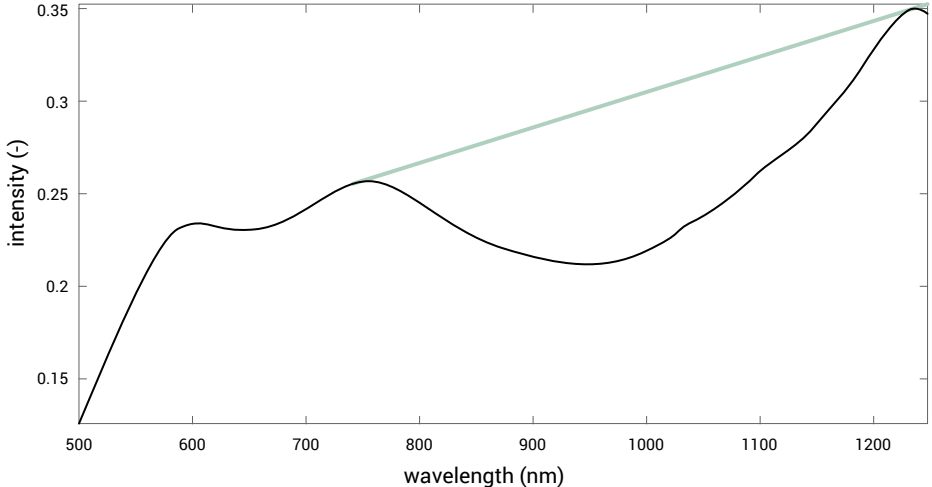
B. subsetted + hull quotient corrected spectrum
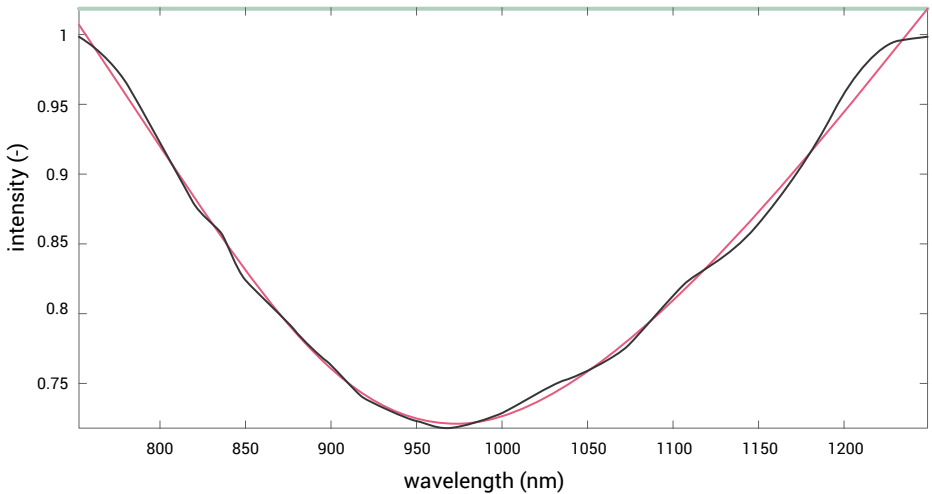
— convex hull on the spectral range of the absorption feature

— Gaussian fit

Figure 7.28: Example of subsetting, hull quotient correction and fitting a Gaussian function to the absorption feature of iron-oxide. .

Mineralogy mapping from SWIR hyperspectral images

The SIMPLISMA method of Windig & Guilment (1991) was used to extract the purest pixel spectra from the SWIR hyperspectral image of each sample. This method was used to ensure that all the different SWIR active minerals that occur within the sample set are identified. The SWIR active mineralogy was determined from the pure spectra by visual inspection and comparison to spectra of the G-MEX spectral interpretation field manual (AusSpec, 2008) and the USGS spectral library (Clark et al., 2007).

A set of mineral reference spectra was selected from the pure spectra and additional spectra were added to this set by extracting them manually from the measured SWIR hyperspectral images. The SWIR spectra that were added were mainly mixed spectra with absorption features of two or more different minerals that were not extracted with the SIMPLISMA method. SWIR spectra containing absorption features of the sample labels were also added. The total set of reference spectra that was collected consisted of 379 different SWIR spectra that represent the spectral variability of the entire sample set as much as possible. This set was used to calibrate and validate PLS-DA classification models that allowed the SWIR spectra to be classified on the occurrence or absence of each SWIR-active mineral that was identified. For each individual mineral a different PLS-DA classification model was produced. The PLS-DA classification models were subsequently used to produce mineral occurrence maps from the SWIR hyperspectral images of all the samples.

To select the optimal number of LVs for the PLS-DA classifications, 80% of the SWIR spectra were used to calibrate the models. The error rate of classification versus the number of LVs was calculated for 1000 randomly chosen calibration and validation subsets. The number of LVs at which the lowest average error rate resulted for the validation subset was selected for creating the PLS-DA classification model. The response threshold used to perform the classification during cross-validation was based on Bayes theorem. The PLS-DA was performed with algorithms from the classification toolbox for Matlab from the Milano Chemometrics and QSAR Research Group (Ballabio, 2013). Before applying the PLS-DA, the data was centred.

After the pixel spectra of the SWIR hyperspectral images of the samples were classified on mineralogy, the absorption intensity that some of the minerals produce was calculated. This was based on the intensity of one of the mineral absorption features that does not overlap with any of the other minerals. Absorption intensities were calculated by subtracting the reflection of the minimum of the absorption feature from the baseline of the hull quotient corrected spectrum. The result is the same as the calculation of absorption intensity illustrated in Figure 6.3 in chapter 6. Absorption intensities > 0 were only calculated if the mineral was classified from a pixel spectrum with the corresponding PLS-DA classification model and if the spectrum has a minimum at the wavelength position where the mineral absorption feature should occur. Additionally, the absorption intensity of the water feature that occurs around 1900 nm was calculated after finding the absorption minimum on the 1850-2100 nm range.

Classification of samples

Apart from mapping the mineralogy, PLS-DA was also applied to investigate whether the information contained in the mineralogy maps can be used to segment a population of waste samples and distinguish between oxide and sulphide ore. Because the drill hole data is not fully representative of the samples, only the samples on which additional geochemical assays were performed were used to calibrate and validate the PLS-DA models for the ore-waste and oxide-sulphide classifications. The drill hole assay data was only used to further test the performance of the models.

Carbonaceous samples were excluded from the PLS-DA classifications because no SWIR-active minerals were mapped on these samples due to their low reflection. Furthermore, several samples were already destroyed for geochemical assays before the VNIR-SWIR hyperspectral imagery data was collected. The PLS-DA classification models were therefore calibrated by using 80 out of the 104 sample assays. 827 gold grade assays and 286 total sulphur assays were available in the drill hole data to test the performance of the models.

The PLS-DA classifications were based on a data matrix containing the relative abundance of each of the identified minerals in the mineralogy maps of every sample. For minerals for which the absorption intensity was characterised also the cumulative distribution of the absorption intensity was added to the data matrix. This was performed by calculating the fraction of pixels with absorption intensities above certain thresholds. Chosen thresholds ranged from 0 to 1 with increments of 0.05. Furthermore, the distribution of the minimum location of the iron-oxide absorption feature was added to the data matrix by first binning the minimum locations and then calculating the fraction of pixels within each bin. The bin size used for calculating this distribution was 20 nm.

The distribution of the minimum position of the iron-oxide absorption feature was not cumulative and sums up to a constant (i.e. 100%). As explained in chapter 6.4.2, this constant sum constraint places restrictions on the correlation structure of the data and can therefore influence the outcomes of the PLS-DA (Aitchison, 1986). To correct for this, a multiplicative zero replacement followed by a centred log-ratio transformation was performed to this data (Aitchison, 1986; Martín-Fernández et al., 2003).

To select the optimal number of LVs for the PLS-DA classification, 80% of the samples were used for model calibration. The remaining samples were used to validate the resulting classifications. The error rate of classification versus the number of LVs was calculated for 1000 randomly chosen calibration and validation subsets. The number of LVs at which the lowest average error rate resulted for the validation subset was selected for creating the PLS-DA classification model. The response threshold used to perform the classification during cross-validation was based on Bayes theorem. The PLS-DA was performed with algorithms from the classification toolbox for Matlab from the Milano Chemometrics and QSAR Research Group (Ballabio, 2013). Before applying the PLS-DA, the data was centred and scaled. Scaling was required because the dataset contains different types of variables with different ranges of values.
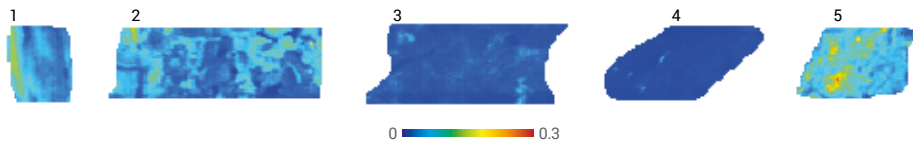
7.7.3. Results

Classification of carbonaceous samples

Figure 7.29 presents an example of the average reflection and classification result of several carbonaceous and non-carbonaceous samples. The brightness of the photos in this figure is somewhat increased in order to enhance the visibility of the samples. In this figure, sample 1 is classified as dark limonite, sample 2 as sulphide breccia, sample 3 as dark sandstone, sample 4 as carbonaceous siltstone, and sample 5 as coal. It can be observed from Figure 7.29 that the carbonaceous siltstone and coal sample cannot be distinguished by using only the average reflection. However, based on the classification of pixels these samples can be distinguished from the occurrence of carbonaceous pixels and the absence of pyrite and dark limonite pixels.
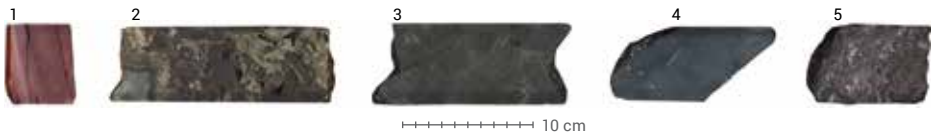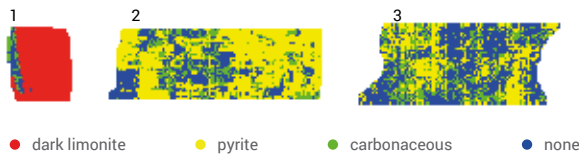

Figure 7.29: Example of the average reflection and carbonaceous pixel classification. Samples are classified as: 1) dark limonite. 2) sulphide breccia. 3) dark sandstone. 4) carbonaceous siltstone. 5) coal.

Figure 7.30 presents the fraction of carbonaceous pixels that were classified on the samples versus the 274 TCM assays of the drill hole data. The pink line in this figure represents a TCM content of 0.5%, which is used to distinguish between carbonaceous and non-carbonaceous ore. Figure 7.30 shows that for most samples with a relatively high TCM content, a high fraction of carbonaceous pixels was classified from the VNIR-SWIR hyperspectral images. However, the figure also shows that samples with a high fraction of carbonaceous pixels and TCM contents < 0.5% occur, as well as samples with a low fraction of carbonaceous pixels and a TCM content

> 0.5%. Based on the drill hole data it therefore results that the classification of carbonaceous pixels from the hyperspectral images could not be used to reliably distinguish between carbonaceous and non-carbonaceous ore. However, the drill hole data is not fully representative of the samples and no additional TCM assays were performed. Because of this, the carbonaceous samples were also identified by visual inspection. During the inspection, carbonaceous samples were classified into 6 different classes. TCM contents and lithological descriptions of the drill hole data were used while doing this. Figure 7.31 shows an example of the different types of carbonaceous samples that were identified. The coal and carbonaceous siltstone samples shown in Figure 7.31 likely have TCM contents above the threshold of 0.5%. For the other types of carbonaceous samples the TCM contents are unsure.
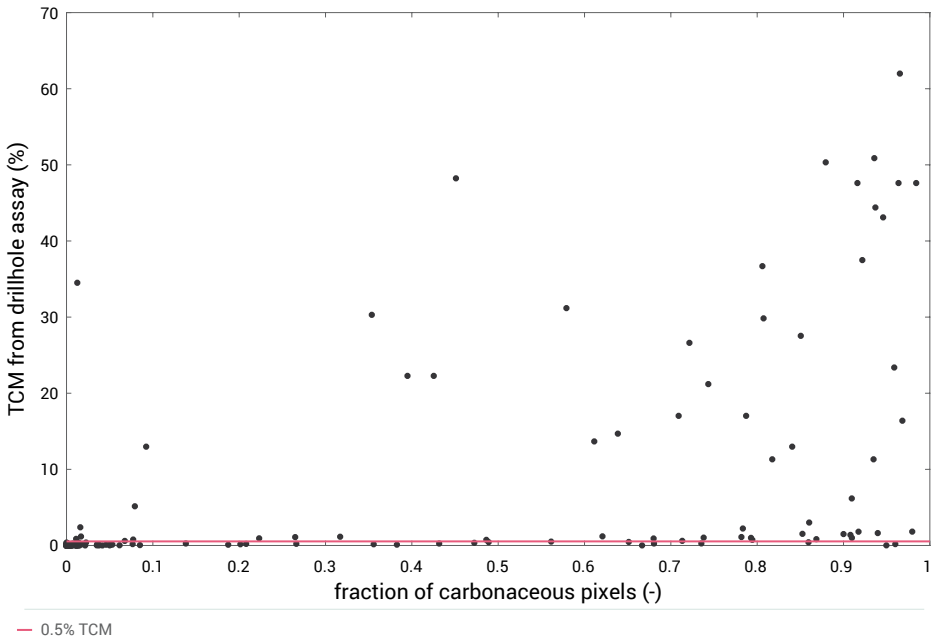

— 0.5% TCM

Figure 7.30: Fraction of carbonaceous pixels versus TCM from drill hole assay

coal

carbonaceous siltstone

slightly carbonaceous siltstone

partly carbonaceous siltstone

altered carbonaceous siltstone

carbonaceous volcanic breccia

10 cm

Figure 7.31: Example of the classification of carbonaceous samples.

Figure 7.32 presents the fraction of carbonaceous pixels versus the classification of carbonaceous and non-carbonaceous samples based on visual inspection. Samples that have > 25% pyrite pixels are marked pink on this figure. Figure 7.32 shows that if samples with > 25% pyrite pixels are eliminated, all the coal samples and carbonaceous siltstone samples can be distinguished from almost all non-carbonaceous samples by using a threshold of 0.15 on the fraction of carbonaceous pixels. This threshold is indicated by the line in Figure 7.32. By inspecting the resulting pixel classifications on the two non-carbonaceous samples that have a fraction of carbonaceous pixels > 0.15, it was observed that for both samples the classification of carbonaceous pixels resulted from shadows. These samples are broken and have surfaces that are not directly exposed to the light source. The misclassification of these samples is therefore due to incorrect illumination and not due to the reflection of the samples themselves.
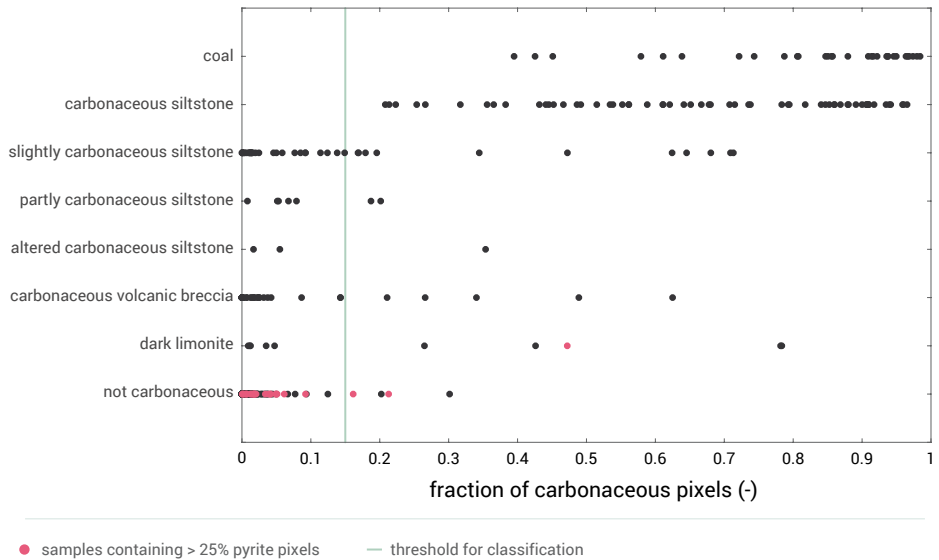

Figure 7.32: Fraction of carbonaceous pixels versus the classification of carbonaceous samples.

Minerals identified from VNIR-SWIR hyperspectral images

Figure 7.33 presents an overview of measured VNIR and SWIR spectra of all the different minerals that were determined on the drill core samples with VNIR-SWIR hyperspectral imagery. All spectra in this figure match those of single minerals except for diaspore and illite (e.g. AusSpec, 2008; Clark et al., 2007). The SWIR spectrum of diaspore that is shown in Figure 7.33 is mixed with pyrophyllite. The illite spectrum shows a weak shoulder on the left side of the absorptions around 1400 and 2200 nm that are most likely produced by pyrophyllite or dickite. Spectral mixtures of illite with pyrophyllite as well as illite with dickite were both observed from the SWIR hyperspectral images of the samples. On some samples also spectral mixtures of illite, pyrophyllite and dickite were observed.
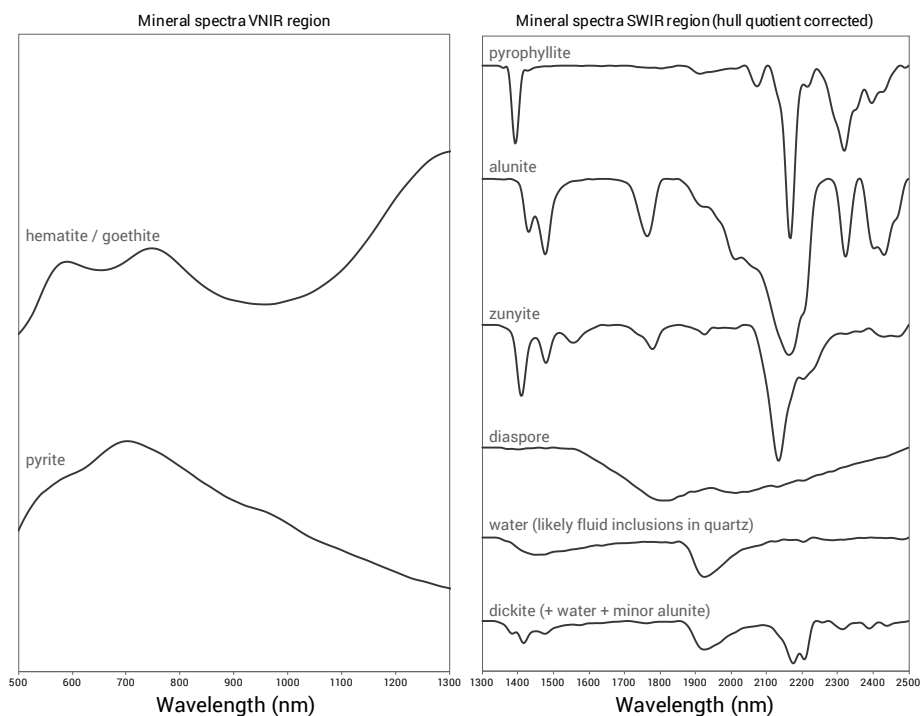
Figure 7.33: Examples of measured VNIR and SWIR mineral spectra.

It should be noted that it was not possible to distinguish between spectral mixtures of illite and pyrophyllite and the SWIR spectrum of kaolinite. This is because the absorption features in the mixed spectrum of illite and pyrophyllite overlap with all the absorption features that are produced by kaolinite. Although there are sometimes subtle spectral differences between the spectrum of kaolinite and mixed spectra of pyrophyllite and illite (e.g. AusSpec, 2008), these were not observed from the measured hyperspectral images. Based on the SWIR hyperspectral images it is therefore unknown if the samples contain kaolinite.

The iron-oxide spectrum that is presented in Figure 7.33 mainly represents a hematite-goethite mixture. It was usually not possible to distinguish between hematite and goethite from the VNIR pixel spectra because these minerals often occur together and their absorption features overlap. For this reason, all the iron-oxide spectra were classified as one group. As discussed in section 7.7.2, the exact minimum position of the feature around 900 nm was calculated to further characterise the iron-oxide mineralogy.

As explained in chapter 7.6.3, the spectrum of water that is shown in Figure 7.33 is likely produced by fluid inclusions in quartz. The occurrence of quartz with fluid inclusions is common at epithermal deposits (Simmons et al., 2005). Finally, Figure 7.33 also shows a spectrum of pyrophyllite

that is mixed with the absorptions of a sample label that was in the core tray while acquiring the hyperspectral images. This spectrum is produced by a shadow of the label on the sample. The absorption features produced by the sample label are the relatively broad features around 1450 and 1700 nm. The mixed spectrum of pyrophyllite and the sample label is presented because it shows that the absorption features of the labels overlap with that of diaspore. This prevented classification of the pixels of the SWIR hyperspectral images on the occurrence of diaspore during the mineral mapping.

The SWIR pixel spectra often contain absorption features of 2 or 3 different minerals. From the VNIR region of the pixel spectra only a dominant mineralogy was classified. Some of the pixel spectra also contained no characteristic absorptions on the VNIR region at all, indicating an absence of iron-bearing minerals.

The occurrence of pyrophyllite, alunite, dickite, illite, diaspore and iron-oxide was validated by XRD. However, XRD could not be used to validate the occurrence of these minerals for every sample on which they were determined from the VNIR-SWIR hyperspectral images. As explained in chapter 7.6.3. this is likely due to the fact that with hyperspectral imagery only the surface of a sample is measured while XRD represents the whole volume of the sample. Furthermore, the occurrence of kaolinite could not be confirmed since the XRD spectra did not allow kaolinite and dickite to be distinguished. The occurrence of zunyite, jarosite and pyrite was not validated by XRD. However, zunyite and pyrite were determined by XRD on the initial sample set, which validates the occurrence of these minerals at Lagunas Norte. Furthermore, all the minerals that were determined from the VNIR-SWIR hyperspectral images including zunyite, jarosite, pyrite, and kaolinite were observed by Cerpa et al. (2013) and Montgomery (2012).
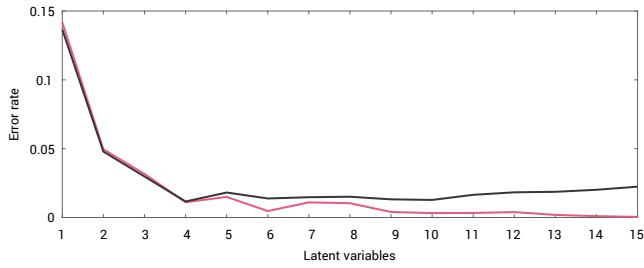
Classification of SWIR spectra

PLS-DA classification models were calibrated on the set of 379 SWIR reference spectra to classify the occurrence of pyrophyllite, alunite, illite-dickite, jarosite, and zunyite. Diaspore was not classified because unsatisfying classification results were obtained due to the overlap of the absorption features of diaspore and that of the shadows of sample labels. Illite and dickite were classified as one group because all the dominant illite absorption features overlap with those of dickite. It was therefore not possible to exclude the presence of illite from a spectrum with dickite absorption features. Although illite also produces two secondary absorption features around 2347 and 2440 nm that do not overlap with dickite (e.g. AusSpec, 2008), these features were not always observed in the illite spectra due to a relatively low signal-to-noise. Furthermore, unsatisfying classification results were obtained when attempting to distinguish between illite and dickite spectra by using PLS-DA. Distinguishing between illite and dickite was performed after the PLS-DA classification by calculating the absorption intensity that each of the minerals produces.

Figure 7.34 presents the error rates versus the number of LVs that are obtained from cross-validating the PLS-DA classification models. The pink lines in this figure represent the calibration sets and the black lines the validation sets. The number of LVs that were used to produce the
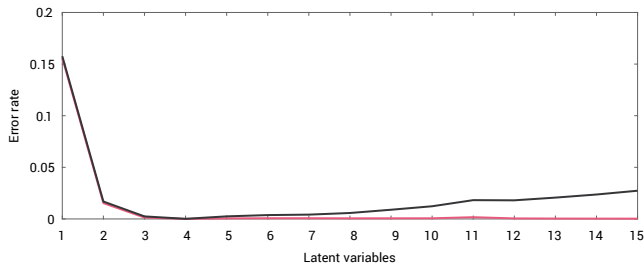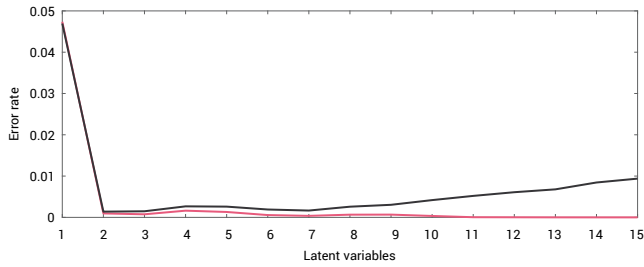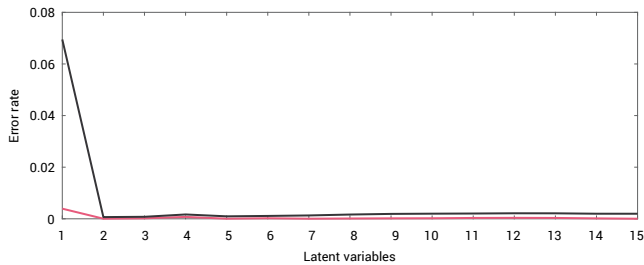
A. pyrophyllite
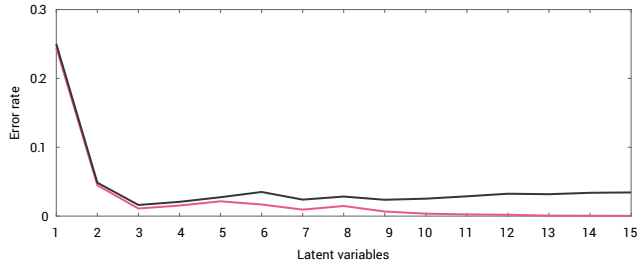
B. alunite

C. illite

D. jarosite

E. zunyite

— validation   — calibration

Figure 7.34: Error rate versus number of LVs of the PLS-DA cross validation for classification of mineral spectra.

classification models was 4 for alunite, 3 for pyrophyllite and illite-dickite, and 2 for jarosite and zunyite. These numbers were chosen because Figure 7.34 shows that the validation subsets have the lowest error rate at these numbers of LVs.

Figure 7.35 presents the PLS-DA responses that were calculated for the classification of mineral spectra. The black colour in this figure represents spectra in which the absorption features of the mineral that is classified were observed by visual inspection. The pink colour represents spectra in which the absorption features of this mineral were not observed. The dots are SWIR spectra that were used for calibrating the classification models and the circles are spectra used for validation. The lines in Figure 7.35 represent the thresholds that were used for the classification of spectra. The selected thresholds were the averages between the maximum response of the spectra containing the mineral absorptions and the minimum response of spectra that do not contain the mineral absorptions. In case misclassification occurred, the misclassified spectra were inspected and if the misclassification was considered acceptable these spectra were not included for calculating the classification threshold.

It can be observed from Figure 7.35 that there is a clear difference between the responses that were calculated for SWIR spectra that contain the absorption features of each mineral and SWIR spectra that do not. Figure 7.35 also shows that for each classification model the responses of the spectra of the validation sets match the range in responses of the spectra that were used to calibrate the model. This indicates that the PLS-DA classification models produce consistent results. Only for zunyite a relatively low number of spectra were used to produce the classification model and just 2 spectra could therefore be used to validate the classification of zunyite. The reason for this is that spectra with zunyite absorption features were observed on only a few pixel spectra of several samples and not much more zunyite spectra were therefore available. However, analysis of the scores and loadings of the PLS-DA models showed that all the classifications, including zunyite, were based on the occurrence of the absorption features of the corresponding mineral.

Figure 7.35 shows that for both pyrophyllite and alunite one spectrum is misclassified by using the response threshold indicated on the figure. For pyrophyllite, inspection of the misclassified spectrum showed that this is a mixed spectrum of pyrophyllite and illite that is relatively noisy. The reason that this spectrum is misclassified is likely due to the noise and the fact that the mixed pyrophyllite-illite spectrum is similar to the spectrum of dickite. Since all the other pyrophyllite spectra were correctly classified, misclassification of a single noisy spectrum was considered acceptable. The alunite spectrum that is misclassified is a mixed spectrum of dickite and alunite in which the dickite absorptions features dominate. Alunite was identified from the occurrence of only one absorption feature with a relatively low intensity. This indicates that if alunite was correctly identified from the SWIR spectrum by visual inspection, it is present in only minor occurrences. Misclassification of this spectrum by the PLS-DA model was therefore also considered acceptable.
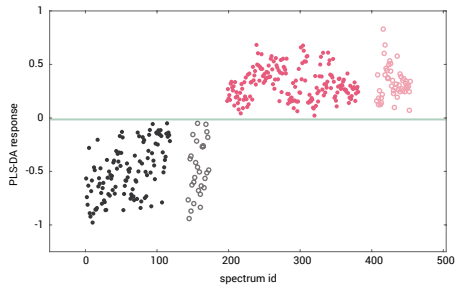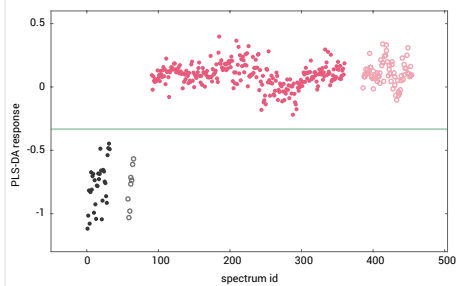
A. pyrophyllite
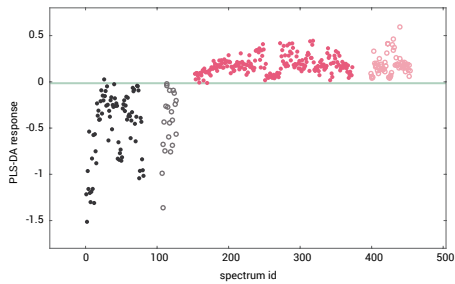
B. alunite
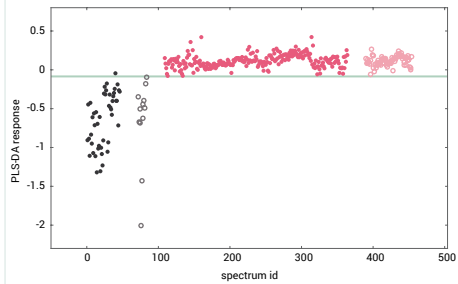
C. illite

D. jarosite

E. zunyite

- ● containing absorptions of the associated mineral calibration
- ○ containing absorptions of the associated mineral validation
- ● not containing absorptions of the associated mineral calibration
- ○ not containing absorptions of the associated mineral validation
- — threshold for classification

Figure 7.35: Calculated responses of the PLS-DA classification of mineral spectra.

Mineralogy mapping

Figure 7.36 presents the results of mapping the mineral absorption intensity from the hyperspectral images of six samples. For the SWIR-active minerals absorption intensities > 0 were only mapped if the mineral that produces the absorption feature was classified from a pixel spectrum with the corresponding PLS-DA classification model. For iron-oxide the absorption intensity and mineral position was mapped if the correlation coefficient between the pixel

spectrum and that of one of the iron-oxide spectra was > 0.9 and higher than that of pyrite or the unknown spectrum. The intensity of the water feature was mapped for all pixel spectra.

The absorption intensity of jarosite and zunyite was not characterised because these minerals occur on only a few samples. The absorption intensity of alunite, pyrophyllite, illite-dickite and dickite that is shown in Figure 7.36 is that of one of the absorption features that each mineral produces around 1400 nm. These absorption features were chosen because these have the least overlap and are relatively intense. Since all the absorption features of illite overlap with dickite, the absorption intensity of illite alone could not be characterised. The occurrence of illite can be inferred from the absence of the dickite absorption while the illite-dickite absorption is present. In Figure 7.36 this is the case for sample 5 for example.

It was mentioned in the previous section that due to overlapping features it was not possible to distinguish between spectral mixtures of illite and pyrophyllite and the SWIR spectrum of kaolinite. This means that if absorption intensities > 0 result for both pyrophyllite and illite it is possible that these pixels actually represent kaolinite. In Figure 7.36 this is the case for sample 2 and partly for sample 4.

It was explained in section 7.7.2. that the 900 nm iron-oxide absorption usually occurs on a 860-890 nm range for hematite and on a 910-940 nm range for goethite. However, Figure 7.36 shows that the minimum positions of the 900 nm iron-oxide absorption in the measured VNIR hyperspectral images occur on a 900 to 1050 nm range. The difference between the minimum positions reported in literature and those calculated from the measured VNIR hyperspectral images likely results from the way the minimum positions were calculated. Minimum positions of the absorption features of iron-oxide minerals reported in literature are based on uncorrected spectra , while on the measured iron-oxide spectra a hull quotient correction was applied in order to calculate the absorption intensity. Since the maximum on the left side of the absorption feature usually has a lower intensity than the maximum on the right side of the feature, a hull quotient correction will shift the minimum position to longer wavelengths. However, this shift in minimum positions will affect all the iron-oxide spectra in the same way and the calculated minimum positions still represent the hematite-goethite mineralogy.

Figure 7.36 shows that mapping the minimum position of the 900 nm iron-oxide absorption reveals some additional differences between samples. Sample 1 in Figure 7.36 for example contains regions where the minimum position of the iron-oxide absorption occurs at relatively long wavelengths. Minimum positions at these wavelengths cannot be observed in the image of sample 2. The occurrence of goethite at the surface of the samples is therefore somewhat higher for sample 1 than for sample 2.

Classification of ore and waste

The definition of ore and waste was based on a cut-off grade of 0.20 ppm Au. The data matrix on which the PLS-DA classification of ore and waste samples was performed contained the cumulative distribution of the absorption intensity of pyrophyllite, alunite, dickite, illite-dickite and

A. photo |—+—+—+—+—+—+—+—+—| 10 cm

1. 2. 3. 4. 5. 6.

B. alunite 0 ▬▬▬ 0.25

1. 2. 3. 4. 5. 6.

C. pyrophyllite 0 ▬▬▬ 0.25

1. 2. 3. 4. 5. 6.

D. illite-dickite 0 ▬▬▬ 0.25

1. 2. 3. 4. 5. 6.

E. dickite 0 ▬▬▬ 0.25

1. 2. 3. 4. 5. 6.

F. water 0 ▬▬▬ 0.3

1. 2. 3. 4. 5. 6.

G. iron-oxide 0 ▬▬▬ 0.5

1. 2. 3. 4. 5. 6.

H. iron-oxide position 800 nm ▬▬▬ 1100 nm
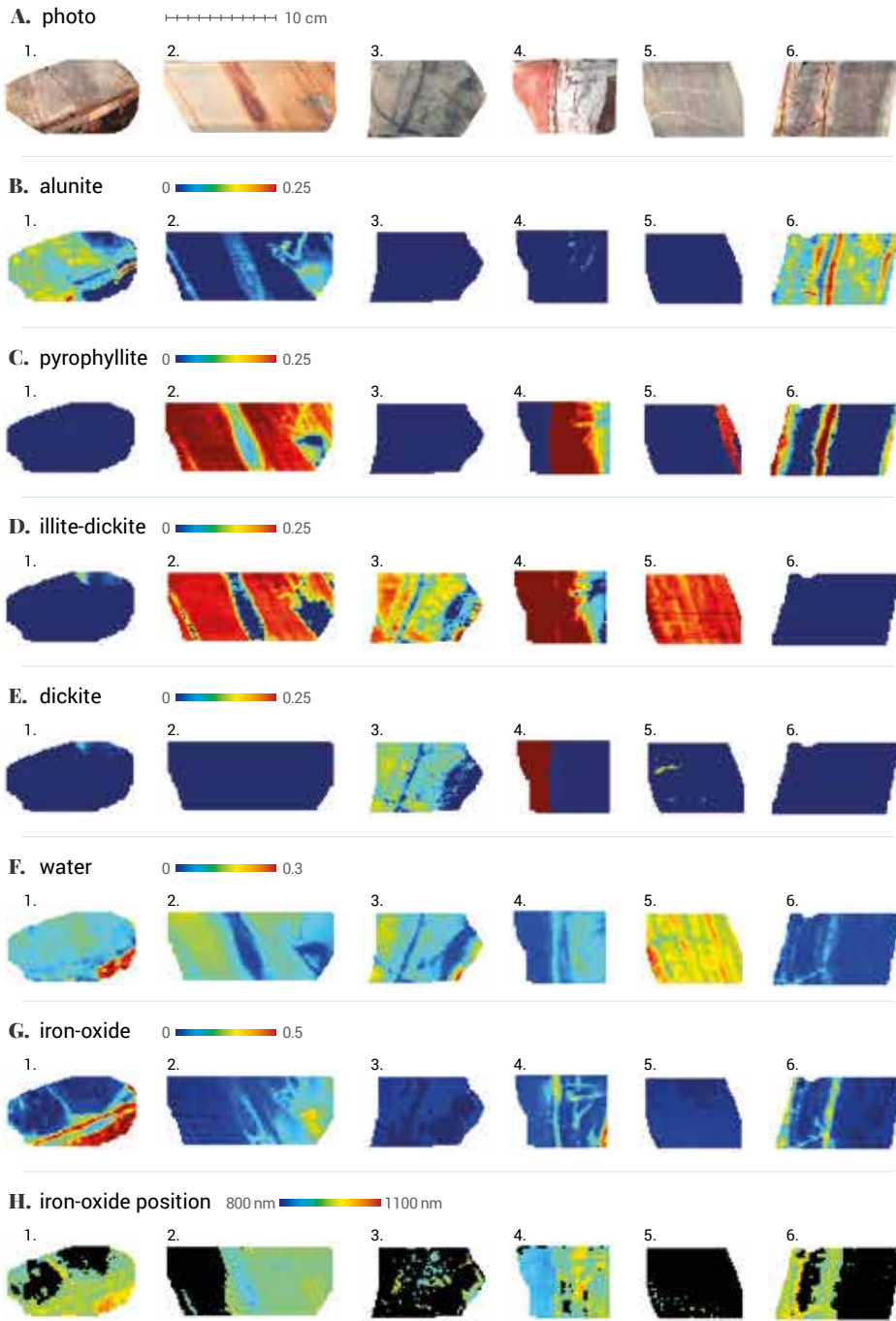
1. 2. 3. 4. 5. 6.

Figure 7.36: Selected examples of mineral maps produced from the VNIR-SWIR hyperspectral images that show the absorption intensity of alunite, pyrophyllite, illite-dickite, dickite, water and iron-oxide and the minimum position of the iron-oxide absorption feature.

iron-oxide. It also contained the fraction of pixels on which jarosite and pyrite were classified and the average intensity of the water feature. The pixel fractions of the zunyite classifications were not included because zunyite was classified on only three samples with a maximum of 0.7% of the pixels. Finally, the distribution of the minimum position of the iron-oxide absorption feature was included in the data matrix after applying a multiplicative zero replacement followed by a centred log-ratio transformation.

Carbonaceous samples were excluded from the PLS-DA classification because no SWIR-active minerals were mapped on these samples due to their low reflection. Identification of carbonaceous samples was based on the classification on the VNIR-SWIR hyperspectral imagery data presented at the start of section 7.7.3.

Figure 7.37 presents the average error rate versus the number of LVs that are obtained from 1000 cross-validations of the PLS-DA classification model. The pink line in this figure represents the calibration set and the black line the validation set. Figure 7.37 shows that the error rate of the validation set only increases when more than one LV is used. Because this indicates that the PLS-DA model is overfitting, one LV was chosen for producing the PLS-DA classification of ore and waste.
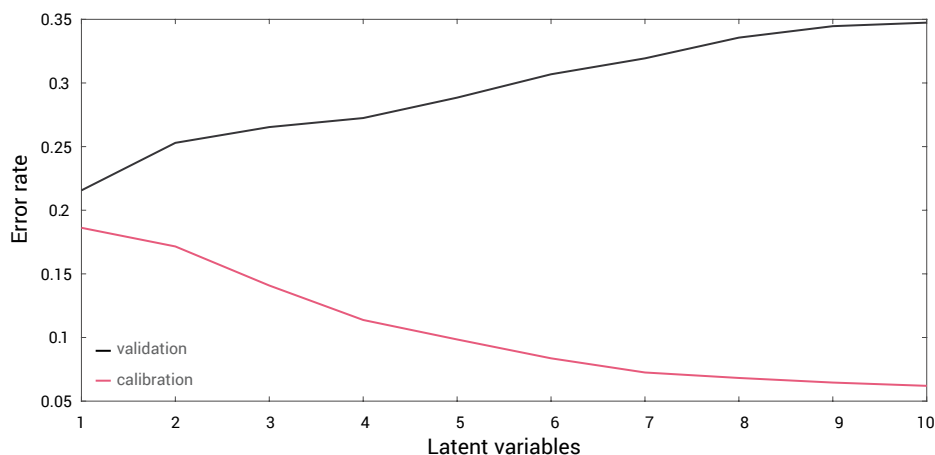

Figure 7.37: Error rate versus number of LVs of the PLS-DA cross validation for classification of ore and waste samples.

Figure 7.38 presents the calculated responses of 80 non-carbonaceous samples from the PLS-DA classification in which the ore-waste designation was based on the sample assays. The pink colour in this figure represents waste samples and the black colour ore samples. The dots are samples that were used for calibrating the PLS-DA classification model and the circles are samples used for validation. It can be observed from Figure 7.38 that the calculated responses of the validation sets match the range in responses of the calibration sets. This indicates that the PLS-DA classification model produces consistent results.

It can be observed from Figure 7.38 that the PLS-DA classification model was not able to fully separate ore from waste. This is likely because some of the waste samples in the samples set have a SWIR-active mineralogy that is similar to some of the ore samples. This was also expected since it is unlikely that there is a discrete difference in alteration mineralogy at some arbitrary cut-off on the gold grade. However, Figure 7.38 also shows that for most of the waste samples a higher response is calculated than for most of the ore samples. The calculated responses can therefore be used to predict whether a sample is more likely to be waste or ore.
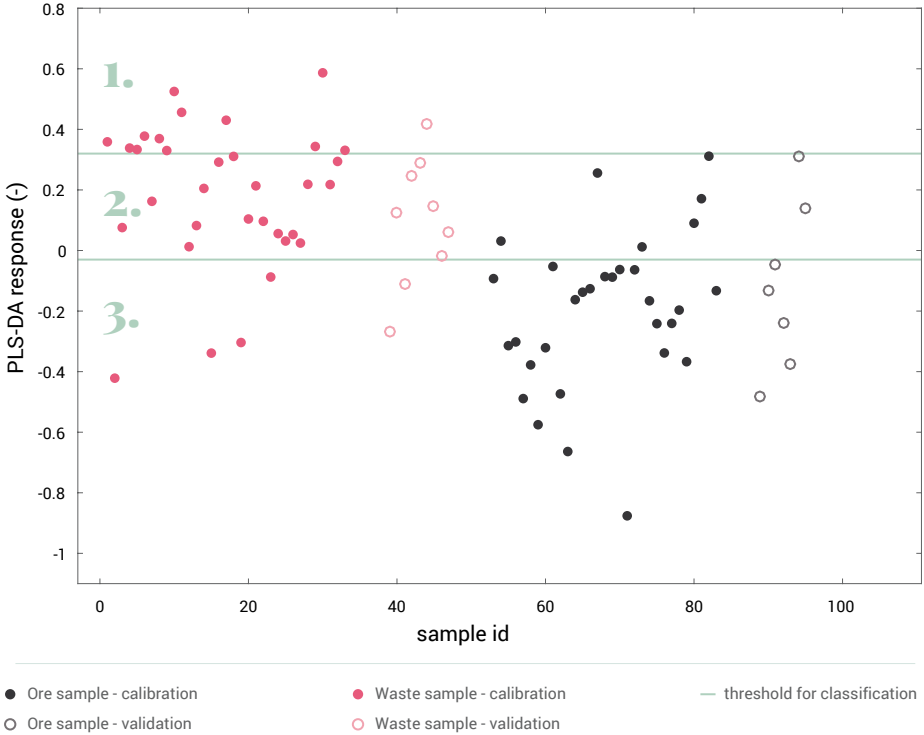

Figure 7.38: Calculated PLS-DA responses of non-carbonaceous ore and waste samples. Ore-waste designation is based on the additional samples assays.

The two lines in Figure 7.38 are two thresholds that were chosen for classification of samples. The threshold at 0.32 was chosen in order to segment a group of samples that are all waste and the threshold at -0.03 was chosen to segment a group that consists mainly of ore samples. Although segmenting ore samples was not one of the objectives of the study, this was performed to illustrate the potential of using PLS-DA classification models to distinguish between gold grades. Table 7.5 presents the resulting gold and silver grades when the responses and thresholds shown in Figure 7.38 are used to classify the samples. The group numbers in this table refer to the numbers annotated on Figure 7.38 and Figure 7.39. It can be observed from Table

7.5 that significant differences between the average gold grades of the three groups result. The silver grade of group 3 is also significantly higher than that of the other two groups.

Figure 7.39 presents the responses of all 827 non-carbonaceous samples for which the ore-waste designation is based on the drill hole data. These responses were calculated by using the same PLS-DA classification model that was used for the classification presented in Figure 7.38. The lines shown in this figure also represent exactly the same thresholds as those in Figure 7.38. The different colours refer in this case to the ore-waste designation that is based on the drill hole data. The ore-waste designation of the samples that were used to calibrate the PLS-DA model is still the same since the drill hole data of samples on which additional assays were performed was replaced by the results of these assays. Because the drill hole data is not fully representative of the samples, the ore-waste designations shown in Figure 7.39 might not be completely correct.
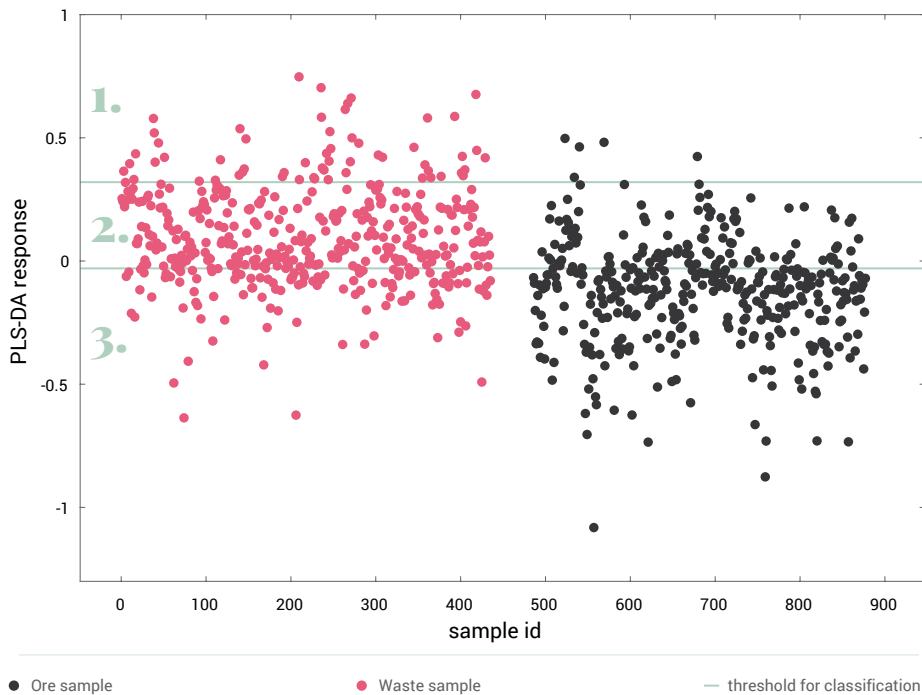
Figure 7.39: Calculated PLS-DA responses of all non-carbonaceous ore and waste samples. Ore-waste designation is based on the drill hole data.

The responses in Figure 7.39 show a similar trend as those in Figure 7.38. Table 7.5 presents the resulting gold grades from the drill hole data when the responses and thresholds shown in Figure 7.39 are used to classify the samples. This table shows that based on the drill hole data, a population of only waste samples is no longer segmented. However, it also shows that the average gold grade of the group of waste samples (group 1) is still significantly lower than the

cut-off grade of 0.20 ppm Au. Furthermore, there are also still significant differences between the average gold grades of the three groups. The drill hole data therefore validates that it is possible to use VNIR-SWIR hyperspectral imagery to distinguish between the gold grades of the samples. The differences in silver grade could not be compared since the drill hole data did not contain silver grades.
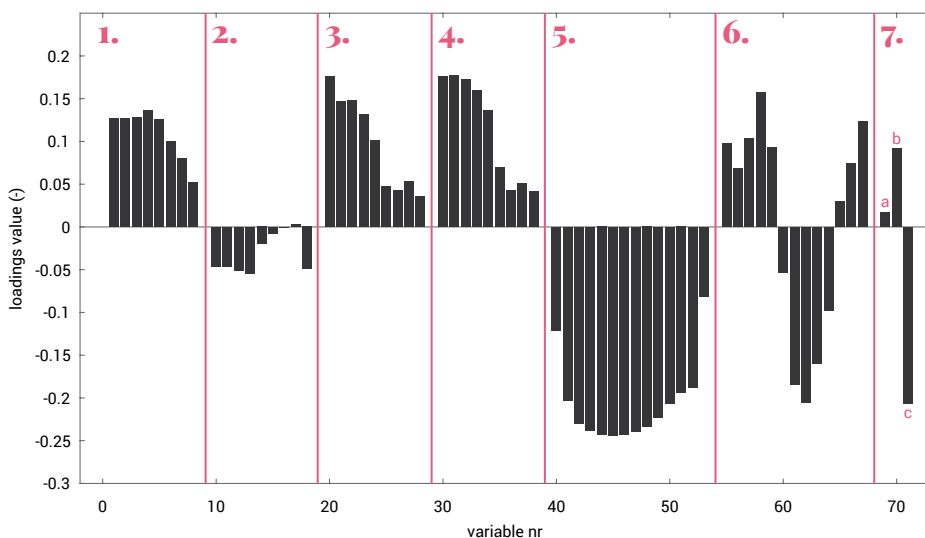
Table 7.5: Results of the PLS-DA classification of ore and waste.

	based on sample assay (figure 7.38)			based on drill hole assay (figure 7.39)		
	group 1	group 2	group 3	group 1	group 2	group 3
Fraction of samples (%)	16.3	38.7	45.0	7.5	45.3	47.2
Au (ppm) minimum	0.00	0.00	0.00	0.00	0.00	0.00
Au (ppm) maximum	0.20	0.96	14.68	1.74	31.22	22.39
Au (ppm) average	0.06	0.19	1.51	0.08	0.48	1.15
Ag (ppm) minimum	0.00	0.00	0.00			
Ag (ppm) maximum	8.00	11.10	33.55			
Ag (ppm) average	0.62	0.56	4.24			

Figure 7.40 presents the loadings of the LV that was used in the PLS-DA classification model. The annotated numbers on Figure 7.40 refer to the different types of variables used in the classification. The cumulative distribution of the absorption intensity of pyrophyllite, alunite, dickite, illite-dickite and iron-oxide are represented by the numbers 1, 2, 3, 4, and 5 respectively. In these distributions the absorption intensity increases from left to right. Number 6 represents the distribution of the minimum position of the iron-oxide absorption feature with increasing wavelength from left to right. The variables represented by number 7 are the fractions of pyrite and jarosite pixels and the average intensity of the water absorption feature.

Analysis of the sample scores on the LV used in the PLS-DA classification model showed that the waste samples have relatively high score values. This means that waste samples are associated with variables that have high loadings values. It can be observed from Figure 7.40 that pyrophyllite, dickite and illite have high loadings values and a relatively high abundance of these minerals in the mineralogy maps is therefore a strong indicator of waste. Regarding dickite and illite, Figure 7.40 also shows that it are mainly the low intensity absorptions of these minerals that indicate waste. Furthermore, Figure 7.40 shows that relatively high fractions of jarosite pixels are more associated with waste samples. However, the fact that the loadings value is of jarosite is not very high does suggest that it is not such a strong indicator of waste as pyrophyllite, dickite or illite. This could also be related to the fact that not many samples contain jarosite.

It can be observed from Figure 7.40 that a relatively high abundance of iron-oxide is strong indicator of ore. The loadings show that this mainly concerns iron-oxide with minimum positions in between 950 and 1050 nm. Furthermore, it can be derived from Figure 7.40 that ore samples are associated with relatively intense water features and ore samples can contain alunite. Finally, Figure 7.40 shows that the pixel fractions of pyrite have a very low loadings value and therefore do not have a large influence on the classifications.

1. pyrophyllite - absorption intensity distribution

2. alunite - absorption intensity distribution

3. dickite - absorption intensity distribution

4. illite-dickite - absorption intensity distribution

5. iron-oxide - absorption intensity distribution

6. iron-oxide absorption feature - minimum position distribution

7. a fraction of pyrite pixels

7. b fraction of jarosite pixels

7. c water absorption feature - average intensity

Figure 7.40: PLS-DA loadings of the classification of ore and waste samples.

Classification of oxide and sulphide ore

It was discussed in chapter 7.6. that sulphide ore samples can be identified from the occurrence of pixel spectra that represent pyrite. Figure 7.41 shows the fraction of pyrite pixels that was classified using correlation coefficients versus the total sulphur content from the drill hole data. The pink line in this figure represents a sulphur content of 0.25%, which is used to distinguish between oxide and sulphide ore. It can be observed from Figure 7.41 that most of the samples with a high fraction of pyrite pixels also have a relatively high sulphur content. The vertical line in Figure 7.41 represents a threshold that was used for classification of sulphide ore samples. Figure 7.41 shows that only one oxide ore sample is misclassified as sulphide ore when this threshold is selected. The result of the classification of sulphide ore is presented in Table 7.6.

This table shows that significant differences result between the average sulphur contents of both groups. However, Figure 7.41 and Table 7.6 also show that there is still overlap between the distributions of the sulphur content of both groups.

— 0.25% sulphur content

— threshold for classification of sulphide ore samples
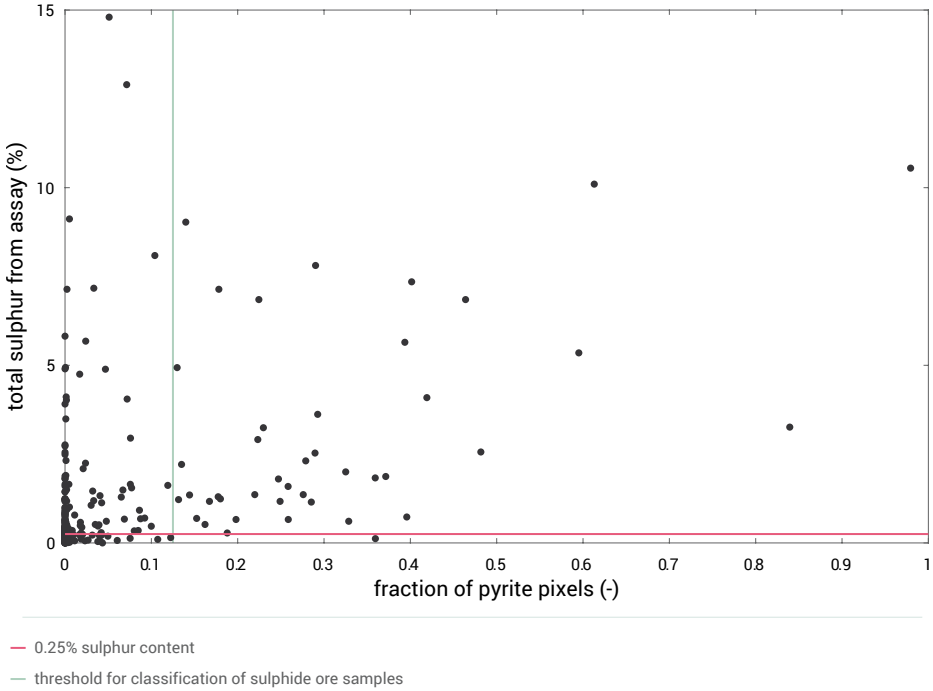
Figure 7.41: Fraction of pyrite pixels versus the total sulphur content based on the drill hole data.

Table 7.6: Results of classification on the fraction of pyrite pixels.

	based on drill hole assay	
	< 12.5 % pyrite pixels	> 12.5 % pyrite pixels
Fraction of samples (%)	85.3	14.7
S (%) minimum	0.00	0.12
S (%) maximum	14.80	10.55
S (%) average	0.90	3.17

PLS-DA was applied to further investigate the possibilities of using the mineralogical information provided by VNIR-SWIR hyperspectral imagery to distinguish between oxide and sulphide

ore. The mineralogical data on which the PLS-DA was performed was the same as the one used for the classification of ore and waste. Carbonaceous samples were also again excluded from the PLS-DA.

Figure 7.42 presents the average error rate versus the number of LVs that are obtained from 1000 cross-validations of the PLS-DA classification model. The PLS-DA classification model was calibrated using two LVs because Figure 7.42 shows a minimum in the error rate of the validation set when this number of LVs is used.
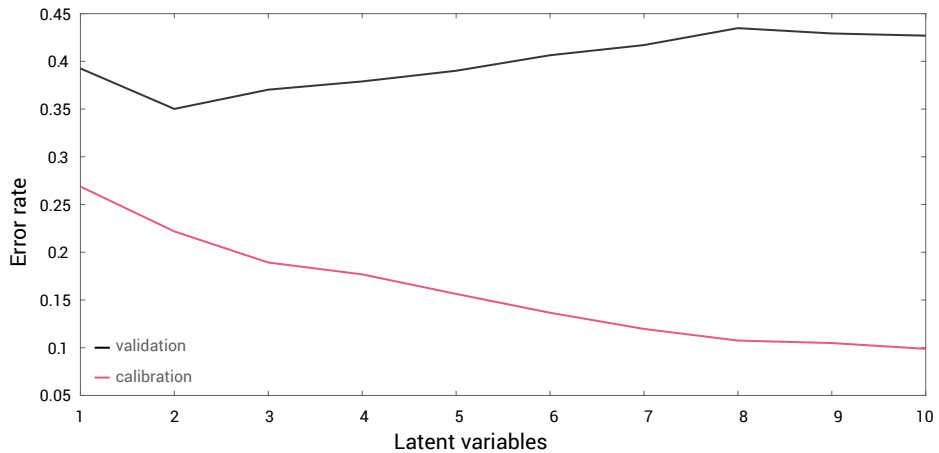

Figure 7.42: Error rate versus number of LVs of the PLS-DA cross validation for classification of oxide and sulphide ore samples.

Figure 7.43 presents the calculated responses of 80 non-carbonaceous samples from the PLS-DA classification in which the oxide-sulphide ore designation was based on the sample assays. It can be observed from this figure that the calculated responses of the validation sets match the range in responses of the calibration sets. This indicates that the PLS-DA classification model produces consistent results.

It can be observed from Figure 7.43 that the PLS-DA classification model is not able to fully separate oxide from sulphide ore. As with the ore-waste classification, this was expected. However, Figure 7.43 also shows that for most of the oxide ore samples a higher response is calculated than for most of the sulphide ore samples. The calculated responses can therefore be used to predict whether a sample is more likely to be oxide or sulphide ore.
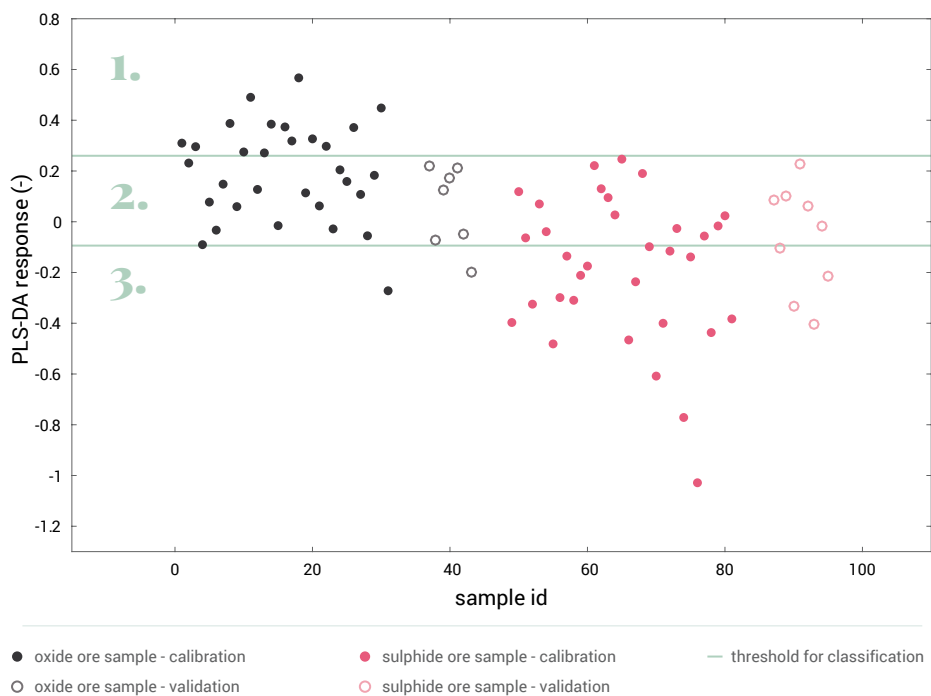
Figure 7.43: Calculated PLS-DA responses of non-carbonaceous oxide and sulphide ore samples. Oxide-sulphide designation is based on the additional samples assays.

The two lines in Figure 7.43 are two thresholds that were chosen for the classification of samples. The threshold at 0.26 was chosen in order to classify a group of samples that are all oxide ore. The threshold at -0.09 was chosen to classify a group of samples that mainly consists of sulphide ore. Figure 7.43 shows that it is also possible to distinguish a group of samples that are all sulphide ore. However, it was observed from the resulting averages in the sulphur content that including a small fraction of oxide ore did not really affect the average sulphur content, but made a large difference on the number of sulphide ore samples that are distinguished. Because of this, the threshold was set at -0.09. In the end any threshold on the responses can be selected in order to produce the classification that is best to meet the needs of the mineral processing facilities. Table 7.7 presents the resulting total sulphur contents when the thresholds are used to classify the samples. The group numbers in this table again refer to the numbers annotated on Figure 7.43 and Figure 7.44. It can be observed from Table 7.7 that significant differences between the average sulphur contents of the three groups result.

Figure 7.44 presents the responses of 286 non-carbonaceous samples for which total sulphur contents were available from the drill hole data. These responses were calculated by using the same PLS-DA classification model that was used for the classification presented in Figure 7.43. The different colours refer in this case to the oxide-sulphide ore designation that is based on the drill hole data. The drill hole assay data did not contain total sulphur contents for all the samples and the total number of samples in Figure 7.44 is therefore smaller than for the

ore-waste classification shown in Figure 7.39. Furthermore, the oxide-sulphide ore designation of the samples that were used to calibrate the PLS-DA model is still the same since the drill hole data of samples on which assays were performed was replaced by the results of these assays.
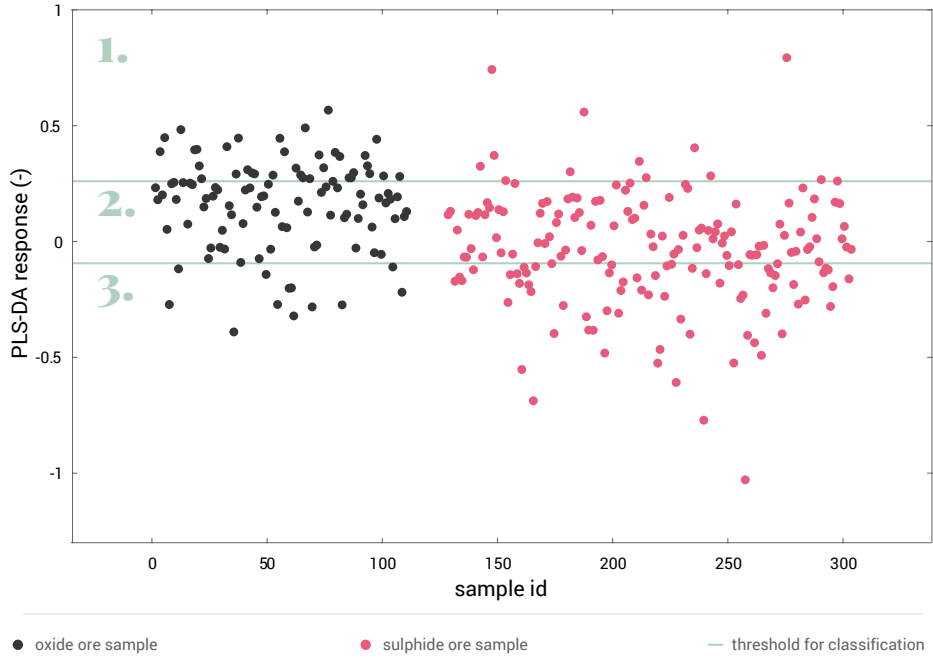
Figure 7.44: Calculated PLS-DA responses of all non-carbonaceous oxide and sulphide ore samples. Oxide-sulphide designation is based on the drill hole data.

It can be observed from Figure 7.44 that based on the drill hole data most of the oxide ore samples have a higher response than most of the sulphide ore samples. The lines in Figure 7.44 represent exactly the same thresholds as those shown in Figure 7.43. Table 7.7 presents the resulting sulphur contents from the drill hole data when these thresholds are used to classify the samples. Figure 7.44 shows that by classifying all the samples with the same PLS-DA classification model it is no longer possible to segment a group of samples that are all oxide or sulphide ore. Furthermore, Table 7.7 shows that the average sulphur content of group 1 is no longer below the cut-off of 0.25% S. However, the table also shows that there are still significant differences between the average sulphur contents of the three groups. The drill hole data therefore validates that it is possible to use VNIR-SWIR hyperspectral imagery to distinguish between the sulphur content of samples.

Table 7.7: Results of the PLS-DA classification of oxide and sulphide ore.

	based on sample assay (figure 7.43)			based on drill hole assay (figure 7.44)		
	group 1	group 2	group 3	group 1	group 2	group 3
Fraction of samples (%)	17.5	51.3	31.2	17.1	54.2	28.7
S (%) minimum	0.00	0.00	0.04	0.00	0.00	0.04
S (%) maximum	0.23	14.80	12.90	7.14	14.80	12.90
S (%) average	0.06	0.72	3.25	0.59	1.02	2.04

The scores and loadings of the PLS-DA classification model are presented in appendix A. The scores and loadings show that a relatively high abundance of alunite in the mineralogy maps of samples is a strong indicator of sulphide ore. To a lesser extent the sulphide ore samples are also associated with higher fractions of pyrite pixels. Oxide ore samples are mainly associated with a relatively high abundance of iron-oxide and more intense absorption features of water.

7.7.4. Comparison to the results on the initial sample set

It resulted from the analysis of VNIR-SWIR point spectra and hyperspectral images of the initial samples that carbonaceous samples can be distinguished by using the average reflection. However, Figure 7.29 showed that based on the VNIR-SWIR hyperspectral images of the drill core samples this is not possible and additional pixel classifications are required to distinguish between carbonaceous samples and dark quartzite. This indicates that the initial sample set is not fully representative of the Lagunas Norte deposit. This is also supported by the fact that different types of carbonaceous samples were identified from the drill core sample set, while in the initial sample set only carbonaceous siltstones were observed. Furthermore, visual inspection of both sample sets also showed much more variety between rock types in the drill core sample set than in the initial sample set.

When comparing the classification results of the drill core samples shown in Table 7.5 with that of the initial samples in Table 7.2 in chapter 7.5 and Table 7.4 in chapter 7.6, it can be observed that similar classification results are obtained considering the average gold and silver grades of the group of waste samples. The main difference is that the fraction of waste samples that can be segmented from the initial sample set is higher. This can be explained by the fact that the initial sample set contains more waste samples (74% vs 53%). This is also reflected by the average gold grade of the two sample sets, which is 0.26 ppm Au for the initial sample set and 0.76 ppm Au for the drill core sample set.

Another difference between the classification results of the initial samples and the drill core samples is that on the drill core sample set it was possible to use the VNIR-SWIR hyperspectral data to further separate the ore samples into a low grade and a high grade ore. Such a distinction into low and high grade ore could not be made on the initial sample set because the size of the sample set was too small to find additional relationships that are statistically significant. This shows that the sample set that is used for investigating sensor-based particle-by-particle sorting solutions should be large enough to be able to explore the full range of potential solutions.

The analysis of VNIR-SWIR point spectra and hyperspectral images of the initial sample set presented in chapter 7.5 and 7.6 showed that the detection of pyrophyllite and diaspore can be used as indicators of waste as long as zunyite is not detected as well. The result that pyrophyllite can be used as an indicator of waste was validated by the analysis of the VNIR-SWIR hyperspectral images of the drill core samples. If diaspore can also be used as an indicator of waste was not validated due to problems with absorption features produced by shadows of sample labels that prevented the mapping of diaspore from the VNIR-SWIR hyperspectral images of the drill core samples. The role of zunyite could also not be confirmed since occurrences of this mineral were mapped for only three samples with a maximum of 0.7% of the pixels. This shows that despite the fact that the drill core sample set is much larger and collected with the aim to represent the variability of the deposit as much as possible, it is still not fully representative of the entire deposit. Additional to the results obtained on the initial sample set, the analysis of the VNIR-SWIR hyperspectral images of the drill core samples showed that detected occurrences of dickite and illite can also be used as indicators of waste.

The analysis of VNIR hyperspectral images of the initial sample set showed that the fraction of pyrite pixels in the produced mineral maps can be used to distinguish sulphide ore. This was confirmed from the analysis of the VNIR hyperspectral images of the drill core samples. Furthermore, the results of the PLS-DA classification presented in section 7.7.3. showed that sulphide ore samples can be identified from a relatively high abundance of alunite in the mineralogy maps. The PLS-DA also showed that a relatively high abundance of iron-oxide and more intense absorption features of water in the mineralogy maps of samples can be used to segment a group of samples that are all oxide ore.

7.7.5. Discussion

PLS-DA proved to be an effective method for mapping mineral occurrences from the SWIR hyperspectral images as well as investigating the possibilities of using the information contained in the mineralogy maps to segment a population of waste samples and distinguish between oxide and sulphide ore. Considering the mineral mapping, PLS-DA is more robust and easier to use than the methods using Spectral Angle Mapping (SAM) or correlation coefficients that were applied in chapter 6.4. and 7.6. This is because the classifications are cross-validated and the classification results can be inspected to assess the performance of the model. Furthermore, the scores and loadings of the model can be inspected to validate that the classifications are

based on the absorption features of the minerals that are classified. PLS-DA does require a sufficiently large set of pre-classified reference spectra that can be used to calibrate a classification model. However, a set of reference spectra is also required when (SAM) or correlation coefficients are used.

When investigating the possibilities of using the information contained in the mineralogy maps to classify samples, PLS-DA has the advantage that by inspecting the scores and loadings it is relatively easy to identify the mineralogical differences on which the resulting classifications are based. It is important though that cross-validation is carried out properly to ensure that the model is not overfitting. Another advantage of PLS-DA is that the responses are calculated in such a way that the relative difference between the responses of the two classes is maximised. This means that when it is not possible to completely separate the classes, a threshold on the calculated responses can sometimes be selected that allows a fraction of the samples from one of the classes to be separated without including samples of the other class. This is especially helpful when investigating solutions for sensor-based particle-by-particle sorting of ore and waste since misclassification of the ore is not desired while it is usually sufficient if only a fraction of the waste material can be segmented. It would be possible to further refine the identification of waste by producing new classification models that are calibrated to discriminate only the fraction of waste samples that could be segmented in an initial PLS-DA classification. This was not performed here since the initial PLS-DA model already satisfied the aim of this study. The different mineral assemblages that were observed from the VNIR-SWIR hyperspectral images are characteristic for different zones of hydrothermal alteration within epithermal deposits (Sillitoe, 1993; Simmons et al., 2005; White & Hedenquist, 1995). The ability to segment a population of waste samples is therefore based on a relationship between gold mineralization and the formation of alteration minerals. This was expected since this relationship was also established in chapter 7.5 and 7.6.

It was discussed in section 7.7.3. that it was not possible to distinguish between SWIR spectral mixtures of illite and pyrophyllite and the SWIR spectrum of kaolinite. This is because the absorption features in the mixed spectrum of illite and pyrophyllite overlap with all the absorption features that are produced by kaolinite. Figure 7.37 showed that the lowest error rate for the validation set results if the PLS-DA model uses one LV and the PLS-DA loadings of this LV show that both illite and pyrophyllite are associated with waste samples. This indicates that if kaolinite actually occurs it is likely also associated with waste samples. This is because if this is not the case it would be expected that a lower error rate can be achieved if the PLS-DA was performed with additional LVs that distinguish between pure and mixed occurrences of pyrophyllite and illite.

Considering the classification on the sulphur content of samples, PLS-DA modelling provides better results than when only the fraction of pyrite pixels in the mineral map of a sample is used. As discussed in section 7.7.3, the PLS-DA loadings showed that the PLS-DA classification on the sulphur content is largely based on the relative abundance of alunite in the mineral map of a sample. This result can be explained by the fact that alunite is a sulphate and therefore contributes to higher sulphur contents. However, it is only the pyrite that occludes the gold when the ore is processed by cyanide leaching methods and the content of alunite therefore

does not influence gold recovery. It is therefore recommended to base the classification of ore types that was presented in Table 7.1 of chapter 7.2 on the actual gold recovery instead of the sulphur content. It is still likely though that the detection of pyrite from the VNIR hyperspectral images of the samples can be used to identify samples with a lower gold recovery since a lower recovery is associated with the occurrence of pyrite.

7.7.6. Conclusions

The following conclusions were drawn from testing VNIR-SWIR hyperspectral imagery on the drill core sample set:

- VNIR-SWIR hyperspectral imagery could be used to segment a population of waste samples. This is based on detecting specific alteration mineral assemblages.

- VNIR-SWIR hyperspectral imagery could be used to separate carbonaceous ore samples. This is based on the average reflection of the samples and on mapping the occurrence of pyrite and dark quartzite.

- VNIR-SWIR hyperspectral imagery could be used to segment a population of ore samples with a high sulphur content. This is based on mapping the absorption intensity of alunite and on mapping the occurrence of pyrite. However, relatively high sulphur contents might not be representative of refractory ore since alunite is a sulphate that does not affect gold recovery during cyanidation. The detection of pyrite might still be indicative of refractory ore.

- VNIR-SWIR hyperspectral imagery could be used to segment a population of oxide ore samples. This is based on mapping the absorption intensity of iron-oxide and water.

- PLS-DA is an effective technique for mapping mineral occurrences from VNIR-SWIR hyperspectral images.

- PLS-DA is an effective technique for investigating the possibilities of using the information contained in the mineralogy maps to classify samples on ore quality parameters.

- The results obtained from analysing VNIR-SWIR point spectra and hyperspectral images of the initial sample set correspond well to those obtained from analysing the VNIR-SWIR hyperspectral images of the drill core samples. However, for separating carbonaceous ore the VNIR-SWIR hyperspectral images of drill core samples showed that additional classification steps are required. Furthermore, it resulted from the VNIR-SWIR hyperspectral images of the drill core samples that additional minerals can be used as indicators of waste and that it is additionally possible to segment a population of oxide ore samples.

- The drill core sample set is probably still not fully representative of the mineralogical variability of the entire Lagunas Norte deposit. This was indicated by the fact that zuynite was often mapped from the VNIR-SWIR hyperspectral images of the initial samples while occurrences of this mineral were observed for only a few pixels in the mineral maps of 3 samples of the drill core sample set.

7.8. Discussion

Of all the sensors that were tested on the Lagunas Norte samples the VNIR-SWIR spectral sensor provides the best sorting opportunities. It was shown that by using this sensor it is possible to fulfil all the sorting objectives stated in chapter 7.2.3. Carbonaceous ore can be separated by using the average reflection on the VNIR-SWIR spectral range in combination with detecting occurrences of pyrite and quartzite. This is based on the fact that the carbon in the ore produces a relatively low reflection. Detecting the occurrences of pyrite and quartzite was used to distinguish the carbonaceous ore from quartzite with a low reflection.

A fraction of the sulphide ore can be segmented with a VNIR-SWIR spectral sensor by detecting the occurrence of pyrite. This can be explained by the fact that pyrite is an iron-sulphide mineral. In the oxide ore, the pyrite was converted to iron-oxides by the supergene oxidation stage that followed the formation of the deposit. Because of this, the detection of iron-oxides with a VNIR-SWIR spectral sensor can be used to segment a fraction of the oxide ore.

It also resulted that detected occurrences of alunite can be used as an indicator of sulphide ore. This can be explained by the fact that alunite is a sulphate and therefore contributes to higher sulphur contents. However, it is only the pyrite that occludes the gold when the ore is processed by cyanide leaching methods and the content of alunite does not influence gold recovery. It is therefore recommended to base the classification of ore types that was presented in Table 7.1 of chapter 7.2 on the actual gold recovery instead of the sulphur content.

The ability to segment a fraction of the waste with VNIR-SWIR spectral sensors was based on an indirect relationship between the detected hydrothermal alteration mineral assemblages and the gold grade. It resulted that detecting occurrences of pyrophyllite, diaspore, dickite and/or illite can be used as indicators of waste. Ore samples contain alunite, zunyite or no VNIR-SWIR-active alteration minerals at all. Additionally, the VNIR-SWIR spectra of ore samples often show absorption features of water that are most likely produced by fluid inclusions within quartz.

The paragenetic sequence presented in Figure 7.1 shows that the formation of pyrophyllite is not associated with gold mineralisation. However, this does not confirm that detecting the occurrence of pyrophyllite with a VNIR-SWIR spectral sensor can be used as an indicator of waste. This is because Figure 7.1 also shows that gold mineralisation occurred during later alteration events, which may have overprinted zones in which pyrophyllite was previously formed. It is possible though that the mineralising fluids of these later events have removed the previously formed pyrophyllite. Additional research is required to confirm this.

Figure 7.1 also shows that the formation of alunite and diaspore is associated with gold mineralisation. Concerning the alunite, this corresponds to the result of this study that ore samples contain alunite. However, that fact that the formation of diaspore is associated with gold mineralisation contradicts the result that diaspore can be used as an indicator of waste. It should be noted though that Figure 7.1 only presents temporal relationships and no spatial relationships. It is therefore still possible that no mineralisation of gold occurred in zones where diaspore was formed.

It was shown in Figure 4.3. in chapter 4.3. that the main ore zone at high-sulphidation epithermal deposits is closest to the epithermal veins. This figure also shows that further away from the veins the alteration mineralogy gradually changes from a vuggy quartz to quartz-alunite to dickite/kaolinite-pyrophyllite to smectite/mixed layer clay. This means that pyrophyllite, dickite and illite are deposited relatively far away from the main ore zone, which confirms that these minerals can be used as indicators of waste. The reason that alunite is associated with ore samples can be explained by the fact that this mineral is deposited closer to the epithermal veins (Sillitoe, 1993; Simmons et al., 2005). Furthermore, the result that an absence of VNIR-SWIR active minerals is associated with ore samples is probably because these samples originate from the zone that is closest to the epithermal veins, where no SWIR-active minerals were formed. The relationship between zunyite and ore grade could not confirmed by using the paragenetic sequence or general alteration-mineralisation relationships.

The LIBS sensor could also be used to segment waste by using the measured LIBS spectra as a chemical fingerprints of the alteration mineralogy. Direct detection of the gold grade of samples with this sensor was not possible. This is mainly caused by the relatively low gold grade and heterogeneous composition of the ore. It was also attempted to use LIBS to detect the sulphur contents of samples. However, this was unsuccessful since no peaks for sulphur were observed in the measured LIBS spectra. Using LIBS to identify carbonaceous ore samples was not performed.

The DE-XRT sensor could only be used to characterise the iron content and identify veins of iron-bearing minerals. Even though gold mineralisation was associated with the formation of iron-bearing minerals, the occurrence of iron-bearing minerals could not be used as an indicator of gold. This was confirmed by the work performed by Groenheide (2014), who tested the applicability of the DE-XRT to characterise the gold grade of a subset of the drill core samples. Furthermore, Bode (2014) tested the applicability of DE-XRT to distinguish between gold-bearing carbonaceous ore samples and barren carbonaceous samples, which was also unsuccessful.

Additional research is required to investigate whether it is economically feasible to use a VNIR-SWIR spectral sensor on sensor-based sorting machines to remove a fraction of the waste, separate a fraction of the sulphide ore, or separate carbonaceous and non-carbonaceous ores. For separating oxide and sulphide ore or carbonaceous and non-carbonaceous ores, this will depend on the costs of sorting, the efficiency of the sorting machine, and the economic benefits of processing the sorted ore types compared to the costs of processing mixed ore types. Considering the removal of waste, the economic feasibility of sensor-based sorting depends on the costs of sorting, the costs of conventional processing, the sorting efficiency, the amount

of waste that is rejected and the value of the gold that is contained by the waste. Sensor-based particle-by-particle sorting provides economic benefits if the value of the amount of gold and silver that are lost by discarding material do not exceed the difference in costs between sensor-based sorting and conventional ore processing.

Table 7.5 in chapter 7.7.3. shows that 16.3% of the samples can be rejected at an average gold grade of 0.06 ppm. This is a significant amount of material at a gold grade that is less than half of the economic cut-off grade of 0.20 ppm Au. Since sensor-based particle-by-particle sorting is generally cheaper than conventional processing methods (Buxton & Benndorf, 2013; Lessard et al., 2014; Salter & Wyatt, 1991; Sivamohan & Forssberg, 1991; Wills & Finch, 2016), this means there is potential that removing this waste with sensor-based sorting can provide economic benefits. The economic feasibility of sensor-based particle-by-particle sorting is influenced by the limitations of using VNIR-SWIR spectral sensors on sensor-based sorter machines that were discussed in chapter 6.5.

Table 7.5 shows that based on the drill hole data, only 7.5% of the samples can be rejected at an average gold grade of 0.08 ppm. This is a significant difference compared to the 16.3% of waste samples that could be distinguished from the subset of samples on which additional geochemical assays were performed. This indicates that the set of samples on which the assays were performed does not fully represent the mineralogical variability of the entire sample set. Since the entire sample set was collected with the aim to represent the mineralogical variability of the deposit as much as possible, the 7.5% of samples that is segmented according to the drill hole data is considered most representative for Lagunas Norte. The ability to reject 7.5% of the mined material at an average grade of 0.08 ppm Au still indicates that there is potential that removing waste with sensor-based particle-by-particle sorting can provide economic benefits.

Concerning representativity, the results obtained from the drill core sample set are likely more representative than those obtained from the initial sample set. The drill core sample set was also selected in such a way that the sample set would represent the variability of the deposit as much as possible. However, by comparing the results obtained with a VNIR-SWIR spectral sensor on both sample sets it was observed that the drill core samples are likely still not fully representative of the variability of the deposit. This mainly results from the fact that in the initial sample set samples occurred with a relatively high abundance of zunyite, while only very minor occurrences (< 0.7%) of zunyite were observed on samples in the drill core sample set. In order to acquire more representative results, it is recommended to use more drill core samples for testing the applicability of sensors. It is considered a good strategy to scan all the drill core that is acquired from a deposit with a VNIR-SWIR hyperspectral imager. This is because this data cannot only be used to assess sensor-based sorting opportunities, but can also be used to increase the understanding of how a deposit was formed and improve the deposit model.

7.9. Conclusions

The following conclusions were drawn from testing DE-XRT, LIBS and VNIR-SWIR spectral sensors on the samples from Lagunas Norte:

- The DE-XRT sensor could not be used to segment waste samples.

- A LIBS sensor could be used to segment a population of waste samples by using the LIBS spectra as chemical fingerprints of the alteration mineralogy. This was based on a relationship between the content of Al- and Ti-bearing alteration minerals and the gold grade of samples.

- VNIR-SWIR spectral sensors could be used to distinguish between different assemblages of hydrothermal alteration minerals of the ore samples collected from the Lagunas Norte epithermal gold-silver deposit.

- An indirect relationship is present between the gold grade of samples and the alteration mineralogy that could be detected with VNIR-SWIR spectral sensors. This indirect relationship is based on sample groups with different VNIR-SWIR active mineral assemblages that represent different zones of hydrothermal alteration and constitute different ranges of gold grades.

- VNIR-SWIR spectral sensors could be used to segment a population of waste samples. This was based on detecting specific alteration mineral assemblages.

- VNIR-SWIR spectral sensors could be used to separate carbonaceous ore samples. This was based on the average reflection of the samples and on detecting occurrences of pyrite and dark quartzite.

- VNIR-SWIR spectral sensors could be used to segment a population of ore samples with a high sulphur content. This was based on detecting occurrences of alunite and pyrite. However, relatively high sulphur contents might not be representative of refractory ore since alunite is a sulphate that does not affect gold recovery during cyanidation. The detection of pyrite is likely still indicative of refractory ore.

- VNIR-SWIR spectral sensors could be used to segment a population of oxide ore samples. This was based on mapping the absorption intensity of iron-oxide and water.

- Additional research is required to investigate whether it is economically feasible to use VNIR-SWIR spectral sensors on sensor-based sorting machines to remove a fraction of the waste, separate a fraction of the sulphide ore, or separate carbonaceous and non-carbonaceous ores.

- The drill core sample set is probably not fully representative of the mineralogical variability of the entire Lagunas Norte deposit. This was indicated by the fact that zuynite was often mapped from the VNIR-SWIR hyperspectral images of the initial samples while occurrences of this mineral were observed for only a few pixels in the mineral maps of 3 samples of the drill core sample set.

7.10. References

AITCHISON, J. 1986. The statistical analysis of compositional data.

AUSSPEC 2008. *G-MEX Spectral Interpretation Field manual*, AusSpec International ltd.

BALLABIO, D. 2013. *Classification toolbox* [Online]. Available: http://michem.disat.unimib.it/chm/download/softwares.htm [Accessed January 2015].

BARRICK. 2016a. *Annual report* [Online]. Available: http://www.barrick.com/investors/annual-report/default.aspx [Accessed July 2017].

BARRICK. 2016b. *Lagunas Norte Refractory Ore Mine Life Extension* [Online]. Available: http://www.barrick.com/investors/news/news-details/2016/Barrick-Reports-Project-Study-Results-022216/default.aspx [Accessed May 2017].

BARRICK. 2016c. *Mineral reserves and mineral resources* [Online]. Available: http://www.barrick.com/investors/quarterly-reports/default.aspx [Accessed July 2017].

BODE, D. C. 2014. Characterisation of carbonaceous Au ores with dual energy X-ray transmission. *BSc thesis TU Delft*.

BUXTON, M. & BENNDORF, J. 2013. The use of sensor derived data in optimization along the Mine-Value-Chain. *Proceedings of the 15th International ISM Congress*, Aachen, Germany, pp. 324-336.

CERPA, L. M., BISSIG, T., KYSER, K., MCEWAN, C., MACASSI, A. & RIOS, H. W. 2013. Lithologic controls on mineralization at the Lagunas Norte high-sulfidation epithermal gold deposit, northern Peru. *Mineralium Deposita*, 48, 653-673.

CLARK, R. N., SWAYZE, G. A., WISE, R., LIVO, E., HOEFEN, T., KOKALY, R. & SUTLEY, S. J. 2007. *USGS digital spectral library splib06a: U.S. Geological Survey, Digital Data Series 231* [Online]. Available: https://speclab.cr.usgs.gov/spectral-lib.html [Accessed January 2012].

GROENHEIDE, S. 2014. Characterisation of gold ores with Dual Energy X-Ray Transmission (DE-XRT). *BSc thesis TU Delft*.

HARMON, R. S., RUSSO, R. E. & HARK, R. R. 2013. Applications of laser-induced breakdown spectroscopy for geochemical and environmental analysis: A comprehensive review. *Spectrochimica Acta Part B: Atomic Spectroscopy,* 87, 11-26.

HUNT, G. R. 1977. Spectral signatures of particulate minerals in the visible and near infrared. *Geophysics*, 42, 501-513.

HUNT, G. R., SALISBURY, J. W. & LENHOFF, C. J. 1971a. Visible and near-infrared spectra of minerals and rocks: III. Oxides and hydroxides. *Modern Geology*, 2, 195-205.

HUNT, G. R., SALISBURY, J. W. & LENHOFF, C. J. 1971b. Visible and near infrared spectra of minerals and rocks. IV. Sulphides and sulphates. *Modern geology*, 3, 1-14.

LECO. 2015. *LECO Carbon / Sulphur analyzers* [Online]. Available: https://www.leco.com/products/analytical-sciences/carbon-sulfur-analyzers [Accessed May 2015].

LESSARD, J., DE BAKKER, J. & MCHUGH, L. 2014. Development of ore sorting and its impact on mineral processing economics. *Minerals Engineering*, 65, 88-97.

MARTÍN-FERNÁNDEZ, J. A., BARCELÓ-VIDAL, C. & PAWLOWSKY-GLAHN, V. 2003. Dealing with zeros and missing values in compositional data sets using nonparametric imputation. *Mathematical Geology*, 35, 253-278.

MARTIN, W. & WIESE, W. 2006. Atomic spectroscopy. *Springer Handbook of Atomic, Molecular, and Optical Physics*. Springer.

MONTGOMERY, A. T. 2012. Metallogenetic controls on Miocene high-sulphidation epithermal gold mineralization, Alto Chicama district, La Libertad, northern Perú. *PhD thesis Queen's University (Canada)*.

NIST. 2015. *NIST atomic spectra database* [Online]. Available: https://www.nist.gov/pml/atomic-spectra-database [Accessed May 2015].

POŘÍZKA, P., DEMIDOV, A., KAISER, J., KEIVANIAN, J., GORNUSHKIN, I., PANNE, U. & RIEDEL, J. 2014. Laser-induced breakdown spectroscopy for in situ qualitative and quantitative analysis of mineral ores. *Spectrochimica Acta Part B: Atomic Spectroscopy*, 101, 155-163.

RADZIEMSKI, L. J. & CREMERS, D. A. 2006. *Handbook of laser induced breakdown spectroscopy.* John Wiley & Sons.

RPA. 2012. *Technical report on the Lagunas Norte mine* [Online]. Available: https://www.sec.gov/Archives/edgar/data/756894/000119312512137647/d323919dex991.htm [Accessed May 2017].

SALTER, J. & WYATT, N. 1991. Sorting in the minerals industry: past, present and future. *Minerals Engineering*, 4, 779-796.

SILLITOE, R. 1993. Epithermal models: genetic types, geometrical controls and shallow features. *Mineral Deposit Modeling: Geological Association of Canada Special Paper*, 40, 403-417.

SIMMONS, S. F., WHITE, N. C. & JOHN, D. A. 2005. Geological characteristics of epithermal precious and base metal deposits. *Economic Geology 100th anniversary volume*, 29, 485-522.

SIVAMOHAN, R. & FORSSBERG, E. 1991. Electronic sorting and other preconcentration methods. *Minerals Engineering*, 4, 797-814.

SJÖSTRÖM, M., WOLD, S. & SÖDERSTRÖM, B. 1986. PLS discriminant plots. *Pattern recognition in practice II*, pp. 461-470.

WHITE, N. C. & HEDENQUIST, J. W. 1995. Epithermal gold deposits: styles, characteristics and exploration. *SEG newsletter*, 23, 9-13.

WILLS, B. A. & FINCH, J. A. 2016. Chapter 14 - Sensor-based Ore Sorting. *Wills' Mineral Processing Technology (Eighth Edition)*. Boston: Butterworth-Heinemann.

WINDIG, W. & GUILMENT, J. 1991. Interactive self-modeling mixture analysis. *Analytical chemistry*, 63, 1425-1432.

YAROSHCHYK, P. & EBERHARDT, J. E. 2014. Automatic correction of continuum background in Laser-induced Breakdown Spectroscopy using a model-free algorithm. *Spectrochimica Acta Part B: Atomic Spectroscopy*, 99, 138-149.

Cortez Hills Carlin-type gold deposit

8.1. Introduction

The Cortez mine is a gold mining district that is located 100 kilometres southwest of Elko, Nevada, USA. The mining district consists of the Pipeline open pit mine and the Cortez Hills open pit and underground mine. The Cortez mining district is fully owned and operated by Barrick gold. The yearly production was 1.06 million ounces of gold during 2016 (Barrick, 2016a). Proven and probable reserves are currently 151 Mt of ore at an average grade of 2.11 g/t Au (Barrick, 2016b).

Operations at Cortez include traditional truck and shovel mining in the Pipeline and Cortez Hills open pit operations. In the Cortez Hills underground mine a cut and fill mining method is used. Ore treatment is performed using three different processing streams. Carbonaceous and sulphidic refractory ores are transported to the Goldstrike property for processing in either the roaster or the pressure oxidation circuit. High grade oxide ore is processed in the Cortez processing facility. This facility consists of a crusher, Semi-Autogenous Grinding (SAG) mill, ball mill, grind thickener, a Carbon-In-Column (CIC) circuit for the grind thickener overflow, a Carbon-In-Leach (CIL) circuit, tailings counter-current-decantation wash thickener circuit, carbon stripping and reactivation circuits and a refinery to produce gold doré. Low grade oxide ore is crushed and processed by heap leaching. The pregnant solution from the heap leach is fed to the CIC circuit of the Cortez processing facility.

The Cortez Hills deposit is subdivided into a Breccia zone, Middle zone and Lower zone. Figure 8.1 shows how these different zones are spatially distributed. This figure also shows the location of the Cortez Hills open pit. The research described in this chapter is focussed on the Lower zone of the Cortez Hills deposit that will be mined in the underground operation.

Figure 8.1: Distribution of the different zones of the Cortez Hills deposit (based on Barrick, 2015). Length of the lower zone is around 1200 m.

8.2. Study description

8.2.1. Geologic setting

This section provides a brief overview of the main characteristics of the Cortez Hills Lower zone deposit. A more extensive description of the geology of the Cortez Hills Lower zone is presented by Arbonies et al. (2010).

The Cortez Hills Lower zone deposit is a Carlin-type gold deposit in which mineralisation is structurally controlled and related to a complex interaction between high-angle faulting, low-angle faulting, folding and porphyry dike intrusion (Arbonies et al., 2010). The most prominent structural control is the Pondorosa fault zone, which is a large low-angle thrust fault that transects the Hanson Creek, Roberts Mountains and Wenban formations. The Hanson Creek formation is of Ordovician age and consists of three principle units; a fine grained crystalline dolomite containing moderate carbon, a highly bioturbated micrite deposited in a lagoon setting, and a massive dolomite characterised by a crackle breccia texture (Arbonies et al., 2010). The Roberts Mountains formation is of Silurian age and comprises a uniformly thinly laminated, planar bedded, silty limestone deposited in a deep continental slope setting. The Wenban formation is of Devonian age and is a silty micrite deposited on the continental slope (Arbonies et al., 2010; Maroun et al., 2017).

Three major alteration phases have occurred at the Cortez Hills Lower zone deposit. The first phase is contact metamorphism, which occurred during the Mesozoic and is probably related to the emplacement of the Jurassic Mill Canyon Stock (Arbonies et al., 2010; Maroun et al., 2017). It resulted in the widespread formation of tremolite porphyroblasts in recrystallized carbonate rocks and is accompanied by sparse base metal sulphide veins including chalcopyrite, sphalerite and galena. The second alteration phase is Eocene-aged hydrothermal alteration that mainly includes sulphidation, decarbonatisation, variable silicification and late calcite flooding (Arbonies et al., 2010; Maroun et al., 2017). Gold mineralisation is associated with all these hydrothermal alteration events and occurs as solid solution within arsenian rims on hydrothermal pyrite.
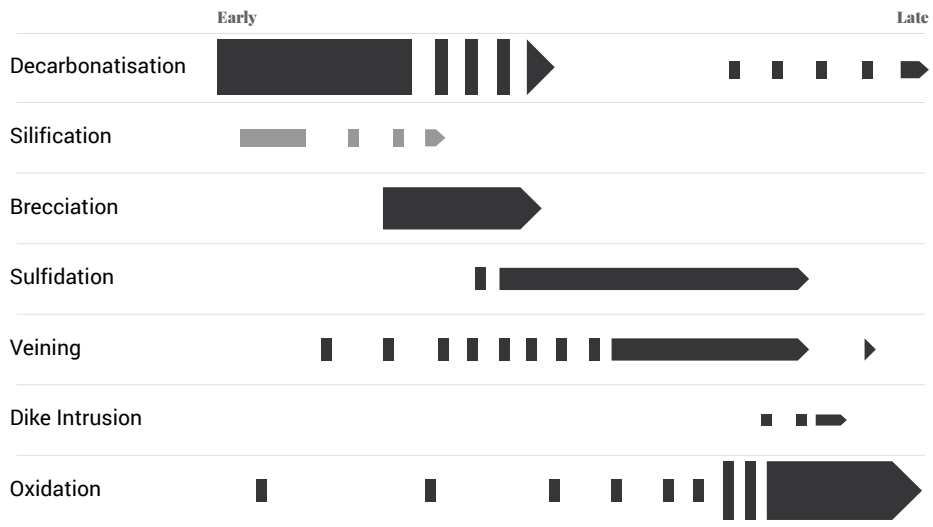
Figure 8.2: Relative timing and paragenetic relationships between alteration events at the Cortez Hills Lower zone deposit (based on Arbonies et al., 2010).

The final alteration phase is supergene alteration and oxidation which occurred during the Miocene to post-Miocene and is related to deep, convection-driven circulation of meteoric hydrothermal fluids (Arbonies et al., 2010; Maroun et al., 2017). During this phase also quartz porphyry dikes were introduced into the Cortez Hills Lower zone deposit, which do not host significant gold mineralisation. The supergene oxidation is mainly characterised by the conversion of iron-sulphides to hematite, jarosite and goethite. Supergene oxidation is present at depths up to 1000 metres below the surface and mainly affected the southern part of the Cortez Hills Lower zone deposit (Arbonies et al., 2010). Figure 8.2 presents the relative timing and paragenetic relationships between the alteration events that occurred at the Cortez Hills Lower zone deposit. Figure 8.3 shows the mineral paragenesis at the Cortez Hills deposit. Minerals marked pink on this figure were only observed for the Breccia zone of the deposit, and not for the Lower zone (Maroun et al., 2017).
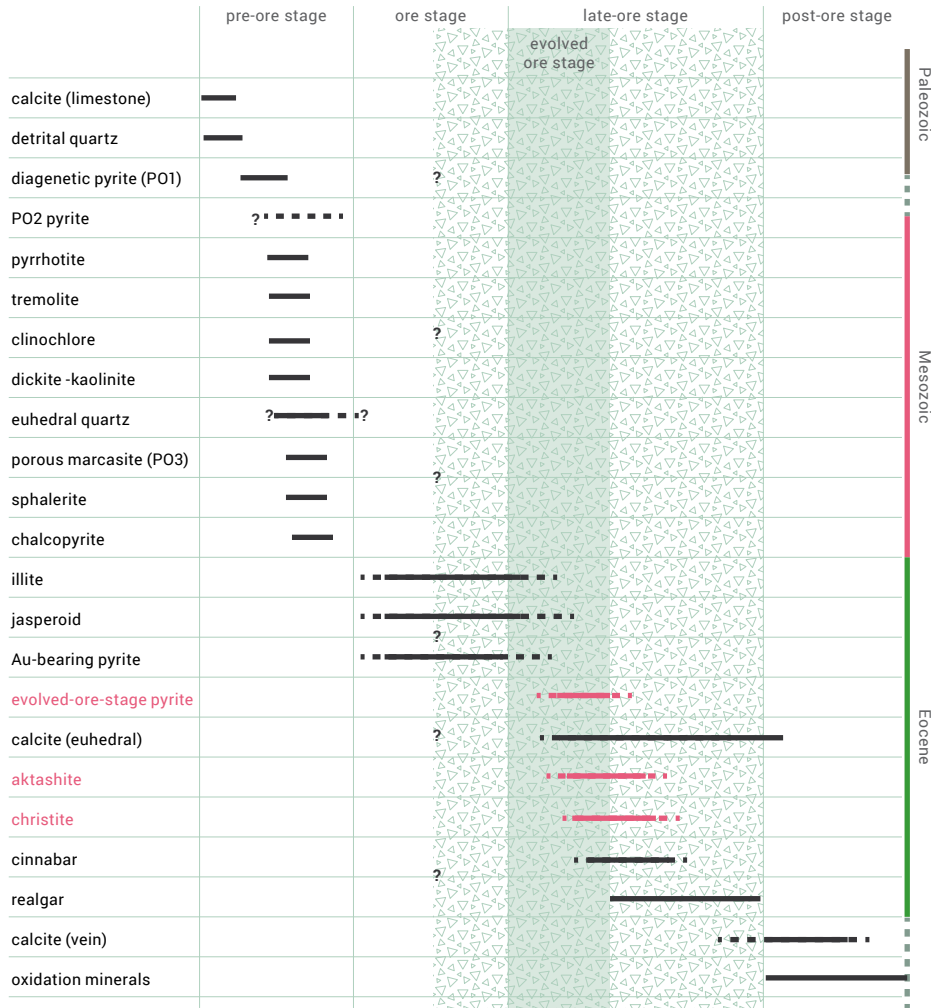
Figure 8.3: Mineral paragenesis at the Cortez Hills deposit (based on Maroun et al., 2017). The formation of evolved-ore-stage pyrite, aktashite, and christite (marked pink) were only observed in the Breccia zone, and not the Lower zone of the deposit (Maroun et al., 2017).

8.2.2. Samples

The research described in this chapter is based on 629 drill core particles of about 5 – 20 cm long. Each individual drill core particle represents a sample. The diameter of the drill core that was sampled is 6.5 cm. Figure 8.4 presents an example of some of the samples in the sample set.

Figure 8.4: Example of drill core samples.

509 of the drill core particles that were collected were previously used as density samples by the geotechnical department of the Cortez mine and were covered in wax. These were whole drill core particles that were splitted in halves along the longitudinal axis after the wax was removed. Splitting the samples was done to create a surface that is not contaminated by wax on which the sensor measurements could be performed.

The geotechnical department of the mine collected the density samples at around 15 m intervals from every drill hole. The density samples used in the study were taken from 41 different drill holes. These drill holes were selected in such a way that the sample set represents the variability of the deposit as much as possible. The drill holes from which the samples were selected were drilled from the exploration drift that is indicated by the pink line in Figure 8.5. The drill holes that were selected for sampling are indicated by the pink colour on Figure 8.6. This figure shows that more drill holes were sampled in the southern part of the deposit than in the northern part. The reason for this is that the density samples of these drill holes were more easily accessible. Figure 8.7 presents a cross section of the geology of the deposit on which the ore shell shown in Figure 8.5 is also indicated.
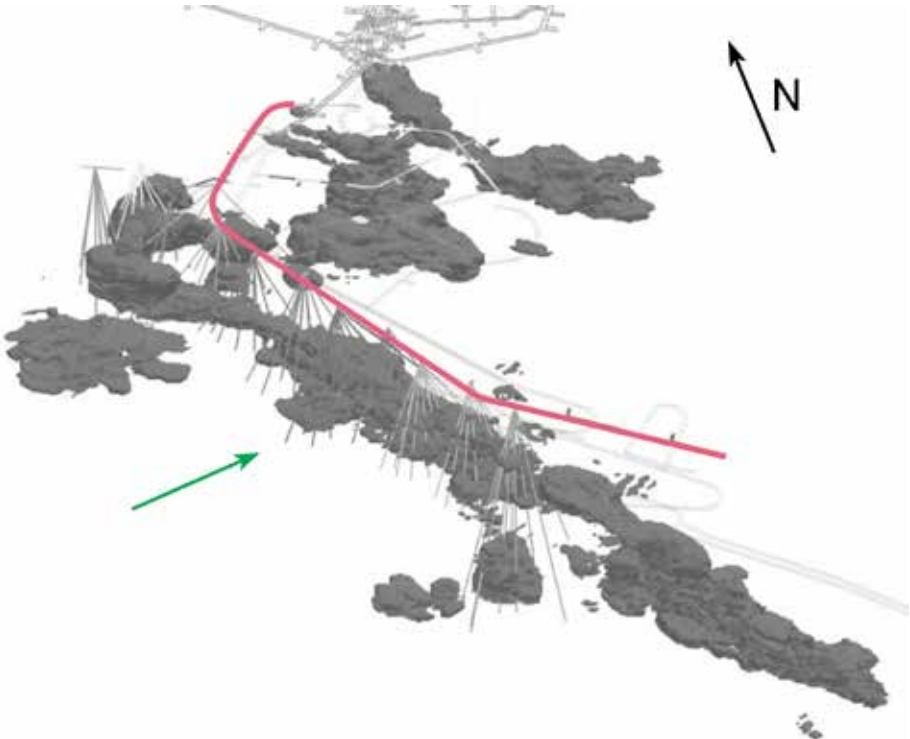

Figure 8.5: > 3.1 ppm Au ore shell of the Cortez Hills Middle and Lower zone deposit (based on Arbonies et al., 2010). The pink line indicates the exploration drift from which the exploration drill holes were drilled. The green arrow indicates the viewing direction of Figure 8.6 and Figure 8.7.
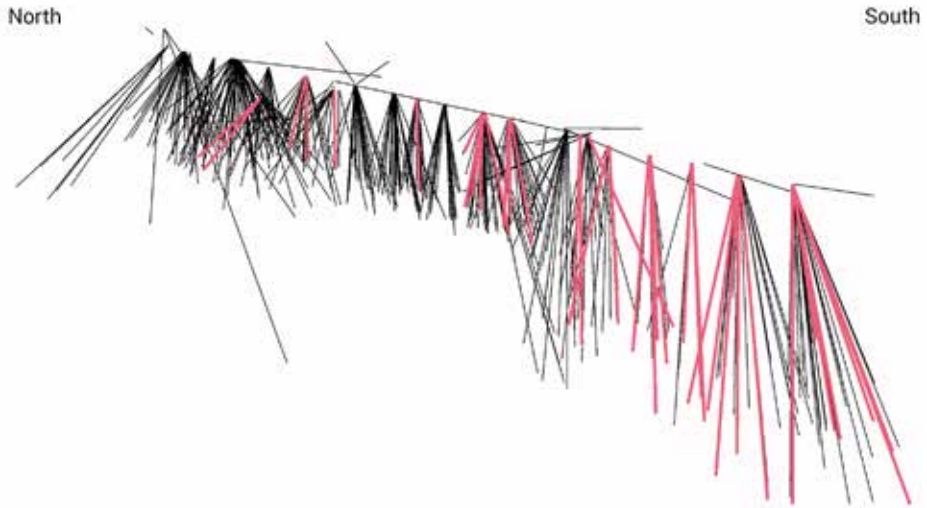
Figure 8.6: Schematic overview of the distribution of exploration drill holes in the Cortez Hills Lower zone deposit. Holes were drilled from the exploration drift indicated by the pink line in Figure 8.5. The pink colour indicates drill holes that were selected for sampling. The viewing direction of the figure is indicated by the green arrow in Figure 8.5.
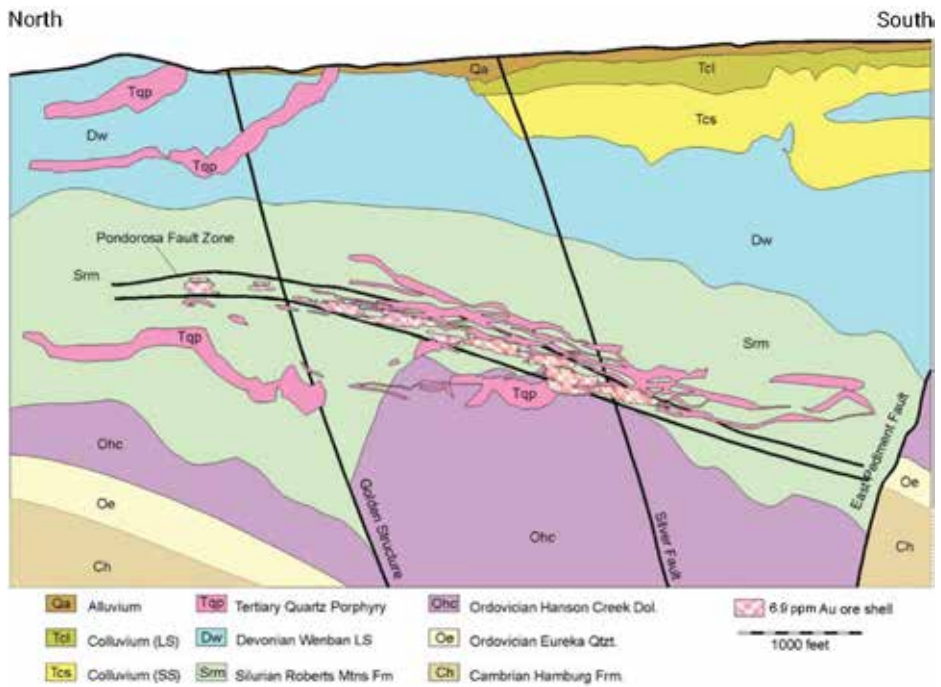

Figure 8.7: Cross section through the Cortez deposit showing the distribution of lithologies, locations of faults and the > 6.9 ppm Au ore shell (Arbonies et al., 2010). The viewing direction of the figure is indicated by the green arrow in Figure 8.5.

Apart from the density samples, 120 additional drill core particles were collected from half of the splitted drill core of five different drill holes. The other half of the drill core was used for geochemical analyses by the exploration department of the mine and no longer available. The density samples of the five drill holes from which the additional drill core particles were taken were also included in the sample set. The reason for collecting additional drill core particles was to include samples that were taken at shorter intervals than the 15 m intervals that on which the density samples were collected. The additional samples were collected at around 1 -3 m intervals and the selection was based on capturing the observed variability of the drill core as much as possible.

8.2.3. Objectives

The aim of the Cortez study was to investigate the opportunities for sensor-based parti-cle-by-particle sorting at this mine. This was focussed at researching the applicability of real-time sensors to segment waste from ore and to distinguish between different ore types. Only the applicability of using real-time sensors to characterise ore particles was investigated. The feasibility of using sensor-based sorting machines to sort the ore is out of scope.

Figure 8.8 presents an overview of the ore routing that is used at Cortez. The routing of ores produced from the underground mine actually only includes the grey part of the overview shown in this figure. This is because in the underground mine an entire stope is classified as one ore type and the ore routing shown in Figure 8.8 is used for all material that is produced from this stope. No waste or heap leach material is produced because all the stopes are within the ore zone of the deposit. However, at a particle size on which sensor-based particle-by-par-ticle sorting can be performed it is likely that some of the particles are actually waste or heap leach material according to Figure 8.8. Because of this, it was investigated if real-time sensors can be used to segment waste and/or heap leach material from the ore that is produced from the underground mine. Figure 8.8 shows that classification of waste is based on a cut-off grade of 0.15 ppm Au and classification of heap leach material is based on a cut-off grade of 5.14 ppm Au. These cut-off grades are based on the economics of the different ore processing methods.

Figure 8.8 shows that the main distinction between ore types is based on the gold recovery. Ores with a gold recovery above 50% are classified as oxide ore and ores with a recovery below 50% as refractory ore. The term refractory refers to carbonaceous and sulphidic ore types. As with the Lagunas Norte study, carbonaceous ores produce a relatively low recovery due to preg-robbing. The sulphide ore has a lower recovery than the oxide ore because it was not affected by the supergene oxidation stage that took place after the gold was deposited. It was discussed in section 8.2.1. that most of the gold was originally deposited within pyrite, which occludes the gold when the ore is processed by cyanide leaching methods. The result of the supergene oxidation is that the pyrite is oxidised, which liberated the gold and made it more amenable to cyanide leaching.

The gold recovery from the refractory ore is increased by using the autoclave or roaster to oxidise the sulphide ore and burn carbonaceous materials prior to cyanide leaching. However, this also increases the ore processing costs. Processing costs are further increased because the refractory ore needs to be transported by truck to the autoclave or roaster at the Goldstrike property, which is located 130 km from the Cortez Hills underground mine. Because of the higher processing costs, it was investigated if real-time sensors can be used to distinguish between oxide and refractory ore.

Figure 8.8 shows that the classification of ore types is also based on the arsenic content. This is because arsenic is a toxic element and there is a lower risk of atmospheric arsenic pollution when ore with high arsenic contents is processed in an autoclave instead of a roaster (Afenya, 1991). The costs of processing the ore using an autoclave are higher than when a roaster is used. Because of this, it was initially also one of the objectives to investigate if real-time sensors can be used to distinguish between ore with a low or high arsenic content. However, based on the available geochemical data only 10 samples occurred in the entire sample set that have arsenic contents > 1200 ppm. Since this number of samples was considered too small to produce statistically significant classifications, this objective was not pursued.

Based on the ore routing presented in Figure 8.8, the objectives of the Cortez study are to use real-time sensor data to:

• Segment a population of samples that all have gold grades below 0.15 ppm.

• Segment a population of samples that all have gold grades below 5.14 ppm.

• Distinguish samples with a gold recovery above or below 50%.

It is not necessarily needed to segment all samples that contain less than 0.15 ppm Au or 5.14 ppm Au since sensor-based particle-by-particle sorting can already provide economic benefits if a significant fraction of the waste or heap leach material can be separated.
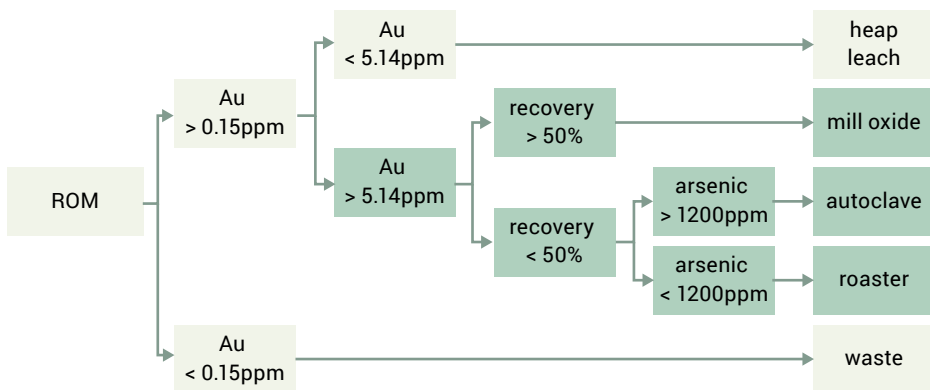

Figure 8.8: Ore routing at Cortez. ROM stands for run of the mine material.

8.2.4. Geochemistry

Two types of geochemical datasets were available on the samples. First of all, geochemical analyses were performed on drill core sections of 1.5 – 3 m long by the exploration department of the mine. This data was linked to the samples based on the interval from which a sample was taken. This geochemical dataset will be referred to as the drill hole data. It should be noted that the drill hole data is not fully representative of the samples since the samples are much smaller than the interval on which the drill hole data was collected. The drill hole data included gold grade by fire assay, gold grade by cyanide leach test, and the contents of Ag, As, Ca, Cu, Hg, Mg, S and Sb determined aqua regia digestion follow by ICP-AES. The gold recovery of samples was determined by calculating the ratio between the gold that is extracted by the cyanide leach test and the gold content determined by fire assay. Cyanide leach tests were performed on 293 samples out of the 629 samples. Selection of the assayed intervals was based on the gold grade and the interpretation of the mine geologists. Finally, the drill hole data also contained a classification of lithology that was performed by the mine geologists.

Because the drill hole dataset was not fully representative of the samples, additional geochemical analyses were performed on 210 drill core samples after the real-time sensor data was collected. The analyses included fire assay followed by AAS for determining gold grades, a cyanide leach test to determine gold recovery, and aqua regia digestion followed by ICP-AES to determine whole rock geochemistry. For the additional assays cyanide leach tests were only performed on samples on which the gold content determined by fire assay > 0.1 ppm. Gold recovery data was therefore available for 124 samples on which additional assays were performed. The additional geochemical assays were performed by Bureau Veritas in Ankara, Turkey. The drill hole data of the 210 samples on which the additional assays were performed was replaced by the results of these assays. Additionally, XRD was performed at TU Delft to determine the mineralogy of 9 samples.

8.3. VNIR–SWIR hyper–spectral imagery

8.3.1. Introduction

As described in chapter 3.3, spectral reflectance measurements on the SWIR spectral range can be used to detect minerals produced by hydrothermal alteration. Chapters 6 and 7 showed that the detection of alteration minerals from VNIR-SWIR spectral reflectance data can be used to segment waste samples from a porphyry copper deposit and from an epithermal gold-silver deposit. It was explained in chapter 4.4. that mineralisation-alteration relationships at Carlin-type gold deposits are usually irregular since the reactions that formed Au-bearing pyrite are generally not the same as the ones that formed the alteration minerals. However, it might still be possible that certain alteration minerals can be used as indicators of waste. VNIR-SWIR hyper-spectral imagery data was therefore acquired on all 629 samples in order to investigate if this type of data allows waste samples and low grade ore samples to be segmented. Low grade ore refers in this case to the classification of heap leach material according to Figure 8.8. It was also investigated if the VNIR-SWIR spectral reflectance data can be used to distinguish between the gold recovery of samples. The thresholds used to classify the samples on gold grade and gold recovery were presented in chapter 8.2.3.

8.3.2. Methods

Data acquisition

VNIR-SWIR hyperspectral images of all the samples within core trays were collected with a Sisu-Rock instrument (SPECIM ltd., Oulu, Finland). The hyperspectral images were acquired simultaneously with those used in the Lagunas Norte study presented in chapter 7.7. This means that the hyperspectral images were recorded on a 380-2500 nm spectral range by using two hyperspectral cameras. The spectral resolution of the images is around 6 nm on the 380-975 nm range and around 10 nm on the 975-2500 nm range. The pixel size of the images is around 2 mm.

As with the Lagunas Norte study, some of the pixel spectra of the samples are contaminated with absorption features that are produced by shadows of the plastic sample labels within the core trays. These sample labels are clearly visible in the photograph in Figure 8.4. The absorption effects produced by the shadows could not be corrected. Furthermore, pixel spectra that

are contaminated with absorption features of wax occurred on some of the samples. This is because the wax that filled the fractures in some of the samples was not always properly removed.

Image (pre-)processing

The pre-processing that was performed on the VNIR-SWIR hyperspectral images of the Cortez samples was exactly the same as the pre-processing performed on the VNIR-SWIR hyperspectral images of the Lagunas Norte drill core samples that was described in chapter 7.7.2. For mapping the mineralogy from the VNIR hyperspectral images also the same as the procedure was followed as the one described in chapter 7.7.2. The only difference was that no pyrite was mapped from the VNIR-SWIR hyperspectral images of the Cortez samples because pyrite spectra were not observed in these images. Furthermore, 451 iron-oxide spectra were added to the set of 389 iron-oxide reference spectra that were already collected from the Lagunas Norte samples. This was because differences were observed between the iron-oxide spectra measured on the Lagunas Norte samples and those measured on the Cortez samples. The pixel spectra of the VNIR hyperspectral images were classified as iron-oxide if the correlation coefficient to one of the iron-oxide reference spectra was ≥ 0.90. Calculating the absorption intensity and minimum position of the iron-oxide absorption feature that occurs around 900 nm was performed by following the procedure described in chapter 7.7.2.

For mapping the mineralogy from the SWIR hyperspectral images also the same procedure was followed as the one used in the Lagunas Norte study. The set of mineral reference spectra used for mapping the mineralogy from the SWIR hyperspectral images of the Cortez samples consisted of 396 different SWIR spectra and included spectra that are contaminated with absorption features of wax or the sample labels. Additional to calculating the absorption intensity of some of the minerals that were mapped, the exact minimum position of selected absorption features was calculated. This is because for some of the SWIR-active minerals that were identified the minimum position of a specific absorption feature reflects differences in mineral composition. Similar to the calculation of the absorption intensity and minimum position of the iron-oxide absorption feature, a Gaussian was fitted to the mineral absorptions before calculating these properties. This was performed to reduce the influence of spectral noise on the calculated properties. This was needed because some of the samples from Cortez are relatively dark and the mineral spectra are therefore sometimes noisy. Wavelength positions of absorption features and absorption intensities > 0 were only calculated if the mineral that produces the absorption feature was classified from a pixel spectrum with the corresponding PLS-DA classification model. As with the Lagunas Norte study presented in chapter 7.7, also the absorption intensity of the water feature that occurs around 1900 nm was calculated by finding the absorption minimum on the 1850-2100 nm range. Additionally, the average reflection on the entire VNIR-SWIR spectral range was calculated for each pixel in the hyperspectral images.

The procedure described in chapter 7.7.2. that was used to identify carbonaceous ore samples from the VNIR-SWIR hyperspectral images of the Lagunas Norte samples was not applied to

the hyperspectral images of the Cortez samples. This is because no geochemical dataset was available that could be used to reliably validate the classification of carbonaceous ores.

Classification of samples

As with the Lagunas Norte study presented in chapter 7.7, PLS-DA was applied to investigate whether the information contained in the mineralogy maps can be used to segment a population of waste samples and distinguish between oxide and refractory ore. Because the drill hole data is not fully representative of the samples, the ore-waste and oxide-refractory ore designations used to produce the PLS-DA classifications were based on the sample assays. This means that the PLS-DA classification models are produced on a subset of the entire sample set. The drill hole assay data was used to validate the classification models.

The PLS-DA classifications were based on a data matrix containing the relative abundance of each of the identified minerals in the mineralogy maps of every sample. For minerals for which the absorption intensity was characterised also the cumulative distribution of the absorption intensity was added to the data matrix. This was performed by calculating the fraction of pixels with absorption intensities above certain thresholds. Chosen thresholds ranged from 0 to 1 with increments of 0.05. Furthermore, the distribution of the minimum position of the absorption feature of iron-oxide and several SWIR-active minerals was added to the data matrix by first binning the minimum locations and then calculating the fraction of pixels within each bin. The bin size used for calculating this distribution was 20 nm for iron-oxide and 5 nm for the SWIR-active minerals. Because the distributions of absorption feature minimum positions sum up to a constant (i.e. 100%), a multiplicative zero replacement followed by a centred log-ratio transformation was applied to this data (Aitchison, 1986; Martín-Fernández et al., 2003). Additionally, the average absorption intensity of the water feature and the distribution of the average reflection of pixels was added to the data matrix on which PLS-DA was performed. The PLS-DA procedure for the classification of samples was the same as the one presented in chapter 7.7.2.

8.3.3. Results

Minerals identified from VNIR–SWIR hyperspectral images

Figure 8.9 presents an overview of the measured SWIR spectra of all the different minerals that were determined on the drill core samples with VNIR-SWIR hyperspectral imagery. This figure also shows a spectrum of wax and a sample label that sometimes contaminated the mineral spectra that were measured on the samples. All spectra in Figure 8.9 match those of single minerals except for phlogopite (e.g. AusSpec, 2008; Clark et al., 2007). The SWIR spectrum of phlogopite that is shown in Figure 8.9 is mixed with chlorite. Phlogopite was identified from the additional absorption features in the chlorite spectrum that occur around 1380 and 2380 nm.

Figure 8.9 shows that the SWIR spectra of some of the minerals that were identified are relatively similar. Calcite and dolomite for example both produce an absorption feature around

2325 nm. These minerals can be distinguished from each other by inspecting the exact minimum position of this absorption feature. The minimum position of calcite usually occurs
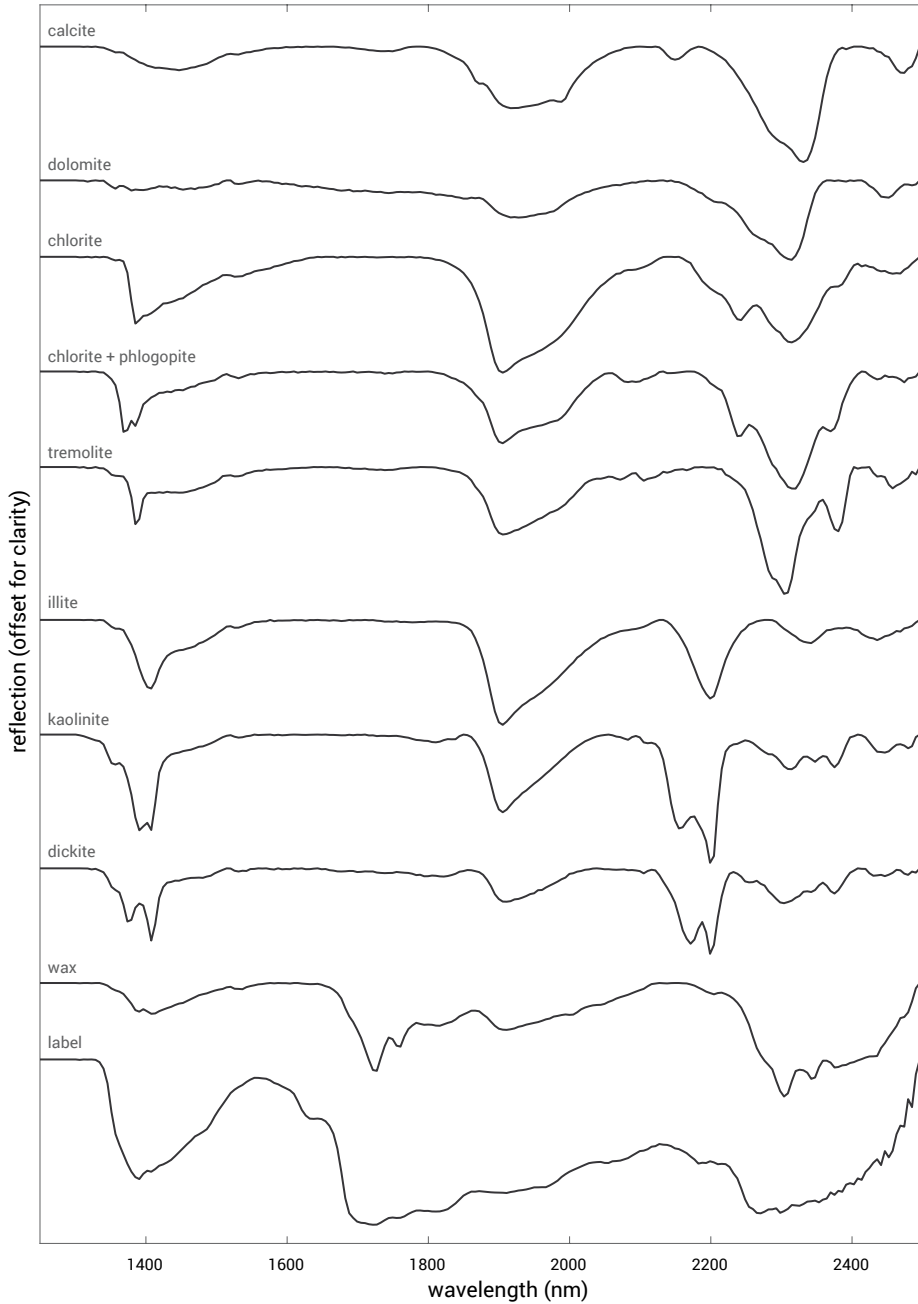

Figure 8.9: Examples of measured SWIR mineral spectra (hull quotient corrected).

around 2325-2335 nm and that of dolomite around 2315-2325 nm. This is slightly different than the calcite and dolomite spectra presented by AusSpec (2008) and Hunt & Salisbury (1971), who report minimum positions around 2340-2350 nm for calcite and around 2320-2340 nm for dolomite. However, the calcite-dolomite SWIR spectra with absorption features around 2325-2335 nm were classified as calcite since XRD showed that this is more accurate.

Apart from calcite and dolomite, also the spectra of kaolinite and dickite are relatively similar. Both these mineral produce a double absorption feature, or doublet, around 2200 and 1400 nm. The minimum position of the absorption feature that forms the right part (longest wavelength) of each doublet is the same for both minerals (AusSpec, 2008). Kaolinite and dickite can be distinguished from each other by inspecting the exact minimum position of the absorption feature that forms the left part (shortest wavelength) of each doublet. For kaolinite this feature usually occurs around 1400 and 2160 nm, while for dickite it occurs around 1385 and 2180 nm (AusSpec, 2008).

The SWIR pixel spectra sometimes contain absorption features of 2 or 3 different minerals. From the VNIR region of the pixel spectra only iron-oxide was classified. An example of an iron-oxide spectrum was shown in Figure 7.32. Some of the VNIR or SWIR pixel spectra also contained no characteristic absorptions, indicating an absence of SWIR-active or iron-bearing minerals.

The occurrence of all minerals that were identified with VNIR-SWIR hyperspectral imagery was validated by XRD. Unlike the Lagunas Norte study, XRD could be used to validate the mineral occurrences on the same samples on which they were identified with VNIR-SWIR hyperspectral imagery.

Classification of SWIR spectra

PLS-DA classification models were calibrated on the 396 SWIR mineral reference spectra to classify the occurrence of carbonate, chlorite, kaolinite-dickite, illite, chlorite+phlogopite, and tremolite. Carbonate represents in this case calcite and dolomite. The spectra of calcite and dolomite were combined for calibrating PLS-DA classification models because it was in some cases very difficult to distinguish between the SWIR spectra of these minerals due to a low signal-to-noise. Unsatisfying classification results were also obtained when attempting to distinguish between calcite and dolomite spectra by using PLS-DA. Distinguishing between calcite and dolomite was performed after the PLS-DA classification by calculating the exact minimum position of the absorption feature that occurs around 2325 nm. The spectra of kaolinite and dickite were also combined for calibrating PLS-DA classification models. The main reason for doing this was that unsatisfying classification results were obtained when using PLS-DA to distinguish between the spectra of these minerals. Distinguishing between kaolinite and dickite was performed after the PLS-DA classification by calculating the exact minimum position of the shorter wavelength absorption feature of the doublet that occurs around 2200 nm.

Because of overlapping absorption features the occurrence of carbonate could not be excluded from the SWIR spectra of chlorite, chlorite+phlogopite and tremolite. These spectra were

therefore assigned to the class of spectra containing carbonate features when calibrating the PLS-DA model for carbonate. For the same reason, the kaolinite-dickite spectra were assigned to the class of spectra containing illite features when calibrating the PLS-DA model for illite. Unlike the PLS-DA mineral mapping performed in the Lagunas Norte study presented in chapter 7.7, the PLS-DA model of kaolinite-dickite could be used to distinguish the kaolinite-dickite spectra from those of illite. This is likely because the illite reference spectra that were collected from the measured SWIR hyperspectral images of the Cortez samples are more representative of pure illite than those collected from the SWIR hyperspectral images of the Lagunas Norte samples. It was also discussed in chapter 7.7.3. that the illite reference spectra that were used in the Lagunas Norte study were mixed with minor absorption features produced by pyrophyllite or dickite. This can also be observed when comparing the illite spectrum presented in Figure 7.32 with that shown in Figure 8.9.

Figure 8.10 presents the error rates versus the number of LVs that are obtained from cross-validating the PLS-DA classification models. The pink lines in this figure represent the calibration sets and the black lines the validation sets. The number of LVs that were used to produce the classification models was 8 for illite, 7 for kaolinite-dickite, 6 for carbonate, chlorite and chlorite+phlogopite, and 5 for tremolite. These numbers were chosen because Figure 8.10 shows that the validation subsets have the lowest error rate at these numbers of LVs. Only for the illite and the kaolinite-dickite classification the error rate does not decrease significantly when using more than 6 and 7 LVs respectively. However, when inspecting the calculated responses it was observed that better classification results were obtained when one more LV was used in these PLS-DA models. Since Figure 8.10 shows that the PLS-DA models are not overfitting when 8 and 7 LVs are used for the illite and kaolinite-dickite classifications, these numbers of LVs were selected for the classification of illite and kaolinite-dickite spectra.

Figure 8.11 presents the PLS-DA responses that were calculated for the classification of mineral spectra. The black colour in this figure represents spectra in which the absorption features of the mineral that is classified were observed by visual inspection. The pink colour represents spectra in which the absorption features of this mineral were not observed. The dots are SWIR spectra that were used for calibrating the classification models and the circles are spectra used for validation. The lines in Figure 8.11 represent the thresholds that were used for the classification of spectra. The selected thresholds were the averages between the maximum response of the spectra containing the mineral absorptions and the minimum response of spectra that do not contain the mineral absorptions. In case misclassification occurred, the misclassified spectra were inspected and if the misclassification was considered acceptable these spectra were not included for calculating the classification threshold.

It can be observed from Figure 8.11 that there is a clear difference between the responses that were calculated for SWIR spectra that contain the absorption features of each mineral and SWIR spectra that do not. Figure 8.11 also shows that for each classification model the responses of the spectra of the validation set matches the range in responses of the spectra that were used to calibrate the model. This indicates that the PLS-DA classification models produce consistent results.

A. carbonate
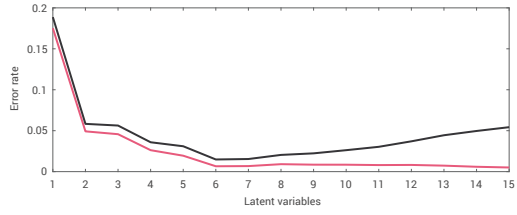
B. chlorite
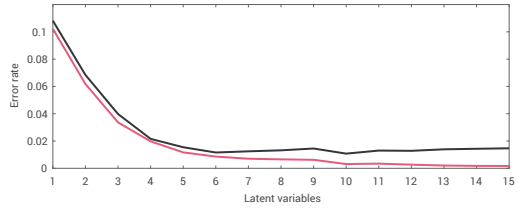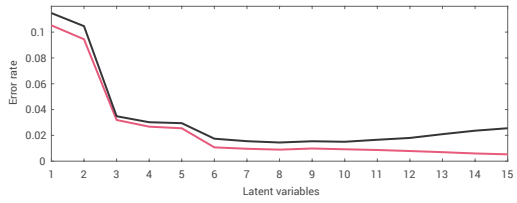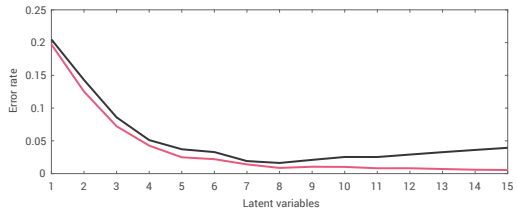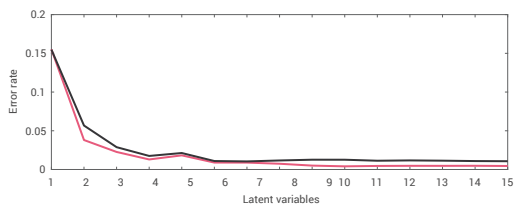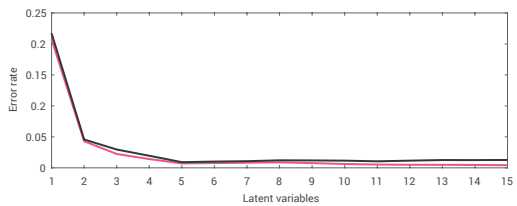
C. kaolinite-dickite

D. illite

E. chlorite
  + phlogopite

F. tremolite

— validation   — calibration

Figure 8.10: Error rate versus number of LVs of the PLS-DA cross validation for classification of mineral spectra.

A. carbonate
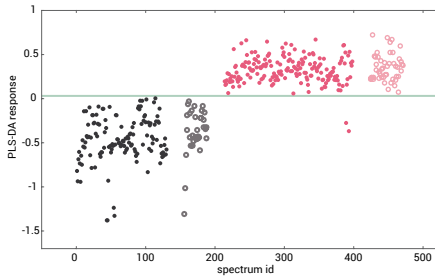
B. chlorite
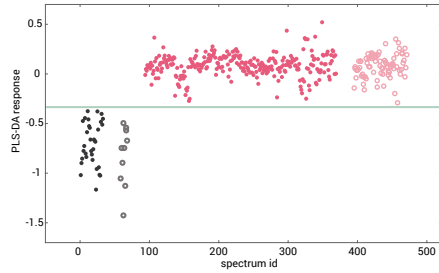
C. kaolinite-dickite
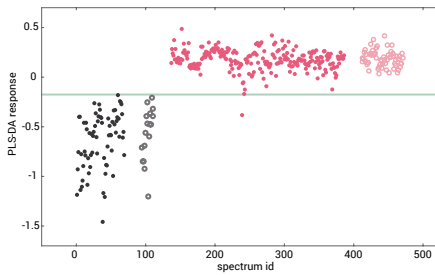
D. illite
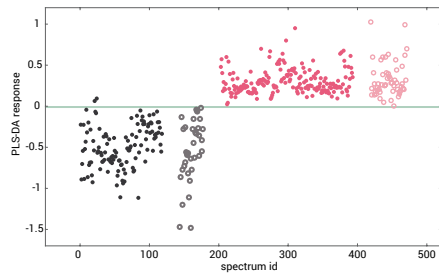
E. chlorite + phlogopite
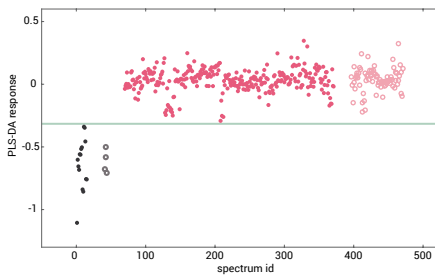
F. tremolite

- ● containing absorptions of the associated mineral calibration
- ○ containing absorptions of the associated mineral validation
- — threshold for classification
- ● not containing absorptions of the associated mineral calibration
- ○ not containing absorptions of the associated mineral validation

Figure 8.11: Calculated responses of the PLS-DA classification of mineral spectra.

Figure 8.11 shows that for carbonate, kaolinite-dickite and illite some misclassification occurs. For carbonate, inspection of the misclassified spectra showed that these are spectra of wax. Misclassification occurs because the wax spectra have absorption features that overlap with those of carbonate. However, since remnants of wax were observed on only a few samples and

cover only a relatively small surface area, misclassification of the wax spectra was considered acceptable. For kaolinite-dickite, the misclassified spectrum is a spectrum that was initially classified as illite. However, closer inspection showed that a weak shoulder occurs on the absorption features of illite that are most likely caused by kaolinite or dickite. This means that the initial classification of this reference spectrum was incorrect and the PLS-DA model actually classified this spectrum correctly. Inspection of the illite spectra that were misclassified showed that the intensity of the absorption features of illite in these spectra is relatively low and the spectra are also relatively noisy. Because most other illite spectra were correctly classified by the PLS-DA model this was considered acceptable.

Mineralogy mapping

Figure 8.12 presents the results of mapping mineral occurrences from the SWIR hyperspectral images for a subset of six samples. In this figure, a green colour was assigned to pixels for which the minerals were classified with the corresponding PLS-DA models. It was discussed in the previous section that the occurrence of carbonate could not be excluded from the SWIR spectra of chlorite, chlorite+phlogopite and tremolite. Since almost all pixels on sample 1 and 3 in Figure 8.12 were classified as chlorite+phlogopite and tremolite respectively, this means that it is uncertain whether these samples actually contain any carbonate. For sample 4 in Figure 8.12 the occurrence of carbonate is certain since this sample contains a significant amount of carbonate pixels on which chlorite, chlorite+phlogopite or tremolite were not classified. The same applies to sample 2, although on this sample the carbonate is mixed with chlorite since chlorite was also classified on a relatively large number of pixels.

It was also discussed in the previous section that the occurrence of illite could not be excluded from the SWIR spectra of kaolinite and dickite. Because of this, it is also uncertain if sample 5 in Figure 8.12 actually contains illite. For sample 6 the occurrence of illite is certain since this sample contains a significant amount of illite pixels on which kaolinite-dickite was not classified.

Figure 8.13 presents the results of mapping the intensity and the minimum position of several mineral absorption features from the VNIR-SWIR hyperspectral images for a subset of seven samples. This subset is different than the one shown in Figure 8.12. Minimum positions and absorption intensities > 0 were only mapped if the mineral that produces the absorption feature was classified from a pixel spectrum with the corresponding PLS-DA classification model. For iron-oxide these characteristics were mapped if the correlation coefficient between the pixel spectrum and that of one of the iron-oxide spectra was > 0.9. The intensity of the water feature was mapped for all pixel spectra. The intensity and minimum position of absorption features produced by chlorite, phlogopite and tremolite were not characterised because these minerals occur on only a few samples. Carbonate, illite, kaolinite-dickite and iron-oxide occur abundantly throughout the sample set.

For carbonate, the intensity and minimum position that is shown in Figure 8.13 is that of the absorption feature that occurs around 2325 nm. It should be noted that these characteristics

are influenced by the presence of chlorite, phlogopite and/or tremolite since these minerals also produce an absorption feature around this wavelength position. It is possible to characterise the relative influence of these minerals on the carbonate absorption by calculating the intensity of one of the absorption features that these minerals produce that does not overlap with carbonate. However, this was not performed since chlorite, phlogopite and tremolite occur on only a few samples.

It was explained in the previous sections that the minimum position of the 2325 nm carbonate absorption is usually on the 2325-2335 nm range for calcite and on the 2315-2325 nm range for dolomite. Figure 8.13 therefore shows that the carbonate classified on sample 1 is more representative of calcite while that on samples 2 and 3 is more representative of dolomite. Furthermore, Figure 8.13 shows relatively intense carbonate absorptions in the top left corner of sample 2. This can be explained by the fact that in this region the sample is broken along a dolomite-bearing vein which results in a higher abundance of dolomite at the surface that is measured.

It was explained in chapter 6.4.3. that the minimum position of the illite absorption feature that is located around 2200 represents the relative amount of Fe and Mg that substitutes Al within the illite crystal structure. If more Al has been substituted by Fe and Mg, the wavelength position of this feature occurs at longer wavelengths (Duke, 1994; Post & Noble, 1993). Sample 3 and 7 in Figure 8.13 therefore represent illite that is more Al-rich while sample 4 contains regions that are more Fe- and Mg-rich. For sample 5 and 6 the wavelength position of the 2200 nm feature is influenced by the absorption features that are produced by kaolinite-dickite. Especially at regions where intense kaolinite-dickite absorption features occur the minimum position of the 2200 nm feature is not representative of the relative content of Al versus Fe and Mg.

For kaolinite-dickite, the intensity and position that is shown in Figure 8.13 is that of the absorption feature that forms the left part (shorter wavelength) of the doublet that occurs around 2200 nm. The intensity is calculated relative to the maximum that occurs on the right side (longer wavelength) of the absorption feature. This is the maximum in between the two absorption features that form the doublet. However, the kaolinite-dickite absorption that forms the left part of the doublet around 2200 nm sometimes only produces a shoulder and not a minimum. Because of this, kaolinite-dickite can still occur at locations where the kaolinite-dickite intensity shown in Figure 8.13 is zero. The occurrence is captured in the mineral occurrence maps such as the ones shown in Figure 8.13 . The position of the shoulder features was calculated by finding the wavelength position at which the slope of the left side of the doublet absorption was smallest.

It was explained in the previous sections that the minimum position of the left part of the kaolinite-dickite doublet absorption that occurs around 2200 nm is usually around 2160 nm for kaolinite and around 2180 nm for dickite. Figure 8.13 therefore shows that on sample 6 dickite occurs and on sample 5 mainly kaolinite occurs. Dickite occurrences are also visible on the left part of sample 5 in Figure 8.13.

A. photo   ⊢⊢⊢⊢⊢⊢⊢⊢⊢⊣10 cm

B. carbonate

C. chlorite

D. chlorite + phlogopite

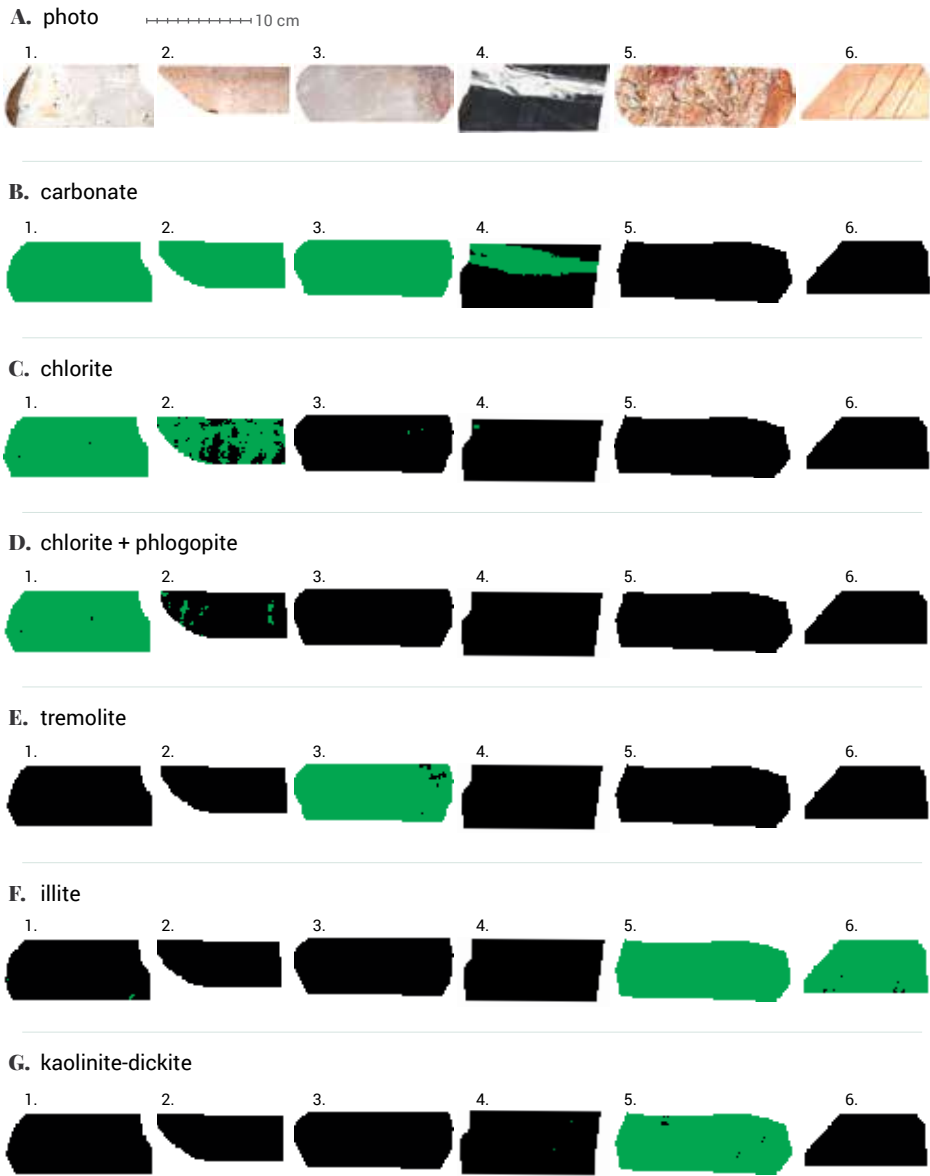E. tremolite

F. illite

G. kaolinite-dickite

Figure 8.12: Selected examples of mineral maps produced from the SWIR hyperspectral images that show the occurrence of carbonate, chlorite, chlorite + phlogopite, tremolite, illite and kaolinite-dickite.

It was explained in chapter 7.7.2. that the 900 nm iron-oxide absorption usually occurs on a 860-890 nm range for hematite and on a 910-940 nm range for goethite. As with the results presented in chapter 7.7.3, the calculated minimum positions of this absorption feature occur at somewhat longer wavelengths as those reported in literature due to the hull quotient correction. However, this type of correction affects all the iron-oxide spectra in the same way and the calculated minimum positions still represent the hematite-goethite mineralogy. Figure 8.13 shows clear differences between the minimum position of the 900 nm iron-oxide absorption. On samples 2 and 6 the iron-oxide mineralogy is more representative of goethite, while on samples 3, 4 and 7 it is more representative of hematite.

Classification of ore and waste

The definition of ore and waste was based on a cut-off grade of 0.15 ppm Au. The data matrix on which the PLS-DA classification of ore and waste samples was performed contained the cumulative distribution of the absorption intensity of carbonate, illite, kaolinite-dickite, and iron-oxide. The distribution of the minimum position of an absorption feature that represents differences in the composition of these minerals was also included in the data matrix. This was done after a multiplicative zero replacement followed by a centred log-ratio transformation was applied to this data. The average intensity of the water feature, the distribution of the average reflection of the pixel spectra, and the fraction of pixels on which chlorite, phlogopite and tremolite were classified were also included in the data matrix.

Figure 8.14 presents the average error rate versus the number of LVs that are obtained from 1000 cross-validations of the PLS-DA classification model. The pink line in this figure represents the calibration set and the black line the validation set. Figure 8.14 shows that the error rate of the validation set starts to diverge from that of the calibration is when more than three LVs are used. Because this indicates that the PLS-DA model is overfitting, three LVs were chosen for producing the PLS-DA classification of ore and waste.

Figure 8.15 presents the calculated responses of the PLS-DA classification in which the ore-waste designation was based on 210 sample assays. The black colour in this figure represents waste samples and the pink colour ore samples. The dots are samples that were used for calibrating the PLS-DA classification model and the circles are samples used for validation. It can be observed from Figure 8.15 that the calculated responses of the validation sets match the range in responses of the calibration sets. This indicates that the PLS-DA classification model produces consistent results.

A. photo

1. 2. 3. 4. 5. 6. 7.

H+++++++++H 10 cm

B₁. carbonate - intensity

0 ▬▬▬ 0.5

1. 2. 3. 4. 5. 6. 7.

B₂. carbonate - position

2300nm ▬▬▬ 2350nm

1. 2. 3. 4. 5. 6. 7.

C₁. illite - intensity

0 ▬▬▬ 0.5

1. 2. 3. 4. 5. 6. 7.

C₂. illite - position

2195nm ▬▬▬ 2220nm

1. 2. 3. 4. 5. 6. 7.

D₁. kaolinite-dickite - intensity

0 ▬▬▬ 0.05

1. 2. 3. 4. 5. 6. 7.

D₂. kaolinite-dickite - position

2150nm ▬▬▬ 2185nm

1. 2. 3. 4. 5. 6. 7.

E₁. iron-oxide - intensity

0 ▬▬▬ 0.3

1. 2. 3. 4. 5. 6. 7.

E₂. iron-oxide - position

800nm ▬▬▬ 1100nm

1. 2. 3. 4. 5. 6. 7.

F. water - intensity

0 ▬▬▬ 0.5

1. 2. 3. 4. 5. 6. 7.
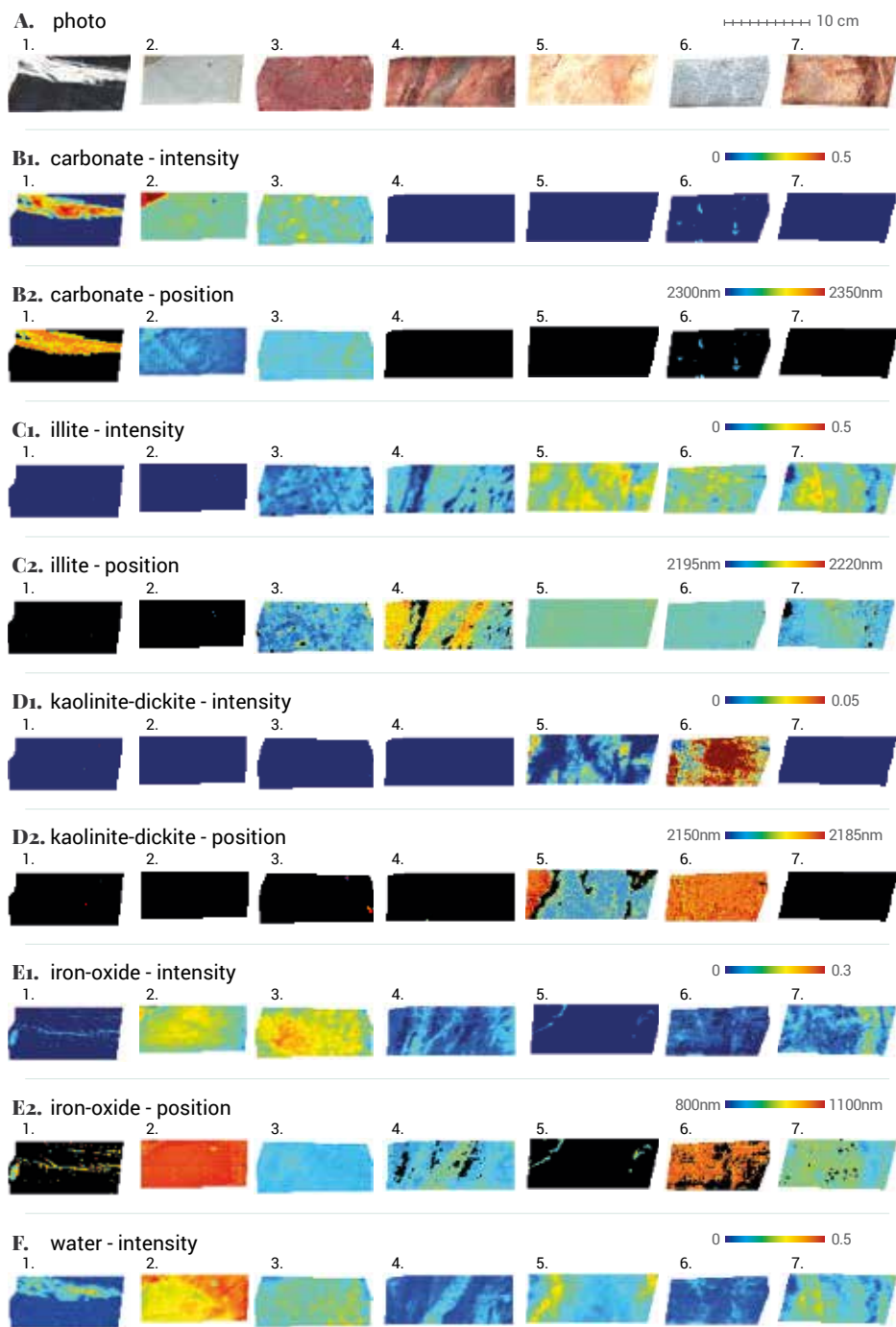
Figure 8.13: Selected examples of mineral maps produced from the SWIR hyperspectral images that show the absorption intensity of water and the absorption intensity and minimum position of carbonate, illite, kaolinite-dickite and iron-oxide.
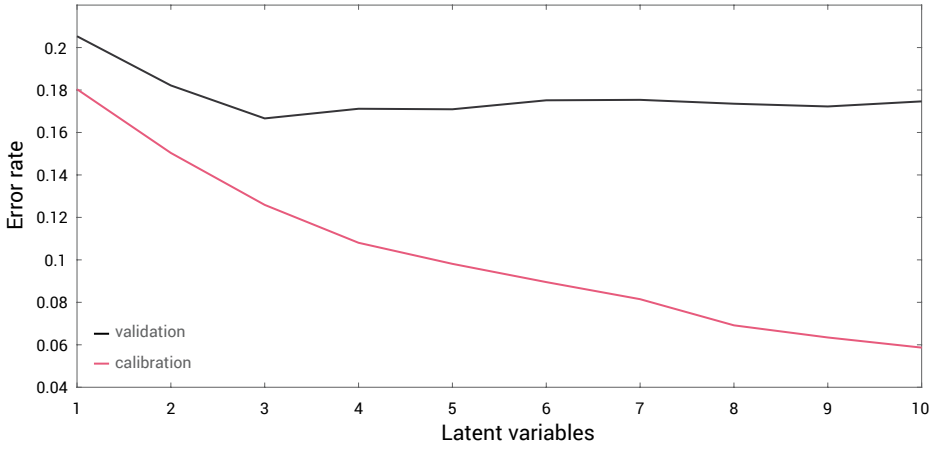
Figure 8.14: Error rate versus number of LVs of the PLS-DA cross validation for classification of ore and waste samples.
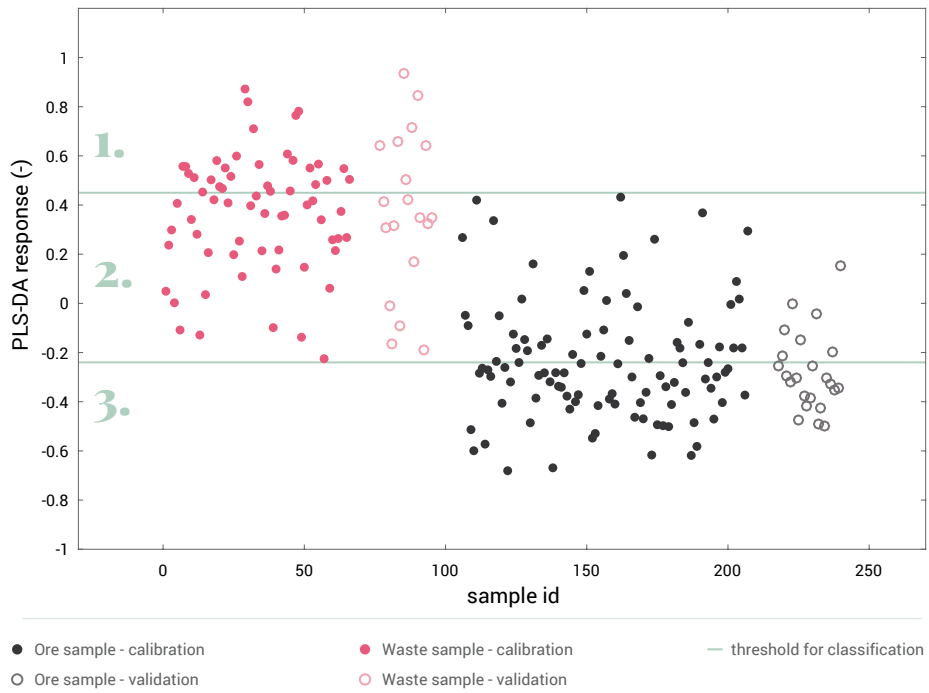
Figure 8.15: Calculated PLS-DA responses of ore and waste samples. Ore-waste designation is based on the additional samples assays.
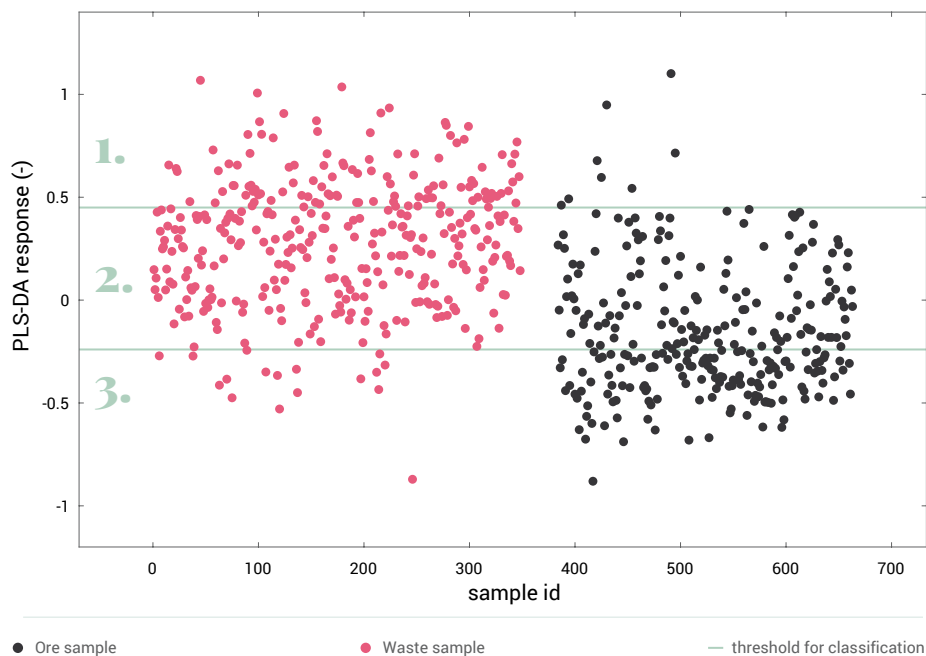
Figure 8.16: Calculated PLS-DA responses of all ore and waste samples. Ore-waste designation is based on the drill hole data.

It can be observed from Figure 8.15 that the PLS-DA classification model was not able to fully separate ore from waste. This is likely because some of the waste samples in the samples set have a SWIR-active mineralogy that is similar to some of the ore samples. As with the Lagunas Norte study, this was expected since it is unlikely that there is a discrete difference in alteration mineralogy at some arbitrary cut-off on the gold grade. However, Figure 8.15 also shows that for most of the waste samples a higher response is calculated than for most of the ore samples. The calculated responses can therefore be used to predict whether a sample is more likely to be waste or ore.

The two lines in Figure 8.15 are two thresholds that were chosen for classification of samples. The threshold at 0.45 was chosen in order to segment a group of samples that are all waste and the threshold at -0.24 was chosen to segment a group of samples that are all ore. Although segmenting ore samples was not one of the objectives of the study, this was performed to illustrate the potential of using PLS-DA classification models to distinguish between gold grades. Table 8.1 presents the resulting gold grade when the two thresholds are used to classify the samples. The group numbers in this table refer to the numbers annotated on Figure 8.15 and Figure 8.16. It can be observed from Table 8.1 that significant differences in the average gold grades of the three groups result. Furthermore, the group of waste samples (group 1) has a gold grade that is far below the cut-off grade of 0.15 ppm Au.

Figure 8.16 presents the responses of all samples that were calculated by using the same PLS-DA classification model that was used for the classification presented in Figure 8.15. The

lines shown in this figure also represent exactly the same thresholds as those in Figure 8.15. The different colours refer in this case to the ore-waste designation that is based on the drill hole data. The ore-waste designation of the samples that were used to calibrate the PLS-DA model is still the same since the drill hole data of samples on which assays were performed was replaced by the results of these assays. Because the drill hole data is not fully representative of the samples, the ore-waste designations shown in Figure 8.16 might not be completely correct.

Table 8.1: Results of the PLS-DA classification of ore and waste.

	based on sample assay			based on drill hole assay		
	group 1	group 2	group 3	group 1	group 2	group 3
Fraction of samples (%)	17.1	46.2	36.7	18.8	56.4	24.8
Au (ppm) minimum	0.00	0.00	0.18	0.00	0.00	0.01
Au (ppm) maximum	0.12	50.60	231.80	4.11	50.60	231.80
Au (ppm) average	0.03	2.80	20.15	0.13	1.84	16.00

The responses in Figure 8.16 show a similar trend as those in Figure 8.15. Table 8.1 presents the resulting gold grades from the drill hole data when the responses and thresholds shown in Figure 8.16 are used to classify the samples. This table shows that based on the drill hole data, a population of only waste samples or only ore samples can no longer be segmented. However, it also shows that the average gold grade of the group of waste samples (group 1) is still lower than the cut-off grade of 0.15 ppm Au. Furthermore, there are also still significant differences between the average gold grades of the three groups. The drill hole data therefore validates that it is possible to use VNIR-SWIR hyperspectral imagery to distinguish between the gold grades of the samples.

The scores and loadings of the PLS-DA classification model are presented in appendix A. The scores and loadings show that relatively high abundances of calcite, chlorite, phlogopite and tremolite in the mineralogy maps are strong indicators of waste. Relatively intense absorption features of water and illite, and low intensity kaolinite absorptions are also more associated with waste samples than with ore samples. Only illite with absorption features having a minimum position > 2214 nm are associated with waste. This relates to illite that is relatively rich in Fe and Mg. Illite with absorption features < 2214 nm, relating to more Al-rich illite, is more associated with ore samples. Furthermore, occurrences of dolomite, dickite and hematite are more associated with ore samples than with waste samples.

Classification of low and high grade ore

Different processing routes are available at Cortez for the processing of low and high grade ore types. Gold extraction from low grade ore is usually performed by heap leaching, while the high

grade ore is treated in the CIC and CIL circuits after it has been pulverised (mill oxide in Figure 8.8). The definition of low and high grade ore is based on a 5.14 ppm Au cut-off grade. The data matrix on which the PLS-DA classification of low and high grade ore samples was performed was exactly the same as the one used for the classification of ore and waste.

Figure 8.17 presents the average error rate versus the number of LVs that are obtained from 1000 cross-validations of the PLS-DA classification model. Two LVs were chosen for producing the PLS-DA classification because Figure 8.17 shows that the error rate of the validation set starts to diverge from that of the calibration is when more than two LVs are used.

Figure 8.18 presents the calculated responses of the PLS-DA classification in which the designation of low and high grade ore was based on the 210 sample assays. This figure shows that the PLS-DA classification model produces consistent result since the calculated responses of the validation sets match the range in responses of the calibration sets. It also shows that for most of the waste samples a higher response is calculated than for most of the ore samples. The calculated responses can therefore be used to predict whether a sample is more likely to be low or high grade ore.
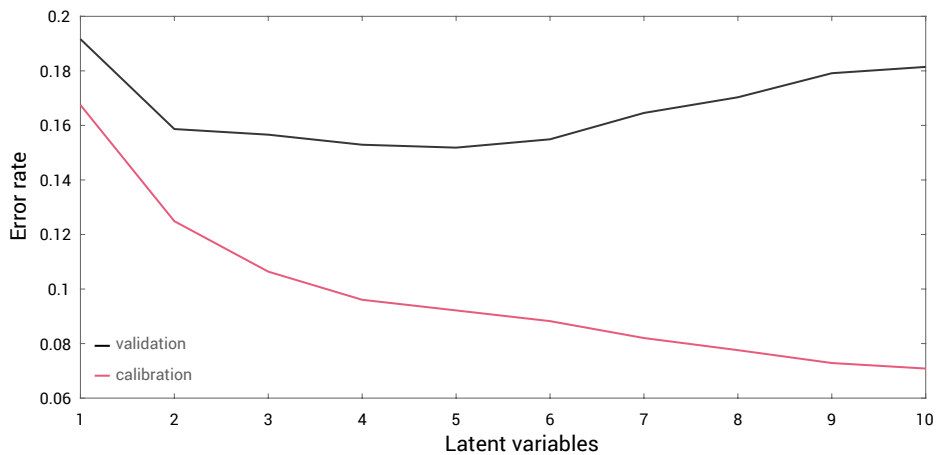

Figure 8.17: Error rate versus number of LVs of the PLS-DA cross validation for classification of low and high grade ore samples.
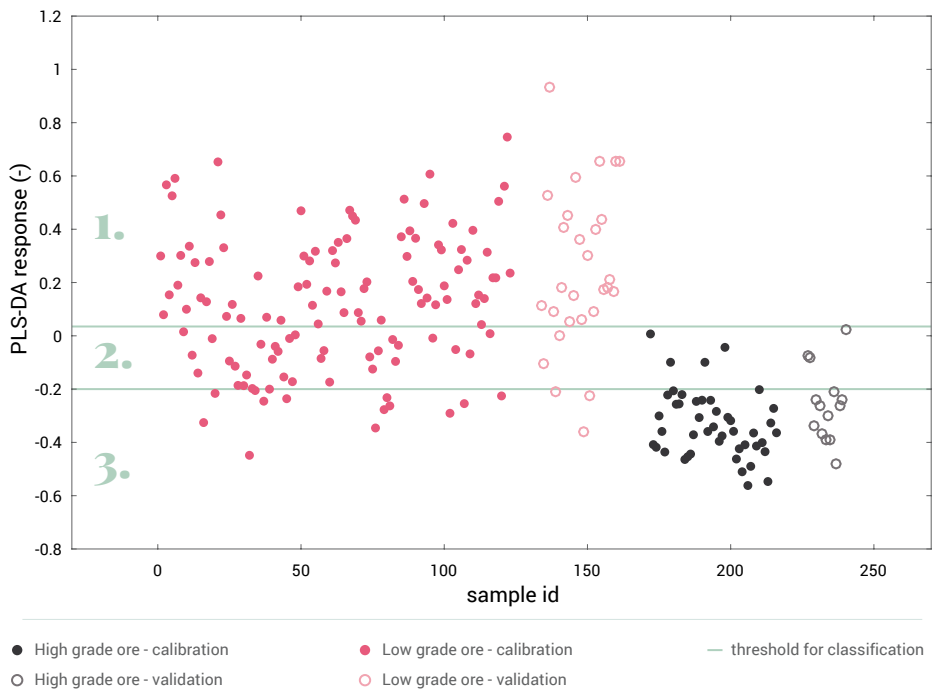
Figure 8.18: Calculated PLS-DA responses of low and high grade ore samples. The designation of low and high grade ore is based on the additional samples assays.

The two lines in Figure 8.18 are two thresholds that were chosen for classification of samples. The threshold at 0.04 was chosen in order to segment a group of samples that are all low grade ore. The threshold at -0.24 was chosen to segment a group that consists mainly of high grade ore samples. Table 8.2 presents the resulting gold grades when these two thresholds are used to classify the samples. The group numbers in this table refer to the numbers annotated on Figure 8.18 and Figure 8.19. It can be observed from Table 8.2 that significant differences in the average gold grades of the three groups result. Furthermore, the group 1 has a gold grade that is far below the cut-off grade of 5.14 ppm Au.

Figure 8.19 presents the responses of all samples that were calculated by using the same PLS-DA classification model that was used for the classification presented in Figure 8.18. The designation of low and high grade ore in this figure is based on the drill hole data. The lines shown in Figure 8.19 represent exactly the same thresholds as those shown in Figure 8.18.

It can be observed that the responses in Figure 8.19 show a similar trend as those in Figure 8.18. However, Figure 8.19 also shows that a population of only low grade ore samples is no longer segmented when the same thresholds as those shown in Figure 8.18 are used. Table 8.2 presents the resulting gold grades from the drill hole data when the responses and thresholds shown in Figure 8.19 are used to classify the samples. This table shows that there are still significant differences between the average gold grades of the three groups. The drill hole data

therefore validates that it is possible to use VNIR-SWIR hyperspectral imagery to distinguish between the gold grades of the samples.

Appendix A presents the scores and loadings of the PLS-DA classification model. The scores and loadings show that almost all mineral occurrences in the mineralogy maps of samples indicate low grade ore samples. High grade ore samples are associated with the occurrence of illite and hematite. Only illite with absorption features having a minimum position < 2203 nm are associated with ore. This relates to illite that is relatively rich in Al. Illite with absorption features > 2203 nm, relating to more Fe- and Mg-rich illite, is more associated with low grade samples.
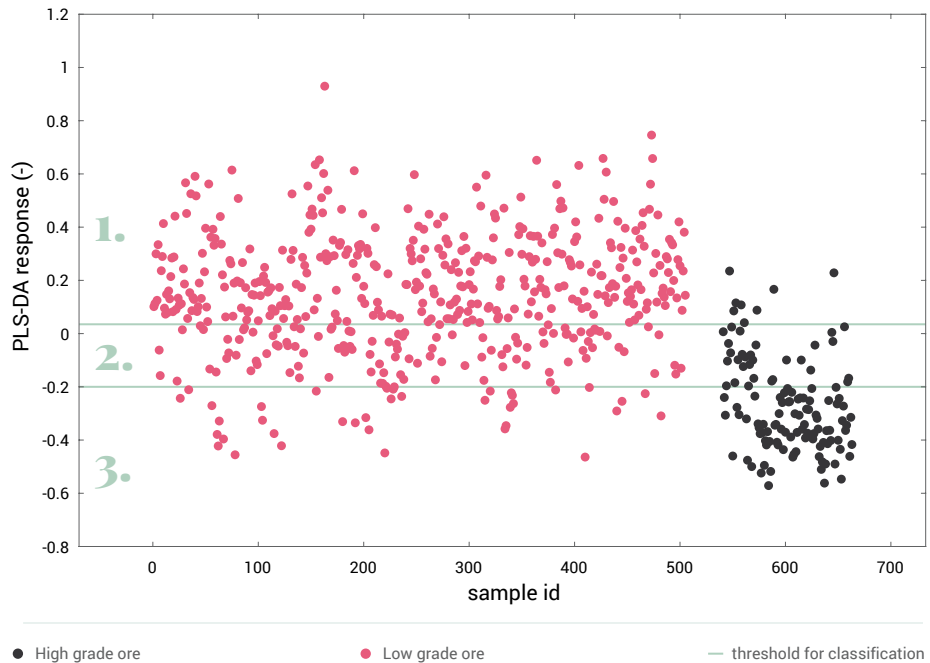

Figure 8.19: Calculated PLS-DA responses of low and high grade ore samples. The designation of low and high grade ore is based on the drill hole data.

Table 8.2: Results of the PLS-DA classification of low and high grade ore.

	based on sample assay			based on drill hole assay		
	group 1	group 2	group 3	group 1	group 2	group 3
Fraction of samples (%)	48.0	19.0	33.0	57.8	22.5	19.7
Au (ppm) minimum	0.00	0.00	0.36	0.00	0.00	0.01
Au (ppm) maximum	4.62	56.00	231.80	31.30	78.50	231.80
Au (ppm) average	0.19	5.90	22.74	0.51	4.79	18.55

Classification of oxide and refractory ore

The definition of oxide and refractory ore is based on the gold recovery. Samples with a gold recovery > 50% are classified as oxide ore and samples with a recovery < 50% as refractory ore. The mineralogical data on which the PLS-DA classification of oxide and refractory ore samples was performed was the same as the one used for the classification of ore and waste and the classification of low and high grade ore.

Figure 8.20 presents the average error rate versus the number of LVs that are obtained from 1000 cross-validations of the PLS-DA classification model. This figure shows that the error rate of the validation set only increases when more than one LV is used. One LV was therefore chosen for producing the PLS-DA classification of oxide and refractory ore.

Figure 8.21 presents the calculated responses of the PLS-DA classification in which the designation of oxide and refractory ore was based on the 124 sample assays. Cyanide leach tests were only performed on samples with a gold grade > 0.10 ppm and the number of samples in Figure 8.21 is therefore smaller than for the classification shown in Figure 8.15 and Figure 8.18. It can be observed from Figure 8.21 that the calculated responses of the validation sets match the range in responses of the calibration sets. This indicates that the PLS-DA classification model produces consistent results. Figure 8.21 also shows that for most of the oxide ore samples a higher response is calculated than for the refractory ore samples. The calculated responses can therefore be used to predict whether a sample is more likely to be oxide or refractory ore.

The two lines in Figure 8.21 are two thresholds that were chosen for the classification of samples. The threshold at 0.02 was chosen in order to classify a group of samples that are all oxide ore. The threshold at -0.20 was chosen to classify a group of samples that are all refractory ore. Table 8.3 presents the resulting total gold recoveries when the thresholds are used to classify the samples. The group numbers in this table refer to the numbers annotated on Figure 8.21 and Figure 8.22. It can be observed from this table that significant differences between the gold recoveries of the three groups result.
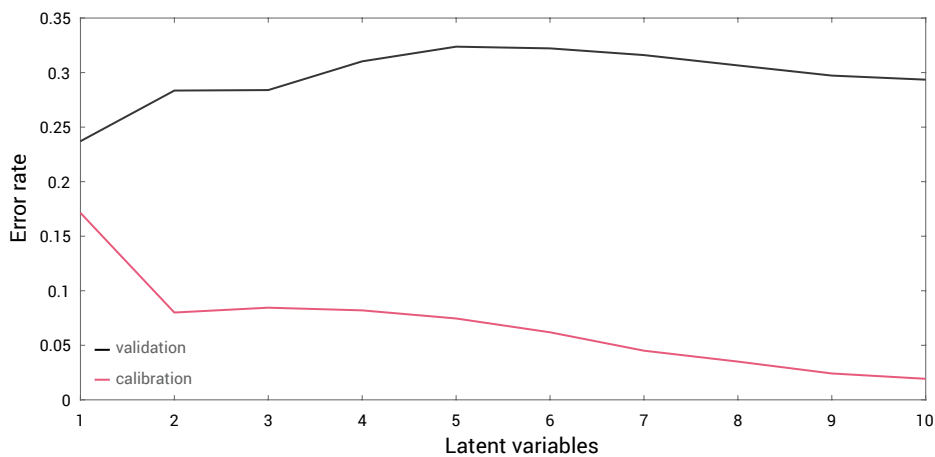
Figure 8.20: Error rate versus number of LVs of the PLS-DA cross validation for classification of oxide and refractory ore samples.

refractory ore - calibration ●   oxide ore - calibration ●   — threshold for classification

refractory ore - validation ○   oxide ore - validation ○

Figure 8.21: Calculated PLS-DA responses of oxide and refractory ore samples. The designation of oxide and refractory ore is based on the additional samples assays.
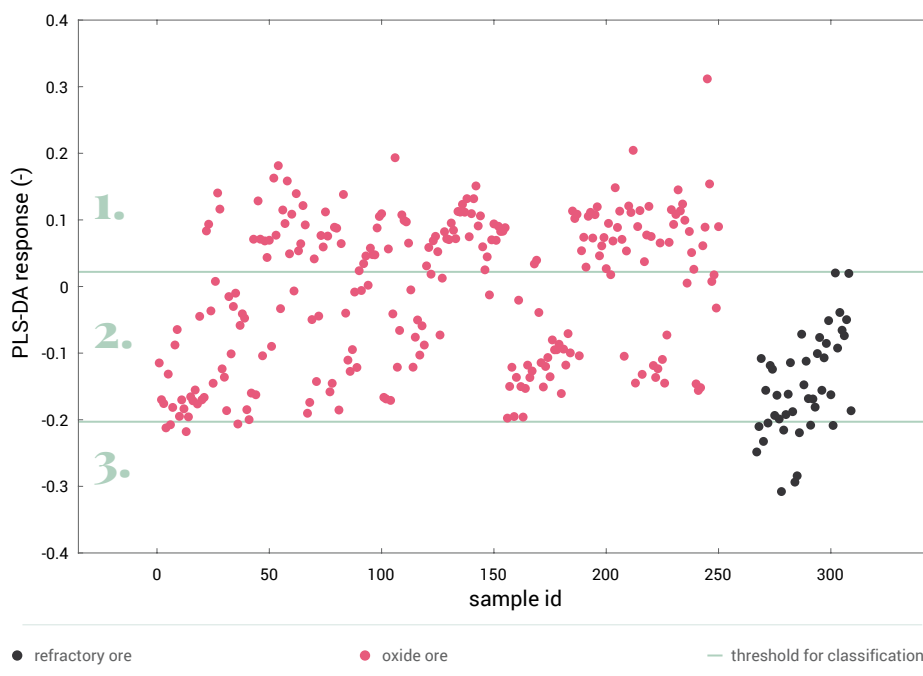
Figure 8.22: Calculated PLS-DA responses of oxide and refractory ore samples. The designation of oxide and refractory ore is based on the drill hole data.

Figure 8.22 presents the responses of the 293 samples for which the gold recovery was available from the drill hole data. These responses were calculated by using the same PLS-DA classification model that was used for the classification presented in Figure 8.21. The different colours refer in this case to the oxide- refractory ore designation that is based on the drill hole data. The lines shown in Figure 8.22 represent exactly the same thresholds as those shown in Figure 8.21.

The responses in Figure 8.22 show that it is still possible to distinguish a population of only oxide ore samples as well as a population of only refractory ore samples. The drill hole data therefore validates that the calculated responses can be used to predict whether a sample is more likely to be oxide or refractory ore. Table 8.3 presents the resulting gold grades from the drill hole data when the responses and thresholds shown in Figure 8.22 are used to classify the samples. This table shows that the average gold recoveries of the three group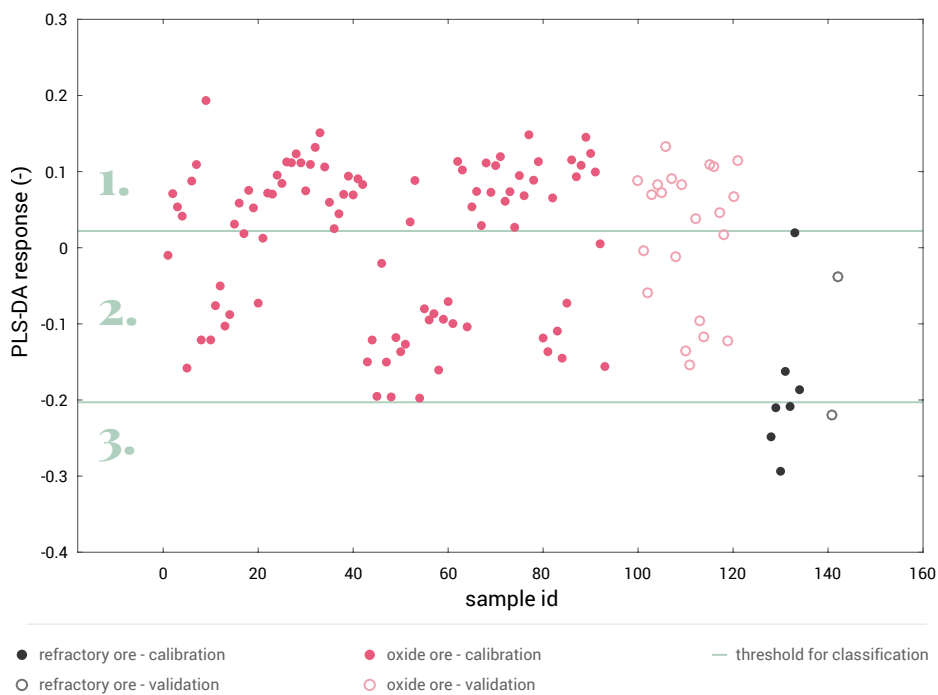s that is based on the drill hole data is almost the same as those based on the sample assays. Only for group 3 the average gold recovery is higher. This is likely caused by the fact that several oxide ore samples are classified into group 3 when the same thresholds as those shown in Figure 8.21 are used.

The scores and loadings of the PLS-DA classification model are presented in appendix A. The scores and loadings show that relatively high abundances of illite and hematite in the mineralogy maps are strong indicators of oxide ore. The scores and loadings also showed that almost all other mineral occurrences in the mineralogy maps are also more associated with oxide ore

than with refractory ore samples. Refractory ore samples are associated with an absence of SWIR-active minerals or minor occurrences of calcite.

Table 8.3: Results of the PLS-DA classification of oxide and refractory ore.

	based on sample assay			based on drill hole assay		
	group 1	group 2	group 3	group 1	group 2	group 3
Fraction of samples (%)	56.5	39.5	4.0	44.0	50.9	5.1
Au recovery (%) min.	56.68	11.55	2.02	56.68	1.60	0.10
Au recovery (%) max.	100.00	100.00	38.46	100.00	100.00	100.00
Au recovery (%) avg.	91.85	77.80	9.98	92.81	71.89	33.99

### Carbonate and illite composition versus gold grade

Figure 8.23 presents a comparison of the gold grade of samples versus the average minimum position of the carbonate absorption feature that occurs around 2325 nm. The average minimum position of this absorption feature was calculated from all the pixel spectra on each sample on which carbonate was classified and on which chlorite, phlogopite and tremolite were not classified. This was done because occurrences of chlorite, phlogopite and tremolite can influence the minimum position of this feature. Only pixel spectra on which the carbonate absorption feature had an intensity > 0.1 were included in calculating the average minimum position to exclude noisy spectra. Finally, only samples on which >10% of the pixels were classified as carbonate were included in Figure 8.23 to exclude samples on which only misclassified carbonate pixels occurred.

It was explained in the previous sections that the minimum position of the 2325 nm carbonate absorption is usually on the 2325-2335 nm range for calcite and on the 2315-2325 nm range for dolomite. Based on this, Figure 8.23 shows that samples containing calcite have lower gold grades than samples containing dolomite. In fact, almost all samples on which the carbonate absorption feature has an average minimum position > 2322 nm (pink line in Figure 8.23) are waste samples. This confirms the analysis of the loadings of the ore-waste classification with PLS-DA, which showed that calcite is an indicator of waste while dolomite is associated with ore samples. Only one ore sample with a gold grade of 0.18 ppm contains carbonate with an average absorption minimum > 2322 m. By using only the detectable differences in carbonate composition it was possible to segment a population of samples that represents 10% of the sample set at an average gold grade of 0.04 ppm.

Figure 8.24 presents a comparison of the gold grade of samples versus the average minimum position of the illite absorption feature that occurs around 2200 nm. The average minimum position of this absorption feature was calculated from all the pixel spectra on each sample

on which illite was classified and on which kaolinite and dickite were not classified. Pixels with kaolinite and dickite absorptions were excluded because these can influence the minimum position of the illite absorption feature. As with the carbonate feature, only spectra with an absorption intensity > 0.1 were included in calculating the average and only samples with > 10% illite pixels are shown in Figure 8.24.

It was explained in chapter 6.4.3. that the minimum position of the illite absorption feature that is located around 2200 represents the relative amount of Fe and Mg that substitutes Al within the illite crystal structure. If more Al has been substituted by Fe and Mg, the wavelength position of this feature occurs at longer wavelengths (Duke, 1994; Post & Noble, 1993). Figure 8.24 shows that samples containing illite that is more Al-rich have higher gold grades than most samples containing illite that is more Fe- and Mg-rich. This confirms the analysis of the loadings of the PLS-DA classification of ore and waste and low and high grade ore. All samples on which the illite absorption feature has an average minimum position < 2205 nm (pink line in Figure 8.24) are ore samples. By using this threshold on the wavelength position of the illite absorption feature a population of samples is segmented that represents 17% of the sample set at an average gold grade of 21.3 ppm.
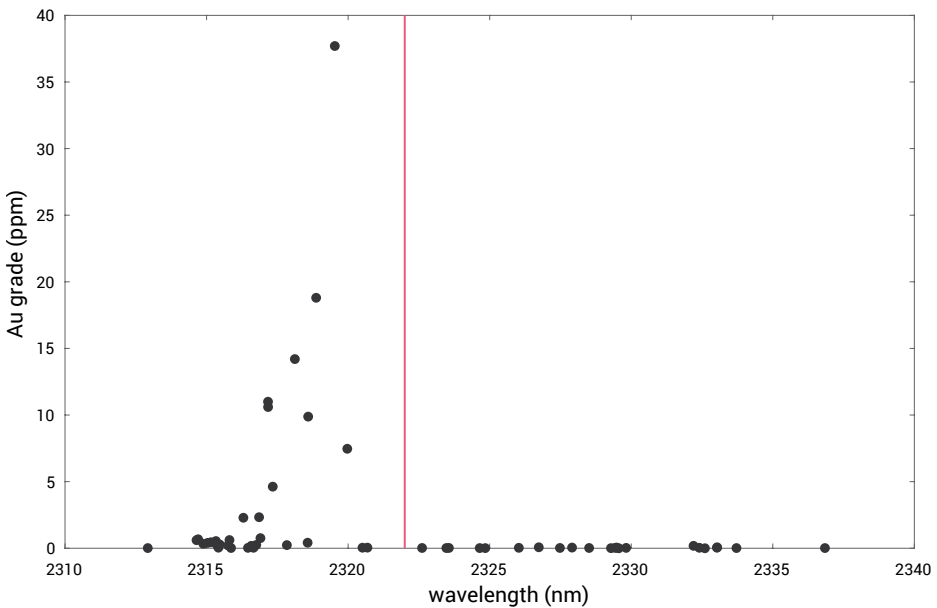
— carbonate absorption feature average minimum position > 2322nm

Figure 8.23: Minimum position of the carbonate absorption feature versus the gold grade.

— illite absorption feature average minimum position > 2205nm
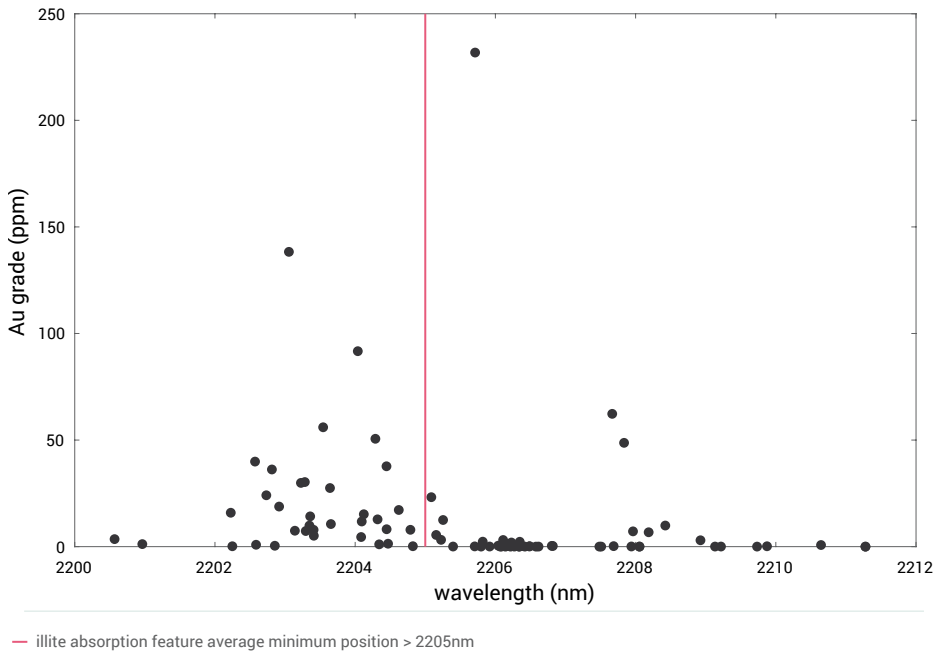
Figure 8.24: Minimum position of the illite absorption feature versus the gold grade.

8.3.4. Discussion

The results of the PLS-DA classification of mineral spectra presented in section 8.3.3 confirm the conclusion of chapter 7.7 that PLS-DA is an effective method for mapping mineral occurrences from SWIR hyperspectral images. PLS-DA could not be used to distinguish between mineral spectra that are relatively similar, such as those of kaolinite and dickite. It was shown that in this case it is possible to classify the mineral spectra as one group and distinguish between the different minerals by calculating the minimum position of a characteristic absorption feature after the classification. The results presented in section 8.3.3 also confirmed that PLS-DA is an effective technique to investigate the possibilities of using the information contained in the mineralogy maps to segment a population of waste samples and distinguish between oxide and refractory ore.

The different mineral assemblages that were observed from the VNIR-SWIR hyperspectral images are characteristic for different hydrothermal alteration environments (Corbett & Leach, 1998; Pirajno, 1992). The ability to segment a population of waste and low grade ore samples is therefore based on a relationship between gold mineralization and hydrothermal alteration. It was shown that especially differences in the composition of carbonate and illite that are detectable from the SWIR hyperspectral images are good indicators of waste and high grade ore.

The loadings of the PLS-DA classification on oxide and refractory ore showed that relatively high abundances of illite and hematite in the mineralogy maps are strong indicators of oxide ore. The reason that hematite indicates oxide ore can be explained by the fact that this is an iron-oxide mineral with was formed by the oxidation of iron-sulphides. However, it is unknown why illite is associated with oxide ore. The loadings of the PLS-DA classification on oxide and refractory ore also showed that refractory ore samples are associated with an absence of SWIR-active minerals and minor occurrences of calcite. This result can be explained by the fact that many of the refractory ore samples are carbonaceous and have a low reflection and dark appearance. Due to the low reflection, the VNIR-SWIR spectra on these samples are relatively noisy and no minerals can be detected from these spectra. If SWIR-active minerals do occur on these samples is unknown. The reason that refractory ore samples are associated with minor occurrences of calcite can be explained by the fact that some of these samples contain calcite veins.

8.3.5. Conclusions

The following conclusions were drawn from testing VNIR-SWIR hyperspectral imagery on the drill core sample set:

- VNIR-SWIR hyperspectral imagery could be used to segment a population of waste samples and heap leach samples. This is based on detecting specific alteration mineral assemblages.

- VNIR-SWIR hyperspectral imagery could be used to segment a population of oxide ore samples. This is mainly based on detecting the occurrence of illite and hematite.

- VNIR-SWIR hyperspectral imagery could be used to segment a population of refractory ore samples. This is mainly based on the absence of detectable SWIR-active minerals, which can be explained by the fact that many of the refractory ore samples are carbonaceous and their VNIR-SWIR spectra have a low reflection.

- It was confirmed that PLS-DA is an effective technique for mapping mineral occurrences from VNIR-SWIR hyperspectral images as well as investigating the possibilities of using the information contained in the mineralogy maps to classify samples on ore quality parameters.

8.4. RGB imaging

8.4.1. Introduction

It was explained in chapter 3.6. that RGB imaging can be used to characterise materials on their visible appearance, such as colour or texture. Since many visible differences could be observed between the samples from Cortez, it was investigated if characterisation of these differences with RGB imagery can be used to classify the samples on the objectives stated in chapter 8.2.3. This investigation was performed by Verhallen (2016) as part of his MSc. thesis. The following sections will present a brief summary of the main results and conclusions of this thesis. A more detailed overview of the methods, results and conclusions of this study is presented in the thesis report (Verhallen, 2016).

8.4.2. Methods

RGB images of all the samples within core trays were collected with a SisuRock instrument (SPECIM ltd., Oulu, Finland). The RGB images were acquired simultaneously with the VNIR-SWIR hyperspectral images used in the study presented in chapter 8.3. Pixel size of the RGB images is around 0.2 mm.

The first step in RGB image processing was to convert the recorded data to relative reflections by using a dark current and white reference calibration. The second step was to mask the images by removing the data of pixels that do not represent a sample. Subsequently, 47 different parameters were extracted from the image of each sample. These parameters were subdivided into color based parameters and textural parameters (Verhallen, 2016). Color based parameters included for example the average reflection on the red, green or blue band of all pixels on a sample, or the fraction of pixels with intensity values above certain thresholds. Textural parameters included the variance or average local entropy within the image of a sample (Verhallen, 2016).

By using the drill hole data and the ore routing scheme presented in Figure 8.8, each sample was classified as one of the ore types shown in this figure. The different ore types were compared with the parameters that were extracted from the RGB images and a classification tree was created that uses some of the parameters in order to group samples with a similar appearance. Furthermore, PCA and PLS-DA was applied to the extracted parameters to further investigate the possiblities of using the RGB image data to distinguish the different ore types.

Table 8.4: Classification tree result based on the drill hole data (based on Verhallen (2016)).

|	group 1	group 2	group 3	group 4	group 5	group 6	group 7	group 8
Appearance	dark black	dark & white	dark	dark & red	red	pink	grey	white
Samples in group (%)	3	20	9	17	17	10	14	10
Au (ppm) average	22.46	1.57	4.50	7.78	4.25	0.32	2.42	0.09
Waste (%)	0	72	58	28	31	84	80	95
Refractory ore (%)	82	7	14	1	0	0	8	0
Mill oxide ore (%)	12	5	18	40	24	2	1	0
Leach oxide ore (%)	6	16	11	30	45	14	11	5

8.4.3. Results

Table 8.4 presents the results of a classification tree that was created by using selected thresholds on on several color based parameters that were extracted from the RGB images of the samples. Figure 8.25 shows an example of a sample that was classified in each of the classes in this table.

It can be observed from Table 8.4 that group 8 contains 10% of all the samples in the sample set and has an average gold grade of only 0.09 ppm. Since this average gold grade is below the cut-off grade of 0.15 ppm, this group of samples represents waste. Table 8.4 also shows that group 1 mainly consists of refractory ore samples and group 4 of mill oxide ore samples. All the other groups shown in Table 8.4 are on average leach grade ore. However, groups 3 and 5 do contain a significant fraction of refractory ore samples and mill oxide ore samples respectively. The average gold grade of both these groups is also relatively close to the cut-off grade of 5.14 ppm Au that is used to distinguish leach grade ore from mill grade ore.

1. Black
sample E347-0567 - classified as Roaster ore.
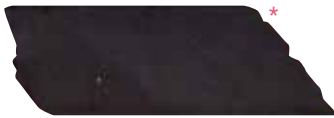
2. Dark and White
sample E347-0259 - classified as Waste.

3. Dark
sample D709-179 - classified as Leach Oxide ore.

4. Dark and Red
sample E339-654 - classified as Leach ore.

5. Red
sample D712-464 - classified as Waste.

6. Pink
sample E347-0920 - classified as Waste.

7. White
sample E347-0499 - classified as Waste.

8. Grey
sample E350-448 - classified as Waste.

* the brightness of these images is increased to enhance visibility

Figure 8.25: Example of a sample in each of the classes of Table 8.4 (Verhallen, 2016).

Table 8.5: Classification result based on combining PLS-DA models calibrated to segment waste, refractory ore and oxide ore. Group 4 represents samples not segmented by any of the models. Results are based on the drill hole data (based on Verhallen, 2016).

	group 1	group 2	group 3	group 4
PLS-DA model	waste	refractory	oxide	
Samples in group (%)	44	8	36	13
Au (ppm) average	0.70	14.87	6.43	2.84
Waste (%)	92	16	39	76
Refractory ore (%)	3	52	1	10
Oxide ore (%)	5	32	60	14

Table 8.5 presents the results of the PLS-DA classification of samples that was based on the 47 different parameters that were extracted from the image of each sample. These results are produced by combining PLS-DA models that were calibrated to segment waste, refractory ore and oxide ore. Class assignments for calibration of the models was based on the drill hole data and the classification objectives presented in chapter 8.2. Samples that were not segmented by any of the PLS-DA models are represented by group 4.

Table 8.5 shows that significant differences between the average gold grade of the four groups result. However, despite the fact that group 1 consists for 92% out of waste samples, this group has an average gold grade that is above the cut-off grade of 0.15 ppm Au. It should be noted though that the results in Table 8.5 are based on the drill hole data. As discussed in chapter 8.2, the drill hole data is not fully representative since the samples used in the study are much smaller than the intervals on which the drill hole data was collected. Since Table 8.5 shows that group 2 consists for 52% out of refractory ore samples and group 3 for 60% out of oxide ore samples, it results that PLS-DA could be used to roughly distinguish between the different ore types.

8.4.4. Discussion

It was possible to group samples with a similar appearance by creating a classification tree on several color based parameters that were extracted from the RGB images of the samples. Comparing these sample groups with the drill hole data showed that an RGB imaging sensor can be used to segment a fraction of the waste, the refractory ore, and the mill-grade oxide ore. The waste samples that can be segmented all have a bright white colour, the refractory ore samples are dark black, and the mill-grade samples are dark and red. All the other sample groups that resulted from the classification tree are on average leach grade ore. However, the

group of dark samples still contains a relatively high fraction of refractory ore samples and the group of red samples contains a relatively high fraction of mill-grade oxide ore samples.

The PLS-DA classifications that were performed on the 47 parameters that were extracted from the images of the samples did not improve the classification results that were obtained with the classification tree. This is probably caused by the fact that the class assignments that were used to calibrate the PLS-DA models were not completely correct. These class assignments were based on the drill hole data, which is not fully representative since the samples used in the study are much smaller than the intervals on which the drill hole data was collected. Using incorrect class assignments when calibrating a PLS-DA model limits the ability of the PLS algorithm to find the optimal set of predictor variables for producing a certain classification. Since the classification tree was aimed at grouping samples with a similar appearance, incorrect class assignments only affect the results of this classification and not the way in which the classification tree was produced. Validation of the classification results with geochemical data that is representative for the samples is still required.

8.4.5. Conclusions

The following conclusions were drawn from testing RGB imagery on the drill core sample set:

- RGB imagery could be used to segment a population of waste samples. This is based on detecting rock types with a bright white appearance.

- RGB imagery could be used to segment a population of oxide ore samples. This is based on detecting rock types with a red appearance.

- RGB imagery could be used to segment a population of refractory ore samples. This is based on detecting rock types with a dark black appearance.

- Validation of the results with geochemical data that is representative for the samples is still required.

8.5. Discussion

The VNIR-SWIR spectral sensor allows all the sorting objectives stated in chapter 8.2.3 to be fulfilled. It was discussed in chapter 8.3.3 that oxide ore could be segmented by detecting the occurrence of hematite and illite. The reason that hematite indicates oxide ore can be explained by the fact that this is an iron-oxide mineral that was formed by the oxidation of iron-sulphides during the supergene oxidation stage. Why illite is associated with oxide ore is unknown.

Refractory ore can be segmented by using the absence of detectable SWIR-active minerals except for minor occurrence of calcite. This result can be explained by the fact that many of the refractory ore samples are carbonaceous. The presence of carbon decreases the reflection of the samples, which prevents the detection of mineral absorptions with a VNIR-SWIR spectral sensor. Minor occurrences of calcite are sometimes still associated with refractory ore because some of the refractory ore samples contain calcite veins.

The ability to segment a fraction of the waste with VNIR-SWIR spectral sensors was based on an indirect relationship between the detected hydrothermal alteration mineral assemblages and the gold grade. It resulted that detecting occurrences of calcite, chlorite, phlogopite and tremolite can be used as indicators of waste. The occurrence kaolinite and Fe- and Mg-rich illite is also more associated with waste samples than with ore samples. Ore samples are associated with occurrences of Al-rich illite, dolomite, dickite and hematite.

The paragenetic sequence presented in Figure 8.3 shows that the formation of tremolite, chlorite (clinochlore) and kaolinite-dickite occurred during the pre-ore stage and is therefore not associated with gold mineralisation. Since Maroun et al. (2017) states that the mineralising ore fluids replaced tremolite, chlorite and dickite by illite, this confirms that detecting the occurrence of chlorite and tremolite with VNIR-SWIR spectral sensors can be used as an indicator of waste. The result that kaolinite and Fe- and Mg-rich illite are more associated with waste and that dickite and Al-rich illite are more associated with ore samples cannot be confirmed based on Maroun et al. (2017) or Arbonies et al. (2010). Additional research is needed in order to better understand the relationship between gold grade, detectable variations in illite composition and detectable occurrences of dickite and kaolinite. Furthermore, the occurrence of phlogopite was not observed by Maroun et al. (2017) or Arbonies et al. (2010). The occurrence of this mineral was validated by XRD analysis.

Figure 8.3 also shows that the formation of calcite is associated with gold mineralisation, while it resulted that calcite can be used as an indicator of waste. It should be noted though that Figure 8.3 only presents temporal relationships and no spatial relationships. Gold mineralisation at

Cortez is associated with zones of intense decarbonatisation (Arbonies et al., 2010; Maroun et al., 2017), which is the dissolution of carbonate minerals by the hydrothermal fluids. It was discussed in chapter 4.4. that decarbonatisation near fluid conduits is commonly zoned outward to dolomite- and then calcite-stable zones (Cline et al., 2005). This means that dolomite occurs closer to the mineralised zone and explains why detected occurrences of calcite could be used as an indicator of waste, while dolomite is associated with ore samples.

The ability to segment a fraction of the heap leach material with VNIR-SWIR spectral sensors was also based on a relationship between the detected hydrothermal alteration mineral assemblages and the gold grade. It resulted that detecting the occurrence of almost any VNIR-SWIR-active mineral can be used as an indicator of heap leach ore. High grade ore is associated with the occurrence of Al-rich illite and hematite. The fact that illite is associated with high grade ore is confirmed by Maroun et al. (2017). However, this author did not investigate the relationship between gold mineralisation and illite composition. It is therefore not confirmed that Fe- and Mg-rich illites are more associated with heap leach material. The reason that hematite is associated with high grade ore probably results from the fact that gold was originally deposited in pyrite, which was oxidised to hematite by the supergene oxidation stage.

It was shown in chapter 8.4. that an RGB imaging sensor can be used to segment populations of samples representing waste, oxide ore, or refractory ore. Waste samples could be segmented by classifying samples that have a bright white appearance. This can be explained by the fact that the bright white samples represent the quartz porphyry dikes that were introduced into the deposit after the gold mineralisation events took place. As explained in chapter 8.2.1, these dikes do not host significant gold mineralisation.

Oxide ore could be segmented with an RGB sensor by classifying samples that have a red appearance. This can be explained by the fact the most abundant iron-oxide minerals that occur within the samples have a red colour. As explained previously, iron-oxide minerals were formed by the oxidation of iron-sulphides during the supergene oxidation stage and are therefore a direct indicator of oxide ore. Carbonaceous refractory ore could be segmented by classifying samples with a dark black appearance. The dark appearance and low gold recovery of this ore both result from the carbon content. It results that the ability to segment oxide and refractory ore is based on the same characteristics that allowed this material to be identified with a VNIR-SWIR spectral sensor.

Additional research is required to investigate whether it is economically feasible to use a VNIR-SWIR spectral sensor or RGB sensor on a sensor-based sorting machine to remove a fraction of the waste, separate a fraction of the heap leach ore, separate a fraction of the oxide ore, or separate a fraction of the refractory ore. For separating heap leach ore, oxide ore or refractory ore, this will depend on the costs of sorting, the efficiency of the sorting machine, and the economic benefits of processing the sorted ore types compared to the costs of processing mixed ore types. Considering the removal of waste, the economic feasibility of sensor-based sorting depends on the costs of sorting, the costs of conventional processing, the sorting efficiency, the amount of waste that is rejected and the value of the gold that is contained by the waste. Sensor-based particle-by-particle sorting provides economic benefits if the value of

the amount of gold that is lost by discarding material does not exceed the difference in costs between sensor-based sorting and conventional ore processing.

Table 8.1 in chapter 8.3.3. shows that 17.1% of the samples can be rejected at an average gold grade of 0.03 ppm. This is a significant amount of material at a gold grade that is less than a third of the economic cut-off grade of 0.15 ppm Au. Since sensor-based particle-by-particle sorting is generally cheaper than conventional processing methods (Buxton & Benndorf, 2013; Lessard et al., 2014; Salter & Wyatt, 1991; Sivamohan & Forssberg, 1991; Wills & Finch, 2016), this means there is potential that removing this waste with sensor-based sorting can provide economic benefits. The economic feasibility of sensor-based particle-by-particle sorting is influenced by the limitations of using VNIR-SWIR spectral sensors on sensor-based sorter machines that were discussed in chapter 6.5.

Table 8.1 shows that based on the drill hole data the average gold grade of the waste that can be segmented is 0.13 ppm. Since this grade is close to the cut-off grade, it is not validated by the drill hole data that sensor-based particle-by-particle sorting can potentially provide economic benefits. However, as discussed in chapter 8.2.4 the drill hole data is not fully representative of the samples since the samples are much smaller than the interval on which the drill hole data was collected.

8.6. Conclusions

The following conclusions were drawn from testing an RGB imaging sensor and VNIR-SWIR spectral sensors on the samples from the Cortez Hills lower zone:

- VNIR-SWIR spectral sensors could be used to distinguish between different assemblages of hydrothermal alteration minerals of the ore samples collected from the Cortez Hills lower zone gold deposit.

- An indirect relationship is present between the gold grade of samples and the alteration mineralogy that could be detected with VNIR-SWIR spectral sensors. This indirect relationship is based on sample groups with different VNIR-SWIR active mineral assemblages that represent different zones of hydrothermal alteration and constitute different ranges of gold grades. Especially variations in the composition of carbonate and illite were useful indicators of gold mineralisation.

- VNIR-SWIR spectral sensors could be used to segment a population of waste samples. This was based on detecting specific alteration mineral assemblages.

- VNIR-SWIR spectral sensors could be used to segment a population of samples representing heap leach grade ore. This was based on detecting specific alteration mineral assemblages.

- VNIR-SWIR spectral sensors could be used to segment a population of oxide ore samples. This was based on mapping the absorption intensity of iron-oxide and illite.

- VNIR-SWIR spectral sensors could be used to segment a population of refractory ore samples. This was based on detecting an absence of SWIR-active minerals or on mapping minor occurrences of calcite veins.

- An RGB sensor could be used to segment waste samples. This was based on the identification of the quartz porphyry dike material that has a bright white appearance. The quartz porphyry dikes do not host significant gold since these were deposited after the mineralisation.

- An RGB sensor could be used to segment oxide ore samples. This was based on the pink or red appearance of oxide ore samples, which results from a relatively high abundance of iron-oxide minerals.

- An RGB sensor could be used to segment refractory ore samples. This was based on the dark black appearance of refractory ore samples, which results from relatively high carbon content.

- Additional research is required to investigate whether it is economically feasible to use a VNIR-SWIR spectral sensor on a sensor-based sorting machine to remove a fraction of the waste, remove a fraction of the heap leach ore, separate a fraction of the oxide ore, or separate a fraction of the refractory ore.

8.7. References

AFENYA, P. 1991. Treatment of carbonaceous refractory gold ores. *Minerals Engineering*, 4, 1043-1055.

AITCHISON, J. 1986. The statistical analysis of compositional data.

ARBONIES, D. G., CREEL, K. D. & JACKSON, M. L. 2010. Cortez Hills Lower Zone discovery and geologic update. *Proceedings of the Geological Society of Nevada symposium: Great Basin evolution and metallogeny*. Reno, Nevada, USA.

AUSSPEC 2008. *G-MEX Spectral Interpretation Field manual*, AusSpec International ltd.

BARRICK. 2015. *Fourth Quarter 2014 Results and 2015 Outlook (presentation)* [Online]. Available: barrick.q4cdn.com/808035602/files/presentation/2015/Barrick-2014-Results-2015-Outlook-Presentation.pdf [Accessed July 2017].

BARRICK. 2016a. *Annual report* [Online]. Available: http://www.barrick.com/investors/annual-report/default.aspx [Accessed July 2017].

BARRICK. 2016b. *Mineral reserves and mineral resources* [Online]. Available: http://www.barrick.com/investors/quarterly-reports/default.aspx [Accessed July 2017].

BUXTON, M. & BENNDORF, J. 2013. The use of sensor derived data in optimization along the Mine-Value-Chain. *Proceedings of the 15th International ISM Congress*, Aachen, Germany, pp. 324-336.

CLARK, R. N., SWAYZE, G. A., WISE, R., LIVO, E., HOEFEN, T., KOKALY, R. & SUTLEY, S. J. 2007. *USGS digital spectral library splib06a: U.S. Geological Survey, Digital Data Series 231* [Online]. Available: https://speclab.cr.usgs.gov/spectral-lib.html [Accessed January 2012].

CLINE, J. S., HOFSTRA, A. H., MUNTEAN, J. L., TOSDAL, R. M. & HICKEY, K. A. 2005. Carlin-type gold deposits in Nevada: Critical geologic characteristics and viable models. *Economic Geology 100th anniversary volume*, 100, 451-484.

CORBETT, G. J. & LEACH, T. M. 1998. *Southwest Pacific Rim gold-copper systems: structure, alteration, and mineralization*, Society of Economic Geologists.

DUKE, E. F. 1994. Near infrared spectra of muscovite, Tschermak substitution, and metamorphic reaction progress: Implications for remote sensing. *Geology*, 22, 621-624.

HUNT, G. R. & SALISBURY, J. W. 1971. Visible and near-infrared spectra of minerals and rocks: II. Carbonates. *Modern Geology*, 2, 23-30.

LESSARD, J., DE BAKKER, J. & MCHUGH, L. 2014. Development of ore sorting and its impact on mineral processing economics. *Minerals Engineering*, 65, 88-97.

MAROUN, L. R. C., CLINE, J. S., SIMON, A., ANDERSON, P. & MUNTEAN, J. 2017. High-Grade Gold Deposition and Collapse Breccia Formation, Cortez Hills Carlin-Type Gold Deposit, Nevada, USA. *Economic Geology*, 112, 707-740.

MARTÍN-FERNÁNDEZ, J. A., BARCELÓ-VIDAL, C. & PAWLOWSKY-GLAHN, V. 2003. Dealing with zeros and missing values in compositional data sets using nonparametric imputation. *Mathematical Geology*, 35, 253-278.

PIRAJNO, F. 1992. *Hydrothermal mineral deposits: principles and fundamental concepts for the exploration geologist*, Berlin Heidelberg, Springer-Verlag.

POST, J. L. & NOBLE, P. N. 1993. The near-infrared combination band frequencies of dioctahedral smectites, micas, and illites. *Clays and clay minerals*, 41, 639-639.

SALTER, J. & WYATT, N. 1991. Sorting in the minerals industry: past, present and future. *Minerals Engineering*, 4, 779-796.

SIVAMOHAN, R. & FORSSBERG, E. 1991. Electronic sorting and other preconcentration methods. *Minerals Engineering*, 4, 797-814.

VERHALLEN, G. J. 2016. Characterizing the valuable content of Au ores from the Cortez Hills underground deposit using digital RGB images. *MSc thesis TU Delft*.

WILLS, B. A. & FINCH, J. A. 2016. Chapter 14 - Sensor-based Ore Sorting. *Wills' Mineral Processing Technology (Eighth Edition)*. Boston: Butterworth-Heinemann.

Chapter 9.

Discussion

9.1. Applicability of sensors

9.1.1. Introduction

The presented study was mainly focussed at assessing the applicability of a VNIR-SWIR spectral sensor. The reason for this was that the first test with this type of sensor already showed that the detected alteration mineralogy could be used to characterise ore grade. For each deposit included in the study this type of indirect characterisation allowed a fraction of the waste samples to be segmented. At Lagunas Norte and Cortez, it was additionally possible to distinguish different ore types by using a VNIR-SWIR spectral sensor to detect minerals that are characteristic for these ore types.

On the Lagunas Norte samples also the applicability of a DE-XRT and a LIBS sensor was investigated. It was shown that detected density differences with the DE-XRT sensor could be used to characterise the iron content of samples and map veins of iron-bearing minerals. Even though gold mineralisation at Lagunas Norte was associated with the formation of iron-bearing minerals, the occurrence of iron-bearing minerals could not be used as an indicator of gold grade. It was therefore not possible to use a DE-XRT sensor to segment a fraction of the waste. Using DE-XRT to distinguish between different ore types was not investigated.

Testing LIBS on the Lagunas Norte samples showed that this type of sensor could not be used to detect the gold grade. This is mainly caused by the relatively low grade and heterogeneous composition of the ore. However, LIBS could be used to segment a fraction of the waste by using the measured LIBS spectra as chemical fingerprints of the alteration mineralogy. This is based on similar alteration-mineralisation relationships that allowed a VNIR-SWIR spectral sensor to be used for segmenting waste. However, the results of testing LIBS are based on a relatively small subset of samples that was selected to cover the range of gold grades of the drill core sample set. Additional research is therefore required on a sample set that covers the mineralogical variability of the ore deposit to validate the relationships between the detected alteration mineralogy and gold grade.

On the Cortez samples also the applicability of an RGB imaging sensor was investigated. This type of sensor was used to characterise differences between the visible appearance of samples, such as colour and texture. It was shown that these characteristics could also be used to segment a fraction of the waste and distinguish between different ore types.

9.1.2. Segmenting waste

Comparison of results

Table 9.1 presents an overview of the results of segmenting waste samples by using different sensors, sample sets, geochemical data sets, and data processing methods. The bold text in this figure indicates the results that are considered most representative for each deposit and sensor type. This is based on the spatial distribution of the sample set and the representativity of the associated geochemical data. In case multiple results are indicated with bold text in Table 9.1, it is unsure which result is most representative. The results of the DE-XRT sensor are not included in Table 9.1 because waste could not be segmented with this type of sensor. The results of testing the LIBS sensor on the Lagunas Norte samples are also not included because this was based on a relatively small subset of samples that did not represent the variability of the entire sample set.

It should be noted that the results for Lagunas Norte that are shown in Table 9.1 are not based on all the available geochemical assays. This is because carbonaceous samples were excluded from the classifications. This was done because no minerals could be detected on the carbonaceous samples with a VNIR-SWIR spectral sensor due to their low reflection and dark black appearance. It was shown in chapter 7 that a VNIR-SWIR spectral sensor can be used to separate the carbonaceous ore samples. Excluding carbonaceous samples from the classification on ore and waste was based on this separation.

Table 9.1 shows that significant differences sometimes occur between the results that were obtained from testing a VNIR-SWIR spectral sensor on the same deposit. For Los Bronces, this difference is mainly due to the different sample sets that were used to generate the results. Table 9.1 shows that the sample set on which SWIR hyperspectral imagery was performed has a lower average copper grade and contains more waste samples than the sample set on which VNIR-SWIR point spectroscopy was tested. This explains why the group of samples that could be segmented by using SWIR hyperspectral imagery is larger. The reason that a larger fraction of the waste can be segmented with SWIR hyperspectral imagery is because this sample set contains more waste samples with low crystalline mica and chlorite compared to waste samples with a different mineralogy. To assess the results of VNIR-SWIR point spectroscopy, geochemical assays were performed on a subset of samples that was selected to represent the entire sample set as much as possible. The subset of 43 samples for testing SWIR hyperspectral imagery was collected by selecting the most different samples within the sample set. This means that the results of testing VNIR-SWIR point spectroscopy are most representative for the entire set of 150 samples.

The differences between the results for Lagunas Norte that are shown in Table 9.1 are mainly due to the different sample sets and geochemical datasets that were used. The random grab samples of the initial sample set have a lower average gold grade and contain more waste samples than the drill core sample set. This explains why the group of samples that is segmented from the initial sample set is larger. The reason that the fraction of waste samples

Table 9.1: Overview of all the results of segmenting waste samples. The bold text indicates the results that are considered most representative for each deposit and sensor type. [1] Results are based on the set of samples on which geochemical assays were performed. [2] This percentage of samples is based on all 150 samples in the sample set. [3] Carbonaceous samples are excluded from this result. (continued on next pages)

Deposit name	Los Bronces	
Deposit type	Porphyry Cu-Mo	
Waste definition	< 0.40% Cu	
Setup		
Sensor	VNIR-SWIR point spectra	SWIR hyperspectral images
Source of sample material	mill pebbles	mill pebbles
Number of samples	150	43
Method for characterisation / mapping	calculated spectral features	spectral angle mapping
Method for data analysis	logistic regression	PCA
Geochemical data	65 sample assays	43 sample assays
Average grade of sample set	0.64% Cu	0.45% Cu
Waste in sample set	44.6%	60.5%
Result[1]		
Samples segmented	**19.3%[2]**	37.2%
Waste samples segmented	**37.9%**	57.7%
Waste samples in segmented group	**100%**	93.8%
Average grade of segmented group	**0.18% Cu**	0.20% Cu
Indicator (minerals)	low crystalline white mica, chlorite	low crystalline white mica, chlorite
Geological relationships	All the indicator minerals are generally not associated with the main ore zone in porphyry deposits.	

Table 9.1 (continued)

	Lagunas Norte			
Deposit name				
Deposit type	Epithermal Au-Ag			
Waste definition	< 0.20 ppm Au			
Setup				
Sensor	VNIR-SWIR point spectra	VNIR-SWIR hyperspectral images	VNIR-SWIR hyperspectral images	
Source of sample material	random grab samples (initial sample set)	random grab samples (initial sample set)	drill core	
Number of samples	94	36	952	
Method for characterisation / mapping	calculated spectral features	spectral angle mapping	PLS-DA & calculated spectral features	
Method for data analysis	logistic regression	PCA	PLS-DA	
Geochemical data	31 sample assays[3]	31 sample assays[3]	80 sample assays[3]	827 drill hole assays[3]
Average grade of sample set	0.26 ppm Au	0.26 ppm Au	0.76 ppm Au	0.76 ppm Au
Waste in sample set	74.2%	74.2%	52.5%	52.6%
Result[1]				
Samples segmented	54.8%	35.5%	16.3%	**7.5%**
Waste samples segmented	73.9%	47.8%	31.0%	**14.3%**
Waste samples in segmented group	100%	100%	**100%**	**91.9%**
Average grade of segmented group	0.08 ppm Au	0.08 ppm Au	**0.06 ppm Au**	**0.08 ppm Au**
Indicator (minerals)	pyrophyllite, diaspore, absence of zunyite	pyrophyllite, diaspore, absence of zunyite	pyrophyllite, dickite, illite	
Geological relationships	All the indicator minerals occur further away from the epithermal veins in which most gold is generally deposited.			

Table 9.1 (continued)

Cortez Hills Lower zone

Deposit name	Cortez Hills Lower zone		
Deposit type	Carlin type Au		
Waste definition	< 0.15 ppm Au		
Setup			
Sensor	VNIR-SWIR hyperspectral images		RGB images
Source of sample material	drill core		drill core
Number of samples	629		629
Method for characterisation / mapping	PLS-DA & calculated spectral features		calculated features
Method for data analysis	PLS-DA		classification tree
Geochemical data	210 sample assays	629 drill hole assays	629 drill hole assays
Average grade of sample set	8.69 ppm Au	5.03 ppm Au	5.03 ppm Au
Waste in sample set	40.5%	55.3%	55.3%
Result[1]			
Samples segmented	17.1%	**18.8%**	**10.3%**
Waste samples segmented	**42.4%**	**31.6%**	**17.8%**
Waste samples in segmented group	**100%**	**93.2%**	**95.4%**
Average grade of segmented group	**0.03 ppm Au**	0.13 ppm Au	**0.09 ppm Au**
Indicator (minerals)	calcite, chlorite, phlogopite, tremolite		white rock type
Geological relationships	Chlorite and tremolite are pre-ore minerals that were destroyed by the mineralising fluids. Calcite generally occurs further away from the mineralised zone. Relationship with phlogopite was not confirmed.		The white rock type represents the barren quartz porphyry dikes that were introduced after the mineralisation events.

that is segmented from the initial sample set is also larger is because more waste samples occur in the drill core sample set that do not contain any of the indicator minerals. However, as discussed in chapter 7.7.3. diaspore could not be mapped from the VNIR-SWIR hyperspectral images of the drill core samples because of interference of absorption features that were produced by shadows of the sample labels. Since the results on the initial sample set showed that diaspore can also be used as an indicator of waste, it is possible that a higher fraction of waste could be segmented from the drill core samples if diaspore was also mapped.

The difference between the two results on the random grab samples of the initial sample set of Lagunas Norte that is shown in Table 9.1 is most likely produced by the method for data analysis. This is because the same geochemical dataset was used in these two studies. Although it was discussed in chapter 6.4.4. that VNIR-SWIR hyperspectral imagery provides more detailed mineralogical information than point spectroscopy, a higher fraction of waste samples was segmented by using the VNIR-SWIR point spectra. This is because the manual classification that was used for the analysis of the VNIR-SWIR hyperspectral images was only based on mineralogical differences that were clearly observed from the produced mineral maps. Relatively subtle differences between samples were not taken into account. The PLS-DA classification model on the other hand finds the optimal solution for separating ore and waste by using all the available data. In order to do this the model may use relatively subtle differences between the samples in order to provide the best classification. Justification that such differences can be used was carried out by using cross-validation. However, since the sample set on which the PLS-DA was performed is relatively small, further validation of the classification results on a sample set that is larger and more representative of the full mineralogical variability of the deposit was needed.

For both Lagunas Norte and Cortez, Table 9.1 shows differences between the results based on sample assays and those based drill hole assays when testing the same sensor. As discussed in chapter 7.2.4. and 8.2.4, the drill hole assays are not fully representative since these were based on drill core sections of around 1 – 3 m long, while the samples that were taken from the drill core are only 5 – 20 cm long.

For Lagunas Norte, Table 9.1 shows that the number of waste samples that are segmented based on the drill hole assays is less than half of that based on the sample assays. However, the average gold grade and fraction of waste samples from the two types of assay data are almost equal. This means that compared to the entire sample set, the set of samples on which sample assays were performed contains more waste samples on which pyrophyllite, dickite and/or illite occur than waste sample with a different mineralogy. The fraction of samples that is segmented according to the drill hole assays is most representative for Lagunas Norte considering that the drill core sample set was collected with the aim to represent the mineralogical variability of the deposit as much as possible.

For Cortez, Table 9.1 shows that there is a relatively large difference between the average gold grade of the segmented group that is calculated from the sample assays data and the one that is calculated from the drill hole assay data. The average gold grade based on the sample assays is likely most representative considering the significant amount of samples on which the

assays were performed. However, in order to confirm this additional geochemical assays will be needed. As with the Lagunas Norte study, the fraction of samples that is segmented based on the drill hole assays is most representative since the drill core sample set was collected with the aim to represent the mineralogical variability of the deposit as much as possible.

Comparing the results of RGB imaging and VNIR-SWIR hyperspectral imaging for Cortez shows that more waste was segmented by using a VNIR-SWIR spectral sensor. Inspection of the segmented waste samples showed that 67% of the samples that were segmented with RGB imaging were not yet segmented with VNIR-SWIR hyperspectral imaging. This means that even more waste can be segmented by combining both sensor techniques.

Geologic relationships

The ability to segment waste with a VNIR-SWIR spectral sensor at each deposit included in the study was based on indirect relationships between detectable alteration mineral assemblages and the copper or gold grade. These relationships are different for each deposit because the physical processes that drive the mineralisation are different.

Table 9.1 shows that at Los Bronces the occurrence of low crystalline white mica and chlorite could be used as indicators of waste. The ore samples from this deposit usually contained high crystalline white mica and tourmaline. It was described in chapter 6.5. that low crystalline white mica and chlorite are more associated with an argillic type of alteration while high crystalline white mica and tourmaline are more associated with a phyllic type of alteration. Figures 4.1 and 4.2 in chapter 4.2. showed that the main ore zone at porphyry copper deposits is related to the boundary between potassic and phyllic hydrothermal alteration, and not to the argillic alteration zone. This confirms that the minerals associated with argillic alteration can be used as indicators of waste.

At Lagunas Norte, the occurrence of pyrophyllite, dickite, illite, and diapsore could be used as indicators of waste. The ore contains alunite, zunyite or no VNIR-SWIR-active alteration minerals at all. Additionally, the VNIR-SWIR spectra of the ore often shows absorption features of water that are most likely produced by fluid inclusions within quartz. The paragenetic sequence presented in Figure 7.1 in chapter 7 shows that the formation of pyrophyllite is not associated with gold mineralisation. However, this does not confirm that detecting the occurrence of pyrophyllite with a VNIR-SWIR spectral sensor can be used as an indicator of waste. This is because Figure 7.1 also shows that gold mineralisation occurred during later alteration events, which may have overprinted zones in which pyrophyllite was previously formed. It is possible though that the mineralising fluids of these later events have removed the pyrophyllite. Additional research is required to confirm this.

Figure 7.1 also shows that the formation of alunite and diaspore is associated with gold mineralisation. Concerning the alunite, this corresponds to the result of this study that ore samples contain alunite. However, that fact that the formation of diaspore is associated with gold mineralisation contradicts the result that diaspore can be used as an indicator of waste. It should be

noted though that Figure 7.1 only presents temporal relationships and no spatial relationships. It is therefore still possible that no mineralisation of gold occurred in zones where diaspore was formed.

It was shown in Figure 4.3. in chapter 4.3. that the main ore zone at high-sulphidation epithermal deposits is closest to the epithermal veins. This figure also shows that further away from the veins the alteration mineralogy gradually changes from a vuggy quartz to quartz-alunite to dickite/kaolinite-pyrophyllite to smectite/mixed layer clay. This means that pyrophyllite, dickite and illite are deposited relatively far away from the main ore zone, which confirms that these minerals can be used as indicators of waste. The reason that alunite is associated with ore can be explained by the fact that this mineral is deposited closer to the epithermal veins (Sillitoe, 1993; Simmons et al., 2005). Furthermore, the result that an absence of VNIR-SWIR active minerals is associated with ore samples is probably because these samples originate from the zone that is closest to the epithermal veins, where no SWIR-active minerals were formed. The relationship between zunyite and ore grade could not confirmed by using the paragenetic sequence or general alteration-mineralisation relationships.

Table 9.1 shows that at Cortez the occurrence of calcite, chlorite, phlogopite and tremolite can be used as indicators of waste. The occurrence kaolinite and Fe- and Mg-rich illite is also more associated with waste than with ore. Ore is associated with occurrences of Al-rich illite, dolomite, dickite and hematite. The paragenetic sequence presented in Figure 8.3 in chapter 8 shows that the formation of tremolite, chlorite (clinochlore) and kaolinite-dickite occurred during the pre-ore stage and is therefore not associated with gold mineralisation. Since Maroun et al. (2017) states that the mineralising ore fluids replaced tremolite, chlorite and dickite by illite, this confirms that detecting the occurrence of chlorite and tremolite with VNIR-SWIR spectral sensors can be used as an indicator of waste. The result that kaolinite and Fe- and Mg-rich illite are more associated with waste and that dickite and Al-rich illite are more associated with ore cannot be confirmed based on Maroun et al. (2017) or Arbonies et al. (2010). Additional research is needed in order to better understand the relationship between gold grade, detectable variations in illite composition and detectable occurrences of dickite and kaolinite. Furthermore, the occurrence of phlogopite was not observed by Maroun et al. (2017) or Arbonies et al. (2010). The occurrence of this mineral was validated by XRD analysis.

Figure 8.3 also shows that the formation of calcite is associated with gold mineralisation, while it resulted that calcite can be used as an indicator of waste. It should be noted though that Figure 8.3 only presents temporal relationships and no spatial relationships. Gold mineralisation at Cortez is associated with zones of intense decarbonatisation (Arbonies et al., 2010; Maroun et al., 2017), which is the dissolution of carbonate minerals by the hydrothermal fluids. It was discussed in chapter 4.4. that decarbonatisation near fluid conduits is commonly zoned outward to dolomite- and then calcite-stable zones (Cline et al., 2005). This means that dolomite occurs closer to the mineralised zone and explains why detected occurrences of calcite could be used as an indicator of waste, while dolomite is associated with ore.

Table 9.1 also shows that an RGB imaging sensor can be used to segment waste by separating white rock particles. This can be explained by the fact that the white rocks represent the quartz

porphyry dikes that were introduced into the deposit after the gold mineralisation events took place. As explained in chapter 8.2.1, these dikes do not host significant gold grades.

As discussed in chapter 2.5, it is uncertain if at other porphyry, epithermal and carlin-type deposits the same alteration-mineralisation relationships that can be used to segment waste as those that were used in this study. This is because the composition of the hydrothermal fluids, the influx of meteoric fluids, the fluid – host rock interaction, and alteration overprinting during deposit formation may vary. However, it did result for each deposit included in the study that the relationships that could be used to segment waste correspond to the alteration-mineralisation relationships that generally occur at that deposit type. This means that there is potential that these relationships can also be used to segment waste at other porphyry, epithermal or carlin-type deposits.

9.1.3. Segmenting refractory ore

Comparison of results

One of the objectives for Lagunas Norte and Cortez was to investigate the possibilities of using sensors to distinguish between oxide and refractory ore. Table 9.2 presents an overview of the results of segmenting refractory ore samples by using different sensors, sample sets, geochemical data sets, and data processing methods. The bold text in this figure indicates the results that are considered most representative for each deposit and sensor type. The DE-XRT and LIBS sensor are not included in Table 9.2 because the possibilities for segmenting refractory ore were not investigated for these sensor types.

Two types of refractory ore are distinguished at Lagunas Norte and Cortez. These are a sulphide refractory ore and a carbonaceous refractory ore. At Cortez these two ore types are both treated in the same way and no attempt was made to use sensors to distinguish between sulphide ore and carbonaceous ore. However, for Lagunas Norte it was investigated if it is possible to first separate the carbonaceous ore from the sample set and then segment a fraction of the sulphide ore. Table 9.2 presents only the results of segmenting the sulphide refractory ore for Lagunas Norte.

Table 9.2: Overview of all the results of segmenting refractory ore samples. The bold text indicates the results that are considered most representative for each deposit and sensor type. [1] Results are based on the set of samples on which geochemical assays were performed. [2] Carbonaceous samples are excluded from this result. [3] The required geochemical data was not available for all samples. Selection of geochemical assays was based on the gold grade and interpretation of the mine geologists. [4] The required geochemical assays were only performed on samples with > 0.1 ppm Au. (next pages)

Lagunas Norte

Deposit name	**Lagunas Norte**			
Deposit type	Epithermal Au-Ag			
Refractory ore definition	> 0.25% S			
Setup				
Sensor	VNIR-SWIR point spectra	VNIR-SWIR hyperspectral images	VNIR-SWIR hyperspectral images	
Source of sample material	random grab samples (initial sample set)	random grab samples (initial sample set)	drill core	
Number of samples	94	36	952	
Method for characterisation / mapping	calculated spectral features	spectral angle mapping	PLS-DA & calculated spectral features	
Method for data analysis	logistic regression	PCA	PLS-DA	
Geochemical data	31 sample assays[2]	31 sample assays[2]	80 sample assays[2]	286 drill hole assays[2,3]
Average grade of sample set	0.76% S	0.76% S	1.40% S	1.24% S
Refractory ore in sample set	38.7%	38.7%	52.5%	61.5%
Result[1]				
Samples segmented	29%	19.4%	**31.2%**	28.7%
Refractory samples segmented	75.0%	50.0%	**54.8%**	39.8%
Refractory samples in segmented group	100%	100%	**92.0%**	85.4%
Average grade of segmented group	2.15% S	2.80% S	**3.25% S**	2.04% S
Indicator (minerals)	pyrite	pyrite	pyrite, alunite (false)	
Geological relationships	Pyrite indicates sulphide ore because in the oxide ore this mineral is usually oxidised to iron-oxides by the supergene oxidation stage that occurred after the mineralisation events. Alunite contains sulphur, but does not influence gold recovery. Alunite is therefore not an indicator of refractory ore.			

Table 9.2 (continued)

Cortez Hills Lower zone

Deposit type	Carlin type Au		
Refractory ore definition	< 50% Au recovery		
Setup			
Sensor	VNIR-SWIR hyperspectral images		RGB images
Source of sample material	drill core		drill core
Number of samples	629		629
Method for character-isation / mapping	PLS-DA & calculated spectral features		calculated features
Method for data analysis	PLS-DA		classification tree
Geochemical data	124 sample assays[4]	293 drill hole assays[3]	629 drill hole assays
Average grade of sample set	83.0% Au recovery	79.2% Au recovery	?
Refractory ore in sample set	7.3%	14.7%	6.0%
Result[1]			
Samples segmented	**4.0%**	5.1%	**2.7%**
Refractory samples segmented	**55.6%**	25.6%	**36.8%**
Refractory samples in segmented group	**100%**	73.3%	**82.4%**
Average grade of segmented group	**10.0% Au recovery**	34.0% Au recovery	?
Indicator (minerals)	absence of SWIR-active minerals except for minor calcite		black rock type
Geological relationships	Low reflection of carbonaceous refractory ore is likely the reason that the absence of detectable SWIR-active minerals is an indicator of refractory ore.		The black colour results from a high carbon content that decreases gold recovery.

Assessing the results of using a VNIR-SWIR spectral sensor to separate the carbonaceous ore from the drill core samples of Lagunas Norte was performed by using a classification of samples that was based on visual inspection. Figure 7.31 in chapter 7 presents an example of the different types of carbonaceous samples that were classified. The coal and carbonaceous siltstone samples shown in this figure were considered carbonaceous refractory ore. Figure 7.32 shows that all these samples can be separated from the rest of the sample set. However, for the other sample groups it is unsure whether the samples represent carbonaceous ore or not. It is therefore also unsure to what extent it is possible to segment carbonaceous ore at Lagunas Norte. Additional TCM assays will be required to assess this. The carbonaceous samples that were segmented by the classification shown in Figure 7.32 were excluded from the classification results presented in Table 9.2. This was done because no minerals could be detected on these samples with a VNIR-SWIR spectral sensor.

It should be noted that data on the sulphur content or gold recovery was not available for all samples since these assays were often only performed when a sample contains a significant amount of gold. This is because distinguishing between oxide ore and refractory ore is not relevant when the gold grade of a sample is below the economic cut-off grade. The number of sample assays shown in Table 9.2 therefore sometimes differs from those in Table 9.1. Furthermore, the result of segmenting refractory ore using RGB images that is shown in Table 9.2 is based on a classification of samples using the available geochemical data and the ore routing scheme presented in Figure 8.8 in chapter 8. Due to missing data the average gold recovery of the segmented samples and the entire sample set is unknown.

The differences between the results for Lagunas Norte that are shown in Table 9.2 are mainly because of the different sample sets and geochemical datasets that were used. Only the difference between the two results on the random grab samples of the initial sample set is most likely produced by the method for data analysis. As explained in section 9.1.2, this is due to the level of detail that was taken into account during the classification of samples.

The difference between the results based on the sample assays and the drill hole assays of VNIR-SWIR hyperspectral imagery on the Lagunas Norte drill core samples is due to the fact that the total sulphur content was not available for all samples in the drill hole assay data. The sample assays on the other hand included determination of the total sulphur content on every sample that was assayed. Furthermore, the drill hole assay data is not fully representative for the samples used in the study because the samples are much smaller than the interval on which the drill hole data was collected. The VNIR-SWIR hyperspectral imagery result based on the 80 sample assays of the drill core sample set is therefore most representative for the Lagunas Norte deposit.

The difference between the two results of VNIR-SWIR hyperspectral imagery on the drill core samples of Cortez occurs for the same reasons as the difference between these results for Lagunas Norte. The gold recovery was not available for all samples in the drill hole assay data and the drill hole data is not fully representative. The gold recovery analyses included in the sample assays were performed on every sample with a gold grade > 0.1 ppm Au. This data is therefore collected by using a more structured approach. The VNIR-SWIR hyperspectral

imagery result based on the 124 sample assays of the drill core sample set is therefore most representative for the Cortez deposit. However, it should be kept in mind that the presented result is based on samples with > 0.1 ppm Au.

Comparing the results of RGB imaging with those of VNIR-SWIR hyperspectral imaging for Cortez shows that more refractory ore was segmented by using a VNIR-SWIR spectral sensor. However, the results of RGB imaging are based on all samples in the sample set while those of VNIR-SWIR hyperspectral imaging are not. When all the 210 sample assays are considered to assess the results of VNIR-SWIR hyperspectral imaging, the percentage of samples that is segmented is only 2.4% instead of the 4.0% that is shown in Table 9.2. The same applies to the results based on the drill hole data. When all the 629 drill core samples are considered, the percentage of samples that is segmented is 2.4% instead of 5.1%. The results of segmenting refractory ore samples at Cortez with VNIR-SWIR hyperspectral imaging are therefore similar to the results obtained with RGB imaging.

Geologic relationships

Table 9.2 shows that sulphide refractory ore at Lagunas Norte can be segmented by using detected occurrences of pyrite, which host the gold. This can be explained by the fact that pyrite is an iron-sulphide mineral. In the oxide ore, the pyrite was converted to iron-oxides by the supergene oxidation stage that followed the formation of the deposit. It also resulted for Lagunas Norte that detected occurrences of alunite can be used as an indicator of sulphide ore. This can be explained by the fact that alunite is a sulphate and therefore contributes to higher sulphur contents. However, it is only the pyrite that occludes the gold when the ore is processed by cyanide leaching methods and the content of alunite does not influence gold recovery. It is therefore recommended to base the classification of ore types that was presented in Table 7.1. in chapter 7 on the actual gold recovery instead of the sulphur content.

It was shown in chapter 7.7.3. that the carbonaceous refractory ore of Lagunas Norte can be separated by using the average reflection on the VNIR-SWIR spectral range in combination with detected occurrences of pyrite and quartzite. This is based on the fact that the carbon in the ore produces a relatively low reflection. Detecting occurrences of pyrite and quartzite was used to distinguish the carbonaceous ore from quartzite with a low reflection.

Table 9.2 shows that the refractory ore at Cortez can be segmented by using the absence of minerals that can be detected with a VNIR-SWIR spectral sensor. This result can be explained by the fact that many of the refractory ore samples are carbonaceous. The presence of carbon decreases the reflection of the samples, which prevents the detection of mineral absorptions with a VNIR-SWIR spectral sensor. Minor occurrences of calcite are sometimes still detected on the refractory ore samples because some of the refractory ore contains calcite veins. Table 9.2 shows that segmenting the refractory ore with an RGB sensor is also based on the low reflection of these samples that is associated with the dark black appearance.

Contrary to the results on Lagunas Norte, it was not possible to detect pyrite on the samples from Cortez with a VNIR-SWIR spectral sensor. This while pyrite does occur within the sulphide refractory ore of the Cortez Hills lower zone deposit (e.g. Arbonies et al., 2010; Maroun et al., 2017). A possible explanation for this is that the grain size of the pyrite is too small to be detected from VNIR-SWIR hyperspectral data that was used in the analysis. Pyrite produces relatively weak features on the VNIR spectral range that can easily be swamped by the reflective properties of surrounding minerals when it occurs as relatively small grain sizes.

It is likely that VNIR-SWIR spectral sensors or RGB imaging sensors can also be used to segment carbonaceous refractory ore at other epithermal and carlin-type deposits by detecting the low reflection or black colour of the ore. This is because the carbon content is directly related to the low reflection and black colour. If identification of sulphide refractory ore can be performed at other epithermal or carlin-type gold deposits is uncertain. This is because pyrite needs to occur in sufficiently large quantities and grain sizes in order to detect this mineral with a VNIR-SWIR spectral sensor and use it as an indicator of sulphide refractory ore.

Table 9.3: Overview of all the results of segmenting oxide ore samples. The bold text indicates the results that are considered most representative for each deposit and sensor type. [1] Results are based on the set of samples on which geochemical assays were performed. [2] Carbonaceous samples are excluded from this result. [3] The required geochemical data was not available for all samples. Selection of geochemical assays was based on the gold grade and interpretation of the mine geologists. [4] The required geochemical assays were only performed on samples with > 0.1 ppm Au. (next pages)

Table 9.3 (continued)

Lagunas Norte

Deposit name	Lagunas Norte	
Deposit type	Epithermal Au-Ag	
Oxide ore definition	< 0.25% S	
Set up		
Sensor	VNIR-SWIR hyperspectral images	
Source of sample material	drill core	
Number of samples	952	
Method for characterisation / mapping	PLS-DA & calculated spectral features	
Method for data analysis	PLS-DA	
Geochemical data	80 sample assays[2]	286 drill hole assays[2,3]
Average grade of sample set	1.40% S	1.24% S
Oxide ore in sample set	47.5%	38.5%
Result[1]		
Samples segmented	**17.5%**	17.1%
Oxide samples segmented	**36.8%**	32.7%
Oxide samples in segmented group	**100%**	73.5%
Average grade of segmented group	**0.06% S**	0.59% S
Indicator (minerals)	iron-oxides	
Geological relationships	Iron-oxides indicate oxide ore because these minerals are formed by the oxidation of pyrite during the supergene oxidation stage that produced the oxide ore.	

Cortez Hills Lower zone

Deposit type	Carlin type Au		
Oxide ore definition	> 50% Au recovery		
Setup			
Sensor	VNIR-SWIR hyperspectral images		RGB images
Source of sample material	drill core		drill core
Number of samples	629		629
Method for characterisation / mapping	PLS-DA & calculated spectral features		calculated features
Method for data analysis	PLS-DA		classification tree
Geochemical data	124 sample assays[4]	293 drill hole assays[3]	629 drill hole assays
Average grade of sample set	83.0% Au recovery	79.2% Au recovery	?
Refractory ore in sample set	92.7%	85.3%	38.7%
Result[1]			
Samples segmented	**56.5%**	44.0%	**17.4%**
Oxide samples segmented	**60.9%**	51.6%	**35.3%**
Oxide samples in segmented group	**100%**	100%	**70.6%**
Average grade of segmented group	**91.9% Au recovery**	92.8% Au recovery	?
Indicator (minerals)	illite, hematite		red rock type
Geological relationships	Hematite indicates oxide ore because this minerals is formed by the oxidation of pyrite during the supergene oxidation stage that produced the oxide ore. Unknown why illite relates to oxide ore.		The red colour results from a relatively high content of iron-oxide minerals such as hematite (see text on left).

9.1.4. Segmenting oxide ore

Comparison of results

Table 9.3 presents an overview of the results of segmenting oxide ore samples by using different sensors, geochemical data sets, and data processing methods. The bold text in this figure indicates the results that are considered most representative for each deposit and sensor type. The DE-XRT and LIBS sensor are not included in Table 9.3 because the possibilities for segmenting oxide ore were not investigated for these sensor types. Furthermore, the possibilities for segmenting oxide ore were not investigated on the random grab samples from Lagunas Norte and Table 9.3 therefore does not include results on these sample sets.

The results shown in Table 9.3 are based on the same classification models as the results of segmenting refractory ore that are presented in section 9.1.3. Because of this, differences between the results of using the same sensor on the same deposit also occur for the same reasons. As for segmenting refractory ore, the most representative results are the ones that are based on the sample assays.

Comparing the results of RGB imaging with those of VNIR-SWIR hyperspectral imaging for Cortez shows that more oxide ore was segmented by using a VNIR-SWIR spectral sensor. As with the classification on refractory ore, a direct comparison can actually not be made since the results of RGB imaging are based on all samples in the sample set while those of VNIR-SWIR hyperspectral imaging are not. When all the 210 sample assays are considered to assess the results of VNIR-SWIR hyperspectral imaging, the percentage of samples that is segmented is 33.3% instead of the 56.5% that is shown in Table 9.3. When all the 629 drill core samples are considered, the percentage of samples that is segmented is 20.5% instead of 44.0%. Compared to the 17.4% of samples that were segmented based on the RGB imagery data, It still results that a larger fraction of the oxide ore can be segmented by using VNIR-SWIR hyperspectral imaging.

Geologic relationships

Considering the fact that hematite is an iron-oxide mineral, Table 9.3 shows that at both Lagunas Norte and Cortez detected occurrences of iron-oxide minerals can be used as an indicator for oxide ore. This can be explained by the fact that the iron-oxides are produced by the oxidation of pyrite during the supergene oxidation stage that formed the oxide ore at these deposits. The iron-oxide minerals are therefore a direct indicator of oxide ore. Because of this, it is likely that VNIR-SWIR spectral sensors can also be used to segment oxide ore at other epithermal and carlin-type deposits. This also applies to the RGB imaging sensor since a relatively high abundance of iron-oxide minerals is the reason for the red colour of the oxide ore samples. Finally, it is unknown why it resulted that illite is associated with the oxide ore of Cortez.

Deposit name	Cortez Hills Lower zone	
Deposit type	Carlin type Au	
Leach ore definition	< 5.14 ppm Au	
Setup		
Sensor	VNIR-SWIR hyperspectral images	
Source of sample material	drill core	
Number of samples	629	
Method for characterisation / mapping	PLS-DA & calculated spectral features	
Method for data analysis	PLS-DA	
Geochemical data	210 sample assays	629 drill hole assays
Average grade of sample set	8.69 ppm Au	5.03 ppm Au
Leach ore in sample set	71.9%	80.3%
Result[1]		
Samples segmented	48.0%	**57.8%**
Leach ore samples segmented	**66.9%**	71.9%
Leach ore samples in segmented group	**100%**	97.8%
Average grade of segmented group	**0.19 ppm Au**	0.51 ppm Au
Indicator (minerals)	calcite, chlorite, phlogopite, tremolite, dolomite, kaolinite, dickite, Fe-/Mg-rich illite	
Geological relationships	Al-rich illite and hematite are associated with mill grade ore. For hematite this is because gold was originally deposited in pyrite, which was oxidised to hematite. The relationship between illite composition and ore grade was not confirmed.	

9.1.5. Segmenting leach grade ore

Comparison of results

One of the objectives for Cortez was to investigate the possibilities of using sensors to distinguish between leach grade and mill grade ore based on a cut-off of 5.14 ppm Au. Table 9.4 presents an overview of the results of segmenting leach grade ore samples by using a VNIR-SWIR spectral sensor. The bold text in this figure indicates the results that are considered most representative. Table 9.4 shows that there is a relatively large difference between the average gold grade of the segmented group that is calculated from the sample assays data and the one that is calculated from the drill hole assay data. This is mainly because the drill hole assays are not fully representative of the samples used in the study. The average gold grade based on the sample assays is therefore most representative. Considering the fraction of samples that is segmented, the result based on the drill hole assays is most representative since this is based on all the samples in the sample set.

Geologic relationships

Table 9.4 shows that occurrences of calcite, chlorite, phlogopite, tremolite, dolomite, kaolinite, dickite, and Fe- and Mg-rich illite can all be used as indicators of heap grade ore. Mill grade ore is associated with the occurrence of Al-rich illite and hematite. The fact that illite is associated with mill grade ore is confirmed by Maroun et al. (2017). However, it is not confirmed that Fe- and Mg-rich illites are more associated with heap leach material. Additional research is needed in order to better understand the relationship between gold grade and detectable variations in illite composition. The reason that hematite is associated with mill grade ore probably results from the fact that gold was originally deposited in pyrite, which was oxidised to hematite by the supergene oxidation stage.

9.1.6. Image data versus point data

Tables 9.1. to 9.4. show that this study was based on VNIR-SWIR spectral data that was acquired with point spectrometers as well as hyperspectral imagers. Hyperspectral imaging has several advantages over point spectrometry regarding the mineralogical information that can be extracted from the VNIR-SWIR data. These advantages are related to the capability of VNIR-SWIR hyperspectral imaging sensors to acquire the data at a relatively high spatial resolution (i.e. small pixel size).

The surface area that is represented by a single SWIR spectrum is much smaller with most hyperspectral imagers than with commonly used point spectrometers. The spot size of SWIR point spectrometers is often in the order of several cm2 (e.g. ASD, 2015), while SWIR hyperspectral imagers usually acquire spectra on a pixel size below 1 mm2 (e.g. Corescan, 2015; Specim, 2015). This relatively small pixel size allows minerals to be detected that occur in relatively low

quantities. Such minerals can sometimes not be detected with point spectrometers because the absorption features can be obscured by those of surrounding minerals.

The relatively small pixel size in hyperspectral imaging also provides spectra of pure minerals while point spectrometry frequently yields mixed spectra with absorption features by two or three minerals. The pure mineral spectra can be used to extract parameters that describe differences in the composition or crystallinity of certain minerals. Although these parameters can also be extracted from mixed mineral spectra, these will be less accurate since they can be affected by the absorption features of the other minerals.

Another advantage of VNIR-SWIR hyperspectral imaging is that a large number of spectra (± 50 000 per sample) are acquired simultaneously. This allows the VNIR-SWIR-active mineralogy at the surface of samples to be quantified by classifying each spectrum on the mineral and/or mineral characteristic that it represents and counting the number of times that a certain classification occurs. This can be used to distinguish between smaller compositional differences such as the occurrence or relative amount of specific mineral species.

Finally, SWIR hyperspectral imaging has the advantage that the spectral information can be displayed in an image. This provides data about the distribution of the SWIR-active mineralogy which can be used to characterize differences in texture including grain sizes and cross-cutting vein structures.

9.2. Research methodology

9.2.1. Sample sets

When investigating the possibilities of using alteration-mineralisation relationships for sensor-based particle-by-particle sorting it is important that the sample set on which this is based covers the geologic and mineralogic variability of the deposit. This is because it is unknown to what extent the obtained results are representative if such a sample set was not used, as was the case for the Los Bronces study. For Los Bronces it can actually be expected that the results are not fully representative because the samples originate from the oversize output of a SAG mill that generally represents the harder portion of the ore that is feeding the processing plant. Furthermore, all samples were collected at one moment in time and it is therefore likely that they mainly represent the portion of the deposit that was being mined at the time. Because of this, validation of the results on a sample set that is representative of the full mineralogical variability of the deposit is still required for Los Bronces.

The importance of using a representative sample set was also shown by the Lagunas Norte study. This study was initially based on a random collection of samples and later on a set of drill core samples that were selected with the aim to represent the variability of the deposit as much as possible. Although most of the results that were obtained on the initial samples were validated by the results obtained on the drill core samples, there were also some differences. On the drill core sample set it resulted for example that the occurrence of dickite and illite can be used as indicators of waste. This did not result from the research on the initial samples because the occurrence of illite was not observed on this sample set and the occurrence of dickite was observed on only a few samples. Furthermore, on the initial sample set it resulted that carbonaceous ore can be identified by using the low reflection that can be detected with a VNIR-SWIR spectral sensor. However, testing the same sensor on the drill core samples showed that also non-carbonaceous samples with a low reflection occurred. Identification of the carbonaceous ore was still possible, but additional data processing steps were needed to distinguish it from the non-carbonaceous ore with a low reflection.

It is recommended to use drill core samples for investigating sensor-based particle-by-particle sorting solutions. This is because the acquisition of drill core samples is already aimed at capturing the geologic and mineralogic variability of a deposit. Using drill core samples also allows sensor-based sorting opportunities to be investigated at a relatively early stage since

drill core samples are usually collected ahead of mining. Another advantage of using drill core samples is that the sensors can also be used to maximise the information that is obtained from exploration drilling. As explained in chapter 2.4, this is likely cost effective since drill core samples are relatively expensive to obtain and analyse. Sensors can provide additional mineralogical and chemical information that can be used to increase the understanding of the physical processes that led to deposit formation and improve deposit models.

When investigating sensor-based particle-by-particle sorting solutions it is important that the particle size of the samples that are used approximately match the particle size on which sensor-based sorting needs to be performed. The reason for this is that the variability in ore grade is often larger for a smaller particle size because the ore minerals are not uniformly distributed. This is also referred to as the nugget effect. Because of the nugget effect, the sensor-based particle-by-particle sorting opportunities on relatively large boulders may be different than those on small grains. Furthermore, it is important that geochemical assays are performed on the individual particles due to the nugget effect. Significant differences were observed between the drill hole data of the Lagunas Norte and Cortez samples and the assays that were performed on these samples. The drill core samples that were assayed were also around 5 − 20 cm long, while the drill hole data was based on 1 − 3 m long drill core samples. Using unrepresentative geochemical data greatly affects the ability to develop sensor-based sorting solutions since the relationships between sensor data and ore grade that are found might not be valid or relationships might not be found while they do exist.

9.2.2. Multivariate data analysis

Principle Component Analysis (PCA), logistic regression, Partial Least Squares (PLS) regression and Partial Least Squares Discriminant Analysis (PLS-DA) were used to facilitate the analysis of the sensor data that was acquired in this study. The advantage of using these multivariate data analysis techniques is that this provides a relatively quick and easy method to investigate whether the sensor data can be used to segment waste from ore or distinguish between different ore types. This is especially the case when the dataset includes many different samples and the sensor data is comprised of many different variables.

Chapter 6.4. showed that PCA is an effective technique to compare the results of mineral mapping from VNIR-SWIR hyperspectral images with the distribution of ore and waste samples. Chapter 7.4. showed that PCA is also useful for comparing the measured LIBS spectra with the distribution of ore and waste. In both cases the ore-waste distribution was largely described by the first Principle Component (PC). This means that the variables in the dataset that constitute the largest amount of variance between the samples are related to differences that occur between ore and waste. However, this will not be the case for every study in which the relationships between sensor data and ore grade are investigated. When the variance of variables that are not related to the ore-waste distribution is relatively large, it is possible that differences between ore and waste are described by higher order PCs that represent only a small portion of the total amount of variance. In this case the differences between ore and waste that

occur within the sensor data are not found when only the score values on the first few PCs are analysed. The risk that this occurs is especially high when PCA is performed on raw spectral data in which differences between ore and waste are represented by relatively small spectral features. In case no relationships between sensor data and the ore-waste distribution are found with PCA, it is recommended to investigate if a classification model such as PLS-DA can be used to segment waste.

Chapter 6.3.3. showed that multivariate logistic regression is an effective technique to investigate whether a set of calculated features from VNIR-SWIR spectral sensor data can be used to estimate a probability that a sample is ore or waste. However, the logistic regression models presented in this chapter show that the classification performance was significantly improved by comparing the initial classification results with the VNIR-SWIR-active mineralogy of samples and redefining the ore and waste classes. This means that the method of using logistic regression for segmenting waste samples is more effective when prior knowledge on the VNIR-SWIR-active mineralogy of samples is available.

It was discussed in chapter 6.3.5. that it was not possible to use Partial Least Squares (PLS) regression to predict the copper grades of samples from the VNIR-SWIR spectral data. This was expected since none of the Cu-bearing minerals that were identified from the Los Bronces samples with petrography produce any diagnostic absorption feature in the VNIR-SWIR spectral range. PLS regression or any other form of regression analysis is only useful when some sort of a direct relationship between the sensor data and ore grade exists. However, it is more likely that relationships between hydrothermal alteration mineralogy and ore grade are indirect, meaning that specific alteration mineral assemblages constitute only certain ranges of ore grades. Instead of using regression to find these relationships, it is therefore better to categorize the distribution of grades and use a classification model such as logistic regression or PLS-DA. Alternatively, PCA or some kind of cluster analysis could be used.

It was shown in chapters 7.5, 7.7. and 8.3. that PLS-DA is a useful technique for investigating the possibilities of using spectral or mineralogical data to segment a population of waste samples and distinguish between oxide and sulphide ore. The main advantage of PLS-DA over logistic regression is that it is able to handle high dimensional data (nr of variables > nr of samples). This is especially useful when investigating classification possibilities based on spectral data. In case logistic regression is applied to spectra, some kind of variable selection is often required in order to cope with the high dimensionality. In chapter 6.3. this was performed by calculating a set of spectral features that represent specific mineral occurrences. However, the PLS-DA model is able to handle such data since the predictions are based on a relatively small set of orthogonal components that describe the covariance between the predictor data and the classes. By using these components PLS-DA is also able to handle strongly collinear and noisy predictor variables (Wold et al., 2001).

Sensor-based particle-by-particle sorting of ore and waste often already provides economic benefits if only a fraction of the waste material can be eliminated. However, misclassification of the ore may significantly reduce the economic viability of the technique. A possible improvement for analysing the possibilities of segmenting waste is therefore to use a classification

model in which a different cost can be assigned to the misclassification of ore and waste during model calibration. It is recommended to investigate the applicability of such models for future research.

9.2.3. Mineralogy mapping from VNIR–SWIR hyperspectral images

Different methods were used throughout chapters 6 and 7 to map the mineralogy from VNIR-SWIR hyperspectral images. First of all, Spectral Angle Mapping (SAM) was used to map the mineralogy from the SWIR hyperspectral images described in chapter 6.4. This method is in general most commonly used (e.g. Girouard et al., 2004; Kruse, 2012; Rowan et al., 2005). Unknown spectra are classified with SAM by calculating the multi-dimensional angles to a set of reference spectra. The mineral or mineral assemblage that is assigned to the unknown spectrum is that of the reference spectrum with the smallest angle.

Instead of multi-dimensional angles, it is also possible to calculate correlation coefficients to the set of reference spectra. In this case the mineral that is assigned to the unknown spectrum is that of the reference spectrum with the highest correlation coefficient. This method was used to map the mineralogy from the SWIR hyperspectral images described in chapter 7.6. The reason for choosing a different method was because different software was used for processing the hyperspectral images. Mineral mapping using SAM or correlation coefficients are mathematically relatively similar.

In chapters 7.7. and 8.3. the mineralogy was mapped from SWIR hyperspectral images by using PLS-DA. This was performed by calibrating a PLS-DA model on the set of reference spectra for each mineral occurrence. This set of reference spectra contained spectra of pure minerals as well as mineral mixtures. One of the advantages of using PLS-DA over SAM or correlation coefficients is that the classification is based on the occurrence of mineral absorption features instead of the similarity between spectra. With SAM or correlation coefficients each different mineral assemblage needs to be classified separately, which often results in a large number of different classes into which spectra are classified. With PLS-DA the occurrence of each mineral is determined regardless of the occurrence or absence of absorption features of other minerals. This makes it easier to inspect the mineral mapping results and to quantify the mineral composition of each sample for further classification. Furthermore, PLS-DA might still be able to classify mineral occurrences from mixed mineral spectra that were not included in the set of reference spectra. However, this was not confirmed.

Another advantage of using PLS-DA over SAM or correlation coefficients is that the classification performance can be evaluated by inspecting the calculated responses. Examples of this are presented in figures 7.35. and 8.11. in chapters 7 and 8. Furthermore, the scores and loadings of the PLS-DA models can be inspected to confirm that the classifications are based on the absorption features of the minerals that are classified.

The only drawback of using PLS-DA for mineral mapping is that it is not always possible to correctly classify mineral spectra that are relatively similar. In the study presented in chapter 8.3. for example it was not possible to use PLS-DA to distinguish between the spectra of kaolinite and dickite. However, with most other methods for mineral mapping, including SAM and correlation coefficients, this problem will likely also occur. A possible solution for this is to reduce the unrelated variability by first sub setting the spectra to the spectral range on which differences between the minerals occur and then apply a classification model. Alternatively, it is possible to classify the mineral spectra that are similar as one group and distinguish between the minerals by calculating characteristic absorption feature positions.

9.3. Feasibility of sensor–based particle–by–particle sorting

For each deposit included in the study a fraction of the waste could be segmented by using a VNIR-SWIR spectral sensor to detect the alteration mineralogy. For Cortez it was additionally possible to segment a fraction of the waste by identifying specific rock types with an RGB imaging sensor. This study therefore contributed towards the development of sensor-based sorting for removing waste from the ore that is mined at hydrothermal deposits. However, for each deposit additional research is required to investigate whether it is economically feasible to use sensor-based sorting machines to remove a fraction of the waste. The economic feasibility depends on the costs of sorting, the costs of conventional processing, the sorting efficiency, the amount of waste that is rejected, and the value of the minerals that are contained by the waste. Sensor-based particle-by-particle sorting provides economic benefits if the value of the minerals that are lost by discarding material do not exceed the difference in costs between sensor-based sorting and conventional ore processing. Based on Table 9.1, there is potential that removing waste with sensor-based particle-by-particle sorting can provide economic benefits for each deposit. This is because this table shows that at each deposit a significant amount of material could be segmented at a grade that is well below the cut-off grade for economic processing.

For Lagunas Norte and Cortez a VNIR-SWIR spectral sensor could also be used to distinguish different ore types. For Cortez it was additionally possible to use an RGB imaging sensor to distinguish different ore types. This study therefore also contributed towards the development of sensor-based sorting of ore types. As for sorting waste, additional research is required to investigate whether it is economically feasible to use sensor-based sorting machines to sort the different ore types. The economic feasibility will depend on the costs of sorting, the efficiency of the sorting machine, and the economic benefits of processing the sorted ore types compared to the costs of processing mixed ore types. The potential of sorting different ore types could not be assessed since it is unknown what the economic benefits are of processing sorted ore types instead of processing mixed ore types.

The next step to introducing sensor-based particle-by-particle sorting at Los Bronces is to validate the results shown in Table 9.1 on a sample set that is representative of the full

mineralogical variability of the deposit. As was done in this study for Lagunas Norte and Cortez, it is recommended to use drill core samples for such a validation step. The next step to introducing sensor-based particle-by-particle sorting at Lagunas Norte and Cortez is to investigate if the results that were obtained in this study can also be achieved with a sensor-based sorting machine. This investigation should be performed on mined material of a sortable particle size. Additionally, it needs to be investigated if other sensor techniques can be used to segment waste from ore and distinguish between ore types. This is because a more robust separation in terms of misclassification can likely be achieved if different types of sensor data can be used to identify waste and different ore types. Furthermore, it might be possible to segment a larger portion of the waste or a specific ore type by integrating the data that is provided by different sensors. It was already discussed in chapter 9.1.2. that for Cortez a larger fraction of the waste can be segmented if the data of a VNIR-SWIR spectral sensor is combined with that of an RGB imaging sensor. Additional research is required, however, to further investigate the classification possibilities of combining both sensor types in more detail.

9.4. References

ARBONIES, D. G., CREEL, K. D. & JACKSON, M. L. 2010. Cortez Hills Lower Zone discovery and geologic update. *Proceedings of the Geological Society of Nevada symposium: Great Basin evolution and metallogeny.* Reno, Nevada, USA.

ASD. 2015. *ASD products & services* [Online]. Available: https://www.asdi.com/products-and-services [Accessed February 2015].

CLINE, J. S., HOFSTRA, A. H., MUNTEAN, J. L., TOSDAL, R. M. & HICKEY, K. A. 2005. Carlin-type gold deposits in Nevada: Critical geologic characteristics and viable models. *Economic Geology 100th anniversary volume*, 100, 451-484.

CORESCAN. 2015. *The corescan system* [Online]. Available: http://www.corescan.com.au/services/the-corescan-system [Accessed February 2015].

GIROUARD, G., BANNARI, A., EL HARTI, A. & DESROCHERS, A. Validated spectral angle mapper algorithm for geological mapping: comparative study between QuickBird and Landsat-TM. *XXth ISPRS Congress, Geo-Imagery Bridging Continents*, Istanbul, Turkey, 2004. 12-23.

KRUSE, F. A. 2012. Mapping surface mineralogy using imaging spectrometry. *Geomorphology*, 137, 41-56.

MAROUN, L. R. C., CLINE, J. S., SIMON, A., ANDERSON, P. & MUNTEAN, J. 2017. High-Grade Gold Deposition and Collapse Breccia Formation, Cortez Hills Carlin-Type Gold Deposit, Nevada, USA. *Economic Geology*, 112, 707-740.

ROWAN, L. C., MARS, J. C. & SIMPSON, C. J. 2005. Lithologic mapping of the Mordor, NT, Australia ultramafic complex by using the Advanced Spaceborne Thermal Emission and Reflection Radiometer (ASTER). *Remote sensing of Environment*, 99, 105-126.

SILLITOE, R. 1993. Epithermal models: genetic types, geometrical controls and shallow features. *Mineral Deposit Modeling: Geological Association of Canada Special Paper*, 40, 403-417.

SIMMONS, S. F., WHITE, N. C. & JOHN, D. A. 2005. Geological characteristics of epithermal precious and base metal deposits. *Economic Geology 100th anniversary volume*, 29, 485-522.

SPECIM. 2015. *Hyperspectral imaging in geology* [Online]. Available: http://www.specim.fi/hyperspectral-imaging-in-geology [Accessed February 2015].

WOLD, S., SJÖSTRÖM, M. & ERIKSSON, L. 2001. PLS-regression: a basic tool of chemometrics. *Chemometrics and intelligent laboratory systems*, 58, 109-130.

Chapter 10.

Conclusions

10.1. Applicability of sensors

Sensors can be applied throughout the entire mining value chain to collect information on the characteristics of the mined ore in real-time. The information that sensors provide can potentially be used to improve deposit models, improve ore quality control and optimise mineral processing. Furthermore, sensor-based sorting offers potential economic and environmental benefits by using it to eliminate waste from subsequent processing steps or to sort different ore types.

For all the deposits included in this study a fraction of the waste could be segmented by using sensors to detect the hydrothermal alteration mineralogy. This was based on indirect relationships between specific alteration mineral assemblages and the copper or gold grade. Since these relationships correspond to the alteration-mineralisation relationships that generally occur at each deposit type, there is potential that sensors can also be used to segment waste at other porphyry, epithermal or carlin-style deposits.

10.2. Los Bronces

For Los Bronces the applicability of VNIR-SWIR spectral sensors was investigated. This type of sensor could not be used to detect copper-bearing minerals directly. It could be used to segment a significant fraction of the waste by detecting specific alteration mineral assemblages. It is recommended to confirm these results on a sample set that is representative of the full mineralogical variability of the deposit before starting test trials with sensor-based sorting machines.

10.3. Lagunas Norte

For Lagunas Norte the applicability of a DE-XRT, LIBS and VNIR-SWIR spectral sensor was investigated. The DE-XRT sensor could not be used to segment waste. A LIBS sensor could be used to segment a fraction of the waste by using the LIBS spectra as chemical fingerprints of the alteration mineralogy. This was based on a relationship between the content of Al- and Ti-bearing alteration minerals and the gold grade. Since the results of testing LIBS are based on a relatively small set of samples, additional research is required on a sample set that covers the full mineralogical variability of the deposit to validate this relationship.

VNIR-SWIR spectral sensors could be used to segment a fraction of the waste from the Lagunas Norte ore by detecting specific alteration mineral assemblages. Furthermore, the VNIR-SWIR spectral sensors could be used to separate carbonaceous ore, a fraction of the sulphide ore, and a fraction of the oxide ore. Carbonaceous ore could be distinguished by using the average reflection and detected occurrences of pyrite and dark quartzite. A fraction of the sulphide ore could be segmented by detecting the occurrence of pyrite. Segmenting oxide ore was based on detecting the occurrence of iron-oxide and water. The sample set used in the Lagunas Norte study may not be fully representative of the geological and mineralogical variability of entire deposit. This was indicated by the occurrence of zunyite throughout two different sample sets.

10.4. Cortez

For Cortez Hills the applicability of an RGB imaging sensor and a VNIR-SWIR spectral sensor was investigated. Both sensors could be used to segment a fraction of the waste, segment a fraction of the refractory ore, and segment a fraction of the oxide ore. The ability to segment waste with an RGB imaging sensor was based on the identification of quartz porphyry dike material having a bright white appearance. This material does not host significant gold since it was deposited after gold mineralisation took place. Segmenting a fraction of the refractory ore with RGB imaging was based on the dark black appearance of this ore type. Oxide ore could be segmented by using the red or pink appearance of this ore type.

The ability to segment waste from the Cortez ore with a VNIR-SWIR spectral sensor was based on detecting specific alteration mineral assemblages. Refractory ore could be segmented with a VNIR-SWIR sensor by using the absence of detectable minerals and minor occurrences of calcite. Segmenting oxide ore was based on detecting occurrences of iron-oxide and illite. Additionally, the VNIR-SWIR spectral sensor could be used to segment a fraction of the heap leach grade ore by detecting specific alteration mineral assemblages. Especially variations in the composition of carbonate and illite were useful indicators of gold mineralisation.

10.5. Overall conclusions and recommendations

For all three deposits additional research is required to investigate whether it is economically feasible to use the discrimination capabilities of the VNIR-SWIR spectral sensor for sensor-based particle-by-particle sorting. The feasibility may be limited by surface contaminations of the ore particles feeding the sorter, the influence of water on the discrimination capabilities of the VNIR-SWIR sensor, and the sorting efficiency resulting from misclassification.

It is recommended to investigate to what extent the results from this study can be reproduced with a sensor-based sorting machine. It is also recommended to investigate if other real-time sensor techniques can be used to segment waste from ore and distinguish between ore types. This is because a more robust separation in terms of misclassification can likely be achieved if different types of sensor data can be used to identify waste and different ore types. Furthermore, it might be possible to segment a larger portion of the waste or a specific ore type by integrating the data that is provided by different sensors.

Another recommendation is to acquire VNIR-SWIR hyperspectral imaging data on all the drill core samples that are obtained from exploration drilling at every hydrothermal ore deposit that will be mined in the future. Utilising these sensors to characterise the drill core samples produced from exploration drilling offers potential to substantially increase the amount of information that is obtained from exploration studies. This is likely cost effective, since drill core samples are relatively expensive to obtain and analyse using conventional methods. Furthermore, the obtained sensor data can be used to investigate potential sensor-based sorting opportunities at a relatively early stage.

Overall, the presented study showed that there is significant potential that the VNIR-SWIR spectral sensor can be used for sensor-based particle-by-particle sorting of waste and different ore types at mining operations exploiting hydrothermal ore deposits. This means that this study contributed towards the development of more efficient and sustainable techniques for the beneficiation of the ores that are extracted from these deposits.

Scores and loadings plots of PLS–DA classifications

A.1. PLS-DA classifications presented in chapter 7.7.

This appendix presents the scores and loadings plots of one of the PLS-DA classifications that were performed on the mineralogical data that was extracted from the VNIR-SWIR hyperspectral images of the drill core samples of the Lagunas Norte study.
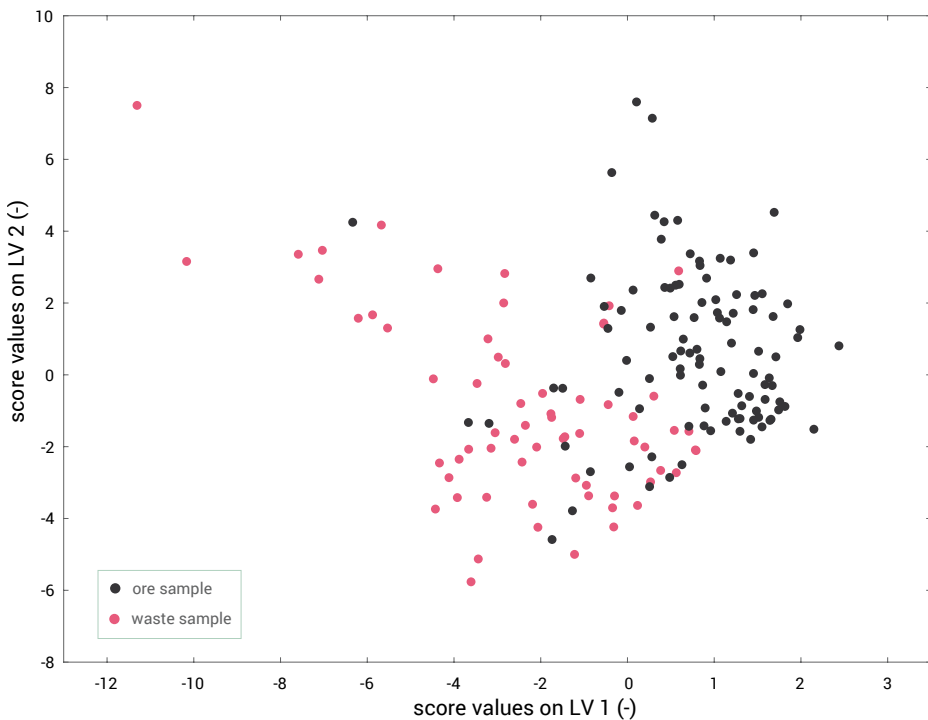
A.1.1. Classification of oxide and sulphide ore

● oxide ore sample   ● sulphide ore sample
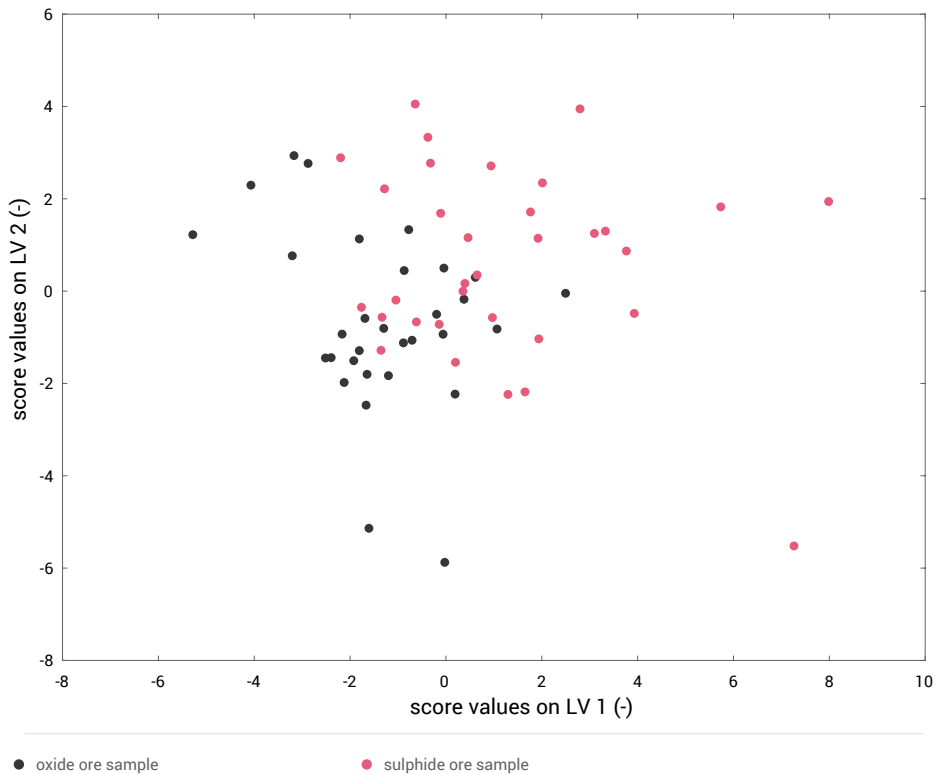
Figure A.1: PLS-DA sample score values on the first and second latent variable (LV) of the classification of oxide and sulphide ore samples.

1. pyrophyllite - absorption intensity distribution

2. alunite - absorption intensity distribution

3. dickite - absorption intensity distribution

4. illite-dickite - absorption intensity distribution

5. iron-oxide - absorption intensity distribution

6. iron-oxide absorption feature - minimum position distribution

7. a fraction of pyrite pixels

7. b fraction of jarosite pixels

7. c water absorption feature - average intensity

Figure A.2: PLS-DA loadings of the first latent variable of the classification of oxide and sulphide ore samples.

1. pyrophyllite - absorption intensity distribution

2. alunite - absorption intensity distribution

3. dickite - absorption intensity distribution

4. illite-dickite - absorption intensity distribution

5. iron-oxide - absorption intensity distribution

6. iron-oxide absorption feature - minimum position distribution

7. a fraction of pyrite pixels

7. b fraction of jarosite pixels

7. c water absorption feature - average intensity

Figure A.3: PLS-DA loadings of the second latent variable of the classification of oxide and sulphide ore samples.

A.2. PLS-DA classi–
fications presented
in chapter 8.3.

This appendix presents the scores and loadings plots of the PLS-DA classifications that were performed on the mineralogical data that was extracted from the VNIR-SWIR hyperspectral images of the drill core samples of the Cortez study.

A.2.1. Classification of ore and waste

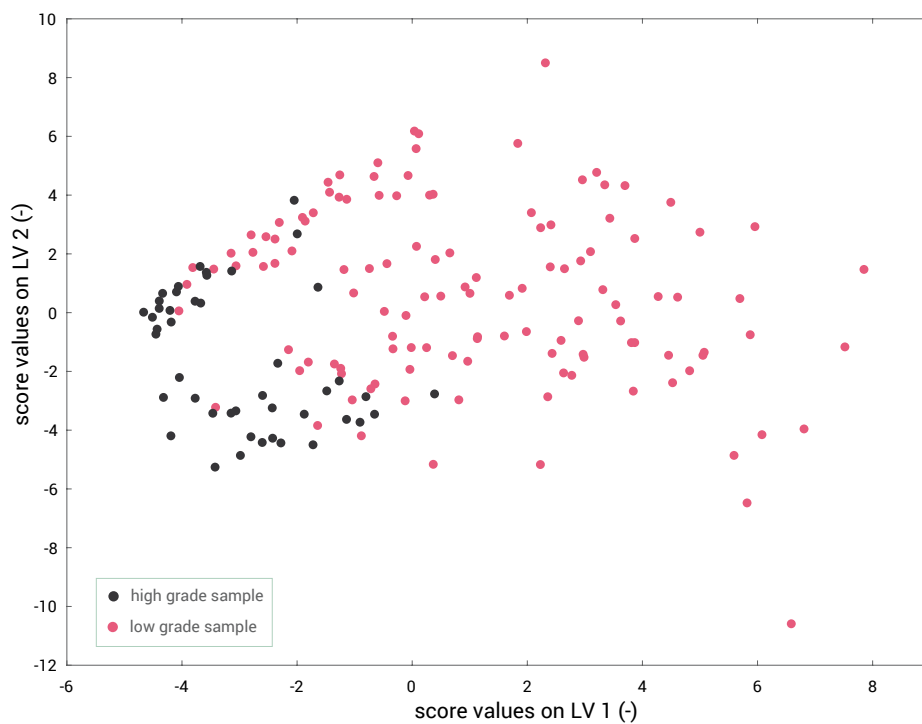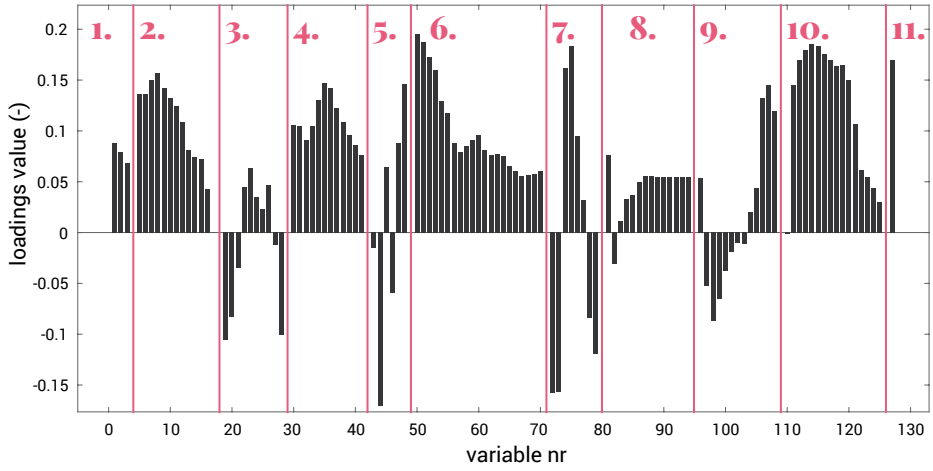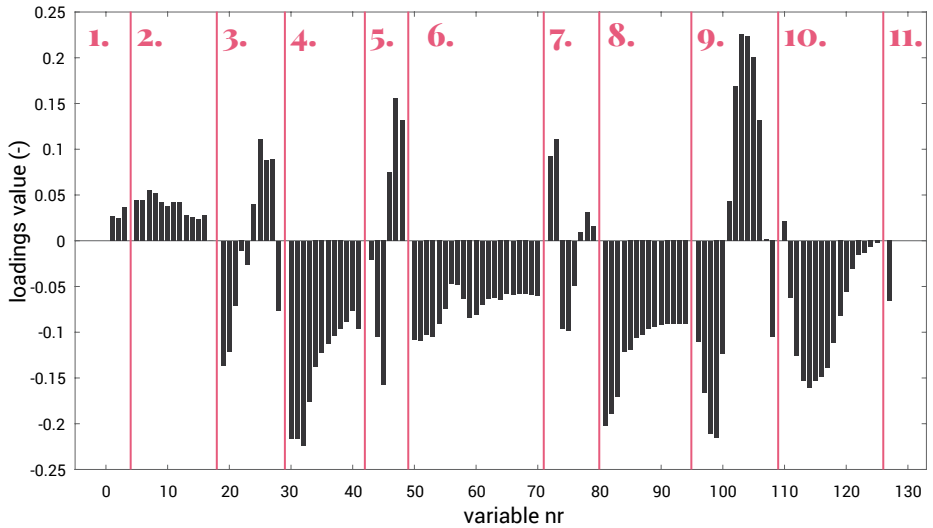*Figure A.4: PLS-DA sample score values on the first and second latent variable (LV) of the classification of ore and waste samples.*
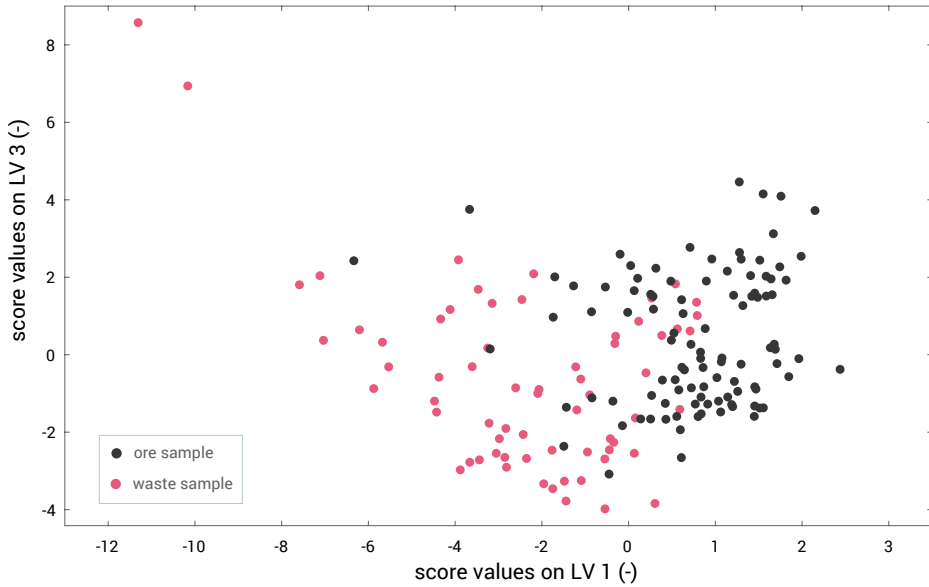
Figure A.5: PLS-DA sample score values on the first and third latent variable (LV) of the classification of ore and waste samples.

1. fraction of pixels with chlorite, phlogopite and tremolite absorption features

2. carbonate - absorption intensity distribution

3. carbonate - distribution of minimum position

4. illite - absorption intensity distribution

5. illite - distribution of minimum position

6. kaolinite-dickite - absorption intensity distribution

7. kaolinite-dickite - distribution of minimum position

8. iron-oxide - absorption intensity distribution

9. iron-oxide - distribution of minimum position

10. distribution of the average reflection of pixels

11. water absorption feature - average intensity

Figure A.6: PLS-DA loadings of the first latent variable of the classification of ore and waste samples.

1. fraction of pixels with chlorite, phlogopite and tremolite absorption features

2. carbonate - absorption intensity distribution

3. carbonate - distribution of minimum position

4. illite - absorption intensity distribution

5. illite - distribution of minimum position

6. kaolinite-dickite - absorption intensity distribution

7. kaolinite-dickite - distribution of minimum position

8. iron-oxide - absorption intensity distribution

9. iron-oxide - distribution of minimum position

10. distribution of the average reflection of pixels

11. water absorption feature - average intensity

Figure A.7: PLS-DA loadings of the second latent variable of the classification of ore and waste samples.

1. fraction of pixels with chlorite, phlogopite and tremolite absorption features

2. carbonate - absorption intensity distribution

3. carbonate - distribution of minimum position

4. illite - absorption intensity distribution

5. illite - distribution of minimum position

6. kaolinite-dickite - absorption intensity distribution

7. kaolinite-dickite - distribution of minimum position

8. iron-oxide - absorption intensity distribution

9. iron-oxide - distribution of minimum position

10. distribution of the average reflection of pixels

11. water absorption feature - average intensity

Figure A.8: PLS-DA loadings of the third latent variable of the classification of ore and waste samples.

A.2.2. Classification of low and high grade ore

Figure A.9: PLS-DA sample score values on the first and second latent variable (LV) of the classification of low and high grade ore samples.

1. fraction of pixels with chlorite, phlogopite and tremolite absorption features
2. carbonate - absorption intensity distribution
3. carbonate - distribution of minimum position
4. illite - absorption intensity distribution
5. illite - distribution of minimum position
6. kaolinite-dickite - absorption intensity distribution
7. kaolinite-dickite - distribution of minimum position
8. iron-oxide - absorption intensity distribution
9. iron-oxide - distribution of minimum position
10. distribution of the average reflection of pixels
11. water absorption feature - average intensity

Figure A.10: PLS-DA loadings of the first latent variable of the classification of low and high grade ore samples.

1. fraction of pixels with chlorite, phlogopite and tremolite absorption features
2. carbonate - absorption intensity distribution
3. carbonate - distribution of minimum position
4. illite - absorption intensity distribution
5. illite - distribution of minimum position
6. kaolinite-dickite - absorption intensity distribution
7. kaolinite-dickite - distribution of minimum position
8. iron-oxide - absorption intensity distribution
9. iron-oxide - distribution of minimum position
10. distribution of the average reflection of pixels
11. water absorption feature - average intensity

Figure A.11: PLS-DA loadings of the second latent variable of the classification of low and high grade ore samples.

A.2.3. Classification of oxide and refractory ore

Only one latent variable (LV) was used in the classification of oxide and refractory ore. On this LV oxide ore samples have relatively high score values and refractory ore samples have low score values.
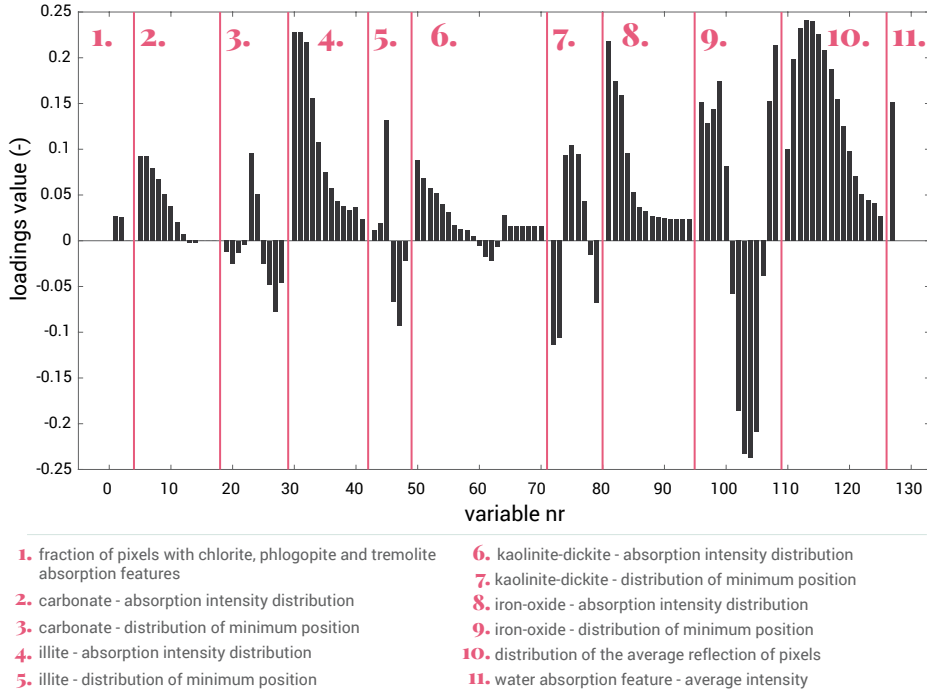

1. fraction of pixels with chlorite, phlogopite and tremolite absorption features
2. carbonate - absorption intensity distribution
3. carbonate - distribution of minimum position
4. illite - absorption intensity distribution
5. illite - distribution of minimum position
6. kaolinite-dickite - absorption intensity distribution
7. kaolinite-dickite - distribution of minimum position
8. iron-oxide - absorption intensity distribution
9. iron-oxide - distribution of minimum position
10. distribution of the average reflection of pixels
11. water absorption feature - average intensity

Figure A.12: PLS-DA loadings of the first latent variable of the classification of oxide and refractory ore samples.

Aknowledgements

Curriculum vitae

Marinus Dalm was born on the 19th of May 1984, in Haarlemmermeer, the Netherlands. He studied Applied Earth Sciences at Delft University of Technology (TU Delft) in the Netherlands, from which he obtained his BSc degree in 2007. He continued his studies in earth sciences following the Resource Engineering track, and obtained his MSc degree in 2011. During his master studies, he took part in the European Mining Course, which was a joint program between Aalto University in Helsinki, Finland, RWTH Aachen University in Germany, University of Exeter in the UK, and TU Delft. After obtaining his MSc degree, Marinus started his doctoral research at the department of Geoscience and Engineering at TU Delft, under the guidance of Dr. M.W.N. Buxton and Dr. F.J.A. van Ruitenbeek. The promotor of his doctorate was Prof. dr. ir. J.D. Jansen.

marinusdalm@hotmail.com

linkedin.com/in/marinusdalm

roadtripping with 700kg of sample material

Publications

Dalm, M., Buxton, M.W.N., Guatame-Garcia, L.A., Desta, F.S., van Ruitenbeek, F.J.A., (2017). A review of sensors applicable to real-time raw material characterisation in mining. Book publication (In preparation).

Dalm, M., Buxton, M.W.N., van Ruitenbeek, F.J.A., 2018. Ore–waste discrimination in epithermal deposits using near-infrared to short-wavelength infrared (NIR-SWIR) hyperspectral imagery. Mathematical geosciences, 1-27.

Dalm, M., Buxton, M.W.N., van Ruitenbeek, F.J.A., 2017. Discriminating ore and waste in a porphyry copper deposit using short-wavelength infrared (SWIR) hyperspectral imagery. Minerals Engineering, 105, 10-18.

Dalm, M., Buxton, M.W.N., 2015. Characterizing the economic value of an epithermal Au-Ag ore with laser induced breakdown spectroscopy (LIBS): possibilities and limitations. Sensor-Based Sorting and Control (SBSC) 2016 – conference proceedings. Aachen, Germany.

Dalm, M., Buxton, M.W.N., van Ruitenbeek, F.J.A., 2015. Applicability of Near-InfraRed Hyperspectral Imagery (NIR-HI) for sensor based sorting of an epithermal Au-Ag ore. Conference Of Metallurgists (COM) 2015 – conference proceedings. Toronto, Canada

Dalm, M., Buxton, M.W.N., van Ruitenbeek, F.J.A., 2015. Application of near-infrared (NIR) spectroscopy to sensor based sorting of an epithermal Au-Ag ore. OCM 2015 – conference proceedings. Karlsruhe, Germany.

Dalm, M., Buxton, M.W.N., van Ruitenbeek, F.J.A., Voncken, J.H.L., 2014. Application of near-infrared spectroscopy to sensor based sorting of a porphyry copper ore. Minerals Engineering, 58, 7-16.

MSc. theses related to this PhD research

Verhallen, G.J., 2016. Characterizing the valuable content of Au ores from the Cortez Hills underground deposit using digital RGB images (based on all the Cortez drill core samples). MSc. thesis TU Delft.

van der Linde, M.M., 2015. Characterization of alteration and mineralization of Chimú Formation quartzite with nearinfrared spectroscopy (based on 281 drill core samples of 6 drill holes of Lagunas Norte). MSc. thesis TU Delft.

BSc. theses related to this PhD research

de Waard, R.B., 2016. Characterization of low-grade epithermal gold ore using long-wavelength infrared spectroscopy (based on all the Lagunas Norte drill core samples). BSc. thesis TU Delft.

Koomen, S., 2016. Characterization of Gold Ores with Dual Energy X-Ray Transmission (based on 210 drill core samples of Cortez). BSc. thesis TU Delft.

Breukelman, H., 2015. Characterization of Epithermal Au-Ag ores using Mid-Infrared Spectroscopy (based on 21 drill core samples of Lagunas Norte). BSc. thesis TU Delft.

Bij, N., 2014. Characterization of gold ores using nearinfrared spectroscopy (based on 35 drill core samples of 1 drill hole of Lagunas Norte). BSc. thesis TU Delft.

Groenheide, S., 2014. Characterization of gold ores with Dual Energy X-Ray Transmission (DE-XRT) (based on 90 drill core samples of 1 drill hole of Lagunas Norte). BSc. thesis TU Delft.

Bode, D.C., 2014. Characterization of carbonaceous Au ores with dual energy X-ray transmission (based on 121 carbonaceous drill core samples of 17 drill holes of Lagunas Norte). BSc. thesis TU Delft.

Kempke, A.T., 2014. Characterization of Lagunas Norte Au ores with Laser Induced Breakdown Spectroscopy (LIBS) (based on 8 drill core samples of Lagunas Norte). BSc. thesis TU Delft.

Roukema, M., 2013. DE-XRT assessment on porphyry copper ore from Chile (based on the samples from Los Bronces). BSc. thesis TU Delft.